

Self-healing Polyimides

Susa, Arijana

DOI

[10.4233/uuid:49ce6618-c9d5-4a46-bbc9-7439484d1ff8](https://doi.org/10.4233/uuid:49ce6618-c9d5-4a46-bbc9-7439484d1ff8)

Publication date

2019

Document Version

Final published version

Citation (APA)

Susa, A. (2019). *Self-healing Polyimides*. [Dissertation (TU Delft), Delft University of Technology]. <https://doi.org/10.4233/uuid:49ce6618-c9d5-4a46-bbc9-7439484d1ff8>

Important note

To cite this publication, please use the final published version (if applicable). Please check the document version above.

Copyright

Other than for strictly personal use, it is not permitted to download, forward or distribute the text or part of it, without the consent of the author(s) and/or copyright holder(s), unless the work is under an open content license such as Creative Commons.

Takedown policy

Please contact us and provide details if you believe this document breaches copyrights. We will remove access to the work immediately and investigate your claim.

Self-healing Polyimides

Arijana Suša

DELFT UNIVERSITY OF TECHNOLOGY

Doctoral dissertation

2019

Self-healing Polyimides

PROEFSCHRIFT

ter verkrijging van de graad van doctor
aan de Technische Universiteit Delft,
op gezag van de Rector Magnificus prof.dr.ir. T.H.J.J. van der Hagen
voorzitter van het College voor Promoties,
in het openbaar te verdedigen op
vrijdag 26 April 2019 om 10:00 uur

door

Arijana SUŠA

Master of Science in Chemical Engineering
University of Zagreb, Kroatië

geboren te Rijeka, Kroatië

This dissertation has been approved by the promotor.

Composition of the doctoral committee:

Rector Magnificus	Chairman
Prof.dr.ir. S. van der Zwaag	Technische Universiteit Delft, promotor
Dr. S.J. García Espallargas	Technische Universiteit Delft, promotor

Independent members:

Prof.dr. A.M. Schmidt	Universität zu Köln, Germany
Prof.dr.ir. S.C.G. Leeuwenburgh	Radboud Universiteit
Dr.ir. A.L.M. Smits	Croda Nederland BV
Prof. C.A. Dransfeld	Technische Universiteit Delft
Prof.dr. S.J. Picken	Technische Universiteit Delft

The research carried out in this thesis was funded by Dutch IOP program on self-healing materials under Grant No. IOP-SHM-012036.



Rijksdienst voor Ondernemend
Nederland



ISBN: 978-94-028-1431-6

An electronic version of this dissertation is available at
<http://repository.tudelft.nl/>.

Cover: High resolution satellite image of Caribbean coast, coral reef and sand structures of Bahamas, contains modified Copernicus Sentinel data.

Design by Tim van Ommeren.

Printed by Ipskamp Printing, Enschede.

Copyright © 2019 by A. Suša

All rights reserved. No part of this publication may be reproduced, stored in a retrieval system or transmitted in any form or by any means, electronic, mechanical, photocopying, recording or otherwise, without the prior written permission of the author.

*Znaš li što ću ja postati
kada odrastem,
za tvoju ljepotu, svijete?*

*Ja kada odrastem
jako veliki,
ja ću postati dijete.*

*Najljepše je kad odrasteš,
a ostaneš dječji stvor,
pa svi misle da si velik
zato što si profesor.*

*Što si doktor od imena,
stručnjak za rakete -
a ne znaju da si velik
zato što si dijete.*

*Možeš biti pilot, rudar...
slavni pisac knjiga -
djetetu je svaki pos'o
lagan kao igra.*

*Ma nosio ja u glavi
i sve fakultete,
kad odrastem jako velik,
ja ću ostat' dijete.*

Enes Kišević

Contents

Chapter 1 - Introduction	1
1.1. Introduction.....	2
1.2. Intrinsic self-healing polymers.....	4
1.2.1. Reversible covalent chemistries.....	5
1.2.2. Reversible non-covalent (supramolecular) chemistries.....	6
1.2.3. Interfacial physical healing.....	7
1.3. Importance of polymer architecture in intrinsic healing.....	8
1.4. Challenges and prospects.....	9
1.5. Thesis scope and outline.....	9
References.....	11
Chapter 2 - Unravelling the self-healing mechanism	17
Abstract.....	18
2.1. Introduction.....	19
2.2. Experimental.....	21
2.2.1. Synthesis.....	21
2.2.2. Characterization methods.....	24
2.3. Results and discussion.....	26
2.3.1. Effect of ODPA/DDI ratio on the branched-PEI properties.....	26
2.3.2. Effect of the polymer architecture on the room temperature healing.....	36
2.3.3. Relationship between polymer architecture and healing.....	38
2.4. Conclusions.....	42
References.....	43
Supporting information.....	48
Chapter 3 - Imaging the molecular motions of autonomous repair in a self-healing polymer	59
Abstract.....	60
3.1. Introduction.....	61
3.2. Experimental.....	62
3.2.1. Materials.....	62
3.2.2. Methods and data analysis.....	63
3.3. Results and discussion.....	64
3.4. Conclusions.....	69
References.....	71
Supporting information.....	74

Chapter 4 - <i>Understanding the effect of the dianhydride structure on polymer properties</i>	91
Abstract.....	92
4.1. Introduction.....	93
4.2. Experimental.....	95
4.2.1. <i>Synthesis</i>	95
4.2.2. <i>Characterization methods</i>	97
4.3. Results and discussion.....	100
4.3.1. <i>Effect of the dianhydride structure on the PIs properties</i>	100
4.3.2. <i>Effect of the low temperature annealing on local ordering</i>	108
4.4. Conclusions.....	113
References.....	114
Supporting information.....	118
Chapter 5 - <i>Identifying the role of primary and secondary interactions on the mechanical and healing properties</i>	129
Abstract.....	130
5.1. Introduction.....	131
5.2. Experimental.....	133
5.2.2. <i>Characterization methods</i>	135
5.2.2.1. <i>Tensile properties and interfacial healing evaluation</i>	135
5.2.2.2. <i>Rheological measurements</i>	136
5.2.2.3. <i>Solid state nuclear magnetic resonance</i>	136
5.3. Results and discussion.....	137
5.3.1. <i>Tensile experiments</i>	137
5.3.1.1. <i>Tensile behaviour of as-produced and annealed undamaged polymers</i>	137
5.3.1.2. <i>Effect of the dianhydride architecture on the macroscopic self-healing efficiency</i>	138
5.3.2. <i>Rheological experiments</i>	142
5.3.3. <i>Molecular dynamics by solid state NMR</i>	147
5.4. Correlation between macroscale healing and polymer dynamics.....	155
5.5. Conclusions.....	157
References.....	158
Supporting information.....	163

Chapter 6 - <i>Demonstrating autonomous healing of fatigue induced cracks in composites bonded with a self-healing polyimide interlayer</i>	173
Abstract.....	174
6.1. Introduction.....	175
6.2. Experimental.....	177
6.2.1. <i>Materials</i>	177
6.2.2. <i>Specimen manufacturing</i>	177
6.2.3. <i>Testing and monitoring the damage</i>	178
6.3. Results and discussion.....	180
6.3.1. <i>Clip-gauge measurements</i>	180
6.3.2. <i>Fibre-optics measurements</i>	184
6.3.3. <i>Comparison of the two test methods</i>	187
6.3.4. <i>Fracture surfaces</i>	188
6.4. Conclusions.....	190
References.....	191
Summary.....	195
Samenvatting.....	199
Acknowledgements.....	203
Curriculum Vitae.....	207
List of publications.....	209

1

Introduction

Out of your vulnerabilities will come your strength.

Sigmund Freud

1.1. Introduction

Traditionally, materials are made with the intention to make them withstand the application requirements in terms of mechanical performance or/and functionality¹ and they are expected to serve a certain lifespan without premature failure of the product or structure. To prevent those failures, the conventional materials design approach is to foresee the accumulation of micro-damages during use which undermine the material performance. Hence current materials are designed on the basis of maximization of the damage resistance, i.e. the material is resistant to damage formation and growth, but any damage formed will be present forever and can only grow.²

As opposed to this ‘damage prevention’ approach by making-materials-stronger-than-necessary, self-healing materials ideally heal damages perpetually during use, prolonging thus the lifespan of a product or structure without the need for properties/performance overcompensation. In other words, self-healing materials work by the ‘damage management’ strategy: damage is anticipated to occur, but the material can autonomously cope with the damage and make it disappear or at least make it harmless.³ For these reasons, self-healing materials are likely to find their application in fields with a long lifespan expectancy, a difficult access for maintenance or a high importance of performance reliability after the occurrence of undetected minor damage, such as encountered in aerospace, automotive, maritime and construction.²

In order to give a conventional material (concrete, metal, ceramic or polymer) a self-healing ability, the generic concept of ‘*local, temporary mobility*’ needs to be implemented.⁴ *Mobility* implies that in the solid materials (specific) atoms or molecules or other entities will move over relevant distances from their original location to the location of the nearest damage site. *Temporary* implies that the movement of the healing ‘agent’ only takes place in case of damage and stops once the damage has been healed. *Local* implies that the region of enhanced and specific mobility is restricted to a region in the vicinity of the damage. Ideally, the self-healing process would be completely autonomous; without a need for human intervention or external stimuli, such as heat, pressure, light and pH. Intuitively, the introduction of mobility in metals or ceramics at ambient conditions seems rather difficult. In contrast, polymers are gifted with a high intrinsic SH potential

to introduce local, temporary mobility. This is one of the main reasons why most of the first generation synthetic self-healing materials were polymers.⁵⁻⁶

The self-healing concepts in polymers are commonly categorized into extrinsic and intrinsic. Extrinsic healing, also called 'first generation' self-healing materials are essentially composites that irreversibly repair but do not restore damaged matrix.⁷ This approach consists of incorporating self-healing agent filled microcapsules or fibres into a non-healable, i.e. inert polymer matrix. In the event of a crack, the capsules or fibres break, releasing the mobile healing agent (generally a liquid, but it can also be bacteria⁸ in the case of concrete) into the crack plane. This healing agent then travels to the crack tip by capillary or other forces and once arrived there loses its mobility by a chemical reaction. For the reaction to take place, often two different reactants are required, and both are to be embedded in the same matrix. The most well-known healing agents reported are systems like epoxy/amine, endo-dicyclopentadiene and thiol/isocyanate,^{4, 9-13} but there have also been attempts to use polymeric solvents as the healing agent.¹⁴

Even though extrinsic self-healing polymers and polymer-based fibre composites usually display decent mechanical properties (provided by the inert matrix material) and do not need external stimuli for healing to take place, the actual concept leads to inherent disadvantages such as complex manufacturing,¹⁵⁻¹⁶ processing difficulties^{13, 17} and limited healing agent delivery, and most importantly a 'single use only'. To deliver sufficient amounts of healing agent, microcapsules were replaced by continuous hollow fibres¹⁸ and microvascular systems.¹⁶ However, upon the crack event, the liquid agent would deplete in excess, thus disabling the opportunity for multiple healing of successive damage events.¹⁸

Multiple healing in extrinsic healing polymer systems was finally achieved by making the fibres not continuous, but by giving them a compartmented structure.^{13, 19} Mookhoek et al. made compartmented alginate fibres containing healing agent filled vacuoles along the fibre direction.¹⁹ Unlike the microcapsules and hollow fibres, this approach led to good distribution of relatively large volumes of healing agent throughout the polymer matrix. However, even after several attempts from other authors to improve the mechanical properties of relatively flexible alginate fibres, their mechanical performance remained unsatisfactory. Therefore the authors raised serious concern whether the self-healing property can

sufficiently compensate the reduction in initial properties and damage resistance of high quality fibre reinforced.²⁰ The common drawback of all extrinsic systems therefore remains the inability to heal the same damaged area multiple times.

1.2. Intrinsic self-healing polymers

As opposed to the extrinsic systems, in intrinsic self-healing polymer the material itself is responsible for the healing process and there are no irreversible aspects in the healing process. For intrinsic self-healing polymers, no external healing agents are needed, processing becomes easier and most importantly they are capable of fully or partially healing the damage at the same location multiple times. They are also called the 'second generation' self-healing materials: materials that reversibly restore damaged matrix.⁷ Even though until recently intrinsic healing was restricted to thermoplastics, it can now be introduced to thermosets²¹⁻²² and elastomers²³⁻²⁴ as well, via a variety of mechanisms.

Generally, intrinsic self-healing polymers are based on specifically designed chemistries which allow for the local temporary mobility when the polymer is subjected to a certain stimulus (heat, pressure, UV or pH change) resulting in repair of broken chemical or physical bonds during stimulus application. The damage repair occurs via its crucial virtue: a temporary increase in mobility resulting in a physical flow of a material into the damaged area. The analogy of this process can be made with the working principle of a zipper: the act of opening (introducing damage) followed by closing (repairing the damage and bringing back the material to its original state).^{7, 25-26}

Apart from when in the molten state, most non-healable covalent polymers have slow molecular dynamics and a high energy barrier for molecular rearrangement which makes the reversible repair kinetically unattainable. For that reason, all second-generation self-healing polymer systems utilize either weak bonds that are reversible at low temperature or application-specific types of damage introduction where the damage itself provides the energy necessary for molecular rearrangement (damage induced localized melting). The common condition to all the successful approaches is that the local reversibility (bond reformation) is

significantly faster than global processes (polymer flow and macroscopic deformation).⁷

Intrinsic self-healing mechanisms are commonly categorized according to the molecular mechanisms responsible for the healing: i) reversible covalent chemistries, ii) supramolecular chemistries and iii) interfacial physical healing.²⁷ In order to increase the mechanical properties of intrinsic self-healing polymers there has been a very recent trend to develop intrinsic polymer systems using combinations of several healing concepts within a single material.²⁸

1.2.1. Reversible covalent chemistries

Reversible covalent bonds have been widely explored in the development of self-healing polymers due to their high bond strength, which results in good mechanical properties. In the design of self-healing polymer, the dissociation and association rates of the dynamic bonds as well as the chain mobility are important parameters.²⁶ From ring-chain equilibria and reactive polymer blends to controlled (living) free radical polymerization allowing a reorganization of the polymer architecture, these chemistries have been known to the polymer community for a long time.²⁵

Contemporary dynamic covalent polymers utilize a wide range of well-known reaction types including ring-chain equilibria and chain-exchange reaction as in the case of retro Diels-Alder (DA) reactions,²⁹⁻³³ alkoxyamines,³⁴ disulfides and polysulfides,^{21, 23, 35-37} trithiocarbonate exchange reactions,³⁸ reversible hydrazone linkages,³⁹ cross-linked poly(dimethylsiloxane)⁴⁰ and diarylbenzofuranone.⁴¹ In general, one important downside of covalent reversible bonds is their high activation energy. As a result, in order to be healed these systems require being heated. For example, in self-healing polymers based on Diels–Alder (DA) reactions, the activation temperature of the retro-DA reaction is 120 °C and this sets the scope for the healing temperature. As such polymers can have a T_g as high as 100 °C, the exposure to the high temperature is not a problem per se, but high temperature exposure may not be possible or desirable from an application-related perspective. Ideally, bond dissociation and re-association should proceed at ambient conditions. Nevertheless, other types of triggers for healing have been explored as well. Some of the examples of alternative triggers include light

irradiation for [2+2] photocycloaddition⁴² or opening/closing a [4+4] photocycle,⁴³⁻⁴⁴ pH changes³⁹ or catalytic additives.²⁶⁻²⁷

1.2.2. Reversible non-covalent (supramolecular) chemistries

The mechanical properties of a supramolecular polymer are due to the self-organization of highly directional and reversible non-covalent interactions. This is achieved by covalently attaching associative groups to side chains or chain ends of the polymer backbone, which transforms the liquid-like polymers into a non-covalently crosslinked network with a plastic or rubbery behaviour. There are several types of supramolecular interactions: hydrogen bonds, metal coordination, ionic interactions, π - π stacking, host-guest interactions and hydrophobic interactions. These interactions are ideal for intrinsic self-healing polymers design, due to their reversibility and speed, directionality and sensitivity. As opposed to covalent bonds, these systems can be remodelled rapidly and reversibly from fluid-like to solid-like states.²⁶

The most studied interactions so far are ionic⁴⁵⁻⁵¹ and hydrogen bonding represented by the well-defined ureidopyrimidinone unit⁵²⁻⁵³ and randomly branched oligomers equipped with self-complementary and complementary hydrogen bonding groups.⁵⁴⁻⁵⁵ In fact, the first commercial self-healing polymer launched as a fruit of collaboration between the School of Industrial Physics and Chemistry of the City of Paris (ESPCI) and Arkema was based on the work of Sijbesma et al^{54, 56} using quadruple hydrogen bonding. Other supramolecular chemistries, such as metal-ligand coordination⁵⁷⁻⁶¹ and π - π stacking⁶²⁻⁶³ have been less studied. Some approaches involve more than one type of supramolecular interactions, such as a combination of π - π stacking and hydrogen bonding⁶³ or π - π stacking and attractive metallophilic interaction of metallic atoms.⁶⁴

Despite the exhaustive variety of successful chemistries available to create intrinsic healing, there is a lack of studies showing that interfacial healing can be obtained purely by chemical approaches with no molecular inter-diffusion step involved.²⁵

1.2.3. Interfacial physical healing

One of the oldest and most accepted theories on the interfacial physical healing is that by Wool and O'Connor.⁶⁵ Their theory distinguishes five stages (see Figure 1.1):

- 1) *Surface rearrangement*, which affects the diffusion initiation function and interfacial topological features;
- 2) *Approach*, which controls the mode of healing;
- 3) *Wetting*, which controls the wetting distribution function;
- 4) *Diffusion*, which controls the development of mechanical properties during healing;
- 5) *Randomization*, which results in a complete disappearance of the former crack interface.⁶⁶

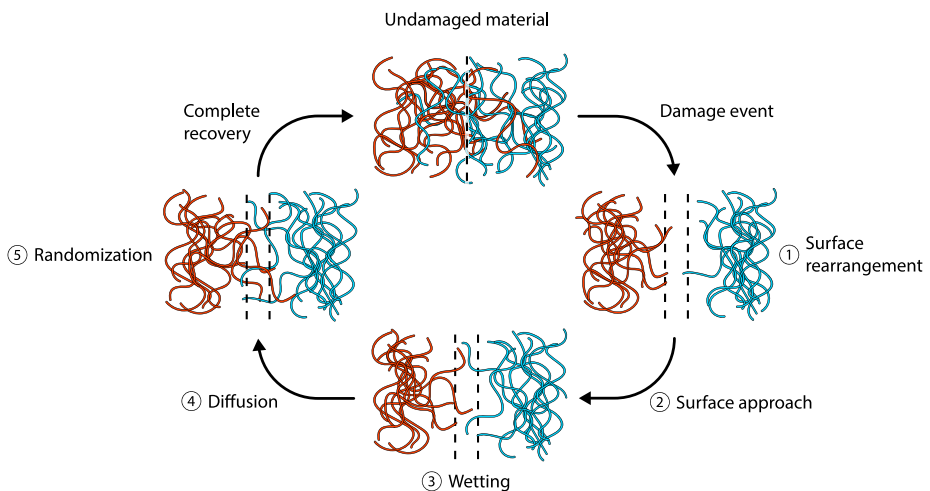


Figure 1.1. The schematic representation of the five-stage physical self-healing.

The above processes can take place at temperatures above the bulk glass transition temperature (T_g)⁶⁶, upon exposure to an external trigger or/and at temperatures above the melting point (T_m) as in thermoplastic welding.⁶⁷ Physical healing of a (weak) gel with a permanent network was achieved by Yamaguchi et al by the interdiffusion of dangling chains and entanglement couplings. In their materials, the

relationship between the healing temperature and T_g determines the time required for healing. In other words, a material shows an immediate onset of healing when its T_g is below healing temperature.⁶⁸

Nevertheless, chain inter-diffusion has also been observed at temperatures below the bulk T_g . This finding points out to the existence of a variation in T_g values between the bulk and the surface in freshly damaged materials which affects the healing process.^{25, 65} The same phenomenon has been also observed in the healing of ice.

A successful way of utilizing localized T_g variations was demonstrated by Chen et al⁶⁹ who created a heterogeneous polymer consisting of a spherical polystyrene rigid phase within a soft polyamide matrix able to form H-bonds. These networks can spontaneously rearrange themselves analogous to liquid crystalline polymers, which is manifested by an increase in entropy, leading to subsequent re-bonding.²⁶ Conversely, Watanabe et al reported that physical healing of thermoplastic elastomers triblock copolymers polystyrene-*b*-polybutadiene-*b*-polystyrene (SBS) and polystyrene-*b*-polyisoprene-*b*-polystyrene (SIS) was impaired when the systems were first allowed to phase-separate upon slow cooling. The improved healing when polymers were fast-cooled (quenched) was attributed to the mutual dissolution of both soft (PB/PI) and hard (PS) segments, responsible for the pronounced molecular mobility.⁷⁰

1.3. Importance of polymer architecture in intrinsic healing

Reversible covalent chemistries can provide polymers with a high T_g and reasonable mechanical properties yet require specific external stimuli to achieve healing. As opposed, supramolecular systems are capable of fully autonomous healing, yet their properties still do not come close to most of those set by application requirements.²⁵ Both of these drawbacks need to be tackled before intrinsic healing concepts can be found in polymers for daily life products. Even though the physical component of the healing process has not been sufficiently studied so far, the emerging studies indicate that the joint work of both chemical and physical aspects is the right way to unite autonomous healing and good mechanical properties. I.e.,

in the self-healing polymers design it is crucial to adjust stability of the reactive groups (both covalent and supramolecular) with the interfacial flow kinetics. For diffusion-driven re-bonding, maintaining local liquid-like mobility in the interfacial regions will be critical.²⁶ Some of the approaches to induce localized mobility into a strong polymer structure is to build the chains comprising both soft (low T_g) and hard (high T_g) segments, which in most of the cases results in the presence of heterogeneities at molecular and mesoscale scale lengths that facilitate self-healing.^{26, 61, 69, 71-72}

1.4. Challenges and prospects

While most of the current studies to obtain self-healing polymers focus on the chemistries to obtain self-healing, physical aspects are equally significant, as the unique self-healing properties are a consequence of a number of orchestrated physical-chemical events. This complexity and interplay of inherent properties makes concept-based self-healing polymer design a really challenging topic.

That being said, there is a need for combining chemical analysis with localized mechanical testing in order to advance our knowledge in the field of intrinsic self-healing polymers.²⁶ Future studies should focus on multiphase polymer design and understanding its effect on the physical healing aspects. This synergistic approach is my preferred route to achieve fast and fully autonomous healing of strong polymers.

1.5. Thesis scope and outline

The research as described in this thesis aims to develop a new type of intrinsic self-healing polymers, in particular polyimides, with improved mechanical properties and good healing kinetics and to study the underlying healing mechanisms from both a chemical and a physical perspective. To that aim, each chapter addresses a different scientific question and the answers together build up a more complete level of understanding of the effects of the polymer architecture on the mechanical properties and self-healing behaviour of these polyimides.

Chapter 2 describes the syntheses and complete chemical, thermal, mechanical and healing characterization of the first self-healing polyimides comprising of a branched dimer diamine as the soft block and an aromatic dianhydride as the hard block. In the chapter it is reported how the polymer architecture changes with the monomers offset ratio and how this affects the mechanical and healing properties.

Chapter 3 reports the first-ever visualization of the molecular repair in a self-healing polymer. It demonstrates how optical micromechanical mapping enables the quantitative imaging of molecular-scale dynamics with high spatiotemporal resolution. This chapter aims to unravel the delocalized viscoelastic relaxation and the localized cohesion-restoring re-bonding processes that occur simultaneously upon damage and healing.

Chapter 4 studies the effect of the hard block dianhydride structure on the overall properties of these polyimides. The detailed analysis considers several aspects of the dianhydrides structure (planarity, rigidity, bridging group between the phthalimides, electronic properties). Moreover, the effects of physical parameters (crystallization and electronic interactions) on the relaxation behaviour are discussed. The results highlight the potential of polymer property design by controlled engineering of the aromatic dianhydride blocks.

Chapter 5 uses the polymers developed in *Chapter 4* to study their self-healing behaviour. I studied the molecular and microscale dynamics of four polyimides containing the same aliphatic branched diamine yet with variable dianhydride rigidities and correlated these to their macroscopic healing kinetics. The study reveals the interplay and relevance of primary and secondary interactions in the development of non-crosslinked strong yet self-healing polymers able to maintain mechanical integrity during healing.

Chapter 6 aims to explore the feasibility of using the most promising polyimide grade developed in this thesis as a thin film self-healing thermoplastic adhesive in an adhesively bonded joint in a glass-fibre reinforced epoxy thermoset composite structure. To that aim, a novel fibre optics local strain monitoring system in combination with the standard clip-gauge device was used to monitor delamination during fatigue loading and interspersed healing treatments, and to get a more detailed insight into the ply-dependent damage and healing behaviour.

References

1. Zhu, M.; Rong, M. Z.; Zhang, M. Q., Self-Healing Polymeric Materials Towards Non-Structural Recovery of Functional Properties. *Polymer International* **2014**, *63* (10), 1741-1749.
2. van der Zwaag, S.; Brinkman, E., Introduction to Self Healing Materials and the IOP Self Healing Materials Program. In *Self Healing Materials-Pioneering Research in the Netherlands*, IOS Press: Amsterdam, 2015; pp vii-xiv.
3. van der Zwaag, S., An Introduction to Material Design Principles: Damage prevention versus Damage Management. In *Self-Healing Materials: An Alternative Approach to 20 Centuries of Materials Science*, van der Zwaag, S., Ed. Springer: Dordrecht, 2007; pp 8-9.
4. White, S. R.; Sottos, N. R.; Geubelle, P. H.; Moore, J. S.; Kessler, M. R.; Sriram, S. R.; Brown, E. N.; Viswanathan, S., Autonomic Healing of Polymer Composites. *Nature* **2001**, *409*, 794.
5. Dry, C. M.; Sottos, N. R. In *Passive Smart Self-Repair in Polymer Matrix Composite Materials*, 1993 North American Conference on Smart Structures and Materials, SPIE: 1993; p 7.
6. Dry, C., Procedures Developed for Self-Repair of Polymer Matrix Composite Materials. *Composite Structures* **1996**, *35* (3), 263-269.
7. Brochu, A. B. W.; Craig, S. L.; Reichert, W. M., Self-Healing Biomaterials. *Journal of Biomedical Materials Research Part A* **2011**, *96A* (2), 492-506.
8. Jonkers, H. M.; Schlangen, E. In *Self-Healing of Cracked Concrete: A Bacterial Approach*, Proceedings of FRACOS6: fracture mechanics of concrete and concrete structures. , Catania, Italy, CRC Press: Catania, Italy, 2007; pp 1821-1826.
9. McIlroy, D. A.; Blaiszik, B. J.; Caruso, M. M.; White, S. R.; Moore, J. S.; Sottos, N. R., Microencapsulation of a Reactive Liquid-Phase Amine for Self-Healing Epoxy Composites. *Macromolecules* **2010**, *43* (4), 1855-1859.
10. Hillewaere, X.; Teixeira, R.; Nguyen, L.-T.; Ramos, J.; Rahier, H.; Du Prez, F., Autonomous Self-Healing of Epoxy Thermosets with Thiol-Isocyanate Chemistry. *Advanced Functional Materials* **2014**, *24* (35), 5575-5583.
11. Neuser, S.; Chen, P. W.; Studart, A. R.; Michaud, V., Fracture Toughness Healing in Epoxy Containing Both Epoxy and Amine Loaded Capsules. *Advanced Engineering Materials* **2014**, *16* (5), 581-587.
12. Hillewaere, X.; Du Prez, F., Fifteen Chemistries for Autonomous External Self-Healing Polymers and Composites. *Progress in Polymer Science* **2015**, *49-50*, 121-153.
13. Post, W. Self-Healing Polymer Composites. Doctoral thesis, Delft University of Technology, Netherlands, 2017.

14. Mookhoek, S. D.; Mayo, S. C.; Hughes, A. E.; Furman, S. A.; Fischer, H. R.; van der Zwaag, S., Applying SEM-Based X-ray Microtomography to Observe Self-Healing in Solvent Encapsulated Thermoplastic Materials. *Advanced Engineering Materials* **2010**, *12* (3), 228-234.
15. Toohey, K. S.; Sottos, N. R.; Lewis, J. A.; Moore, J. S.; White, S. R., Self-Healing Materials with Microvascular Networks. *Nature Materials* **2007**, *6*, 581.
16. Toohey, K. S.; Hansen, C. J.; Lewis, J. A.; White, S. R.; Sottos, N. R., Delivery of Two-Part Self-Healing Chemistry via Microvascular Networks. *Advanced Functional Materials* **2009**, *19* (9), 1399-1405.
17. Kessler, M. R.; Sottos, N. R.; White, S. R., Self-Healing Structural Composite Materials. *Composites Part A: Applied Science and Manufacturing* **2003**, *34* (8), 743-753.
18. Pang, J.; Bond, I. P., A Hollow Fibre Reinforced Polymer Composite Encompassing Self-Healing and Enhanced Damage Visibility. *Composites Science and Technology* **2005**, *65* (11-12), 1791-1799.
19. Mookhoek, S. D.; Fischer, H. R.; van der Zwaag, S., Alginate Fibres Containing Discrete Liquid Filled Vacuoles for Controlled Delivery of Healing Agents in Fibre Reinforced Composites. *Composites Part A: Applied Science and Manufacturing* **2012**, *43* (12), 2176-2182.
20. Post, W.; Jeoffroy, E.; García, S. J.; van der Zwaag, S., Self-Healing Glass Fiber Reinforced Polymer Composites Based on Montmorillonite Reinforced Compartmented Alginate Fibers. *Polymer Composites* **2017**.
21. Abdollahzadeh, M.; Esteves, A. C.; van der Zwaag, S.; Garcia, S. J., Healable Dual Organic-Inorganic Crosslinked Sol-Gel Based Polymers: Crosslinking Density and Tetrasulfide Content Effect. *Journal of Polymer Science Part A: Polymer Chemistry* **2014**, *52* (14), 1953-1961.
22. Hu, Z.; Zhang, D.; Lu, F.; Yuan, W.; Xu, X.; Zhang, Q.; Liu, H.; Shao, Q.; Guo, Z.; Huang, Y., Multistimuli-Responsive Intrinsic Self-Healing Epoxy Resin Constructed by Host-Guest Interactions. *Macromolecules* **2018**, *51* (14), 5294-5303.
23. Hernández, M.; Grande, A. M.; Dierkes, W.; Bijleveld, J.; van der Zwaag, S.; García, S. J., Turning Vulcanized Natural Rubber into a Self-Healing Polymer: Effect of the Disulfide/Polysulfide Ratio. *ACS Sustainable Chemistry & Engineering* **2016**, *4* (10), 5776-5784.
24. Ellingford, C.; Zhang, R.; Wemyss, A. M.; Bowen, C.; McNally, T.; Figiel, Ł.; Wan, C., Intrinsic Tuning of Poly(styrene-butadiene-styrene)-Based Self-Healing Dielectric Elastomer Actuators with Enhanced Electromechanical Properties. *ACS Applied Materials & Interfaces* **2018**, *10* (44), 38438-38448.

25. Garcia, S. J., Effect of Polymer Architecture on the Intrinsic Self-Healing Character of Polymers. *European Polymer Journal* **2014**, *53*, 118-125.
26. Yang, Y.; Ding, X.; Urban, M. W., Chemical and Physical Aspects of Self-Healing Materials. *Progress in Polymer Science* **2015**, *49-50*, 34-59.
27. Garcia, S. J.; Fischer, H. R., Self-Healing Polymer Systems: Properties, Synthesis and Applications. In *Smart Polymers and their Applications*, Aguilar, M. R.; San Román, J., Eds. Woodhead Publishing: 2014; pp 271-298.
28. Grande, A. M.; Bijleveld, J. C.; Garcia, S. J.; van der Zwaag, S., A Combined Fracture Mechanical – Rheological Study to Separate the Contributions of Hydrogen Bonds and Disulphide Linkages to the Healing of Poly(urea-urethane) Networks. *Polymer* **2016**, *96*, 26-34.
29. Chen, X.; Dam, M. A.; Ono, K.; Mal, A.; Shen, H.; Nutt, S. R.; Sheran, K.; Wudl, F., A Thermally Re-mendable Cross-Linked Polymeric Material. *Science* **2002**, *295* (5560), 1698-1702.
30. Chujo, Y.; Sada, K.; Saegusa, T., Reversible Gelation of Polyoxazoline by Means of Diels-Alder Reaction. *Macromolecules* **1990**, *23* (10), 2636-2641.
31. Murphy, E. B.; Bolanos, E.; Schaffner-Hamann, C.; Wudl, F.; Nutt, S. R.; Auad, M. L., Synthesis and Characterization of a Single-Component Thermally Remendable Polymer Network: Staudinger and Stille Revisited. *Macromolecules* **2008**, *41* (14), 5203-5209.
32. Coope, T. S.; Turkenburg, D. H.; Fischer, H. R.; Luterbacher, R.; van Bracht, H.; Bond, I. P., Novel Diels-Alder Based Self-Healing Epoxies for Aerospace Composites. *Smart Materials and Structures* **2016**, *25* (8), 084010.
33. Zeng, C.; Seino, H.; Ren, J.; Hatanaka, K.; Yoshie, N., Bio-Based Furan Polymers with Self-Healing Ability. *Macromolecules* **2013**, *46* (5), 1794-1802.
34. Otsuka, H.; Aotani, K.; Higaki, Y.; Amamoto, Y.; Takahara, A., Thermal Reorganization and Molecular Weight Control of Dynamic Covalent Polymers Containing Alkoxyamines in Their Main Chains. *Macromolecules* **2007**, *40* (5), 1429-1434.
35. Canadell, J.; Goossens, H.; Klumperman, B., Self-Healing Materials Based on Disulfide Links. *Macromolecules* **2011**, *44* (8), 2536-2541.
36. Otsuka, H.; Nagano, S.; Kobashi, Y.; Maeda, T.; Takahara, A., A Dynamic Covalent Polymer Driven by Disulfide Metathesis under Photoirradiation. *Chemical Communications* **2010**, *46* (7), 1150-1152.
37. Lafont, U.; van Zeijl, H.; van der Zwaag, S., Influence of Cross-linkers on the Cohesive and Adhesive Self-Healing Ability of Polysulfide-Based Thermosets. *ACS Applied Materials & Interfaces* **2012**, *4* (11), 6280-6288.
38. Amamoto, Y.; Kamada, J.; Otsuka, H.; Takahara, A.; Matyjaszewski, K., Repeatable Photoinduced Self-Healing of Covalently Cross-Linked Polymers

through Reshuffling of Trithiocarbonate Units. *Angewandte Chemie International Edition* **2011**, 50 (7), 1660-1663.

39. Deng, G.; Tang, C.; Li, F.; Jiang, H.; Chen, Y., Covalent Cross-Linked Polymer Gels with Reversible Sol–Gel Transition and Self-Healing Properties. *Macromolecules* **2010**, 43 (3), 1191-1194.

40. Zheng, P.; McCarthy, T. J., A Surprise from 1954: Siloxane Equilibration Is a Simple, Robust, and Obvious Polymer Self-Healing Mechanism. *Journal of the American Chemical Society* **2012**, 134 (4), 2024-2027.

41. Imato, K.; Nishihara, M.; Kanehara, T.; Amamoto, Y.; Takahara, A.; Otsuka, H., Self-Healing of Chemical Gels Cross-Linked by Diarylbibenzofuranone-Based Trigger-Free Dynamic Covalent Bonds at Room Temperature. *Angewandte Chemie International Edition* **2012**, 51 (5), 1138-1142.

42. Ling, J.; Rong, M. Z.; Zhang, M. Q., Photo-Stimulated Self-Healing Polyurethane Containing Dihydroxyl Coumarin Derivatives. *Polymer* **2012**, 53 (13), 2691-2698.

43. Froimowicz, P.; Frey, H.; Landfester, K., Towards the Generation of Self-Healing Materials by Means of a Reversible Photo-induced Approach. *Macromolecular Rapid Communications* **2011**, 32 (5), 468-473.

44. Ghosh, B.; Urban, M. W., Self-Repairing Oxetane-Substituted Chitosan Polyurethane Networks. *Science* **2009**, 323 (5920), 1458-60.

45. Kalista, S. J., Self-Healing Ionomers. In *Self-healing Materials: Fundamentals, Design Strategies, and Applications*, Wiley-VCH Weinheim: 2009; pp 73-100.

46. Varley, R. J.; van der Zwaag, S., Towards an Understanding of Thermally Activated Self-Healing of an Ionomer System during Ballistic Penetration. *Acta Materialia* **2008**, 56 (19), 5737-5750.

47. Varley, R. J.; Shen, S.; van der Zwaag, S., The Effect of Cluster Plasticisation on the Self Healing Behaviour of Ionomers. *Polymer* **2010**, 51 (3), 679-686.

48. Kalista, S. J.; Pflug, J. R.; Varley, R. J., Effect of Ionic Content on Ballistic Self-Healing in EMAA Copolymers and Ionomers. *Polymer Chemistry* **2013**, 4 (18), 4910-4926.

49. Reisch, A.; Roger, E.; Phoeung, T.; Antheaume, C.; Orthlieb, C.; Boulmedais, F.; Lavalle, P.; Schlenoff, J. B.; Frisch, B.; Schaaf, P., On the Benefits of Rubbing Salt in the Cut: Self-Healing of Saloplastic PAA/PAH Compact Polyelectrolyte Complexes. *Advanced materials (Deerfield Beach, Fla.)* **2014**, 26 (16), 2547-51.

50. Huang, Y.; Lawrence, P. G.; Lapitsky, Y., Self-Assembly of Stiff, Adhesive and Self-Healing Gels from Common Polyelectrolytes. *Langmuir* **2014**, 30 (26), 7771-7777.

51. Post, W.; Bose, R.; García, S.; van der Zwaag, S., Healing of Early Stage Fatigue Damage in Ionomer/Fe₃O₄ Nanoparticle Composites. *Polymers* **2016**, *8* (12), 436.
52. Sijbesma, R.; Beijer, F.; Brunsveld, L.; Folmer, B.; Hirschberg, J.; Lange, R.; Lowe, J.; Meijer, E., Reversible Polymers Formed from Self-Complementary Monomers Using Quadruple Hydrogen Bonding. *Science* **1997**, *278* (5343), 1601-1604.
53. Bosman, A. W.; Sijbesma, R. P.; Meijer, E. W., Supramolecular Polymers at Work. *Materials Today* **2004**, *7* (4), 34-39.
54. Cordier, P.; Tournilhac, F.; Soulié-Ziakovic, C.; Leibler, L., Self-Healing and Thermoreversible Rubber from Supramolecular Assembly. *Nature* **2008**, *451*, 977.
55. Montarnal, D.; Tournilhac, F.; Hidalgo, M.; Couturier, J.-L.; Leibler, L., Versatile One-Pot Synthesis of Supramolecular Plastics and Self-Healing Rubbers. *Journal of the American Chemical Society* **2009**, *131* (23), 7966-7967.
56. <https://www.arkema.com/en/>.
57. Williams, K. A.; Boydston, A. J.; Bielawski, C. W., Towards Electrically Conductive, Self-Healing Materials. *Journal of the Royal Society Interface* **2007**, *4* (13), 359-362.
58. Burnworth, M.; Tang, L.; Kumpfer, J. R.; Duncan, A. J.; Beyer, F. L.; Fiore, G. L.; Rowan, S. J.; Weder, C., Optically Healable Supramolecular Polymers. *Nature* **2011**, *472*, 334.
59. Bode, S.; Zedler, L.; Schacher, F. H.; Dietzek, B.; Schmitt, M.; Popp, J.; Hager, M. D.; Schubert, U. S., Self-Healing Polymer Coatings Based on Crosslinked Metallo-supramolecular Copolymers. *Advanced Materials* **2013**, *25* (11), 1634-1638.
60. Wang, Z.; Urban, M. W., Facile UV-Healable Polyethylenimine–Copper (C₂H₅N–Cu) Supramolecular Polymer Networks. *Polymer Chemistry* **2013**, *4* (18), 4897-4901.
61. Bose, R. K.; Enke, M.; Grande, A. M.; Zechel, S.; Schacher, F. H.; Hager, M. D.; Garcia, S. J.; Schubert, U. S.; van der Zwaag, S., Contributions of Hard and Soft blocks in the Self-Healing of Metal-Ligand-Containing Block Copolymers. *European Polymer Journal* **2017**, *93*, 417-427.
62. Burattini, S.; Colquhoun, H. M.; Fox, J. D.; Friedmann, D.; Greenland, B. W.; Harris, P. J. F.; Hayes, W.; Mackay, M. E.; Rowan, S. J., A Self-Repairing, Supramolecular Polymer System: Healability as a Consequence of Donor–Acceptor π – π Stacking Interactions. *Chemical Communications* **2009**, (44), 6717-6719.
63. Burattini, S.; Greenland, B. W.; Merino, D. H.; Weng, W.; Seppala, J.; Colquhoun, H. M.; Hayes, W.; Mackay, M. E.; Hamley, I. W.; Rowan, S. J., A

Healable Supramolecular Polymer Blend Based on Aromatic π - π Stacking and Hydrogen-Bonding Interactions. *Journal of the American Chemical Society* **2010**, *132* (34), 12051-12058.

64. Mei, J.-F.; Jia, X.-Y.; Lai, J.-C.; Sun, Y.; Li, C.-H.; Wu, J.-H.; Cao, Y.; You, X.-Z.; Bao, Z., A Highly Stretchable and Autonomous Self-Healing Polymer Based on Combination of Pt \cdots Pt and π - π Interactions. *Macromolecular Rapid Communications* **2016**, *37* (20), 1667-1675.

65. Döhler, D.; Michael, P.; Binder, W., Principles of Self-Healing Polymers. In *Self-Healing Polymers*, Binder, W., Ed. Wiley-VCH: Weinheim, Germany, 2013.

66. Wool, R. P.; O'Connor, K. M., A Theory Crack Healing in Polymers. *Journal of Applied Physics* **1981**, *52* (10), 5953-5963.

67. Wu, D. Y.; Meure, S.; Solomon, D., Self-Healing Polymeric Materials: A Review of Recent Developments. *Progress in Polymer Science* **2008**, *33* (5), 479-522.

68. Yamaguchi, M.; Maeda, R.; Kobayashi, R.; Wada, T.; Ono, S.; Nobukawa, S., Autonomic Healing and Welding by Interdiffusion of Dangling Chains in a Weak Gel. *Polymer International* **2012**, *61* (1), 9-16.

69. Chen, Y.; Kushner, A. M.; Williams, G. A.; Guan, Z., Multiphase Design of Autonomic Self-Healing Thermoplastic Elastomers. *Nature Chemistry* **2012**, *4*, 467.

70. Watanabe, R.; Sako, T.; Korkiatithaweechai, S.; Yamaguchi, M., Autonomic Healing of Thermoplastic Elastomer Composed of Triblock Copolymer. *Journal of Materials Science* **2017**, *52* (2), 1214-1220.

71. Song, Y.; Liu, Y.; Qi, T.; Li, G. L., Towards Dynamic but Supertough Healable Polymers through Biomimetic Hierarchical Hydrogen-Bonding Interactions. *Angewandte Chemie* **2018**, *130* (42), 14034-14038.

72. Kim, S.-M.; Jeon, H.; Shin, S.-H.; Park, S.-A.; Jegal, J.; Hwang, S. Y.; Oh, D. X.; Park, J., Superior Toughness and Fast Self-Healing at Room Temperature Engineered by Transparent Elastomers. *Advanced Materials* **2018**, *30* (1), 1705145.

2

Unravelling the self-healing mechanism

Mystery creates wonder and wonder is the basis of man's desire to understand.

Neil Armstrong

This chapter has been published as:

A. Susa, R. K. Bose, A. M. Grande, S. van der Zwaag, S. J. García,
ACS Applied Materials and Interfaces 2016, 8 (49), 34068-34079

Abstract

Traditional polyetherimides (PEIs) are commonly synthesized from an aromatic diamine and an aromatic dianhydride (e.g. 3,4'-oxydianiline (ODA) and 4,4'-oxydiphtalic anhydride (ODPA)) leading to the imide linkage and outstanding chemical, thermal and mechanical properties yet lacking any self-healing functionality. In this work, we have replaced the traditional aromatic diamine by a branched aliphatic fatty dimer diamine (DD1). This led to a whole family of self-healing polymers not containing reversible chemical bonds, capable of healing at (near) room temperature yet maintaining very high elastomeric-like mechanical properties (up to 6 MPa stress and 570% strain at break). In this work, we present the effect of the DD1/ODPA ratio on the general performance and healing behaviour of a room temperature healing polyetherimide. A dedicated analysis suggests that healing proceeds in three steps: (i) an initial adhesive step leading to the formation of a relatively weak interface; (ii) a second step at long healing times leading to the formation of an interphase with different properties than the bulk material and (iii) disappearance of the damaged zone leading to full healing. We argue that the fast interfacial adhesive step is due to Van der Waals interactions of long dangling alkyl chains followed by an interphase formation due to polymer chain interdiffusion. An increase in DD1 content leads to an increase in the healing kinetics and displacement shift of the first healing step towards lower temperatures. Too high excess of DD1 leads to the crosslinking of the polymer thereby restricting the necessary mobility for the interphase formation and limiting the self-healing behaviour. The results here presented offer a new route for the development of room temperature self-healing thermoplastic elastomers with improved mechanical properties using fatty dimer diamines.

2.1. Introduction

The field of intrinsic self-healing polymers increasingly focuses on the use of different types of reversible covalent and non-covalent bonds, such as disulfide linkages, hydrogen bonds and ionic interactions.¹⁻³ Since reversible bonds are weaker than their non-reversible counterparts, self-healing polymers generally show relatively low mechanical properties when they heal at room temperature or need energy input (heating) in case of variants with a higher strength. Room temperature self-healing polymers with high mechanical properties are yet to be developed.^{1,4,5} To do so the role of the polymer architecture is crucial for balancing healing and mechanical properties.⁶ In this respect, starting from a high-performance polymer to implement the self-healing characteristics is the strategy we use here.

In the present work we use polyimides as the starting material to develop polymers capable of autonomous self-healing at room temperature yet having good mechanical properties. Aromatic polyimides (PIs) have been widely used in highly demanding applications for decades due to their thermal stability, chemical resistance, high glass-transition temperature and mechanical integrity. Rigid aromatic backbones are known to be responsible for the high thermal stability and mechanical properties of PIs. Properties of PIs can be tailored by macromolecular architecture modification using various rigid and flexible monomers (cycloaliphatic, aliphatic) as the molecular dynamics are altogether decided by the combination of molecular packing (e.g. charge transfer complexes, CTC) and chain motions^{7,8} with aliphatic groups generally disrupting the molecular packing.⁹ As in many other material classes, the traditional approach to increase the service life of polyimides has been by increasing their thermal and mechanical stability.¹⁰⁻¹² However, a small amount of work has already been done on turning polyimides into self-healing grades. Nevertheless, these efforts have not been very successful so far and resulted in polymers with low mechanical properties or needing heating to induce healing.¹³⁻¹⁶

In a recent work,^{17,18} we proposed the use of a long chain aliphatic branched fatty dimer diamine (DD1) to develop intrinsic room temperature healing polyimides by polycondensation. The approach consisted in the partial or full replacement of the traditional aromatic diamine (3,4'-oxydianiline (3,4'-ODA)) by DD1

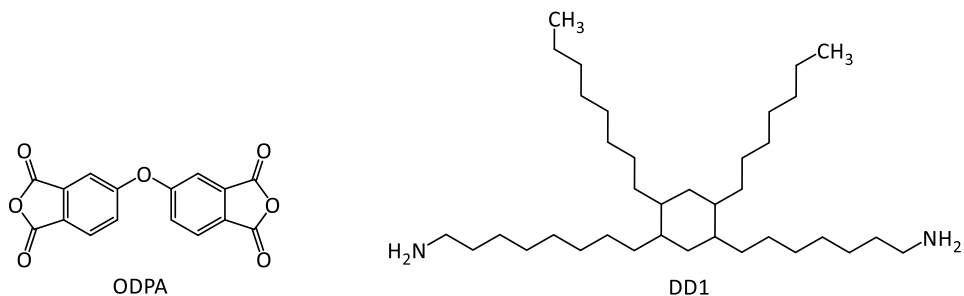
maintaining the dianhydride used in traditional synthesis of LaRCTM-IA type polyetherimide (4,4'-oxydiphthalic anhydride (ODPA)). Interestingly, other groups have also recently reported fatty dimer building blocks in the creation of self-healing polymers although in those cases the healing capabilities were implemented by non-covalent interactions such as H-bonds and ionic interactions. For instance, Cordier et al used fatty diacids and triacids to obtain a self-healing thermoreversible rubber from supramolecular assembly, with the hydrogen bonding as healing mechanism.¹⁹ Lutz et al developed a shape-recovery PU-acrylate-based coating with thermally activated self-healing ability using a fatty dimer diol with recrystallization as the mechanism responsible for healing.²⁰ While Aboudzadeh et al synthesized fully bio-based supramolecular networks with room temperature self-healing ability based on reversible ionic interactions between DD1 and different carboxylic acids.²¹ A different approach based on physical healing was followed by Yamaguchi et al.²²⁻²⁴ In their work, healing was attributed to entanglement couplings and interdiffusion of un-reacted chain-ends in non-branched soft polymer gels.

In this work we show for the first time that the dangling side chains in branched polymers (i.e. branches) can be responsible for full physical healing of strong polymers, without requiring other non-covalent interactions. Starting from DD1 branched diamine and a standard aromatic dianhydride, we have developed room temperature intrinsic self-healing polyetherimides with high mechanical properties. We investigate the effect of the aliphatic diamine to aromatic dianhydride ratio on the general polymer properties and healing behaviour by means of mechanical and rheological testing. Such an approach enabled the identification and quantification of different molecular processes influencing macroscopic healing (cut-heal). The results show a high dependence of healing on the hydrophobic alkyl groups of the long branches of the aliphatic diamine.

2.2. Experimental

2.2.1. Synthesis

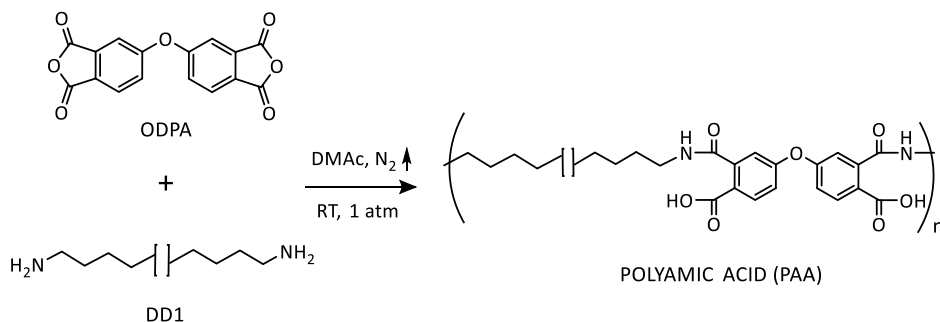
Four different polyimides were synthesized using a two-step polymerization process as described below. The monomers used (Scheme 2.1) were an aromatic dianhydride 4,4'-oxydiphthalic anhydride (ODPA) (98%, TCI Europe N.V.) and a fatty dimer diamine derived from vegetable oil (Priamine™ 1075, here called DD1) (Croda Nederland B.V.). Both monomers were used as received (¹H NMR spectra of the monomers are shown in Figure S-2.2, SI). DD1 is a mixture of mostly saturated C36 isomers with close to 100% amine difunctionality. Four polymers with different DD1/ODPA molar ratios with respect to the theoretical stoichiometric ratio were synthesized: D-0.9 (with 10 mol.% excess of ODPA), D-1.0 (at the theoretical stoichiometric ratio DD1/ODPA), D-1.1 (with 10 mol.% excess of DD1) and D-1.2 (with 20 mol.% excess of DD1). The amounts of each monomer were calculated according to the molecular weights of the monomers ($MW_{\text{ODPA}}=310.20$ g/mol and $MW_{\text{DD1}}=536.80$ g/mol) and assuming both chemicals are 100% difunctional. The synthesis was conducted in N,N-dimethylacetamide (DMAc, 99.5% extra dry, Acros Organics) polar aprotic solvent with total solids (monomers) content of 20 wt.%.



Scheme 2.1. Idealized structures of the monomers used in the SH-PEI synthesis. Left shows 4,4'-oxydiphthalic anhydride (4,4'-ODPA) and right shows a generalized structure of the dimer diamine (DD1).

1st step: Polyamic acid synthesis (PAA)

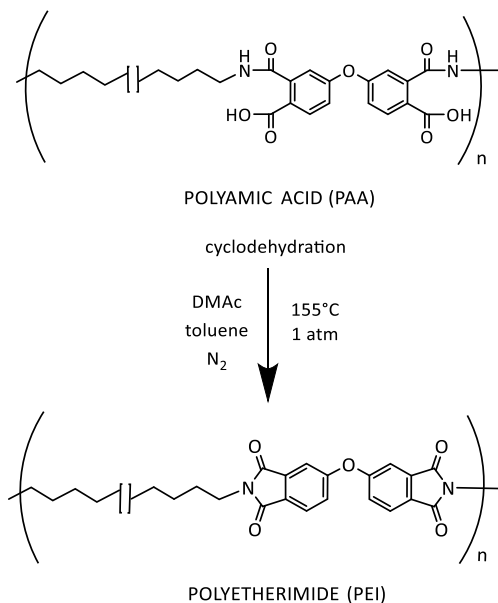
The diamine is weighed and dissolved in 9/10 (vol.) of the solvent (DMAc) in a three neck round bottom flask. The dianhydride is then added to the flask with the help of a funnel rinsed by the rest of the solvent (1/10 (vol.)). The mixture is then magnetically stirred at 200 rpm under nitrogen flow at room temperature and left to react until the solids are dissolved and the solution appears clear and light yellow suggesting the formation of the polyamic acid, PAA (Scheme 2.2). The monomers conversion and PAA formation was controlled by ATR-FTIR (Figure S-2.1, SI).



Scheme 2.2. Schematic representation of the polyamic acid synthesis. DD1 structure is shown in a simplified way where the brackets refer to the branched section, which can be positioned at different places along the main C18 chain.

2nd step: Thermal imidization in solution (PEI)

The thermal cyclodehydration in solution was used to form the bulk polyetherimides (Scheme 2.3). For this the three-neck round bottom flask containing the prepared polyamic acid solution is attached to the 10 mL Dean-Stark apparatus with a reflux condenser in order to perform the azeotropic distillation. After stirring under nitrogen flow at 150 rpm for 6 hours at 155°C and 1 atm the aqueous phase was removed in a Dean-Stark trap by azeotropic distillation with 10 vol% toluene as an azeotrope.



Scheme 2.3. Schematic representation of the thermal imidization reaction in case of stoichiometric reaction (cyclodehydration of polyamic acid into a polyetherimide).

The solution is then left to cool down overnight. Upon cooling down to room temperature, a very viscous/rubbery polyimide product is obtained at the bottom of the flask. The remaining DMAC is then poured off and the polymer is transferred from the flask to a glass tray and put to dry in a vacuum oven for 2 hours at 80°C, 1 hour at 120°C and 1 hour at 200°C. Cooling down to room temperature is done in vacuum as well. The glass tray with the thick polyimide film is then soaked in lukewarm water (~40°C) overnight. Upon drying at room temperature, the polyimide film is peeled off from the substrate and stored in a desiccator partially filled with dry silica gel. The films are then manually granulated and re-shaped in a dog-bone-shaped PTFE mould with dimensions according to ASTM D1708 (length, $l=22$ mm; width, $w=5$ mm; thickness, $t=2\pm 0.3$ mm). Once in the mould the samples were brought to a post-treatment in a vacuum oven at 150°C for 11h followed by 1h at the atmospheric pressure. After heating the samples were allowed to cool down in air to room temperature overnight. This led to the bulk polyimide samples necessary to evaluate the generic properties and healing.

2.2.2. Characterization methods

Infrared spectroscopy

Attenuated Total Reflectance Fourier Transform Infrared (ATR-FTIR) spectroscopy was employed in order to follow reaction completion and detect possible unreacted groups influencing the healing process at freshly cut surfaces. Each IR spectrum was recorded as an average of 3 scans in the wavenumber range 4000-500 cm^{-1} . The scans were performed at the newly created surfaces immediately after manually cutting the bulk sample with a razor blade.

Gel permeation chromatography

Molecular weight distributions of synthesized polymers were determined by gel permeation chromatography (GPC) using polystyrene as the standard. Polymer solutions were prepared in tetrahydrofuran (THF), concentrations 1 mg/mL.

Thermal analysis

Thermal properties were evaluated by thermogravimetric analysis (TGA) and differential scanning calorimetry (DSC). All measurements were performed under nitrogen. TGA was run from room temperature to 595°C at 10°C/min. DSC measurements were carried out at 10°C/min following this procedure: (1) heating from -50°C to 200°C; (2) maintaining for 2 min at 200°C; (3) cooling down to -50°C and (4) repeat steps 1 to 3. The glass transition temperature (T_g) was determined from the second heating cycle. No crystallization nor melting peaks were detected in any of the samples in the tested temperature range.

Density determination

The density of the polymers was determined by hydrostatic weighing method coupled with an analytical laboratory scale with a precision of 0.1 mg.

Tensile properties and interfacial healing evaluation

Tensile mechanical tests were performed using dog-bone specimens according to the ASTM D1708 standard (thicknesses, $t=2\pm 0.3$ mm) at 80 mm/min crosshead speed. To determine the healing behaviour, pristine samples were cut with a sharp razor blade at room temperature. After cutting, the two broken pieces were carefully repositioned in the dog-bone PTFE mould and allowed to heal at the required temperature with around 40% RH for 1, 5 and 11 days. For each polymer composition, three samples were tested in the pristine state and three samples in the healed state. The healing efficiency was calculated based on the following equation:

$$\text{Healing efficiency (\%)} = \frac{\sigma_b^{\text{healed}}}{\sigma_b^{\text{pristine}}} \times 100 \quad (2.1.)$$

where σ_b^{healed} and $\sigma_b^{\text{pristine}}$ are the stress at break for healed and pristine samples, respectively.

Rheological measurements

The linear viscoelastic properties of SH PEIs were investigated by the Haake Mars III rheometer, using the parallel plate geometry, with plate diameter of 8 mm. Preliminary strain amplitude sweeps at 1 Hz were performed at the highest and the lowest tested temperatures, from 0.001% to 10% strain to determine the linear viscoelastic region for the different polymers. Based on these results, a shear strain amplitude of 0.04% for D-1.2 and 0.5% for the other three polymers was used to ensure the tests were performed in the linear viscoelastic region. Frequency sweep experiments from 10 to 0.1 Hz were performed at temperatures between 110 and 10°C, in steps of 5°C. The rheological mastercurves at the reference temperature of 25°C were constructed from the obtained data applying the time-temperature superposition principle (TTS) using the dedicated Rheowin software. Each polymer was tested twice showing high reproducibility.

2.3. Results and discussion

2.3.1. Effect of ODPA/DD1 ratio on the branched-PEI architecture and properties

The conversion of monomers to PAA and subsequent imidization of PAA to PEI was monitored by FTIR as shown in Figure 2.1 for D-1.1. The imidization of PAA into PEI can be confirmed by the disappearance of the amic acid peaks typically visible at 1716, 1640 and 1550 cm^{-1} in PAA spectra and the appearance of the characteristic peaks of imide bonds at 1770, 1710, 1360 and 745 cm^{-1} in PEI spectra. The imidization reaction was confirmed for all the polymers (Figure S-2.1, SI) and supported by ^1H NMR analysis (Figure S-2.3, SI). The percent yields were calculated by the standard approach shown in Supporting Information. Yields of 45% for D-0.9, 89% for D-1.0, 85% for D-1.1, 93% for D-1.2 were obtained. The lower yield obtained in the case of the excess of ODPA system is in line with other reports on polyimide synthesis with an excess of dianhydride.²⁵

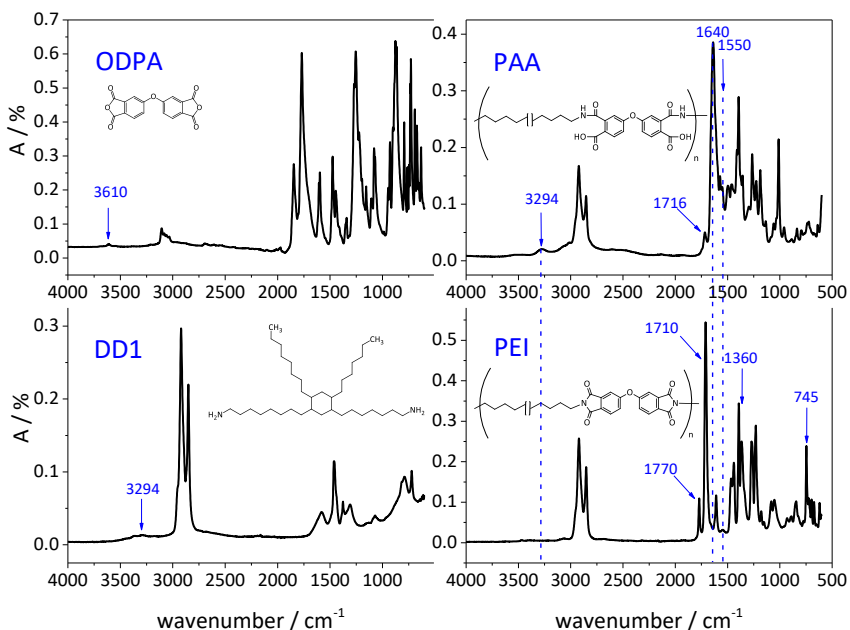


Figure 2.1. IR spectra of monomers ODPA and DD1 (left), prepolymer PAA and polymer PEI of sample D-1.1 (right). Figure shows the conversion of monomers into PAA and imidization of PAA into PEI.

Table 2.I. Effect of the DD1 content (i.e. offset from theoretical stoichiometric ratio) on M_w , M_n and PDI as calculated from the major peak obtained in GPC. T_g obtained from DSC and temperatures for 2% weight loss obtained from TGA.

Polymer	M_w (g/mol)	M_n (g/mol)	PDI	DSC T_g (°C)	TGA T (2% wt. loss) (°C)	Density (g/cm ³)
D-0.9	18k	11k	1.6	17	360	1.06
D-1.0	32k	16k	2.0	13	380	1.05
D-1.1	35k	15k	2.3	8	400	1.04
D-1.2	*	*	*	5	360	0.98

* GPC data not available since D-1.2 is not soluble in the GPC solvents available.

The resulting polymers were then analysed by GPC and the relevant information is presented in Table 2.I. The results show that the synthesis led to polymers with a normal polydispersity that increases with DD1 content. Polymers D-1.0 and D-1.1 show a M_w twice that of the D-0.9. No information is shown for D-1.2 because, as opposed to the other three polymers, this sample was swelling but not soluble in any of the solvents tested in this work (toluene, chloroform and THF) suggesting its partial crosslinking.

The effect of the DD1/ODPA ratio on the branched-PEI polymer architecture was further confirmed by a detailed FTIR analysis of the freshly cut polymer surfaces as shown in Figure 2.2 for selected regions of interest (full IR spectra can be seen in the Supporting Information, SI, Figure S-2.1). Figure 2.2a shows a presence of the peak at 3670 cm⁻¹ for the sample D-0.9, which is not present in the other samples. This peak, corresponding to free –OH groups, can be associated to the presence of –COOH terminated chains produced due to the excess of dianhydride as proposed in Scheme 2.4a.

On the other hand, the IR spectrum of polymer D-1.2 shows the presence of a broad peak in the region 3400-3280 cm⁻¹ and two peaks at 1660 and 1540 cm⁻¹, this being an indication of the formation of mono-substituted amides during chemical crosslinking and formation of a polyimide-amide network²⁶ as shown in Scheme 2.4b.

These results confirm that the maximum polymer chain length is obtained for compositions close to the stoichiometric ratio. However, when a certain amount

of diamine surpasses a critical limit chemical crosslinks are promoted, and chain formation is reduced. WAXS and SAXS (Figures S-2.2a and S-2.2b, SI) further showed the absence of crystallinity, ordered regions, and phase separation thereby confirming the amorphousness and homogeneity of all the polymers.

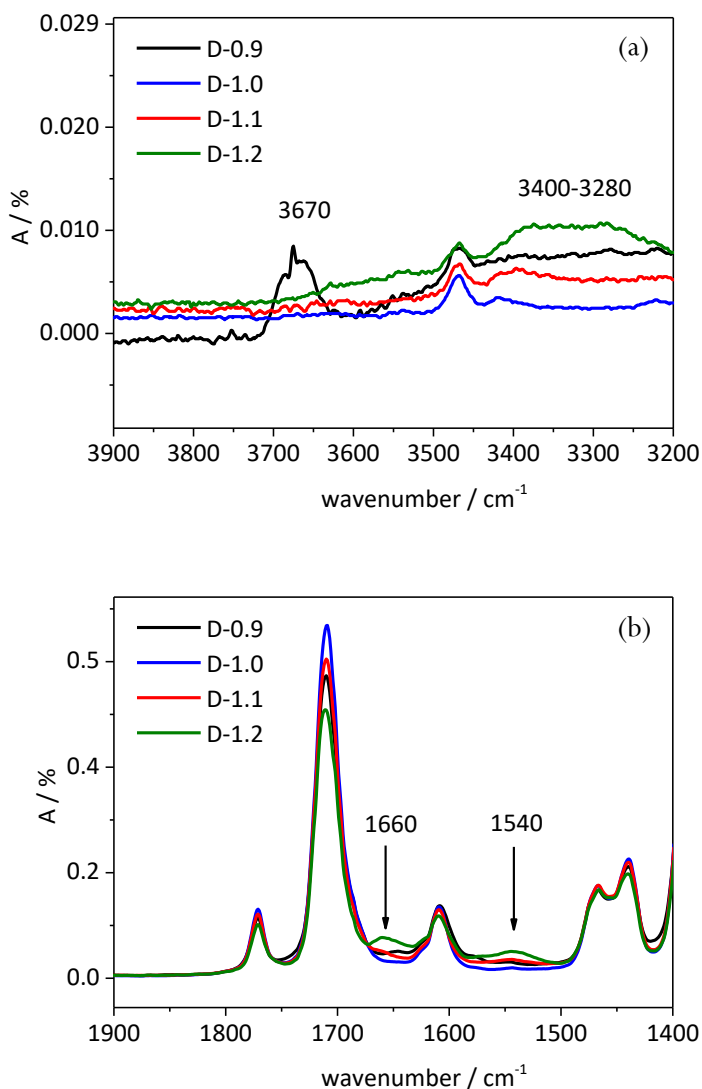
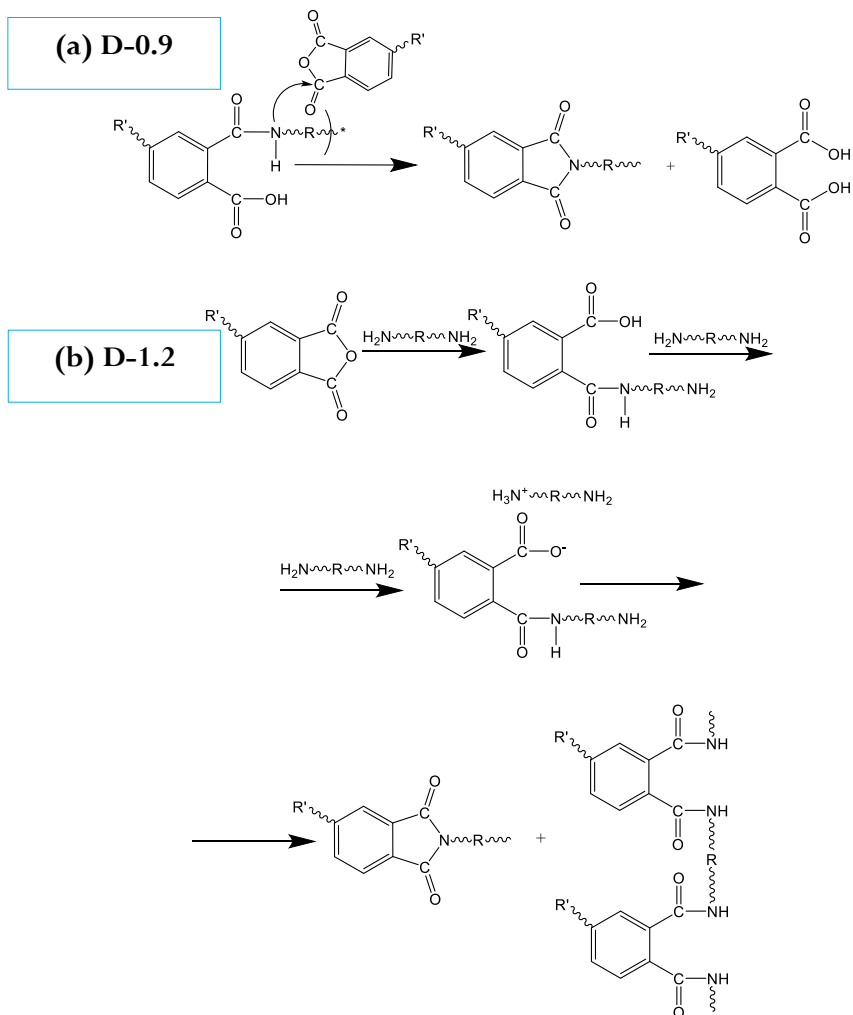


Figure 2.2. Magnified IR spectra of the regions of interest for the SH-PEI polymers as a function of the offset from the theoretical stoichiometric ratio. a) free -OH groups in D-0.9 and -NH stretch for D-1.2; b) amide II bands in D-1.2. Full spectra can be found in Figure S-2.1, SI.



Scheme 2.4. Schematic representation of the effect of the excess (a) dianhydride; (b) diamine during imidization reaction. DD1 structure is simplified.

The effect of the polymer architecture on the thermal and mechanical behaviour was further studied by TGA, DSC and tensile testing. All polymers show a high thermal stability independent of their architecture with values for the onset degradation temperature (2% weight loss) at around 400°C (Table 2.1) similar to those of traditional commercial polyimides such as LaRC-IA. Furthermore, all

samples (Figure S-2.5, SI) showed only a small weight loss up to 0.4% until 200°C suggesting that almost no solvent (toluene or DMAc) was entrapped during the imidization and that the monomers were fully reacted. It should be noted that samples D-0.9 and D-1.2 show slightly lower degradation onset temperatures probably due to the lower M_w of D-0.9 and the presence of more thermally sensitive amide linkages in the case of D-1.2.²⁷ DSC shows that higher DD1 contents lower the T_g of the polymers from 17°C to 5°C (Table 2.I), but did not show any melting nor crystallization peaks in agreement with XRD results. Such a decrease in T_g , even for the crosslinked polymer, can be justified by a local plasticizing effect of the dangling chains according to the “iso-free volume” hypothesis and the “tent-pole-effect”.²⁸ In line with this, the apparent density was found to decrease linearly with the DD1 increase although D-1.2 appears as an outlier to the trend (Table 2.I). This trend is in agreement with previous reports showing that the large Van der Waals radii of branching points can sterically hinder the charge transfer complexes formation in aromatic polymers (e.g. polyimides) thereby leading to a higher free volume due to a chain packing decrease.²⁹ The outlier behaviour of D-1.2 can be related to the presence of bulky DD1 groups as cross-linkers between chains in a partially crosslinked network, thereby reducing the chain packing density significantly more than the expected effect of more DD1 in a linear polymer. The promotion of chemical crosslinking with the DD1 increase was further confirmed by a swelling test, as shown in the Supporting Information, Table S-2.I.

Figure 2.3 shows the stress-strain curves of the four polymers (detailed characteristic parameters can be seen in Supporting Information, Table S-2.II). All polymers exhibit rather high values for fracture stress and strain at break. The ultimate tensile strength decreases with DD1 content which can be explained by a gradual increase in the amount of amide bonds formed instead of the stronger imide bonds preferentially formed below and at the theoretical optimal stoichiometric ratio. However, the strain at break follows a clear trend from D-0.9 to D-1.1 increasing with the amount of branched DD1 units. This trend is not followed when the DD1 excess reaches 20 mol.% (D-1.2). At this point, the amide crosslinks formed do not allow the network to stretch as much as the DD1 content would predict thereby reducing the elongation at break.

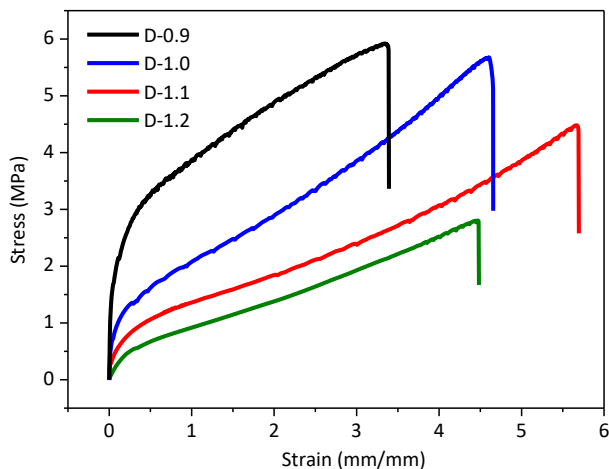


Figure 2.3. Stress-strain curves at 80 mm/min strain rate showing the effect of the DD1/ODPA ratio on the general mechanical performance.

In order to obtain a deeper understanding of the branching effect on the dynamic behaviour of the polymers, frequency sweep rheology in parallel-plate geometry was performed for its potential to discriminate dynamic behaviours at different time scales.³⁰ In order to be able to analyse a broad frequency range beyond the experimental practical limits the time-temperature superposition (TTS) approach was employed. It should be noted that the TTS is in principle applicable only to polymers that are thermo-rheologically simple. Typically, copolymers, polymer blends, or polymers with strong secondary supramolecular interactions show difficulties in obtaining a good superposition. However, previous studies show that in certain thermo-rheologically complex polymers, TTS might still be a useful and valid tool at certain temperature and frequency regimes.³¹ In this study, we found that TTS is applicable to these polyetherimides within the frequency range of interest ($10^{-7} < f < 10^5$ Hz). The mastercurves of the elastic modulus (G'), viscous modulus (G'') and $\tan\delta$ shifted to a reference temperature of 25°C (healing T) are shown in Figure 2.4 while the most relevant parameters obtained from the rheological tests are listed in Table 2.II. Shift factors plotted versus inverse temperature can be found in the Figure S-2.6b, SI).

From an initial analysis it can be observed that the obtained mastercurves for the different PEIs resemble the ones of lightly entangled polymers^{32,33} with four polymer-state regions identified by the intersection points between G' and G'' , as shown in Figure 2.4 for the polymer D-1.0 and reported in Table 2.II.

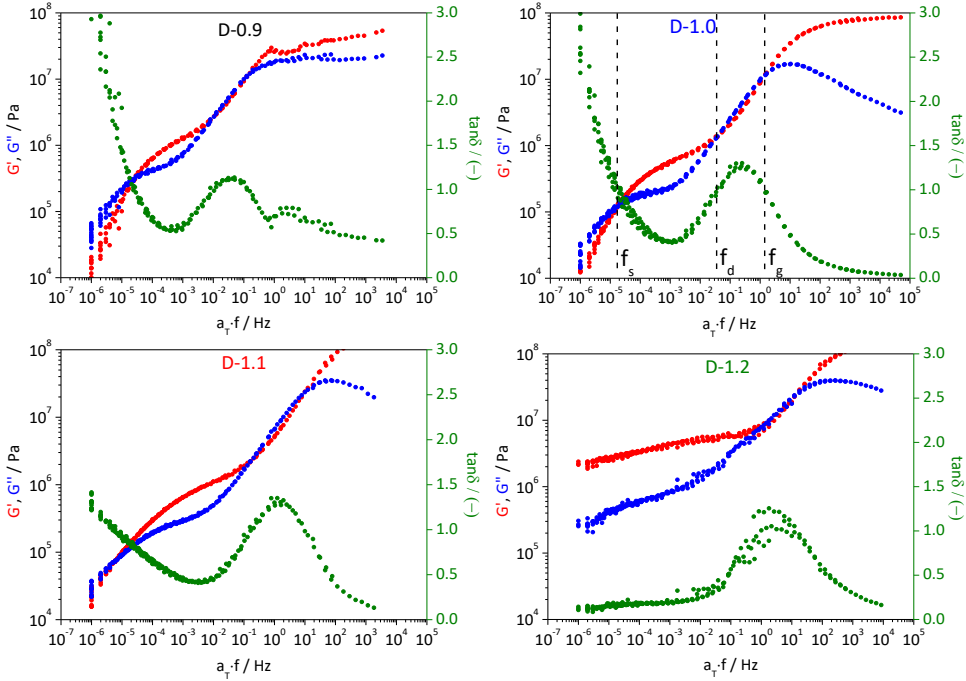


Figure 2.4. TTS mastercurves at $T_{ref}=25^{\circ}\text{C}$. Storage modulus (G' , red symbols), loss modulus (G'' , blue symbols) and loss tangent ($\tan\delta$, green symbols) as a function of shifted frequency ($a_T f$) for four different PEIs with respect to the stoichiometric offset.

The four polymer-state regions identified by the intersection points between G' and G'' :

(I)	$f > f_g$	$G' > G''$	Glassy regime
(II)	$f_d < f < f_g$	$G' < G''$	Dissipative regime
(III)	$f_s < f < f_d$	$G' > G''$	Apparent elastic plateau
(IV)	$f < f_s$	$G' < G''$	Viscous flow

Table 2.II. Characteristic parameters obtained from rheology.

Polymer	f_s (Hz)	f_d (Hz)	f_g (Hz)	τ_s (s)	τ_d (s)	τ_g (s)	G' slope at $f < f_s$	G'' slope at $f < f_s$	G_N^* (Pa)	M_c^{**} (g/mol)
D-0.9	2.6 $\cdot 10^{-5}$	0.011	0.14	$3.8 \cdot 10^4$	91	7.1	1.63	0.95	$1.25 \cdot 10^6$	2100
D-1.0	2.0 $\cdot 10^{-5}$	0.035	1.5	$5.0 \cdot 10^4$	28	0.7	1.25	0.83	$6.09 \cdot 10^5$	4270
D-1.1	5.2 $\cdot 10^{-6}$	0.180	10	$1.9 \cdot 10^5$	5.5	0.1	0.73	0.58	$9.21 \cdot 10^5$	2800
D-1.2	-	1.500	>10	-	0.7	<0.1	0.09	0.16	$1.62 \cdot 10^6$	1500 (M_c)

* G_N calculated from the van Gorp-Palmen plot, $\delta(|G|^*)$, (Figure S-2.6a, SI);^{34,35} with exception of D-1.2 where the minimum G' value from the mastercurve is used.

** M_c were calculated according to $M_c = \rho RT / G_N$ (Doi and Edwards) equation, using experimentally determined densities (Table 2.I). M_c values must be considered as pseudo- M_c values governed by 'transient interactions' not as molecular weight between entanglements, while M_c value for D-1.2 are related to the permanent crosslinks present in this polymer grade.

The rheology plots are also similar to those reported for supramolecular polymers. In supramolecular polymers, the lowest frequency crossover is usually associated to the relaxation of the supramolecular or secondary interactions. Above this crossover, the supramolecular crosslinks or constraints are intact, and the network is in its closed state. Below this frequency ($f < f_s$), the network is said to be in terminal flow regime ($G'' > G'$), e.g. in its open state. As expected, this crossover is seen for all the polymers except for D-1.2 which further confirms the presence of a permanently crosslinked network in this polymer.³⁶

Moreover, several studies have shown that polymers with supramolecular or transient interactions have two relaxation plateaus for the elastic modulus.^{37,38} Following this, in the polyimides studied in this work, which show multiple relaxations, the plateau at intermediate frequencies ($f_s < f < f_d$) could be attributed to transient constraints. As seen in Table 2.II, the plateau moduli (G_N) for these polyimides are in the order 10^5 - 10^6 Pa. Such values are in agreement with similar values obtained for supramolecular self-healing polymers based on metal ionic interactions in rubbery poly(n-butyl acrylate) ionomers,³⁹ hydrogen bonding end groups in poly(isobutylene)⁴⁰ and ionic networks between neutralized citric acid and aliphatic diamines.⁴¹

When the relation of rubber elasticity, $G_N = \rho RT/M_e$, is applied to these polymers and the molecular weight between effective interactions M_e is calculated, values of M_e between 2000 and 4000 g/mol are obtained (Table 2.II). These values suggest that the rubbery plateau is not governed by chain entanglements but by other type of interactions.⁴² Based on the architecture of these polymers with a high branching density we propose that the apparent elastic plateau is governed by secondary but numerous Van der Waals interactions between the dangling chains, where apparent entanglements must be given by branching and interchain interactions. This interpretation is nevertheless not applicable to the sample D-1.2. In the latter case the plateau is related to its crosslinking nature and M_e can be interpreted as molecular weight between crosslinks (M_c). Swelling tests confirmed the crosslinking nature of D-1.2 leading to M_c values of 929 ± 14 g/mol.

A detailed analysis of the G' and G'' slopes in the dissipative ($f_d < f < f_g$) and terminal relaxation ($f < f_s$) regions also gave relevant information related to the dynamic interactions within the polymer (Table 2.II). Generally, for polymers showing true terminal relaxation the slope of G' is 2 and that of G'' is 1, which fits the well-known Maxwell model for polymers.⁴³ The PEIs here investigated show slope values in the terminal relaxation region ($f < f_s$) lower than 2 and 1 which at the same time decrease with the amount of branched DD1 (Table 2.II). On the other hand, the slopes of G' and G'' at the dissipative region ($f_d < f < f_g$) are equal to 0.5. In previous works on supramolecular polymers, authors have related slope values similar to those in the dissipative region of our polymers to the presence of multiple supramolecular stickers⁴⁴ hindering chain reptation, while the strength and number of the supramolecular stickers make the terminal relaxation to follow sticky Rouse-like or constrained dynamics.^{30,45-47}

Based on this it seems reasonable to state that the slope values here obtained also give an indication of secondary interactions affecting chain dynamics. The most likely explanation is therefore that the aliphatic branches act as stickers controlling the molecular motion of polymer main chains. Interestingly, in the dissipative region no differences in the slopes are observed while the relaxation time constants τ_g and τ_d decrease with the DD1 increase. Such observation indicates that these

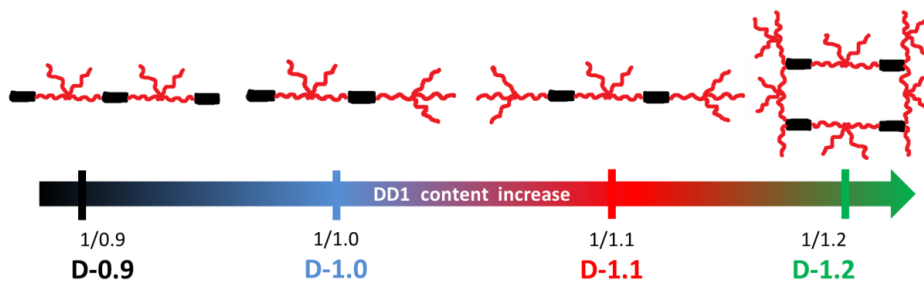


Figure 2.5. Sketch depicting the effect of the ODPA/DD1 offset ratio on the PEI polymer architecture

motions occur at shorter time constants for the polymer with the highest DD1 content but once they are taking place, the kinetics of motion is the same. Contrary to this effect, the motions at low frequencies (long times) seem to initiate later in time for D-1.1 (higher τ_s) and once in operation these motions occur at lower kinetics than in D-0.9 and D-1.0. Based on these results and the polymer architecture we propose that the first dissipative motions are related to dangling chain interactions governed by T_g while motions at low frequencies correlate to long range chain motions (i.e. reptation or interdiffusion) highly restricted by the dangling chains where the more the dangling branches (higher DD1 content) the higher the restriction to motion (i.e. D-1.1 is more restricted than D-0.9).

Four idealized polymer architectures of the amorphous branched thermoplastic elastomeric PEIs can be sketched as shown in Figure 2.5: low molecular weight polymer with near room temperature T_g (D-0.9), two systems with similar M_w but different T_g (D-1.0 and D-1.1), and a partially crosslinked branched polyamide-imide (D-1.2). This set of samples allowed for a detailed study of the effect of the architecture on the healing properties of these new room temperature healing polymers as shown in the next sections.

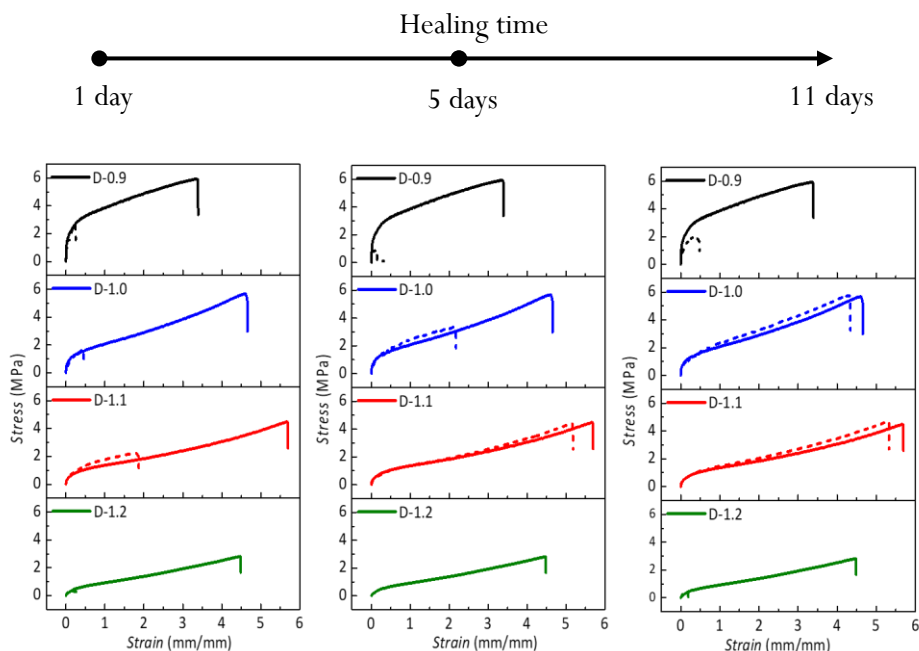


Figure 2.6. Stress-strain curves showing the PEIs healing behaviour at the room temperature as function of the stoichiometric offset and healing time. Full lines represent pristine (—) and dashed lines represent healed (- - -) samples.

2.3.2. Effect of the polymer architecture on the room temperature healing

Figure 2.6 shows the representative healing results of the developed PEIs obtained for samples tested in tension as function of the healing time and DD1/ODPA ratio at room temperature ($23\pm 2^\circ\text{C}$). From this figure, it becomes evident that near 100% healing efficiency can be obtained with both D-1.0 and D-1.1 samples in the time studied. Nevertheless, there is a significant difference between these two with respect to the healing kinetics. While D-1.1 achieves apparent maximum healing somewhere between 1 and 5 days, D-1.0 maximum healing occurs somewhere between 5 and 11 days. The sample with the lowest and the highest DD1 content (D-0.9 and D-1.2) show no significant healing in the investigated time and healing temperature. It is worth mentioning that all the samples fractured at the healed interface for healing times up to 11 days.

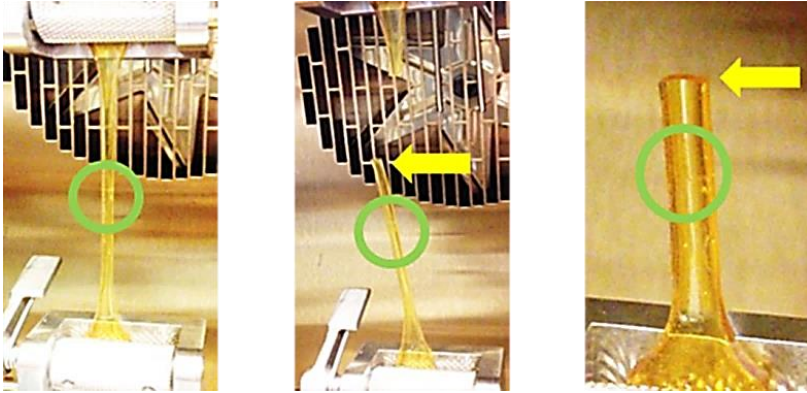


Figure 2.7. Captures from a video showing the D-1.1 sample breaking away from the healed spot after 30 days of healing at RT. The green circle points out the healed location.

However, when D-1.0 and D-1.1 samples were given 30 days to heal, fracture always took place far away from the healed original fracture plane (Figure 2.7). This demonstrates that the original fracture plane is no longer the weak part of the specimen and strength has recovered. In contrast, the two grades D-0.9 and D-1.2 still showed fracture at the healed interface region even after 30 days. Based on these results a three-stage healing process at the macroscale can be suggested as shown in Figure 2.8.

The full process is more clearly seen for samples D-1.0 and D-1.1. During the first healing stage, an adhesive process leading to weak interfacial restoration takes place (visible in D-0.9, D-1.0, D-1.1 and in a lower degree D-1.2 at short times). The length of the initial stage shortens as the DD1 content increases as can be seen in Figure 2.6. As long as contact time advances interfacial wetting increases and a second stage takes place in the D-1.0 and D-1.1 samples.

Second stage allows the transition from an interface phenomenon (surface contact) into an interphase formation (volume involved in the healing) most likely due to chain interdiffusion. The absence of the last two stages in polymer D-1.2 can be explained by its crosslinked nature that only allows some interfacial initial adhesion. The transition of an interface into an interphase failure can be detected in mechanical fracture testing by the failure mode transition switching from adhesive to cohesive with deformation at the damaged zone before failure.^{48,49}

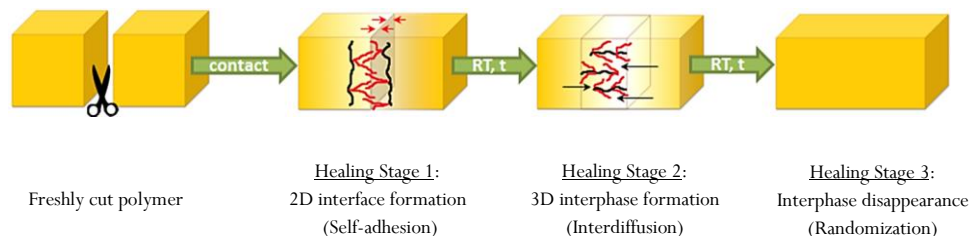


Figure 2.8. Sketch depicting the stages of the SH PEI healing process.

2.3.3. Relationship between polymer architecture and healing

When relating the rheological results to the macroscopic healing behaviour and the general polymer architecture, several correlations emerge. The first observation is that a large excess of DD1 leading to a partially crosslinked network leads to a non-healing material irrespective of the testing temperatures and times. Contrary to this, the other three samples show a strong time-dependency of healing with no healing for D-0.9 at room temperature.

We and other research groups have related the dynamics of reversible self-healing to the supramolecular bond lifetime (τ_b). τ_b values between 10 s and 100 s are claimed to lead to a combination of healing in reasonable times and decent mechanical properties.³⁹ Nevertheless, in the present work, the τ_b principle was not applicable as three crossovers interplay and affect healing as shown in section 2.3.1. A different approach was therefore here used to characterize and understand the behaviour of this new type of room-temperature self-healing polymers with complex behaviour.

In Figure 2.6 faster healing is observed for the sample D-1.1 while the rheological data in Figure 2.4 suggests that healing should be faster for sample D-0.9 as this one has lower τ_s and higher slope (kinetics of the motion are faster). The first thing to note here is that the TTS principle typically loses validity when multiple molecular motion mechanisms play a role and the polymer system is more temperature sensitive. In our case the higher the DD1 content the more temperature sensitive the network is, and therefore the TTS approach loses theoretical validity at higher frequencies, affecting mainly the calculated τ_s values

(the G' and G'' slopes are not affected). Despite the absolute τ_s values could therefore be inaccurate, we believe the trend and slopes would not be highly influenced and the conclusion would remain the same. The second remarkable point is that the dynamics at short times occur faster in the case of D-1.1.

When looking at the times at which the motions occur and compare the values to the obtained macroscopic healing times (i.e. tensile) it can be found that at the tested times all the motions should have started at least for the 5 days testing (as $\tau_s < 2$ days according to rheology). What can be seen in the macroscopic healing is that, at these testing times, only the D-1.1 sample has reached maximum healing while D-0.9 still shows low healing. This observation suggests that healing is in this case controlled by another factor.

The nature of this additional factor can be found in the dissipative region observed in rheology. High contents of branching with no crosslinking (D-1.1 and D-1.0) show dissipative motions occurring earlier in time (τ_g smaller) but also reach the plateau earlier in time (τ_d smaller) than D-0.9, which makes that the three polymers can show similar initial sticking and rubbery behaviour in the mechanical testing. This can be seen in the short-term macroscopic healing tests for which all three samples show sticking seen as small mechanical recovery (at 1-day healing test). After reaching this point the chains should be able to interdiffuse in order to lead to full healing but for this to occur it is necessary that the temperature of healing is significantly higher than the T_g (else the necessary condition of chain motion will not be met). This last condition is certain for D-1.1 but not for D-1.0 and D-0.9. In order to prove this hypothesis, we healed D-0.9 at a higher temperature than room temperature ($T_g + 12^\circ\text{C} = 29^\circ\text{C}$) and tested it at room temperature. The results shown in Figure S-2.7 (SI) show a faster healing than for D-1.1 reaching a maximum $\sim 75\%$ healing already at 1-day healing time thereby proving our hypothesis.

To confirm the effect of the branches on healing, a comparable PEI with no alkyl-dangling branches was synthesized by replacing the DD1 with a linear C12 aliphatic diamine (1, 12-diaminododecane) at theoretical stoichiometric ratio with the same dianhydride, ODP. This non-branched polymer is expected to have more dense chain packing, partially due to charge transfer interactions as the aromatic groups are not hindered by bulky alkyl chains.^{7,31} As shown in Table S-2.3 in SI, this sample

(ND-1.0) showed a significant increase in the T_g (69°C) but showed no healing even upon heating up to temperatures as high as 90°C. As can be seen in the TTS mastercurve, in Figure S-2.8a (SI), the relaxation transitions appear at much lower frequencies than for its branched counterpart. Furthermore, the non-branched polymer shows the appearance of a marked rubbery plateau thereby confirming the effect of the branches on the global polymer dynamics and their role on healing.

When unravelling the effect of the branches on healing and relating rheology to macroscopic healing it is also relevant to compare the results found in this work to other reported comparable self-healing supramolecular polymers. On the one hand, some authors have used branched aliphatic monomers similar to DD1 to create supramolecular networks although in their work they included secondary ionic interactions.²¹ Such polymers showed a lack of terminal flow zone for certain network compositions as in our case, but it was attributed to block-like ordering in the network promoted by the ionic interactions and verified using calorimetric analysis showing a second thermal transition referred to as the order-disorder transition temperature. On the other hand, Chen et al⁵⁰ presented self-healing branched polymers but reported that healing was related to phase separation-induced order-disorder. However, none of the previously reported works presented a concept similar to the one here introduced where healing is dominated by alkyl chains with no phase separation nor reversible covalent or strong non-covalent interactions.

To prove this concept more dedicated tests were performed. To show the potential elastic contribution of the DD1 to healing, rheological temperature sweeps were performed for the liquid branched dimer diamine DD1 used in this work (Figure S-2.9, SI). The results revealed its elastic behaviour up to a temperature of 40°C, analogous to the non-Newtonian behaviour in structured fluids, which was also noticed before by Aboudzadeh et al.²¹ This elastic nature hints towards the presence of attractive interactions between the alkyl groups of the dangling branches forming some kind of chain ordering such as micro phase-separation.⁵⁰ However, small angle X-ray scattering (SAXS) tests (Figure S-2.4b, SI) did not provide evidence of any phase separated ordering or block-like structure in the domain size range of 5-100 nm. DSC results also showed no thermal transition other than T_g , thus confirming completely amorphous polymers without structural ordering. It should

also be noted that, based on the monomers and spectroscopic analysis, it is safe to say that there are no other chemical functionalities in these polymers that can lead to hydrogen-bonding or ionic interactions and that the charge transfer complexes formation is hindered by the bulky branches. Hence based on the rheological observations, we can conclude that the weak but numerous Van der Waals interactions between the alkyl groups of the dangling branches of the aliphatic diamine create a transient supramolecular network which makes these polymers mechanically robust yet self-healing.

This is the first time, to the best of our knowledge, that a self-healing polymer based on this principle is presented. Furthermore, the combination of healing at room temperature and the relatively high values of the mechanical properties obtained for the best performing polyimides reported here is, to the best of our knowledge, unique. The (room temperature) Young modulus (E) values of the polyimides presented here are in the range from 30 to 110 MPa. These values are up to two orders of magnitude higher than the values reported for other elastomers healing at room temperature, such as the ones based on H-bonds ($E \sim 0.25$ MPa),¹⁹ those based on the combination of H-bonds and aromatic disulfides ($E \sim 0.10$ MPa)⁵¹ or the H-bonds multiphase brush polymers from Chen et al ($10 < E < 40$ MPa).⁵⁰ Intrinsic self-healing polymers with higher modulus exist, but these require temperatures well above room temperature for healing. Our inability to compare the healing performance of polymers in an objective and quantitative manner stems from the multi-dimensional nature of the issue and the absence of accepted testing protocols.⁵²

2.4. Conclusions

New room temperature healing semi-aromatic thermoplastic elastomer polyetherimides based on aliphatic branched dimer diamine were synthesized and fully characterized. The polymers show remarkable healing behaviour at room temperature combined with mechanical properties close to application relevance. General polymer properties and healing efficiency were found to be dependent on the branched diamine content for which an optimum value was found. High contents of branched diamine led to disabling the macroscopic healing due to partial crosslinking reactions. On the other hand, low branching led to a decrease of the healing kinetics.

A dedicated macroscopic healing kinetics study combined with a frequency sweep rheology analysis for both linear and branched polymers confirmed the role of the aliphatic branches on the healing mechanism and kinetics. The proposed healing mechanism is based on a two-step process with fast Van der Waals interactions between dangling aliphatic chains forming a 2D interface followed by a second slower step where chain interdiffusion leads to a 3D interphase formation. Provided sufficient equilibration time, the interphase disappears leading to the full restoration of polymer properties. Even though similar branched dimer building blocks were used before in self-healing polymers, this is the first time, to the best of our knowledge, that the healing was obtained without thermo-reversible bonds or supramolecular interactions (hydrogen, ionic, etc.) other than Van der Waals. Although the concept has been proven for polyimides it is believed that introducing long aliphatic branched monomers into a robust polymer backbone can lead to high mechanical properties combined with healing at moderate temperatures in other polymer classes as well.

References

1. Döhler, D.; Michael, P.; Binder, W. H. Principles of Self-Healing Polymers. In *Self-Healing Polymers: From Principles to Applications*; Binder, W. H., Ed.; Wiley-VCH: Weinheim, 2013; pp 7-60.
2. Zhong, N.; Post, W. Self-repair of Structural and Functional Composites with Intrinsically Self-Healing Polymer Matrices: A Review. *Compos. Part A Appl. Sci. Manuf.* **2015**, *69*, 226–239.
3. Kuhl, N.; Bode, S.; Bose, R. K.; Vitz, J.; Seifert, A.; Hoepfener, S.; Garcia, S. J.; Spange, S.; van der Zwaag, S.; Hager, M. D.; Schubert, U. S. Acylhydrazones as Reversible Covalent Crosslinkers for Self-Healing Polymers. *Adv. Funct. Mater.* **2015**, *25*, 3295–3301.
4. van der Zwaag, S. An Introduction to Material Design Principles: Damage prevention versus Damage Management. In *Self-Healing Materials: An Alternative Approach to 20 Centuries of Materials Science*; van der Zwaag, S., Ed.; Springer: Dordrecht, 2007; pp 8-9.
5. Garcia, S. J.; Fischer, H.R.; van Der Zwaag, S. A Critical Appraisal of the Potential of Self-Healing Polymeric Coatings. *Prog. Org. Coat.* **2011**, *72*(3), 211-221.
6. Garcia, S.J. Effect of Polymer Architecture on the Intrinsic Self-Healing Character of Polymers. *Eur. Polym. J.* **2014**, *53*, 118-125.
7. Cristea, M.; Ionita, D.; Hulubei, C.; Popovici, D.; Simionescu, B. C. Chain Packing Versus Chain Mobility in Semialiphatic BTDA-based Copolyimides. *Polymer* **2011**, *52*(8), 1820-1828.
8. Eichstadt, A. E.; Ward, T. C.; Bagwell, M. D.; Farr, I. V.; Dunson, D. L.; McGrath, J. E. Synthesis and Characterization of Amorphous Partially Aliphatic Polyimide Copolymers Based on Bisphenol-A Dianhydride. *Macromolecules* **2002**, *35*(20), 7561-7568.
9. Wakita, J.; Jin, S.; Shin, T. J.; Ree, M.; Ando, S. Analysis of Molecular Aggregation Structures of Fully Aromatic and Semialiphatic Polyimide Films with Synchrotron Grazing Incidence Wide-Angle X-ray Scattering. *Macromolecules* **2010**, *43* (4), 1930–1941.
10. Thiruvassagam, P. Synthesis of New Unsymmetrical Diamine and Polyimides: Structure–Property Relationship and Applications of Polyimides. *J. Polym. Res.* **2012**, *19* (9), 1-9.
11. Thiruvassagam, P. Synthesis and Characterization of AB-type Monomers and Polyimides: A Review. *Des. Monomers Polym.* **2013**, *16* (3), 197-221.
12. Dingemans, T. J.; Mendes, E.; Hinkley, J. J.; Weiser, E. S.; StClair, T. L. Poly(ether imide)s from Diamines with Para-, Meta-, and Ortho-Arylene

Substitutions: Synthesis, Characterization, and Liquid Crystalline Properties. *Macromolecules* **2008**, *41* (7), 2474–2483.

13. Yokota, K.; Abe, S.; Tagawa, M.; Iwata, M.; Miyazaki, E.; Ishizawa, J. I.; Kimoto, Y.; Yokota, R. Degradation Property of Commercially Available Si-containing Polyimide in Simulated Atomic Oxygen Environments for Low Earth Orbit. *High Perform. Polym.* **2010**, *22* (2), 237-251.

14. Lei, X.F.; Chen, Y.; Zhang, H. P.; Li, X. J.; Yao, P.; Zhang, Q. Y. Space Survivable Polyimides with Excellent Optical Transparency and Self-Healing Properties Derived from Hyperbranched Polysiloxane. *ACS Appl. Mater. Interfaces* **2013**, *5* (20), 10207-10220.

15. Périchaud, A. A.; Isakov, R. M.; Kurbatov, A.; Akhmetov, T. Z.; Prokohdiko, O. Y.; Razumovskaya, I. V.; Bazhenov, S. L.; Apel, P. Y.; Voytekunas, V. Y.; Abadie, M. J. M. Auto-Reparation of Polyimide Film Coatings for Aerospace Applications Challenges & Perspectives. In *High Performance Polymers – Polyimides Based – From Chemistry to Applications*; Abadie, M. J. M., Ed.; InTech: Rijeka, 2012; pp. 215-244.

16. Jolley, S.T.; Williams, M. K.; Gibson, T. L.; Smith, T. M.; Caraccio, A. J.; Li, W. Self-Healing Polymer Materials for Wire Insulation, Polyimides, Flat Surfaces, and Inflatable Structures. U.S. Patent 20,120,321,828 A1, December 20, 2012.

17. Smits, A. L. M.; van Triet, R. B.; Dingemans, T. J.; Garcia-Espallargas, S. J.; Polyimide composition. WO Patent 2,014,029,966 A1, February 27, 2014.

18. Susa, A.; van der Zwaag, S.; Garcia, S. J. Room temperature self-healing polyetherimides based on a long chain aliphatic diamine. In *Self-healing materials – Pioneering research in the Netherlands*; van der Zwaag, S.; Brinkman, E., Eds.; IOS Press: Amsterdam, 2015; pp 19-26.

19. Cordier, P.; Tournilhac, F.; Soulié-Ziakovic, C.; Leibler, L. Self-Healing and Thermoreversible Rubber from Supramolecular Assembly. *Nature* **2008**, *451*, 977-980.

20. Lutz, A.; van der Berg, O.; van Damme, J.; Verheyen, K.; Bauters, E.; De Graeve, I.; Du Prez, F. E.; Terryn, H. A Shape-Recovery Polymer Coating for the Corrosion Protection of Metallic Surfaces. *ACS Appl. Mater. Interfaces* **2015**, *7*, 175–183.

21. Aboudzadeh, A.; Fernandez, M.; Muñoz, M. E.; Santamaría, A.; Mecerreyes, D. Ionic Supramolecular Networks Fully Based on Chemicals Coming from Renewable Sources. *Macromol. Rapid Commun.* **2014**, *35*, 460–465.

22. Yamaguchi, M.; Ono, S.; Terano, M. Self-Repairing Property of Polymer Network with Dangling Chains. *Mater. Lett.* **2007**, *61*, 1396–1399.

23. Yamaguchi, M.; Ono, S.; Okamoto, K. Interdiffusion of Dangling Chains in Weak Gel and its Application to Self-Repairing Material. *Mater. Sci. Eng. B* **2009**, *162*, 189–194.
24. Yamaguchi, M.; Maeda, R.; Kobayashi, R.; Wada, T.; Ono, S.; Nobukawa, S. Autonomic Healing and Welding by Interdiffusion of Dangling Chains in a Weak Gel. *Polym. Int.* **2012**, *61*, 9–16.
25. Takekoshi, T. Synthesis of Polyimides. In *Polyimides: Fundamentals and applications*; Ghosh, M. K.; Mittal, K. L., Eds.; Marcel Dekker, Inc.: New York, 1996; pp. 7-44.
26. Soroko, I.; Bhole, Y.; Livingston, A. G. Environmentally Friendly Route for the Preparation of Solvent Resistant Polyimide Nanofiltration Membranes. *Green Chem.* **2011**, *13*, 162-168.
27. Wang, H. H.; Wu, S.-P. Thermal and Thermo-Oxidative Degradation Properties of Poly(benzimidazole amide imide) Copolymers. *J. Appl. Polym. Sci.* **2004**, *93*(5), 2072–2081.
28. Lee, Y.-L.; Sung, P.-H.; Liu, H.-T.; Chou, L.-C.; Ku, W.-H. Dangling Polymer Networks: Glass Transition of PU Elastomers. *J. Appl. Polym. Sci.* **1993**, *49*, 1013-1018.
29. Lei, T.; Wang, J.-Y.; Pei, J. Design, Synthesis, and Structure–Property Relationships of Isoindigo-Based Conjugated Polymers. *Acc. Chem. Res.* **2014**, *47* (4), 1117–1126.
30. Herbst, F.; Döhler, D.; Michael, P.; Binder, W. H. Self-Healing Polymers via Supramolecular Forces. *Macromol. Rapid Commun.* **2013**, *34*, 203-220.
31. Müller, M.; Seidel, U.; Stadler, R. Influence of Hydrogen Bonding on the Viscoelastic Properties of Thermoreversible Networks: Analysis of the Local Complex Dynamics. *Polymer* **1995**, *36*, 3143-3150.
32. Callies, X.; Fonteneau, C.; Véchambre, C.; Pensec, S.; Chenal, J. M.; Chazeau, L.; Bouteiller, L.; Ducouret, G.; Creton, C. Linear Rheology of Bis-Urea Functionalized Supramolecular Poly(butylacrylate)s: Part I – Weak Stickers. *Polymer* **2015**, *69*, 233-240.
33. Callies, X.; Véchambre, C.; Fonteneau, C.; Pensec, S.; Chenal, J. M.; Chazeau, L.; Bouteiller, L.; Ducouret, G.; Creton, C. Linear Rheology of Supramolecular Polymers Center-Functionalized with Strong Stickers. *Macromolecules* **2015**, *48*, 7320-7326.
34. Trinkle, S.; Friedrich, C. Van Gorp-Palmen-Plot: a Way to Characterize Polydispersity of Linear Polymers. *Rheol. Acta* **2001**, *40*, 322-328.
35. Trinkle, S.; Walter, P.; Friedrich, C. Van Gorp-Palmen Plot II – Classification of Long Chain Branched Polymers by Their Topology. *Rheol. Acta* **2002**, *41*, 103.

36. Kramer, O.; Greco, R.; Neira, R. A.; Ferry, J. D. Rubber Networks Containing Unattached Macromolecules. I. Linear Viscoelastic Properties of the System Butyl Rubber–Polyisobutylene. *J. Polym. Sci. Part B Polym. Phys.* **1974**, *12*, 2361-2374.
37. Yount, W. C.; Loveless, D. M.; Craig, S. L Strong Means Slow: Dynamic Contributions to the Bulk Mechanical Properties of Supramolecular Networks. *Angew. Chem. Int. Ed. Eng.* **2005**, *44*, 2746-2748.
38. Stadler, F. J.; Pyckhout-Hintzen, W.; Schumers, J.-M.; Fustin, C.-A.; Gohy, J.-F.; Bailly, C. Linear Viscoelastic Rheology of Moderately Entangled Telechelic Polybutadiene Temporary Networks. *Macromolecules* **2009**, *42*, 6181-6192.
39. Bose, R. K.; Hohlbein, N.; Garcia, S. J.; Schmidt, A. M.; van der Zwaag, S. Connecting Supramolecular Bond Lifetime and Network Mobility for Scratch Healing in Poly(butyl acrylate) Ionomers Containing Sodium, Zinc and Cobalt. *Phys. Chem. Chem. Phys.* **2015**, *17*, 1697-1704.
40. Herbst, F.; Seiffert, S.; Binder, W. H. Dynamic Supramolecular Poly(isobutylene)s for Self-Healing Materials. *Polym. Chem.* **2012**, *3*, 3084-3092.
41. Aboudzadeh, M. A.; Muñoz, M. E.; Santamaría, A.; Fernández-Berridi, M. J.; Irusta, L.; Mecerreyes, D. Synthesis and Rheological Behavior of Supramolecular Ionic Networks Based on Citric Acid and Aliphatic Diamines. *Macromolecules* **2012**, *45*, 7599-7606.
42. Graessley, W. W. *Polymeric Liquids & Networks: Dynamics and Rheology*; Taylor & Francis Inc.: London, 2004.
43. Knoben, W.; Besseling, N. A. M.; Bouteiller, L.; Cohen Stuart, M. A. Dynamics of Reversible Supramolecular Polymers: Independent Determination of the Dependence of Linear Viscoelasticity on Concentration and Chain Length by Using Chain Stoppers. *Phys. Chem. Chem. Phys.* **2005**, *7*, 2390-2398.
44. Ahmadi, M.; Hawke, L. G. D.; Goldansaz, H.; van Ruymbeke, E. Dynamics of Entangled Linear Supramolecular Chains with Sticky Side Groups: Influence of Hindered Fluctuations. *Macromolecules* **2015**, *48*, 7300-7310.
45. Green, M. S.; Tobolsky, A. V. A New Approach to the Theory of Relaxing Polymeric Media. *J. Chem. Phys.* **1946**, *14*, 80-92.
46. Tanaka, F.; Edwards, S. F. Viscoelastic Properties of Physically Crosslinked Networks. 1. Transient Network Theory. *Macromolecules* **1992**, *25*, 1516-1523.
47. Rubinstein, M.; Semenov, A. N. Thermoreversible Gelation in Solutions of Associating Polymers. 2. Linear Dynamics. *Macromolecules* **1998**, *31*, 1386-1397.
48. Grande, A. M.; Garcia, S.J.; van der Zwaag, S. On the Interfacial Healing of a Supramolecular Elastomer. *Polymer* **2015**, *56*, 435-442.

49. Grande, A. M.; Bijleveld, J. C.; Garcia, S. J.; van der Zwaag, S. A Combined Rheological Fracture Mechanical–Rheological Study to Separate the Contributions of Hydrogen Bonds and Disulphide Linkages to the Healing of Poly(urea-urethane) Networks. *Polymer* **2016**, *96*, 26-34.
50. Chen, Y.; Kushner, A. M.; Williams, G. A.; Guan, Z. Multiphase Design of Autonomic Self-Healing Thermoplastic Elastomers. *Nat. Chem.* **2012**, *4*, 467–472.
51. Rekondo, A.; Martin, R.; Ruiz de Luzuriaga, A.; Cabañero, G.; Grande, H. J.; Odriozola, I. Catalyst-free Room-Temperature Self-healing Elastomers Based on Aromatic Disulfide Metathesis. *Mater. Horiz.* **2014**, *1*, 237-240.
52. Bode, S.; Enke, M.; Hernandez, M.; Bose, R. K.; Grande, A. M.; van der Zwaag, S.; Schubert, U. S.; Garcia, S. J.; Hager, M. D. Characterization of self-healing polymers: From macroscopic healing tests to the molecular mechanism. *Adv. Polym. Sci.*, **2016**, *273*, 113-142.

SUPPORTING INFORMATION

ATR/FTIR spectra

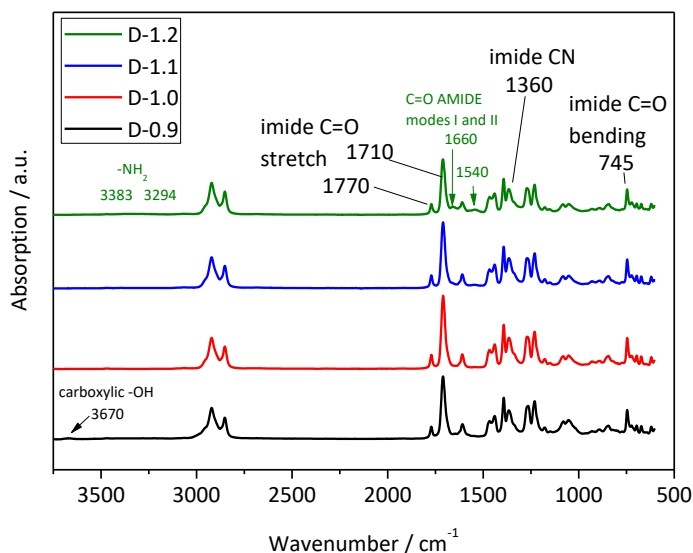


Figure S-2.1. Full IR spectra of the four PEIs as a function of the offset from the theoretical stoichiometric ratio.

Yield

Percent yield of the polymer was calculated according to equation:

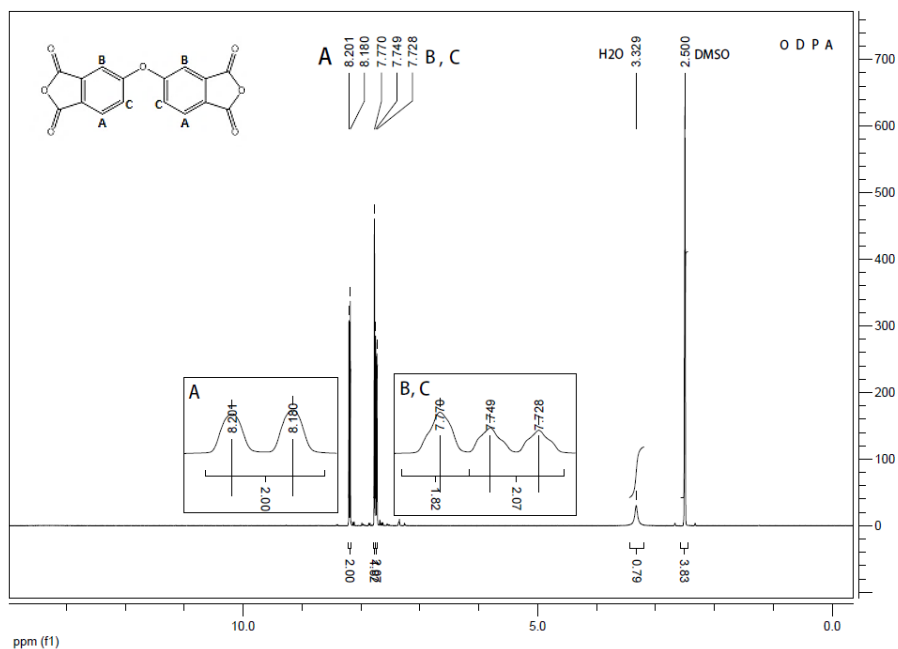
$$\text{Percent yield (\%)} = 100 \left(\frac{\text{Actual mass of the product}}{\text{Predicted mass of the product}} \right)$$

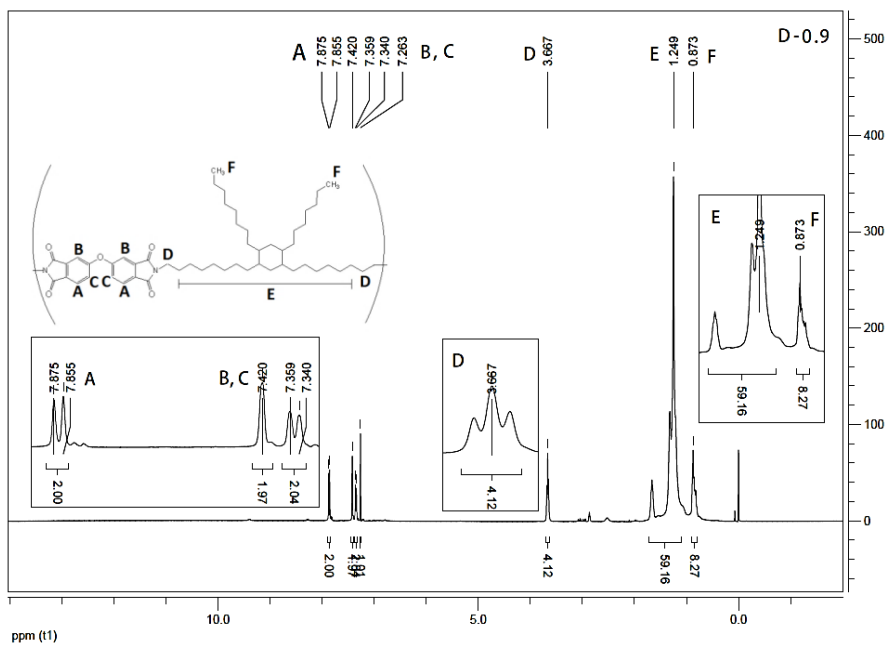
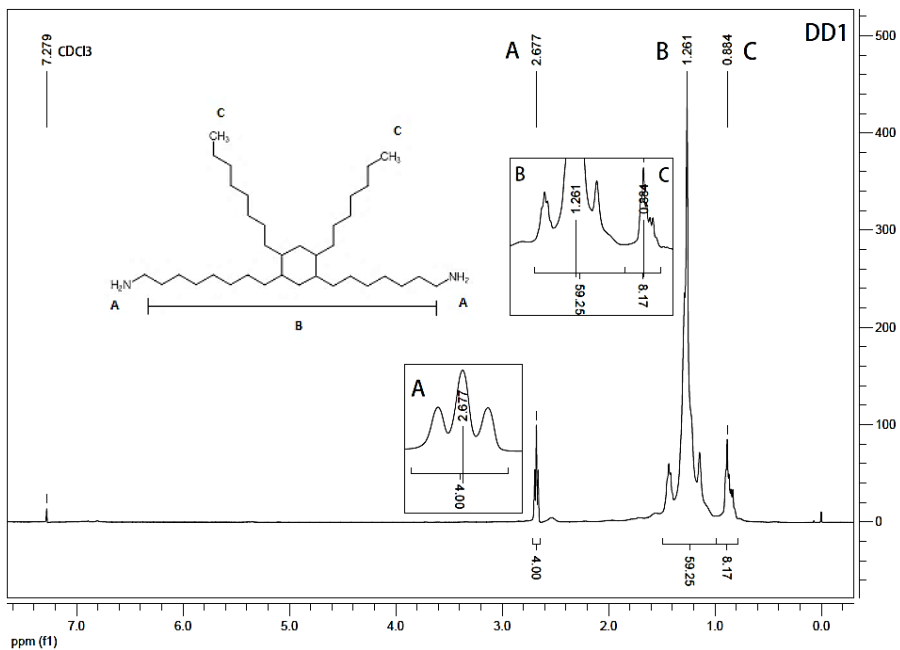
where predicted mass of the product was calculated according to the stoichiometric balance, assuming that 1 mol of ODPA and 1 mol of DD1 give 1 mol of PEI and 2 mol of water (4.25 wt% of water):

$$\text{Predicted mass of the product/g} = m(\text{ODPA}) + m(\text{DD1}) - m(\text{H}_2\text{O})$$

¹H NMR

Solution state ¹H NMR spectra were collected using the Agilent-400 MR DD2 at 25°C and 400 MHz. The solutions of polymers and DD1 were prepared in CDCl₃, and ODPA was measured in deuterated DMSO. Spectra were referenced to the solvent residual peak for DMSO and to TMS for CDCl₃, respectively. Spectra were not normalized. PAA's were not tested due to the insolubility in the available NMR solvents. Furthermore, D-1.2 was insoluble as well, but due to the partial crosslinked nature.





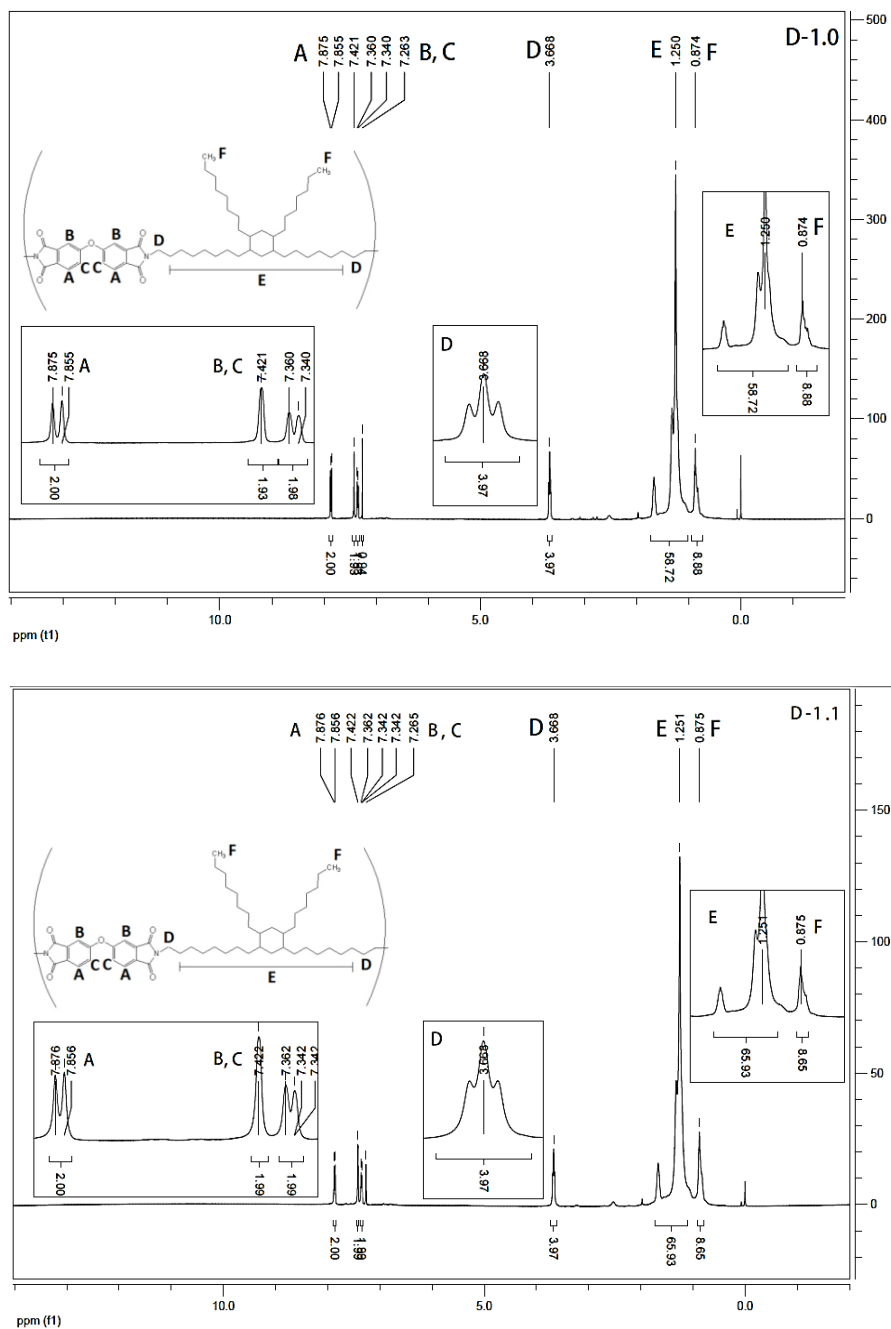


Figure S-2.3. ^1H NMR spectra of the three polymers in CDCl_3 and their assignments to the polymer structure.

X-ray diffraction measurements

Wide Angle X-ray diffraction (WAXS) data were collected on a Bruker D8 Advance diffractometer with Co K α radiation at the room temperature. Temperature controlled Small Angle X-ray Scattering (SAXS) was conducted using an AXS D8 Discover instrument from Bruker AG. SAXS scans were collected at five different temperatures: preliminary scan at room temperature followed by heating to 60°C. In a cooling ramp at the 0.5°C/min rate, the scans were further collected at 50, 25 and 5°C.

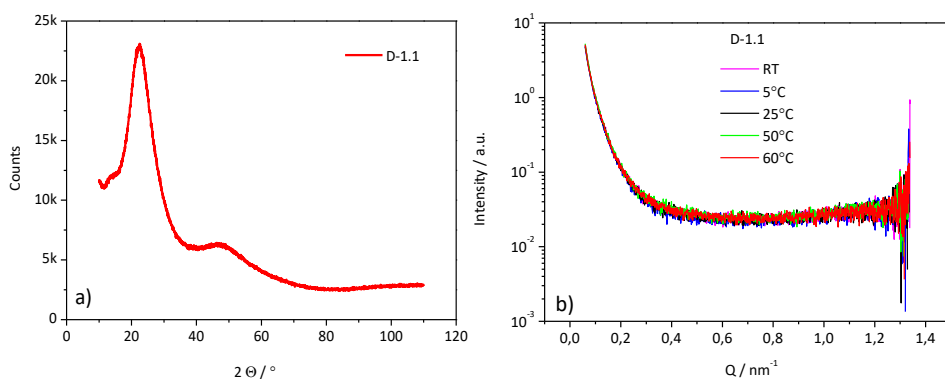


Figure S-2.4. a) WAXS and b) temperature controlled SAXS diffractogram of the D-1.1 polymer with representative patterns of all polymers in this work.

Thermal analysis

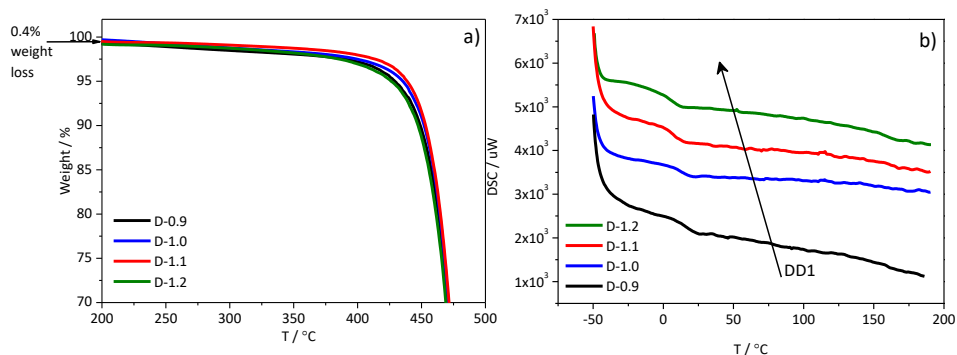


Figure S-2.5. a) TGA curves showing weight loss of SH-PEIs in the high temperature range; b) DSC curves from the second heating cycle showing glass transitions.

Swelling tests

The crosslinking density was determined by solvent-swelling measurements for 72h and calculated according to the Flory–Rehner equation (eq. S1).

$$\ln(1 - \Phi_r) + \Phi_r + \chi \Phi_r^2 = -\frac{\rho_r}{M_c} V_s \left(\Phi_r^{1/3} - \frac{2\Phi_r}{f} \right) \quad (\text{S-2.1})$$

where:

Φ_r = volume fraction of swollen polymer

χ = polymer-solvent interaction parameter. In this work a value of 0.3 (cis-polybutadiene raw elastomer-toluene¹) was taken as reference due to the lack of existing values for this new class of polymers.

ρ_r = polymer density

M_c = molecular weight of polymer between two crosslinks

V_s = molar volume of solvent (106.8 mL/mol for toluene¹)

f = functional cross-links (3)

The volume fraction (Φ_r) of swollen polymer was calculated according to:

$$\Phi_r = \frac{w_i/\rho_r}{w_i/\rho_r + (w_s - w_d)/\rho_s} \quad (\text{S-2.2})$$

where:

w_i = initial weight of the sample

w_s = swollen weight of the sample after 72h of immersion

w_d = weight of the sample dried at 60°C in vacuum for 72h

ρ_s = solvent density (0.87 g/cm³ for toluene)

The crosslink density ν is then calculated as:

$$\nu = \frac{1}{2M_c} \quad (\text{S-2.3})$$

¹ Hansen, C.M., *Hansen solubility parameters: a user's handbook*, CRC Press LLC: USA, 2000.

Table S-2.I. Results of the swelling tests.

Polymer	Q, Swelling ratio after 72h (%)	Soluble fraction (%)	M_c (g/mol)	ν , Crosslinking density (mol/cm ³)
D-0.9	/	100	/	/
D-1.0	/	100	/	/
D-1.1	2680±186	60±8	2609±62	1.92±0.05
D-1.2	441±8	13±0.3	929±14	5.39±0.08

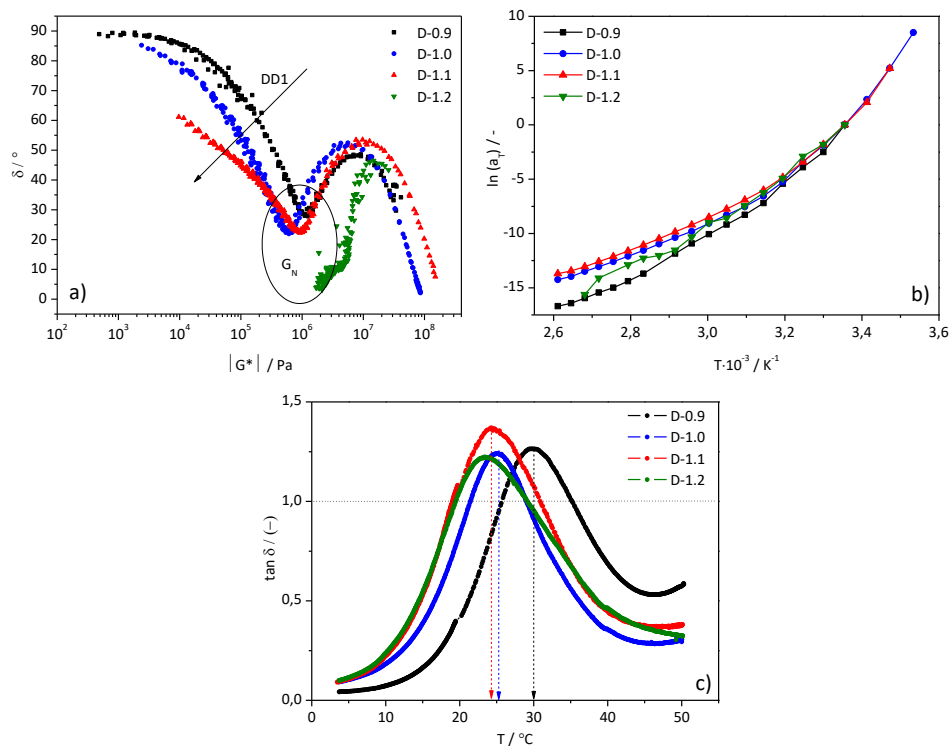
Rheological parameters

Figure S-2.6: a) van Gurp-Palmen plot; b) horizontal shift factors (a_T) from the TTS mastercurves, $T_{\text{ref}}=25^\circ\text{C}$; c) loss tangent ($\tan \delta$) as a function of temperature (T) from the temperature sweep experiments. Dotted lines are guidance for a reader's eye showing the elastic/viscous dominance region determined by $\tan \delta = 1$. Arrows point the values of $T(\tan \delta_{\max})$ for the non-crosslinked polymers that heal at 25 $^\circ\text{C}$ (red and blue) and does not heal at 25 $^\circ\text{C}$ (black).

Tensile test**Table S-2.II:** Tensile properties of the virgin polymers.

Polymer	σ_b (MPa)	ϵ_b (%)	E (MPa)
D-0.9	5.9±0.2	330±20	110
D-1.0	5.7±0.1	440±20	54
D-1.1	4.4±0.2	560±10	33
D-1.2	2.0±0.4	360±50	6.5

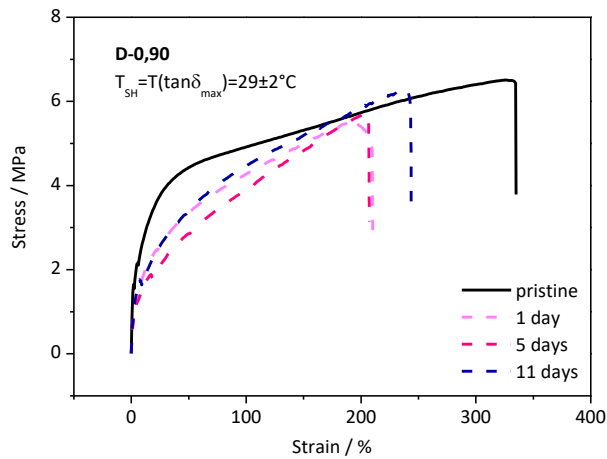


Figure S-2.7. Stress-strain curves showing the D-0.9 healing behaviour at the higher healing T , that corresponds to T of the maximum of $\tan\delta$ determined from the rheological T -sweep test, as function of the healing time. Full lines represent pristine (—) and dashed lines represent healed (---) samples after given healing time.

Reference: non-branched PEI**Table S-2.III.** Effect of branching on the generic polymer properties. ND-1.0 contains a linear non-branched C12 aliphatic diamine and D-1.0 a branched C18 aliphatic diamine (DD1) in (theoretical) stoichiometric ratio.

Polymer	Mw (g/mol)	Mn (g/mol)	PDI	DSC T_g (°C)	TGA T (2% weight loss) (°C)	Density (g/cm ³)
ND-1.0	*	*	*	69	435	1.20
D-1.0	32k	16k	2.0	13	380	1.05

* GPC data not available since ND-1.0 is not soluble in the GPC solvents available.

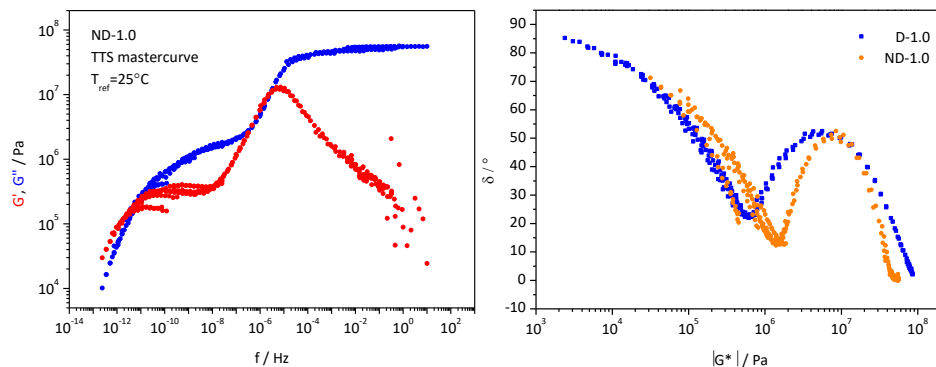
**Figure S-2.8.** a) TTS mastercurve of ND-1.0 and b) Van Gurp-Palmen plots of the referent non-branched PEI (orange) ND-1.0 in comparison to its branched counterpart D-1.0 (blue). $T_{ref}=25^{\circ}\text{C}$

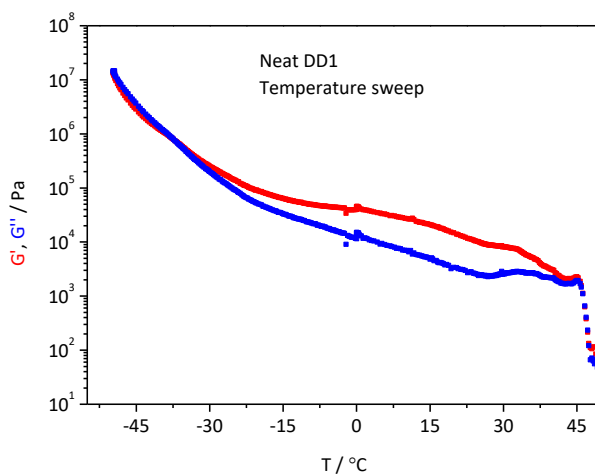
Table S-2.IV. Characteristic parameters obtained from rheology for the non-branched PEI (ND-1.0) as compared to its branched counterpart (D-1.0).

Polymer	f_s (Hz)	f_d (Hz)	f_g (Hz)	τ_s (s)	τ_d (s)	τ_g (s)	G' slope at $f < f_s$	G'' slope at $f < f_s$	G_N^* (Pa)	M_e^{**} (g/mol)
ND-1.0	7.5 $\cdot 10^{-12}$	3.8 $\cdot 10^{-7}$	2.8 $\cdot 10^{-6}$	13.3 $\cdot 10^{11}$	2.6 $\cdot 10^6$	3.6 $\cdot 10^5$	1.06	0.49	1.39 $\cdot 10^6$	2140
D-1.0	2.0 $\cdot 10^{-5}$	0.035	1.5	5.0 $\cdot 10^4$	28.0	0.7	1.25	0.83	6.09 $\cdot 10^5$	4270

* G_N calculated from the Van Gorp-Palmen plot, $\delta(|G|)^{2,3}$

** M_e were calculated using experimentally determined densities (Table S-2.III) according to $M_e = \rho RT / G_N$ (Doi and Edwards) equation.

Neat branched dimer diamine (DD1); T-sweep

**Figure S-2.9.** Temperature dependant rheological behaviour of the neat DD1.

² Ahmadi, M.; Hawke, L. G. D.; Goldansaz, H.; van Ruymbeke, E. *Macromolecules* **2015**, *48*, 7300.

³ Trinkle, S.; Friedrich, C. *Rheol. Acta* **2001**, *40*, 322.

3

Imaging the molecular motions of autonomous repair in a self-healing polymer

Technology, like art, is a soaring exercise of the human imagination.

Daniel Bell

This chapter has been published as:

H. M. van der Kooij, A. Susa, S. J. García, S. van der Zwaag, J. Sprakel, *Advanced Materials* 2017, 29 (26), 1701017

This work is going to be part of the PhD thesis of Hanne van der Kooij (Wageningen University) as well.

Abstract

Self-healing polymers can significantly extend the service life of materials and structures by autonomously repairing damage. Intrinsic healing holds great promise as a design strategy to mitigate the risks of damage by delaying or preventing catastrophic failure. However, experimentally resolving the microscopic mechanisms of intrinsic repair has proven highly challenging.

The current work demonstrates how optical micromechanical mapping enables the quantitative imaging of these molecular-scale dynamics with high spatiotemporal resolution. This approach allows disentangling delocalized viscoplastic relaxation and localized cohesion-restoring rebonding processes that occur simultaneously upon damage to a self-healing polymer. Moreover, frequency- and temperature-dependent imaging provide a way to pinpoint the repair modes in the relaxation spectrum of the quiescent material. These results give rise to a complete picture of autonomous repair that will guide the rational design of improved self-healing materials.

3.1. Introduction

Functional materials inevitably suffer mechanical damage during their use, as a result of scratching, abrasion, fracture or impact.¹⁻² Preventing material failure by managing the effects of damage is one of the foremost challenges in the design of high-performance materials.³ Self-healing has emerged as a powerful approach to spontaneously repair damage before it can lead to catastrophic failure of the material as a whole.⁴⁻⁶ Encoding self-healing capabilities in new materials is thus a promising strategy to enhance the durability and reliability of functional materials and coatings. A diversity of self-healing strategies has been developed in the past decades, ranging from extrinsic healing based on healing agents or capsules,⁷⁻⁸ to intrinsic repair by the autonomous reformation of reversible chemical or physical bonds in the polymer itself.⁹⁻¹¹

At its core, intrinsic self-healing is driven by the dynamics of polymer chains and supramolecular bonds at the molecular scale.¹²⁻¹⁴ However, to date it remains a major challenge to experimentally unravel these dynamics in situ with appropriate spatial and temporal resolution. Although mechanochromic probes have been widely employed for real-time monitoring of bond failure,¹⁵⁻¹⁷ methods to quantitatively visualize bond reformation are unavailable. Yet, such experiments are not only crucial to understand self-healing materials but could also aid in the rational design of new and improved materials. By definition, molecular mechanisms of repair act strongly confined to the site of damage and may involve a wide range of characteristic relaxation time scales. Thus, to directly probe these mechanisms in situ with high resolution requires new methods that quantify microscopic polymer dynamics in both space and time.

In this paper we visualize for the first time the microscale dynamics governing the macroscopic repair of a polymer using the optical method Laser Speckle Imaging (LSI).¹⁸⁻²⁰ We study autonomous healing in a thermoplastic, polyimide-based elastomer that exhibits excellent mechanical properties and spontaneous healing under ambient conditions.²¹ By analysing the thermal motion of a small amount of embedded nanoparticles that act as tracers,²² we extract the local dynamics within the material; we have confirmed that these nanoparticles do not significantly alter the properties of the polymer matrix (Figure S-3.6c). This strategy allows us to

create four-dimensional micromechanical maps of repair, as a function of two spatial coordinates, time and relaxation frequency. Using this in situ and non-invasive approach, we disentangle the combination of delocalized viscoplastic flow and localized cohesion restoration that occur after damage and during self-healing. Moreover, we show that frequency-dependent imaging²³ makes it possible to connect molecular relaxation spectra obtained using conventional macroscopic measurements to the repair mechanisms occurring at the site of damage. These results provide unique insight into the molecular dynamics of repair and improve our understanding of their spatiotemporal scale in an intrinsic self-healing polymer.

3.2. Experimental

3.2.1. *Materials*

See the Supporting Information text and Figure S-3.1 and S-3.2 for the materials and procedure used to prepare the polymers for this study. These thermoplastic elastomers are amorphous semi-aromatic polyimides prepared from an aromatic dianhydride and an aliphatic branched dimer diamine in different stoichiometric ratios. Table S-3.1 summarizes their main characteristics. Both their mechanical integrity and self-healing ability arise predominantly from intermolecular Van der Waals interactions between the dangling branches of the diamines, which act as temporary crosslinks to create a transient supramolecular network.

The polymers used in this study contain 0.5 wt% of iron(II,III) oxide nanoparticles to ensure strong multiple scattering and high LSI contrast. These nanoparticles are inert, do not interact and can be dispersed homogeneously. We have verified that at this low concentration, the presence of the nanoparticles affects the mechanical and self-healing properties only to a small extent (compare Figure S-3.5 and S-3.6 with reference).

3.2.2. Methods and data analysis

Laser Speckle Imaging (LSI) is based on the multiple scattering of light, essentially the imaging equivalent of Diffusive Wave Spectroscopy.²⁴ See¹⁹ for a detailed description of the technique. In our experimental LSI set-up (Figure S-3.3), we project an expanded and coherent laser beam (Cobolt Samba, 1 W, $\lambda=532$ nm) onto the turbid sample of interest. The photons in the illumination beam become multiply scattered by the embedded nanoparticles in the sample. As a result of these many scattering events, the photons essentially perform a random walk within the sample, rather than a ballistic trajectory. Each photon traverses a different diffusive path; the resulting path length differences give rise to a random alternation of constructive and destructive interference, which is recorded on a camera as a random pattern of bright and dark spots called speckles. The camera (Dalsa Genie M640-1/2, Stemmer Imaging) is here placed in the backscatter geometry. Specular and low-order scattering paths are filtered from the backscattered light by a linear polarizer perpendicular to the polarization of the incident laser beam.

As the tracer particles move within the sample, for example by Brownian motion, viscoplastic relaxation of the polymer matrix or rebonding processes, all photon path lengths change, reflected by changes in the speckle pattern. Analysing these temporal fluctuations in the speckle intensity allows us to extract information about the internal dynamics and accordingly create image contrast. In LSI, we quantify the rate with which the speckle intensity I of a speckle at time t and position x, y fluctuates by the intensity structure function d_2 :²⁵

$$d_2(x, y, t, \tau) = \frac{\langle [I(x, y, t) - I(x, y, t + \tau)]^2 \rangle}{\langle I(x, y, t) \rangle \cdot \langle I(x, y, t + \tau) \rangle} \quad (3.1.)$$

If the tracer particles embedded in the polymer matrix were very mobile, the speckle intensity fluctuated rapidly, and d_2 reached its maximum at short correlation time τ or high frequency $f=1/\tau$. By contrast, if the particles moved slowly, the speckle intensity varied more slowly and d_2 increased more gradually with increasing τ . Thus, by computing $d_2(x, y, t, \tau)$ it could be determined how fast particles were moving at a certain time and location in the sample, which was a direct measure for the local polymer dynamics. d_2 was used consistently in this work to create image contrast, rather than the commonly used absolute intensity I .

Heterogeneities in absolute intensities were therefore irrelevant, while contrast from dynamic heterogeneities might emerge (see Figure 3.1 and Movies S-1 and S-4, Supporting Information and Online Wiley website). More detailed information about the technique and data analysis is provided in Figure S-3.3 (Supporting Information) and the Supporting Information text.

In addition, the Supporting Information contains detailed descriptions of the freeze-fracture method and characterization of the polymers in terms of self-healing performance, mechanical and rheological properties.

3.3. Results and discussion

Our experiments start by thermostating a slab of the thermoplastic elastomer and creating a through-cut with a scalpel. After reuniting the two cut surfaces (Figure 3.1, steps 1–2), we begin the LSI measurement. LSI involves the coherent illumination of the sample and detection of the backscattered light, which here originates from photons multiply scattered by the nanoparticle tracers. Photon path length differences within the sample result in an interference, or speckle, pattern that is recorded on a camera (Movie S1, Supporting Information).

A static snapshot of the speckle pattern contains no information about the healing process (Figure 3.1, step 4). Instead, we extract information from the raw data by analysing the temporal fluctuations in speckle intensity by means of the contrast function $d_2(x, y, t, \tau)^{26}$ (see the Methods Section and the Supporting Information text). Within the microrheology approach,²² the thermal motion of the nanoparticles, evaluated here as a function of spatial coordinates x, y , time after damage t and relaxation frequency $f=1/\tau$, can be directly related to the micromechanical properties of the polymeric medium.

A single LSI experiment yields a four-dimensional data set, from which we reconstruct spatiotemporal maps of the dynamics at some particular frequency (Figure 3.1, step 5, and Movie S1, Supporting Information).²⁷⁻²⁸

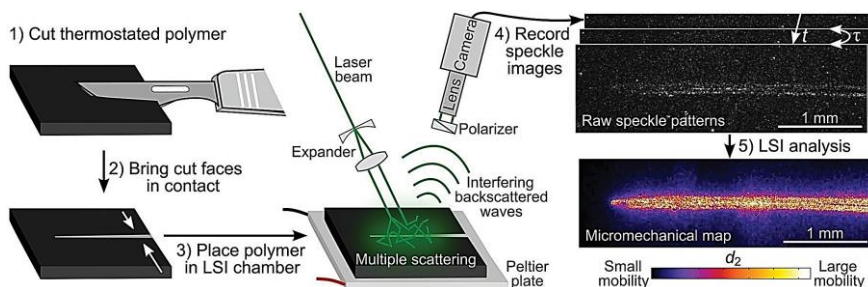


Figure 3.1. Visualizing the molecular dynamics of repair. 1) A thermostated slab of the polymer is cut through with a scalpel. 2) The cut surfaces are brought into contact and 3) probed using Laser Speckle Imaging. The multiply scattered light is detected in backscatter geometry as 4) a time sequence of speckle images of the damage zone. 5) The speckle fluctuations are quantified, pixel by pixel, by the contrast function d_2 , which encodes the local molecular mobility at position (x, y) , time after damage t , and characteristic frequency $f=1/\tau$. The resulting time-lapse micromechanical maps reveal strong localization of dynamics near the cut, here at $t=10$ s and $f=1$ Hz.

These micromechanical maps, color-coded by the local value of d_2 , reveal localized molecular mobility at the cut. The correlation time τ acts as a tuning knob for the type of dynamics we aim to probe: low values of τ bring to light fast, high-frequency dynamics, bounded experimentally by the frame rate of acquisition, here $f_{\max}=64$ Hz; high values of τ enable the study of low-frequency processes, limited by the length of the image sequence, here $f_{\min}=10^{-3}$ Hz. Thus, each experiment harbours information about spatially and temporally resolved healing processes across almost five decades in relaxation frequency. We start our study with a non-healing version of the thermoplastic elastomer (B-D-1.0, see Table 3.I) in which viscoplastic relaxation occurs but cohesion-restoring processes are suppressed.

Table 3.I. Specifications of the polymers used in this study. Optimal healing temperature (T_{heal}), weight-average molecular weight (M_w), number-average molecular weight (M_n), polydispersity index (PDI), and glass transition temperature (T_g). See Susa et al²¹ for a comprehensive characterization of the unfilled D-1.1 and D-0.9 polymers.

Polymer name	T_{heal} °C ^a	M_w (g/mol) ^b	M_n (g/mol) ^b	PDI (-)	T_g °C ^c
B-D-1.0	n/a	26k	14k	1.9	19
D-1.1	24	35k	15k	2.3	8
D-0.9	30	18k	11k	1.6	17

^a Deduced from rheological temperature sweep measurements of $\tan\delta$ see Figure S-3.6d (Supporting Information) and Susa et al.²¹

^b Determined by gel permeation chromatography using polystyrene as standard; 1 mg mL⁻¹ in THF

^c Determined by differential scanning calorimetry from the second heating curve; 10°C min⁻¹ in N₂ flow

Micromechanical maps reveal pronounced relaxation dynamics in a relatively large area around the cut (Figure 3.2a, Movies S1 and S2, Supporting Information). As time progresses, these delocalized relaxations subside until equilibrium is reached. We speculate that the rate of this viscoplastic relaxation is governed by the thermally activated motion of polymer chains within the material. As expected, increasing the temperature leads to an increase in the rate at which these relaxations decay (Figure 3.2a and Figure S-3.4, Supporting Information). For a more quantitative test of our hypothesis, we determine the characteristic relaxation time of the material in equilibrium τ_r by computing the field autocorrelation function $g_1(\tau)^{24}$ in a region of interest (ROI) away from the damage zone. The field autocorrelation function is related to the contrast function d_2 as described in the Supporting Information. At all temperatures, g_1 exhibits a terminal relaxation at large correlation times τ (Figure 3.2b). The characteristic relaxation time τ_r , extracted by fitting $g_1(\tau)$ to a stretched exponential decay, obeys the Arrhenius equation $\tau_r \propto e^{E_a/RT}$, with RT the thermal energy per mole and E_a the activation energy for relaxation of $47 \text{ kJmol}^{-1} \approx 19k_B T$ (Figure 3.2b, inset). Interestingly, from a single LSI experiment we can probe both the kinetic relaxation after cutting and the equilibrium relaxations of the material at rest.

In a self-healing version of this thermoplastic elastomer, similar viscoplastic relaxations are expected to occur, but simultaneously, strongly localized cohesion-restoring dynamics must take place at the cut interface. The polymer under study exhibits spontaneous repair at room temperature (D-1.1, see Table 3.1 and Susa et al²¹), as evidenced from bulk mechanical and rheological analysis (Figures S-3.5 and S-3.6, Supporting Information). After cutting, both stiffness and strength restore fully and autonomously within 10 days. Based on macroscopic testing, it was proposed that repair occurs through fast adhesion of the cut surfaces, by Van der Waals interactions between dangling chains, followed by slow polymer interdiffusion across the cut.²¹ Although bulk measurements are valuable to establish the conditions and completeness of self-healing at the macroscopic scale, they do not provide direct insight into its microscopic origins. By contrast, micromechanical mapping with LSI allows us to shed light on these microscopic mechanisms. Self-healing manifests as a zipper-like closure of the cut, from its tip inward, with a tangential closure velocity of $\approx 30 \mu\text{m s}^{-1}$ (Figure 3.3a, Figures S-3.7 and S-3.8, and Movie S3, Supporting Information).

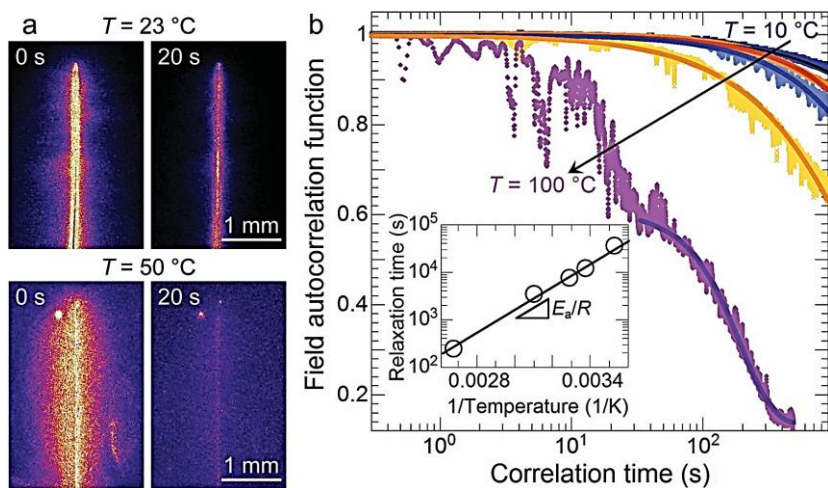


Figure 3.2. Viscoplastic relaxation around a cut in non-healing polymer B-D-1.0. a) Time evolution of dynamics at two temperatures using d_2 ($f=1$ Hz) as the contrast function. b) Measured field autocorrelation function $g_1(\tau)$ of the equilibrium polymer dynamics at $T=10, 23, 30, 50$ and 100°C (symbols), fitted to a stretched-exponential function (lines) to extract the thermal relaxation time τ_r , which obeys Arrhenius behaviour (inset) with an activation energy of $47\text{kJ mol}^{-1}=19k_{\text{B}}T$. The fluctuations in the high-temperature correlation curves are not experimental noise but correspond to reproducible intermittent “spikes” in the overall dynamics.

This zipping is driven by the inward tension on the cut which diverges at the tip, where the stress field exhibits a singularity.²⁹ These effects are further amplified by the gradient in width of the cut opening, which vanishes at the tip; the close proximity between the two surfaces at the cut tip allows for rapid adhesion and start of the interdiffusion process. This picture is corroborated by the absence of zipping, and homogeneous dynamics when a cut surface is exposed to air (Figure 3.3b and Figure S-3.9, Supporting Information). We confirm that the rate of polymer relaxation inherent to the material is a crucial step in the healing process by studying the recovery of the same polymer after a linear indentation, resulting in similar relaxation dynamics (Figure S-3.10, Supporting Information). Repair requires cohesion to be restored across the cut interface. To disentangle these cohesion-restoring dynamics from the delocalized plastic relaxation inherent to a cut made in a ductile solid, we prepare a brittle crack in the same material by fracturing a pre-notched sample frozen in liquid N_2 , thereby minimizing the degree of plastic deformation. Interestingly, the polymer exhibits excellent and fast healing of the brittle fracture when reheated to room temperature (Figure S-3.5c, Supporting Information).

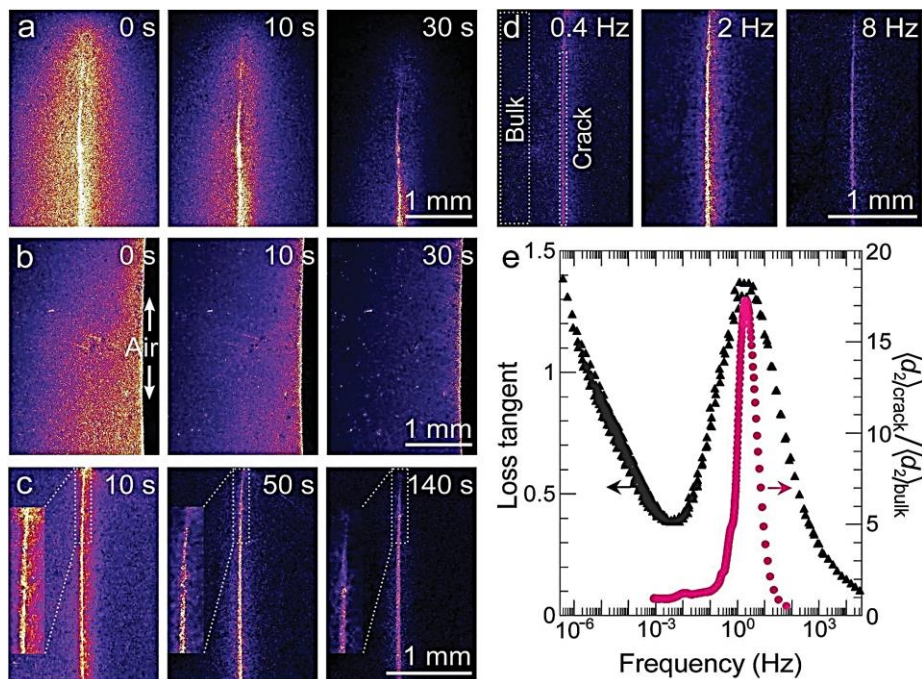


Figure 3.3. Resolving the mechanisms of repair. Time-lapse micromechanical maps for D-1.1, at $f=1\text{Hz}$; of a) self-healing of a cut made at room temperature, b) viscoplastic relaxation at a cut-air interface, and c) self-healing of a brittle freeze-fracture. d) Frequency dependence of the self-healing mobility for the freeze-fracture at $t=40\text{s}$. The colour scales are normalized by the respective values of $\langle d_2 \rangle_{\text{crack}} / \langle d_2 \rangle_{\text{bulk}}$ and all have the same limits. e) Comparison between bulk rheology of the frequency dependence of the loss tangent $\tan\delta$ and the enhancement of self-healing mobility at the crack interface with respect to the bulk of the material. The dotted lines in (d) indicate the ROIs in which these two properties are measured.

In the absence of long-ranged plastic relaxation, we instead observe only localized dynamics at the fracture interface (Figure 3.3c and Movie S4, Supporting Information). We attribute these to the molecular motions involved in adhesion and subsequent intermixing of polymer chains. A close-up of the tip shows that also this brittle crack closes like a zipper, with a tangential closure velocity of $\approx 5 \mu\text{m s}^{-1}$ (Figure 3.3c, insets). As this directional closure requires a tip where the crack width vanishes, and stress field diverges, zipping motion is indeed absent for brittle fractures that traverse the entire sample and lack a distinct tip (Figure S-3.11b, Supporting Information).

These data illustrate that self-healing is a combination of delocalized viscoplastic flow (Figure 3.3b) and localized cohesion-restoring processes (Figure 3.3c), which

raises the question how these dynamics are related to the linear relaxation spectrum of the material. To answer this question, we make use of the multidimensional nature of LSI to reconstruct frequency-dependent micromechanical maps during healing. Visual inspection of these maps at a brittle crack reveals that the self-healing dynamics are most pronounced and localized at a frequency of ~ 2 Hz (Figure 3.3d). To quantify this frequency dependence, we measure the average molecular mobility at the crack by means of the contrast function d_2 , normalized by that in the bulk of the sample, $\langle d_2 \rangle_{\text{crack}} / \langle d_2 \rangle_{\text{bulk}}$, as a function of the relaxation frequency f . Indeed, the self-healing mobility displays a distinct peak at $f \approx 2$ Hz (pink \bullet in Figure 3.3e and Figure S-3.12, Supporting Information). At frequencies below ~ 0.1 Hz and above ≈ 100 Hz, localized repair dynamics vanish.

In linear bulk mechanical experiments, the frequency dependence of relaxation processes can for example be evaluated by means of the loss tangent $\tan \delta$, as a measure for the relative importance of viscous and elastic processes. Strikingly, a time-temperature superposition mastercurve of $\tan \delta$ from such macroscopic measurements, referenced to 25°C , exhibits a peak at exactly the same frequency (Figure 3.3e, \blacktriangle). Thus, the local response to a strongly nonlinear deformation, i.e. a brittle fracture, can be directly mapped onto the governing dissipative mechanisms of the material in equilibrium.

For a variant of this polymer which self-heals at 30°C (D-0.9, see Table 3.1 and Susa et al²¹), we observe a strong temperature dependence of the closure mode of the cut (Figure 3.4a and Figure S-3.13, Supporting Information). We represent time series of these micromechanical maps as kymographs, in which the average values of d_2 in a strip along the cut are plotted as a function of time. Such kymographs in the space-time domain reveal three distinct closure modes (Figure 3.4b and Movies S5-S7, Supporting Information). At 23°C , the cut closes homogeneously, except at the tip itself. At the optimal healing temperature, 30°C , a front of enhanced mobility advances away from the tip, closing the cut like a zipper. At much higher temperatures, where the rate of polymer motion is strongly enhanced (Figure 3.2b), we observe rapid filling of the cut through a break-up process that is reminiscent of a Rayleigh-Plateau instability, driven by capillary pressure.³⁰

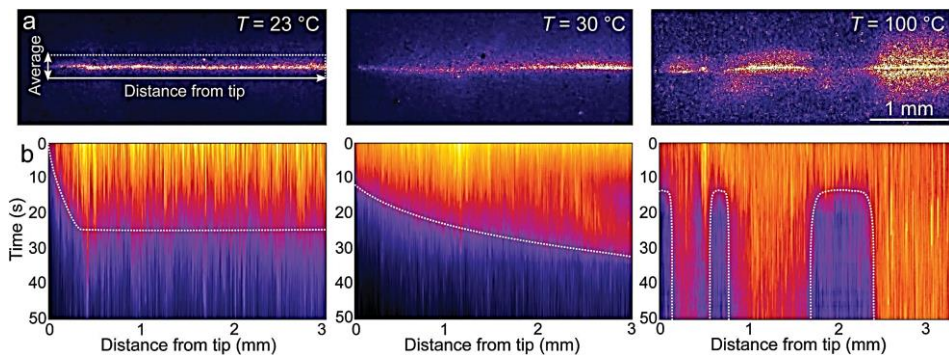


Figure 3.4. Modes of cut closure. a) Micromechanical d_2 ($f=1$ Hz) maps at $t=25$ s after creating a cut in D-0.9 at different temperatures. All images have the same scale and color coding. b) Kymographs of the average mobility around the cut versus distance from the cut tip. With increasing temperature, the closure mode transitions from homogeneous relaxation (23°C) to zipper-like closure (30°C) and a fluid-like Rayleigh-Plateau instability (100°C). The dotted lines are guides to the eye.

These experiments give rise to a microscopic picture of repair in these self-healing polymers. Damaging the polymer results in both the breaking of cohesive interactions and viscoplastic deformations, which heal autonomously via: (i) Van der Waals interactions to restore cohesion across the cut or crack, which involves (ii) a zipper-like motion in the presence of a distinct tip, and finally culminates in (iii) reptational intermixing and restoration of the material cohesion. Moreover, the latter process occurs at a distinct frequency that can be mapped onto the linear relaxation spectrum of the material.

3.4. Conclusions

Our results highlight how LSI allows the optical micromechanical mapping of strongly nonlinear processes, as a function of spatial coordinates, experimental time and relaxation frequency, with unprecedented detail. Due to the simplicity and noninvasive nature of the method, we envisage its extension to other materials, such as extrinsic self-healing systems, and to the study of different nonlinear mechanical phenomena, such as the mechanisms of fracture and fatigue. Illuminating and disentangling the rich convolution of diverse dynamics inherent to such strongly localized mechanics will not only deepen our insight into the physics of nonlinear mechanics but may ultimately enable the tailored design of high-quality self-healing materials.

References

1. Ghosh, B.; Urban, M. W., Self-repairing Oxetane-substituted Chitosan Polyurethane Networks. *Science* **2009**, 323 (5920), 1458-1460.
2. Gupta, S.; Zhang, Q.; Emrick, T.; Balazs, A. C.; Russell, T. P., Entropy-driven Segregation of Nanoparticles to Cracks in Multilayered Composite Polymer Structures. *Nat. Mater.* **2006**, 5 (3), 229-233.
3. Hager, M. D.; Greil, P.; Leyens, C.; van der Zwaag, S.; Schubert, U. S., Self-healing Materials. *Adv. Mater.* **2010**, 22 (47), 5424-5430.
4. Blaiszik, B. J.; Kramer, S. L. B.; Olugebefola, S. C.; Moore, J. S.; Sottos, N. R.; White, S. R., Self-healing Polymers and Composites. *Annu. Rev. Mater. Res.* **2010**, 40 (1), 179-211.
5. Brochu, A. B. W.; Craig, S. L.; Reichert, W. M., Self-healing Biomaterials. *J. Biomed. Mater. Res., Part A* **2011**, 96 (2), 492-506.
6. Yang, Y.; Urban, M. W., Self-healing Polymeric Materials. *Chem. Soc. Rev.* **2013**, 42, 7446-7467.
7. White, S. R.; Sottos, N. R.; Geubelle, P. H.; Moore, J. S.; Kessler, M. R.; Sriram, S. R.; Brown, E. N.; Viswanathan, S., Autonomic Healing of Polymer Composites. *Nature* **2001**, 409, 794.
8. Zhao, Y.; Fickert, J.; Landfester, K.; Crespy, D., Encapsulation of Self-healing Agents in Polymer Nanocapsules. *Small* **2012**, 8 (19), 2954-2958.
9. Cordier, P.; Tournilhac, F.; Soulie-Ziakovic, C.; Leibler, L., Self-healing and Thermoreversible Rubber from Supramolecular Assembly. *Nature* **2008**, 451 (7181), 977-980.
10. Chen, Y.; Kushner, A. M.; Williams, G. A.; Guan, Z., Multiphase Design of Autonomic Self-healing Thermoplastic Elastomers. *Nat. Chem.* **2012**, 4 (6), 467-472.
11. Wang, C.; Wu, H.; Chen, Z.; McDowell, M. T.; Cui, Y.; Bao, Z., Self-healing Chemistry Enables the Stable Operation of Silicon Microparticle Anodes for High-energy Lithium-ion Batteries. *Nat. Chem.* **2013**, 5 (12), 1042-1048.
12. Bode, S.; Zedler, L.; Schacher, F. H.; Dietzek, B.; Schmitt, M.; Popp, J.; Hager, M. D.; Schubert, U. S., Self-healing Polymer Coatings Based on Crosslinked Metallo-supramolecular Copolymers. *Adv. Mater.* **2013**, 25 (11), 1634-1638.
13. Kupfer, S.; Zedler, L.; Guthmuller, J.; Bode, S.; Hager, M. D.; Schubert, U. S.; Popp, J.; Grafe, S.; Dietzek, B., Self-healing Mechanism of Metallopolymers Investigated by QM/MM Simulations and Raman Spectroscopy. *Phys. Chem. Chem. Phys.* **2014**, 16, 12422-12432.

14. Yan, T.; Schroter, K.; Herbst, F.; Binder, W. H.; Thurn-Albrecht, T., Unveiling the Molecular Mechanism of Self-healing in a Telechelic, Supramolecular Polymer Network. *Sci. Rep.* **2016**, *6*, 32356.
15. Davis, D. A.; Hamilton, A.; Yang, J.; Cremar, L. D.; Van Gough, D.; Potisek, S. L.; Ong, M. T.; Braun, P. V.; Martinez, T. J.; White, S. R., Force-induced Activation of Covalent Bonds in Mechanoresponsive Polymeric Materials. *Nature* **2009**, *459* (7243), 68-72.
16. Ciardelli, F.; Ruggeri, G.; Pucci, A., Dye-containing Polymers: Methods for Preparation of Mechanochromic Materials. *Chem. Soc. Rev.* **2013**, *42*, 857-870.
17. Ducrot, E.; Chen, Y.; Bulters, M.; Sijbesma, R. P.; Creton, C., Toughening Elastomers with Sacrificial Bonds and Watching Them Break. *Science* **2014**, *344* (6180), 186-189.
18. Dunn, A. K.; Bolay, H.; Moskowitz, M. A.; Boas, D. A., Dynamic Imaging of Cerebral Blood Flow Using Laser Speckle. *J. Cerebr. Blood F. Met.* **2001**, *21* (3), 195-201.
19. van der Kooij, H. M.; Fokkink, R.; van der Gucht, J.; Sprakel, J., Quantitative Imaging of Heterogeneous Dynamics in Drying and Aging Paints. *Sci. Rep.* **2016**, *6*, 34383.
20. Nagazi, M.-Y.; Brambilla, G.; Meunier, G.; Marguerès, P.; Périé, J.-N.; Cipelletti, L., Space-resolved Diffusing Wave Spectroscopy Measurements of the Macroscopic Deformation and the Microscopic Dynamics in Tensile Strain Tests. *Opt. Laser Eng.* **2017**, *88*, 5-12.
21. Susa, A.; Bose, R. K.; Grande, A. M.; van der Zwaag, S.; Garcia, S. J., Effect of the Dianhydride/Branched Diamine Ratio on the Architecture and Room Temperature Healing Behavior of Polyimides. *ACS Appl. Mater. Interfaces* **2016**, *8* (49), 34068-34079.
22. Mason, T. G.; Ganesan, K.; van Zanten, J. H.; Wirtz, D.; Kuo, S. C., Particle Tracking Microrheology of Complex Fluids. *Phys. Rev. Lett.* **1997**, *79*, 3282-3285.
23. Hajjarian, Z.; Nia, H. T.; Ahn, S.; Grodzinsky, A. J.; Jain, R. K.; Nadkarni, S. K., Laser Speckle Rheology for Evaluating the Viscoelastic Properties of Hydrogel Scaffolds. *Sci. Rep.* **2016**, *6*, 37949.
24. Pine, D. J.; Weitz, D. A.; Zhu, J. X.; Herbolzheimer, E., Diffusing-wave Spectroscopy: Dynamic Light Scattering in the Multiple Scattering Limit. *J. Phys. France* **1990**, *51* (18), 2101-2127.
25. Schatzel, K., Correlation Techniques in Dynamic Light Scattering. *Appl. Phys. B: Lasers Opt.* **1987**, *42* (4), 193-213.
26. Zakharov, P.; Scheffold, F., Light Scattering Reviews 4: Single Light Scattering and Radiative Transfer. Kokhanovsky, A. A., Ed. Springer: Berlin, 2009; pp 433-467.

27. Sessoms, D. A.; Bissig, H.; Duri, A.; Cipelletti, L.; Trappe, V., Unexpected Spatial Distribution of Bubble Rearrangements in Coarsening Foams. *Soft Matter* **2010**, *6*, 3030-3037.
28. Amon, A.; Nguyen, V. B.; Bruand, A.; Crassous, J.; Clement, E., Hot Spots in an Athermal System. *Phys. Rev. Lett.* **2012**, *108*, 135502.
29. Rice, J. R.; Rosengren, G. F., Plane Strain Deformation near a Crack Tip in a Power-law Hardening Material. *J. Mech. Phys. Solids* **1968**, *16* (1), 1-12.
30. de Gennes, P.-G.; Brochard-Wyart, F.; Quere, D., Capillarity and Wetting Phenomena: Drops, Bubbles, Pearls, Waves. Springer: New York, 2004; pp 107-138.

SUPPORTING INFORMATION

Materials

The monomers used in this study are depicted in Figure S-3.1. The aromatic monomers 4,4'-oxydiphthalic anhydride (ODPA) and 3,3',4,4'-biphenyltetracarboxylic dianhydride (BPDA) are purchased from TCI Europe N.V. The fatty dimer diamine (Priamine™ 1075, here called DD1), derived from vegetable oil, is purchased from Croda Nederland B.V. *N,N*-dimethylacetamide (DMAc, 99.5% extra dry) is obtained from Acros Organics. Spherical iron(II,III) oxide nanoparticles sized 50-100 nm are obtained from Sigma-Aldrich.

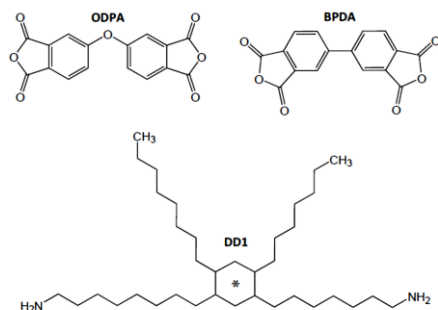


Figure S-3.1. Monomers used for the polyimide syntheses. DD1 is actually a mixture of C36 isomers with ~95% saturated bonds and ~5% double bonds, alicyclics and aromatics in the 'linker' (*).

Preparation of thermoplastic elastomers

Three different polyimides (PIs) are synthesized using the two-step polymerization process out-lined below and described in detail in a previous work: a non-healing reference polymer (B-D-1.0) composed of BPDA and DD1 in stoichiometric ratio; a polymer which self-heals around 24°C (D-1.1) composed of ODPA and DD1 in a 1:1.1 molar ratio; and a polymer which self-heals around 30°C (D-0.9) composed of ODPA and DD1 in a 1:0.9 molar ratio. The respective mass ratios are calculated using the molecular weights of the monomers ($MW_{BPDA}=294.2$ g/mol, $MW_{ODPA}=310.2$ g/mol and $MW_{DD1}=536.8$ g/mol) and assuming all monomers are 100% difunctional.

The polymers are synthesized in the polar aprotic solvent DMAc with a total solids (monomers) content of 20 wt%. First, the diamine DD1 is dissolved in 2/3 (vol.) of the DMAc in a three-neck round-bottom flask, followed by the dianhydride (BPDA or ODPA) and the remainder of the solvent (1/3 (vol.)). The mixture is magnetically stirred at 200 rpm under nitrogen flow at room temperature and left to react until the solids are fully dissolved in the DMAc and the solution is clear and light yellow suggesting the formation of the polyamic acid (PAA) (Figure S-3.2a). Subsequently, the three-neck round-bottom flask containing the PAA solution is attached to a 10 mL Dean-Stark apparatus with reflux condenser. The reaction mixture is stirred at 150 rpm under nitrogen flow for 6 hours at 160°C and 1 atm to induce thermal imidization, yielding the polyimide (Figure S-3.2a). The formed aqueous phase is removed in the Dean-Stark trap by azeotropic distillation with 10 wt% toluene.

To render the PI multiply scattering, a dispersion of 20 wt% iron oxide nanoparticles in DMAc is subsequently added at a total nanoparticle concentration of 0.5 wt% by mixing the appropriate amount with the hot polymer solution (150°C), and the mixture is immediately placed in an ice bowl. Once cooled down, the polymer is not soluble in DMAc anymore and consequently precipitates together with the nanoparticles (Figure S-3.2b). The DMAc is decanted from the flask and the precipitate is transferred into a rectangular polytetrafluoroethylene (PTFE) mold of length=70 mm, width=20 mm and thickness=1±0.5 mm. The samples in the molds are thermally post-treated in a vacuum oven at 150°C for 12 hours, after which they are allowed to cool down in air at room temperature overnight. This yields bulk polyimides with 0.5 wt% embedded tracer nanoparticles (Figure S-3.2c) whose properties are summarized in Table 3.I of the main text.

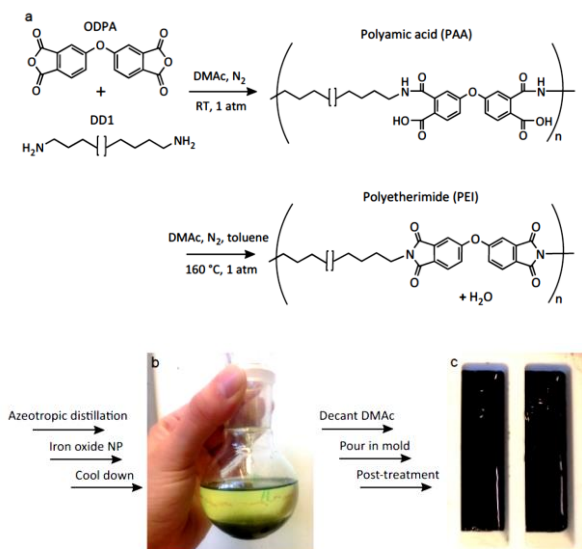


Figure S-3.2. Preparation of the thermoplastic elastomers used in this study. a) Schematic representation of the polyamic acid synthesis followed by cyclodehydration into a polyimide. The structure of DD1 is shown in a simplified way, with the brackets denoting the branched section that can be at different locations along the main C18 chain. The reaction between BPDA and DD1 occurs analogously. b) Insoluble PI-nanoparticle precipitate with solvent DMac on top, after bulk imidization and cooling down. c) Final thermoplastic elastomers containing iron oxide tracer nanoparticles.

Freeze-fracturing

To avoid deformation during damage and subsequent viscoplastic recovery that might obscure the self-healing dynamics, we introduce a brittle freeze-fracture in the D-1.1 thermoplastic elastomer (Figure 3.3c-e of the main text). We study both a crack that halves the sample (Figure S-3.5c and S-3.11b) and a partial fracture that stops within the sample to circumvent separation and re-positioning of the two halves (Figure 3.3c-e of the main text). In both cases we first make a pre-notch, after which we either freeze the entire sample in liquid nitrogen at $196^\circ C$, or only the pre-notched half. We subsequently fracture the sample by hand at the pre-notched location and reunite the two crack surfaces.

In the partially frozen specimen, the crack invariably stops at the boundary of the frozen and unfrozen sections; after creating the crack, we freeze the entire sample to prevent asymmetric thermal stresses caused by different expansion rates of the two halves upon thawing. Finally, we tape a temperature sensor onto the specimen and monitor the dynamics at the crack tip using LSI.

Tensile mechanical and self-healing evaluation

Tensile mechanical tests are performed using dog-bone specimens according to the ASTM D1708 standard at 80 mm/min crosshead speed. To determine the self-healing performance, pristine samples are cut with a sharp razor blade at 23°C. Subsequently, the two cut surfaces are carefully repositioned in the dog-bone PTFE mold, either immediately or after a delay of 24 hours, and allowed to heal at 23°C for 1, 5 and 10 days. The same is done for the freeze-fractured samples. All tests are performed in triplicate with excellent reproducibility.

Rheology

The bulk linear viscoelastic properties of the polymers are measured using a Haake Mars III rheometer in the parallel-plate geometry, with a plate diameter of 8 mm. First, the linear viscoelastic range is determined by a 1 Hz oscillatory strain amplitude sweep at the highest and lowest temperature, from 0.001% to 10% strain. Frequency sweep measurements from 10 Hz to 0.1 Hz are subsequently performed from 110°C to 10°C in steps of 5°C, at a shear strain amplitude of 0.5%. The mastercurves of the storage modulus G' , loss modulus G'' and loss tangent $\tan\delta$, at a reference temperature of 25°C, are constructed from the acquired data by employing the time-temperature superposition (TTS) principle using Haake RheoWin software. All tests are performed in triplicate with excellent reproducibility.

LSI data processing

As described in the Methods Section of the main text, we consistently use the intensity structure function d_2 to create imaging contrast, rather than the more common intensity autocorrelation function g_2 . In the case of a stationary ergodic process with large sampling size, the two are directly related by: $d_2(x, y, t, \tau) = 2[g_2(x, y, t, 0) - g_2(x, y, t, \tau)]^{25}$. However, d_2 is less sensitive to noise and intensity drift and therefore preferred over g_2 in most practical applications.

To quantify the non-healing relaxation mode (Figure 3.2a of the main text and Figure S-3.4) in more detail, we compute the field autocorrelation function g_1 from d_2 :

$$g_1(\tau) = \sqrt{1 - d_2(\tau)/2\beta} \quad (\text{S-3.1})$$

where we have applied the Siegert relation $g_1(\tau) = \sqrt{(g_2 - 1)/\beta}$ and the fact that $\langle g_2(0) \rangle = \beta + 1$, with β the spatial coherence factor that accounts for the number of speckles detected. As camera-based detection inevitably involves $\beta < 1$, we choose β such that $g_2(\tau) - 1 \rightarrow \beta$ for $\tau \rightarrow 0$. The angular brackets here indicate a spatial, multi-speckle average, over a 2 mm² section of the material sufficiently far from the cut. We do this at $t=5$ minutes after the onset of self-healing to probe only the equilibrium and thermal relaxation modes of the material at rest. Thanks to the multi-speckle averaging, time averaging is not required; as a result, temporal heterogeneities in the dynamics, such as the distinct intermittency observed in Figure 3.2b of the main text, are conserved, which would be lost by averaging the intensity fluctuations over time. We subsequently extract the relaxation time τ_r by fitting the field autocorrelation functions to a stretched-exponential decay:

$$g_1(\tau) = \exp[-\gamma(\tau/\tau_r)^\alpha] \quad (\text{S-3.2})$$

with α the stretching exponent and γ a numerical prefactor. In previous experiments, we have determined that for our experimental set-up, $\gamma \approx 1.5$.¹⁹

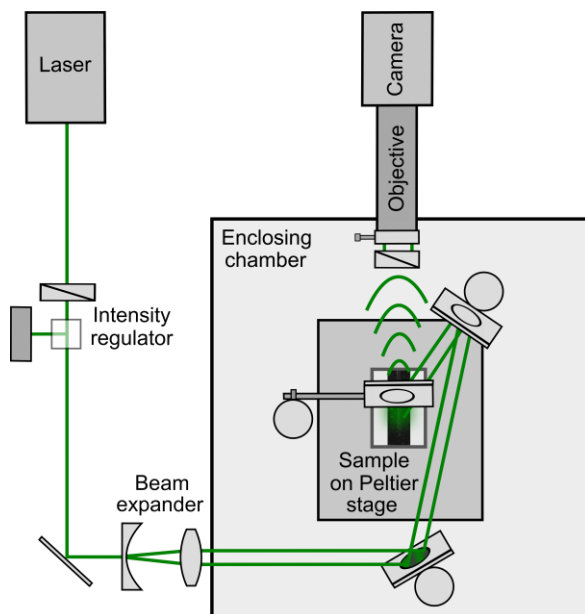


Figure S-3.3. Schematic top view of the Laser Speckle Imaging set-up in the backscatter geometry. The sample is illuminated with an expanded laser beam, whose intensity is regulated by passing the beam through a half-wave plate and polarizing beam splitter cube; the latter decomposes the beam into two perpendicular polarization components, one of which is directed into a beam dump. Adjustment of the rotation angle of the half-wave plate thus allows controlling the intensity of the transmitted component. After reflection by a mirror, the beam is expanded to a diameter of 1 cm by a Galilean beam expander. The beam is subsequently directed downward onto the sample via two mirrors, at a small angle with respect to the detection path to avoid intensity enhancement by coherent backscattering. The backscattered light is reflected by a mirror onto a linear polarizer perpendicular to the polarization of the incident laser beam, which filters photons with low-order scattering paths. The transmitted photons are collected by a Qioptiq zoom lens and focused through an iris diaphragm and extension tubes onto a CCD camera. The magnification of the imaging system is 1.8 and the depth of focus is 0.1 mm. To optimize the spatial resolution whilst retaining a good signal-to-noise ratio, the speckle size is tuned by the diaphragm to be slightly larger than the pixel size, typically 2-3x. The camera operates at a frame rate of 64 Hz, and the exposure time is adjusted to cover the full dynamic range. A tailor-made enclosing chamber eliminates air convection and stray light. The polymers are placed on a Peltier stage with temperature controller (PE 94, Linkam Scientific Instruments), and the temperature is measured using an external thermistor probe (TSP01, Thorlabs). The entire set-up is mounted on an optical breadboard with an active vibration isolation system (Vario Basic 60, Accurion). Adapted from our previous work,¹⁹ under the Creative Commons license.

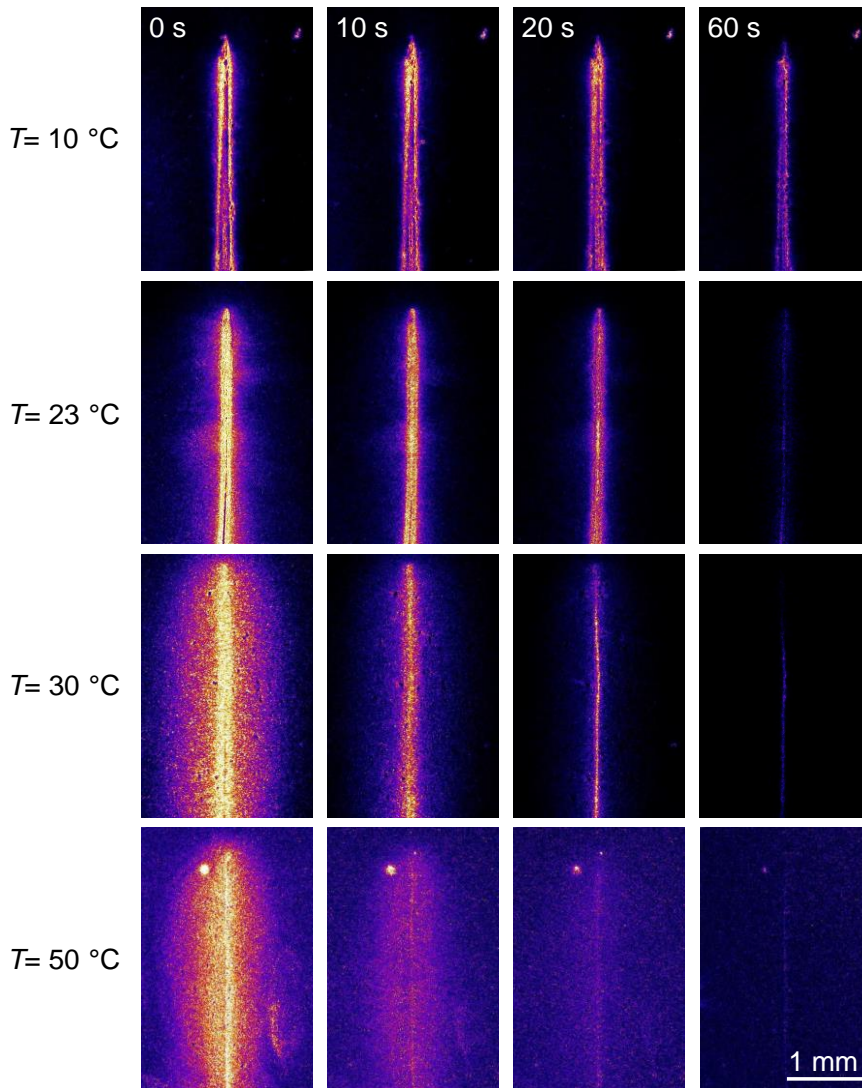


Figure S-3.4. Viscoplastic relaxation around a non-healing cut. Time-lapse micromechanical maps for reference polymer B-D-1.0, as a function of temperature. d_2 ($f=1$ Hz) is used as the contrast function. All images have the same scale bar and all rows display the same time points.

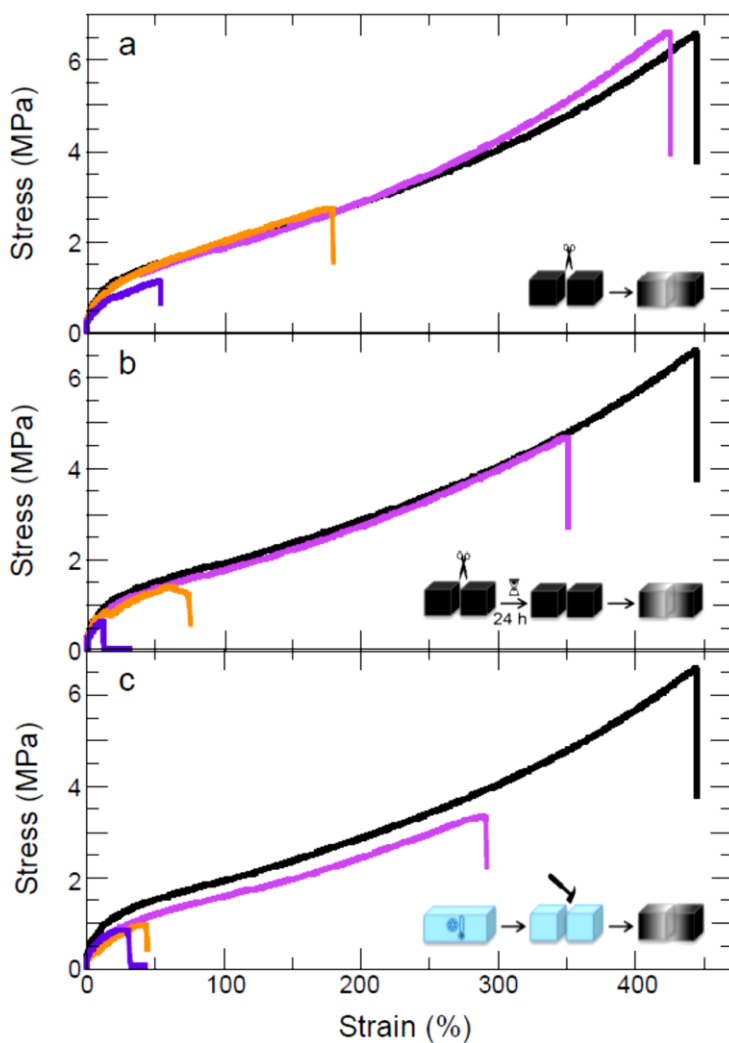


Figure S-3.5. Tensile mechanical and self-healing performance of D-1.1 for different fracture modes: a) blade-cut at 23°C followed by immediate contact between the cut surfaces; b) blade-cut at 23°C followed by 24 hours delay until contact; c) brittle freeze-fracture at 196°C followed by immediate contact between the crack surfaces. The pristine sample is indicated in each graph by —. All fracture modes are examined for three healing times: 1 day (—), 5 days (—) and 10 days (—). Stress–strain curves similar to (a) for D-1.1 without embedded nanoparticles can be found in reference,²¹ Figure 6.

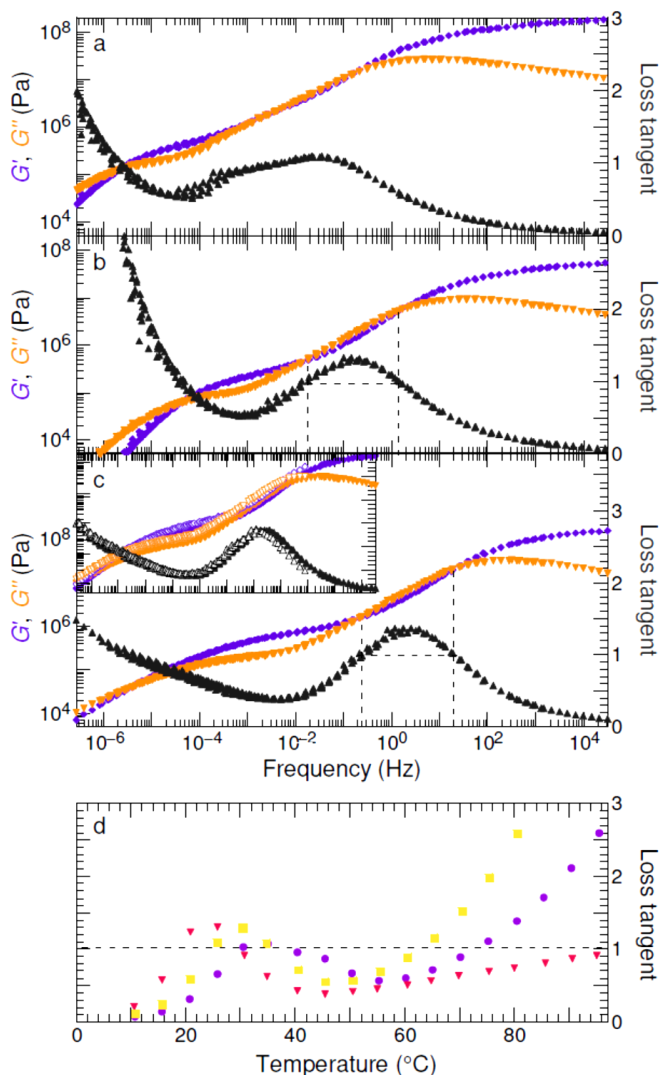


Figure S-3.6. Bulk rheology of the linear viscoelastic properties of the three thermoplastic elastomers. (a–c) Time-temperature superposition master curves of the storage modulus G' (\bullet), loss modulus G'' (\blacktriangledown) and loss tangent $\tan \delta = G''/G'$ (\blacktriangle), referenced to 25°C, for a) B-D-1.0, b) D-0.9 and c) D-1.1. The inset shows that the TTS curves of the unfilled D-1.1 polymer (open symbols) closely resemble those of the polymer with embedded nanoparticles (filled symbols). d) Temperature dependence of $\tan \delta$ for B-D-1.0 (\bullet), D-0.9 (\blacksquare) and D-1.1 (\blacktriangledown). The dashed lines indicate the windows where viscous processes dominate, and self-healing can proceed, determined by $\tan \delta > 1$. The non-healing polymer B-D-1.0 does not display such a window; D-0.9 exhibits the optimum loss tangent and healing capabilities at 30°C, and D-1.1 at 24°C. More extensive rheological characterization of D-0.9 and D-1.1 without embedded nanoparticles can be found in reference,²¹ Figure 4 and S6.

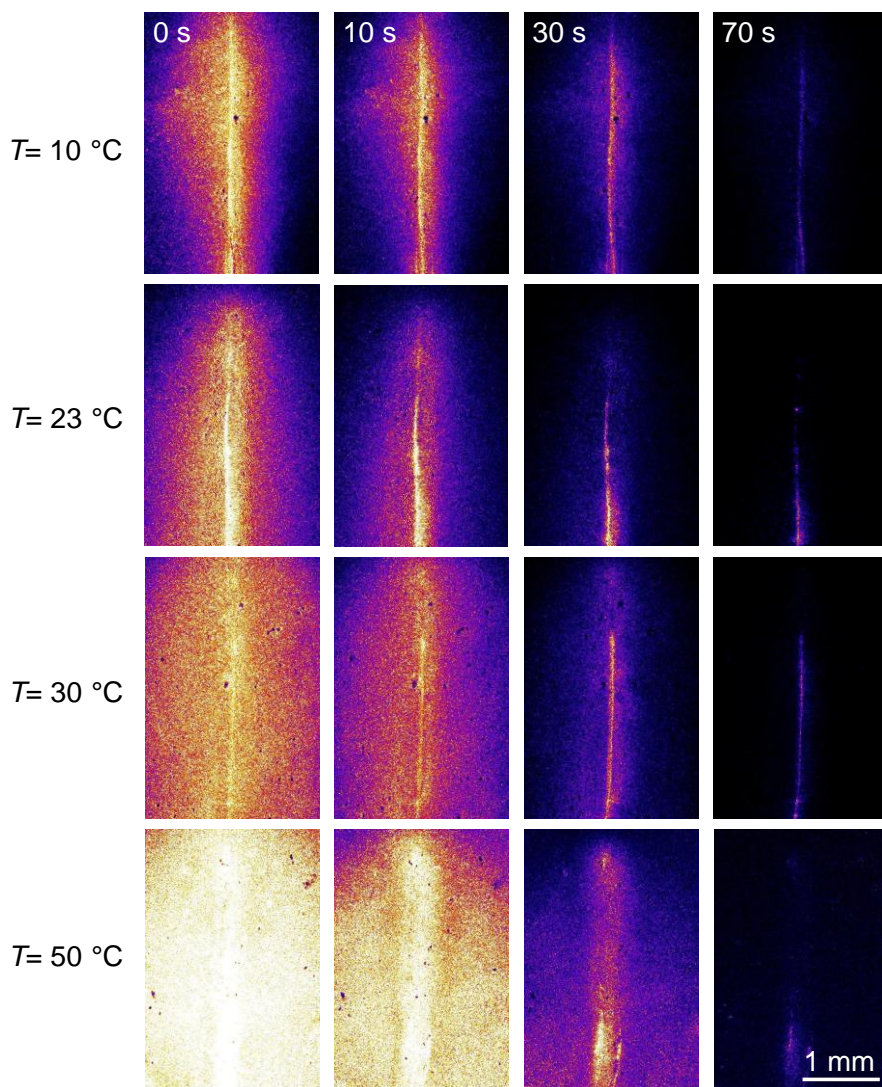


Figure S-3.7. Time-lapse micromechanical maps for polymer D-1.1 at different temperatures. d_2 ($f=1$ Hz) is used as the contrast function. All images have the same scale and color coding, and all rows display the same time points. Only at 23°C, the cut closes in a zipper-like manner and self-heals, implying that bond reformation is essentially dictated by kinetics: it is limited to a narrow temperature window, where re-bonding across the cut is not too slow yet re-bonding by backfolding of polymer chains is not too fast either.

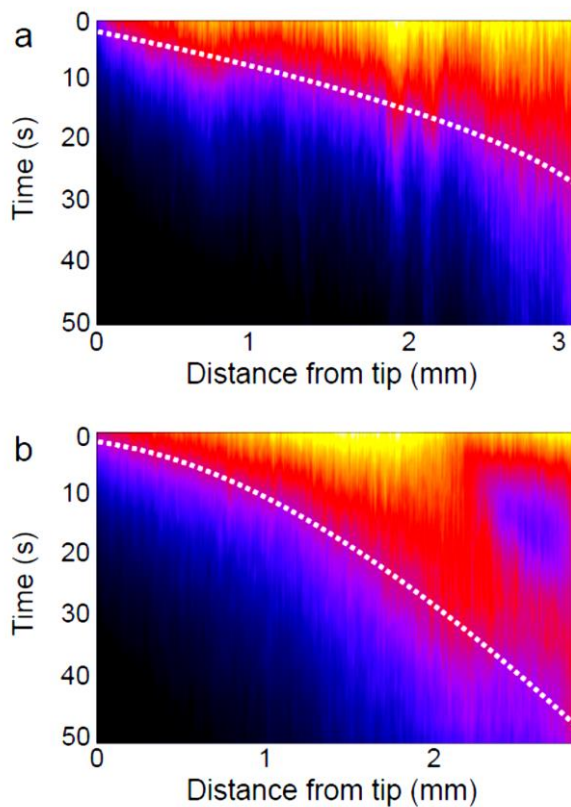


Figure S-3.8. Kymographs of cut closure in D-1.1 at 23°C. Horizontal cross-sections represent the molecular mobility along the cut, quantified by d_2 ($f=1$ Hz) where averaging is over 50 pixels in the perpendicular direction. The kymograph in (a) corresponds to the time series in Figure 3.3a of the main text, and that in (b) to a second, independent measurement. Both feature a front of mobility which advances away from the tip, characteristic of a zipper-like closure. The dotted lines are guides to the eye.

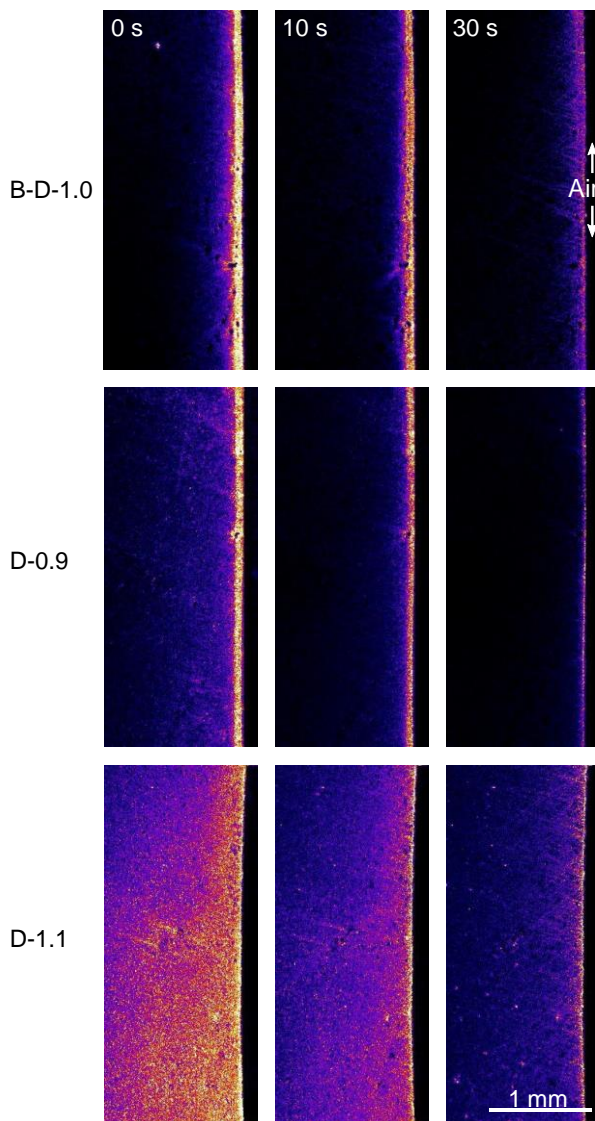


Figure S-3.9. Time-lapse micromechanical maps of the viscoplastic relaxation at a cut-air interface, at 23°C. d_2 ($f=1$ Hz) is used as the contrast function. All images have the same scale bar and all rows display the same time points. Small amounts of noise in the air background are masked. See Movie S8 for the full-time series of the non-healing polymer. Note that the dynamics are considerably longer-ranged for D-1.1, indicating stronger viscoplastic deformation during cutting due to a lower glass transition temperature ($T_g=8^\circ\text{C}$ for D-1.1 versus 19°C for B-D-1.0 and 17°C for D-0.9, see Table 3.1 of the main text). We observe the same difference in spatial extent of the relaxation for reunited cut surfaces (compare Figure S-3.4, S-3.7 and S-3.13).

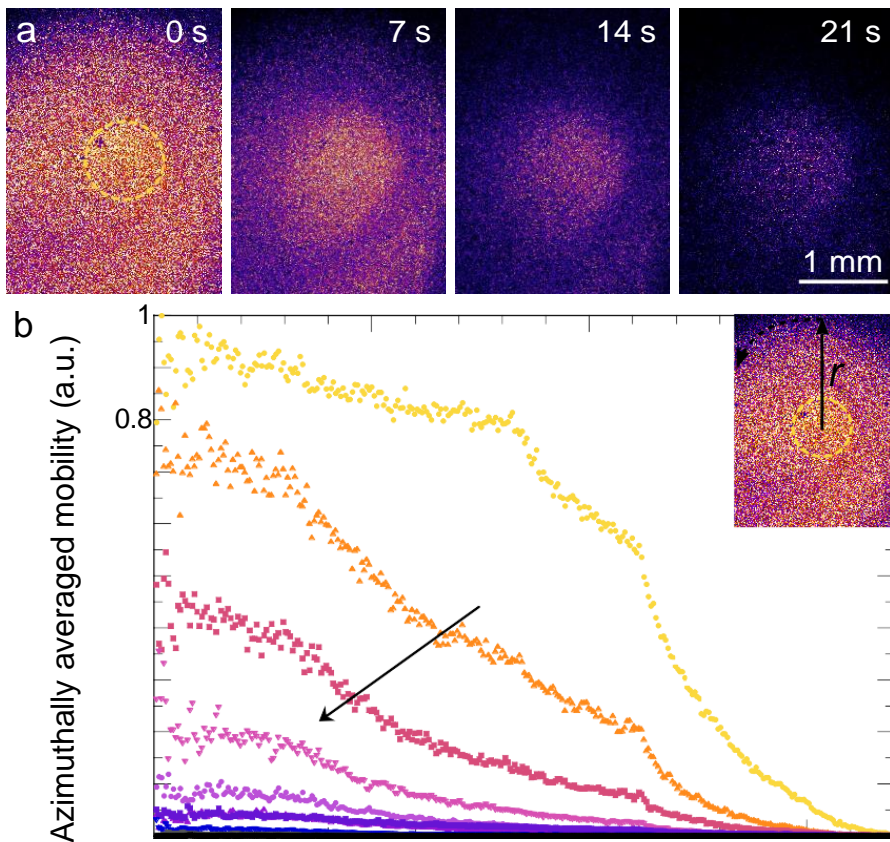


Figure S-3.10. Viscoplastic relaxation dynamics in linear conditions. a) Time-lapse micromechanical maps, at $f=1$ Hz, of the viscoplastic recovery of D-1.1 after spherical indentation with small strain. The original location of the indenter is delineated with a dashed yellow line. See movie S9 for the full-time series. b) Azimuthally averaged radial profiles from $t=0$ s (\circ) to $t=70$ s (\blacksquare) after indentation, with 7 s intervals. The inset shows the definition of the radial distance r . This experiment confirms that the delocalized dynamics we observe in e.g. Figure 3.3a and 3.3b of the main text are purely viscoplastic relaxations as a result of local deformation of the material.

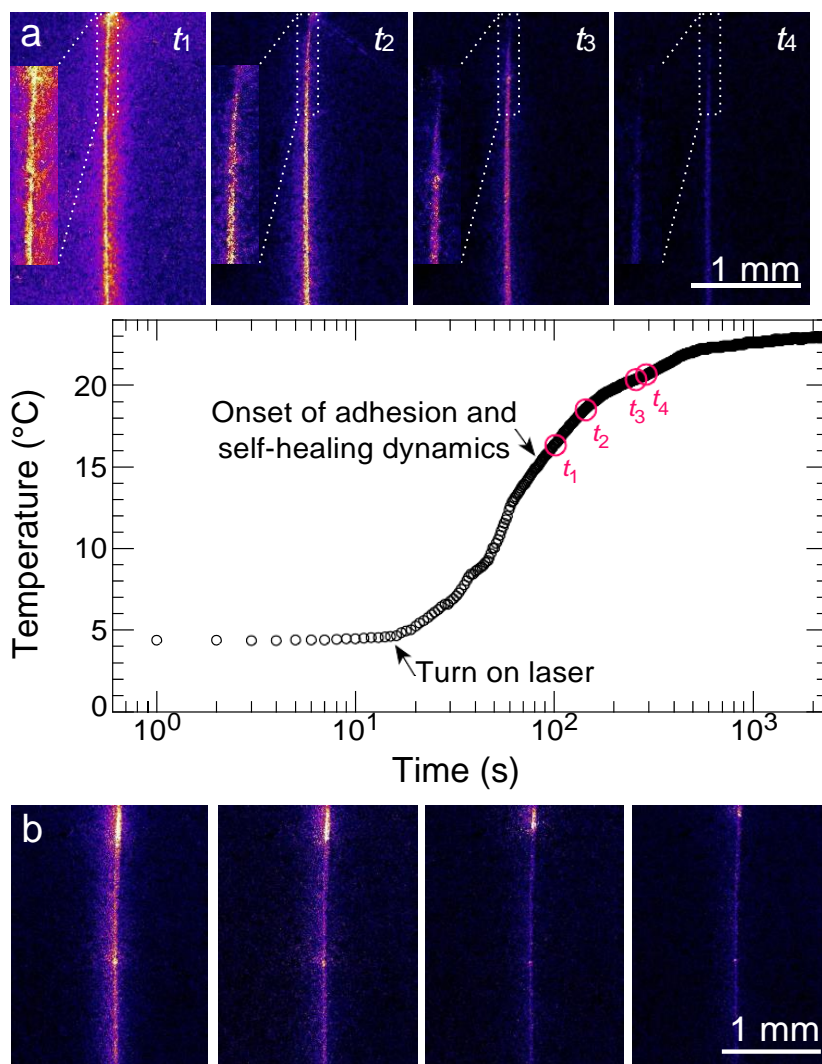


Figure S-3.11. Temperature dependence and modes of freeze-fracture healing. a) Evolution of the dynamics (top) and temperature (bottom) after freezing and semi-fracturing polymer D-1.1, elaborating on Figure 3.3c of the main text. The temperatures corresponding to times t_1 to t_4 are indicated in the graph, and are successively: 16.2, 18.6, 20.2 and 20.6°C. Note that after switching on the laser, the sample heats up considerably faster due to light absorption. Because of the lower initial self-healing temperature compared to cuts made at 23°C, the zipper propagates slower along the freeze-fracture and the instantaneous self-healing dynamics are weaker, yet they proceed longer (compare e.g. Figure S-3.7). Furthermore, this brittle fracture is much straighter and smoother than the ductile cut made at room temperature and exhibits more well-defined fracture planes. b) A freeze-fracture that traverses the entire sample lacks a distinct tip and unidirectional zipper-like motion. Nevertheless, several locations of enhanced mobility are visible across the crack, which propagate and diminish over time.

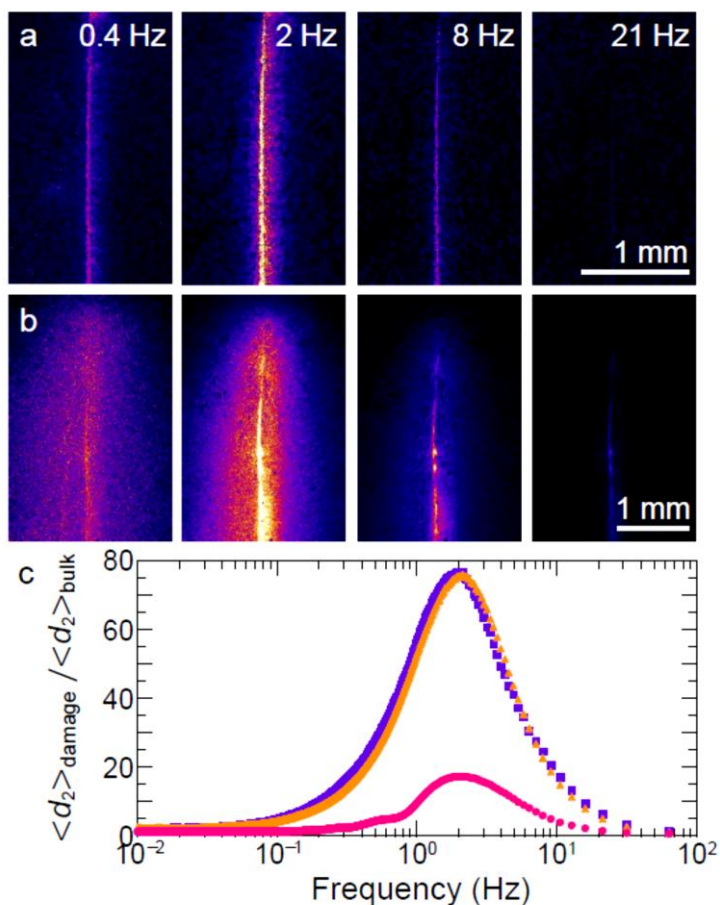


Figure S-3.12. Reproducibility of frequency-resolved self-healing mobility. a) Frequency dependence of the processes governing repair of a freeze-fracture, similar to Figure 3.3d of the main text, and of (b) a cut made at room temperature. The color scales are normalized by the respective values of $\langle d_2 \rangle_{\text{bulk}}$ and all have the same limits. c) Enhancement of self-healing dynamics at the damage interface with respect to the bulk of the material, $\langle d_2 \rangle_{\text{damage}} / \langle d_2 \rangle_{\text{bulk}}$ for the brittle fracture (\circ), the ductile cut (\triangle), and a second, independent measurement of a ductile cut made at room temperature (\blacksquare). The peak for the freeze-fracture is considerably lower because the instantaneous self-healing dynamics are weaker in that case, being spread out over a longer time period (see Figure S-3.11a). Note that the widths of these self-healing peaks are narrower than the $\tan\delta$ peaks in bulk rheological measurements (see Figure S-3.4c and Figure 3.3e of the main text); this is possibly due to kinetic broadening of the peaks in rheology due to finite frequency and temperature ramp rates.

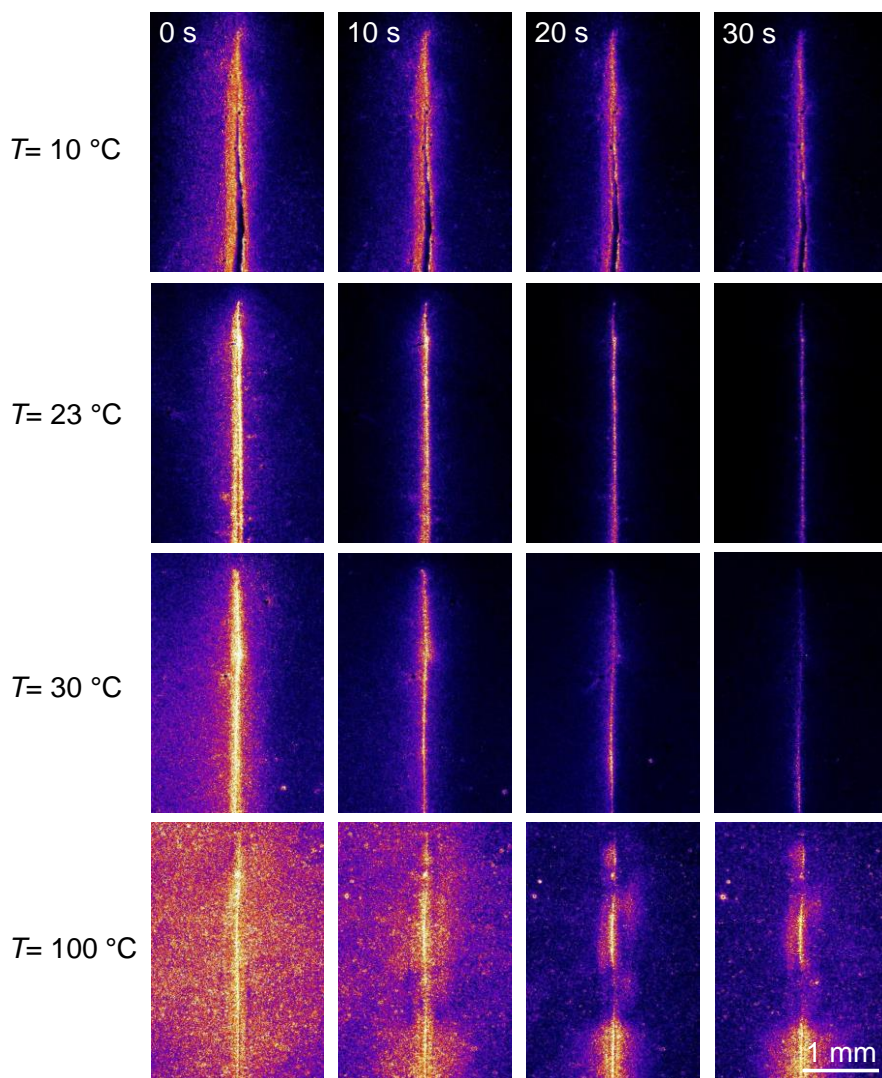


Figure S-3.13. Time-lapse micromechanical maps for polymer D-0.9 at different temperatures. d_2 ($f=1$ Hz) is used as the contrast function. Only at the optimal healing temperature of 30°C the cut closes in a zipper-like manner. At 100°C , a Rayleigh-Plateau instability develops. All images have the same scale and color coding, and all rows display the same time points.

Captions for Supporting Movies

Available at Wiley Online Library:

<https://onlinelibrary.wiley.com/doi/full/10.1002/adma.201701017>

Movie S1. Speckle–LSI movie of the relaxation dynamics around a non-healing cut at 23°C. Full time series corresponding to Figure 3.1 and 3.2a (top) of the main text, showing the first 150 s after cutting. The speckle and LSI movie run synchronously, 10x real time.

Movie S2. LSI movie of the homogeneous viscoplastic relaxation around a non-healing cut at 50°C. Full time series corresponding to Figure 3.2a (bottom) of the main text. First 70 s after cutting, 10x real time. Notice the intermittent ‘spikes’ in the overall dynamics, which are also visible in Figure 3.2b of the main text.

Movie S3. LSI movie of the zipper-like self-healing of a cut in D-1.1 at 23°C. Full time series corresponding to Figure 3.3a of the main text. First 200 s after cutting, 10x real time.

Movie S4. Speckle–LSI movie of the repair dynamics of a partial freeze-fracture in D-1.1. Full time series corresponding to Figure 3.3c of the main text. The speckle and LSI movie run synchronously, 10x real time. The temperature increases in the movie from 15.7°C to 21.5°C.

Movie S5. LSI movie of the homogeneous viscoplastic relaxation around a cut in D-0.9 at 23°C. Full time series corresponding to Figure 3.4a (left) of the main text. First 70 s after cutting, 10x real time.

Movie S6. LSI movie of the zipper-like self-healing of a cut in D-0.9 at 30°C. Full time series corresponding to Figure 3.4a (middle) of the main text. First 70 s after cutting, 10x real time.

Movie S7. LSI movie of the fluid-like Rayleigh–Plateau instability around a cut in D-0.9 at 100°C. Full time series corresponding to Figure 3.4a (right) of the main text. First 220 s after cutting, 10x real time. Note that the abrupt fluctuations are not experimental noise but correspond to reproducible intermittent ‘spikes’ in the overall dynamics.

Movie S8. LSI movie of the relaxation at a cut–air interface of the non-healing polymer at 23°C. Full time series corresponding to Figure S-3.9 (top). First 120 s after cutting, 10x real time.

Movie S9. LSI movie of the viscoplastic relaxation of D-1.1 after spherical indentation at 23°C. Full time series corresponding to Figure S-3.10. First 60 s after indentation, 3x real time.

4

Understanding the effect of the dianhydride structure on polymer properties

Zar ne misliš da je dirljivo smiješna ova mala čekaonica između lutanja i lutanja ?

Mika Antić

This chapter has been published as:

A. Susa, J. Bijleveld, M. Hernandez Santana, S. J. García,
ACS Sustainable Chemistry and Engineering 2018, 6 (1), 668-678

Abstract

In this work we report the effect of the hard block dianhydride structure on the overall properties of partially bio-based semi-aromatic polyimides. For the study, four polyimides were synthesized using aliphatic fatty dimer diamine (DD1) as the soft block and four different commercially available aromatic dianhydrides as the hard block: 4,4'-(4,4'-isopropylidenediphenoxy) bis-(phthalic anhydride) (BPADA), 4,4'-oxydiphthalic anhydride (ODPA), 4,4'-(Hexafluoroisopropylidene) diphthalic anhydride (6FDA) and 3,3',4,4'-biphenyltetracarboxylic dianhydride (BPDA). The polymers synthesized were fully organo-soluble thermoplastic branched polyimides with glass transition temperatures close to room temperature. The detailed analysis considered several aspects of the dianhydrides structure (planarity, rigidity, bridging group between the phthalimides, electronic properties) and related them to the results obtained by differential scanning calorimetry, rheology, fluorescence and broadband dielectric spectroscopy. Moreover, the effect of physical parameters (crystallization and electronic interactions) on the relaxation behaviour are discussed. Despite the presence of the bulky branched soft block given by the dimer diamine, all polyimides showed intermolecular charge transfer complexes, whose impact depends on the electronic properties of the dianhydride hard block. Furthermore, the results showed that polyimides containing flexible and bulky hard blocks turned out fully amorphous while the more rigid dianhydride (BPDA) led to a nanophase separated morphology with low degree of crystallinity resulting in constrained segmental relaxation with high effect on its mechanical response with the annealing time. This work represents the first detailed report on the development and characterization of polyimides based on a bio-based fatty dimer diamine. The results highlight the potential of polymer property design by controlled engineering of the aromatic dianhydride blocks.

4.1. Introduction

Due to the raising concerns regarding environmental sustainability, highly directed by growing and demanding ecological regulations, renewable resources are increasingly receiving both industrial and academic attention.¹⁻³ Amongst the different renewable sources vegetable oils are generally considered the most important class due to their availability and versatility. Vegetable oils are used to synthesize different types of polymers⁴ such as polycarbonates, polyurethanes, polyesters, polyethers, polyamides and polyolefins⁵ for paints, adhesives, composites and biomedical applications.³ Various thermoset and thermoplastic polymers can be obtained, resulting in miscellaneous characteristics to meet many different industrial requirements, thereby confirming vegetable-oil based polymers' potential as alternatives to petroleum-based ones.⁶⁻⁷

Vegetable oils are composed of different triglycerides which are the esterification products of glycerol with various fatty acids. The heterogeneity and variability of the triglycerides, which is due to the statistical distribution of fatty acids per triglyceride, makes a clear and reproducible correlation between the material properties and the monomer structures difficult. However, utilizing difunctional fatty acid-based monomers (diols, diamines, diacids) with a well-defined molecular structure can lead to bio-based polymers with better tuneable properties.⁸ Fatty dimers have been used in the past to prepare polymers with innovative molecular architectures, such as supramolecular polymers with hydrogen bonding⁹ or reversible ionic interactions¹⁰ and PU-acrylate coatings.¹¹ They are reportedly being utilized for suppressing H-bonding, inducing phase segregation and tuning viscosity, crystallinity and thermo-mechanical properties in renewable polyurethanes and polyamides¹²⁻¹³ and their bio-composites.¹⁴⁻¹⁵ More recently bio-based fatty dimer diamines with long alkyl branches (Priamine™) were reported as useful building blocks to develop room temperature self-healing polyimides with high mechanical properties.¹⁶⁻¹⁷ In that previous work we reported¹⁶ the effect of the stoichiometric offset of the DD1/ODPA ratio on the dynamic mechanical and self-healing properties of the resulting polymers. However, the role of the dianhydride architecture on the overall properties of these fatty dimer diamine-based polyimides was not examined, leaving room for further dedicated research.

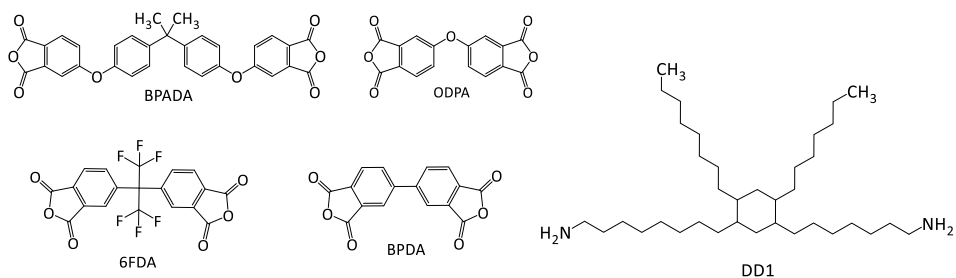
Polyimides are known for their capability of forming intra- and inter-chain electronic interactions called charge-transfer complexes (CTC), which are the reason behind their high thermo-mechanical properties and deep coloration.¹⁸ However, most of the aromatic polyimides are insoluble in any organic solvent. That, in addition to very high glass transition temperatures, often higher than their decomposition temperatures, limits their usefulness for many applications.¹⁹ Flexible and bulky linkage groups are traditionally being introduced between aromatic rings in the dianhydride monomer²⁰⁻²¹ to enhance solubility, transparency and processing. The goal of these modifications is to either disrupt their aromaticity (to prevent intramolecular conjugation) or to make the chains pack less efficiently (to prevent intermolecular CTC formation). Naturally, modification of molecular architecture of polyimides influences their mechanical properties and molecular dynamics as well.²²⁻²⁴

In this work we report the effect of the aromatic dianhydride structure on the thermal, optical, mechanical properties and relaxation behaviour of a set of polyimides based on a bio-based aliphatic dimer diamine (DD1). The results are discretized with regards to several aspects: planarity, rigidity, bridging group between the phtalimides, electronic properties and the combinations thereof. Moreover, the effect of different physical constraints (crystal formation and electronic interactions) on the relaxation behaviour is discussed in detail. Despite their partially aliphatic and densely branched architectures, it was found that the synthesized polyimides are still able to form intermolecular charge transfer complexes, playing an important role in the overall properties of these semi-aromatic thermoplastic polyimides. To the best of our knowledge, this is the first time that the effect of fatty dimer diamine is explored in a set of different polyimides with varying dianhydride architecture.

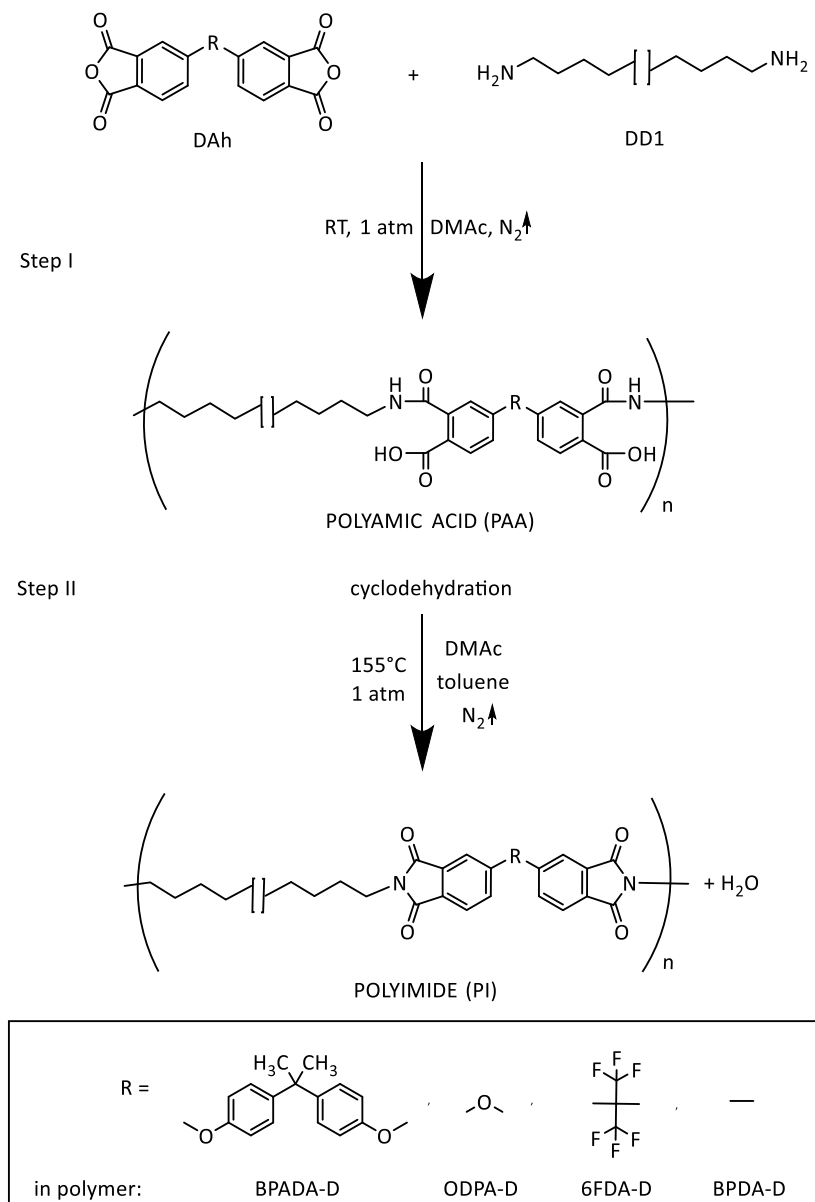
4.2. Experimental

4.2.1. Synthesis

Four aromatic dianhydrides were used as hard aromatic block (Scheme 1): 4,4'-(4,4'-isopropylidenediphenoxy) bis-(phthalic anhydride) (BPADA) (97%, Sigma Aldrich), 4,4'-oxydiphthalic anhydride (ODPA) (98%, TCI Europe N.V.), 4,4'-(Hexafluoroisopropylidene) diphtalic anhydride (6FDA) (98%, TCI Europe N.V.), 3,3',4,4'-biphenyltetracarboxylic dianhydride (BPDA) (98%, TCI Europe N.V.). The soft block was in all cases a fatty dimer diamine derived from vegetable oil (Priamine™ 1075, here called DD1) (Croda Nederland B.V.) with structure as shown in Scheme 4.1. DD1 appears as a light-yellow viscous liquid with melting point at -30°C and 100% renewable carbon content. Theoretical stoichiometric ratio calculated according to the molecular weights of the monomers ($MW_{\text{BPADA}}=520.49$ g/mol, $MW_{\text{ODPA}}=310.20$ g/mol, $MW_{\text{6FDA}}=444.24$ g/mol, $MW_{\text{BPDA}}=294.22$ g/mol and $MW_{\text{DD1}}=536.80$ g/mol) and assuming all chemicals are 100% difunctional, were used. The synthesis was conducted in *N,N*-dimethylacetamide (DMAc, 99.5% extra dry, Acros Organics) polar aprotic solvent with total solids (monomers) content of 20 wt.%. Using a two-step polymerization process as described in the Scheme 4.2, four polymers were obtained: BPADA-D, ODPA-D, 6FDA-D and BPDA-D. The details of the synthesis procedure in Scheme 4.2 can be found elsewhere.¹⁶



Scheme 4.1. Structures of the monomers used in the polyimides synthesis. Left side shows four dianhydrides used (BPADA, ODPA, 6FDA and BPDA) and right side shows a generalized structure of the dimer diamine (DD1).



Scheme 4.2. Schematic representation of the thermal imidization reaction (cyclodehydration of polyamic acid into a polyimide).

4.2.2. Characterization methods

Infrared spectroscopy

Attenuated Total Reflectance Fourier Transform Infrared (ATR-FTIR) spectroscopy was employed in order to follow reaction completion. Each IR spectrum was recorded as an average of 2 scans in the wavenumber range 4000-500 cm^{-1} .

Gel permeation chromatography (GPC)

Molecular weight distributions of synthesized polymers were determined by GPC on a Shimadzu Prominence GPC system equipped with a Shodex LF-804 column and a refractive index detector. The flow rate of the eluent tetrahydrofuran (THF) was 1 ml/min and polystyrene was used as standard. Polymer solutions prepared in THF at 1 mg/mL and the samples were filtered (0.45 μm syringe filter) prior to use.

Thermal analysis

Thermal properties were evaluated by Perkin Elmer Pyris Diamond TG/DTA thermogravimetric analysis (TGA) and Perkin Elmer Sapphire differential scanning calorimetry (DSC). All measurements were performed under nitrogen. TGA was run from room temperature to 500°C at 10°C/min. DSC measurements were carried out at 10°C/min following this procedure: (1) heating from -50°C to 200°C; (2) holding at 200°C for 2 min; (3) cooling down to -50°C and (4) repeat steps 1 to 3. The glass transition temperature (T_g) was determined from the second heating cycle.

Density determination

The density of the polymers was determined by hydrostatic weighing method coupled with an analytical laboratory scale with a precision of 0.1 mg.

Rheological measurements

The linear viscoelastic properties of the PIs were investigated by the Haake Mars III rheometer, using the parallel plate geometry, with plate diameter of 8 mm. Preliminary strain amplitude sweeps at 1 Hz were performed at the highest and the lowest tested temperatures, from 0.001% to 10% strain to evaluate the extension of the linear viscoelastic region for the different polymers. Based on these results, a shear strain of 0.5% for all polymers was used to ensure the tests were performed in the linear viscoelastic region. Temperature sweep experiments were performed at 1 Hz in a cooling ramp from 50 to 5°C. The $\tan\delta$ curves from the temperature sweeps were used to determine T_g from the maximum of the $\tan\delta$ peak ($T_g=T(\tan\delta_{\text{MAX}})$). For the aim of activation energies, E_a , calculations, the frequency sweep experiments from 10 to 0.1 Hz were performed at temperatures between 110 and 10°C, in steps of 5°C. Tests were repeated twice-showing high reproducibility. The rheological mastercurves at the reference temperature of the previously determined $T_g=T(\tan\delta_{\text{MAX}})=T_{\text{ref}}$ were constructed from the obtained data applying the time-temperature superposition principle (TTS) using the dedicated Rheowin software. From the shift factors, a_T , the Arrhenius plots ($\ln a_T$ vs. $1000/T$) were constructed and the activation energies were calculated from the slopes of the linear fit,²⁵ as shown in the Supporting Information (S-4.6).

Broadband dielectric spectroscopy (BDS)

BDS measurements were performed on an ALPHA high resolution dielectric analyzer (Novocontrol Technologies GmbH). All samples were mounted in the dielectric cell between two parallel gold-plated electrodes. The complex permittivity $\varepsilon^*(\omega) = \varepsilon'(\omega) - i\varepsilon''(\omega)$ of each sample was measured by performing consecutive isothermal frequency sweeps over a frequency window of $10^{-1} < f < 10^6$ (where $f=\omega/2\pi$ is the frequency of the applied electric field) in the temperature range from 0 to 100°C in steps of 5°C. The resulting relative error of each parameter is less than 3%.

Tensile properties

Tensile mechanical tests were performed on an Instron model 3365 universal testing systems equipped with a 1 kN load cell, using dog-bone specimens according to the ASTM D1708 standard (thickness, $t=2\pm 0.5$ mm) at 80 mm/min crosshead speed and ambient temperature ($23\pm 2^\circ\text{C}$).

Fluorescence spectroscopy

The fluorescence spectra of polyimides were obtained using a PTI QuantaMaster Photoluminescence Spectrometer equipped with 75 W Xe lamp and using a PMT voltage of 1000 V. The same specimen geometry as for the tensile test was used. First the excitation scan was run in the range 280-400 nm, collecting emission at 410 nm. From this, the fluorescent peak was determined at 360 nm. Further, the samples were excited at that particular wavelength and monitored over the range 370–700 nm using an aperture slit width of 2 nm with 1 nm step size and 0.1 s integration time during monitoring. Each measurement was repeated three times, showing good reproducibility. The sample thickness was found not to have an effect on the measured peak.

4.3. Results and discussion

4.3.1. Effect of the dianhydride structure on the PIs properties

The imidization of PAA into PI can be confirmed by IR spectroscopy using the disappearance of the amic acid peaks typically visible at 1716, 1640 and 1550 cm^{-1} in PAA spectra and the appearance of the characteristic peaks of imide bonds at 1770, 1710, 1360 and 745 cm^{-1} in PI spectra. The imidization reaction was confirmed for all the polymers (Figure 4.1) and supported by ^1H NMR analysis (Figure S-4.1, Supporting Information). The percentage yields were calculated by the standard approach shown in Supporting Information. Yields of 83% for BPADA-D, 89% for ODPA-D, 74% for 6FDA-D and 73% for BPDA-D were obtained.

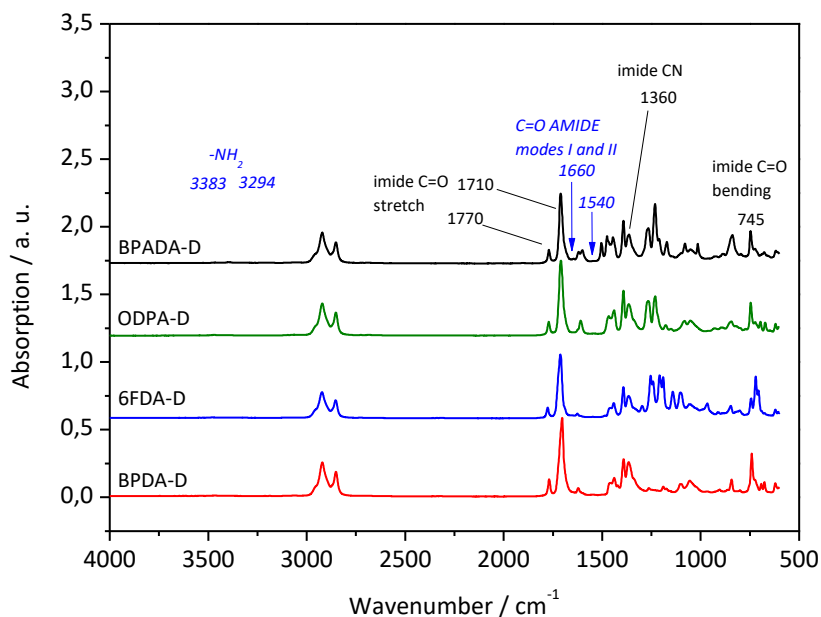


Figure 4.1. IR spectra of four PIs with different dianhydrides showing characteristic imide peaks (labeled black) and absence of pre-polymer (amide) peaks (labeled italic blue).

Table 4.I. Effect of the DAh type on M_w , M_n and PDI as calculated from the major peak obtained in GPC. T_g obtained from DSC, rheology and BDS and temperatures for 2% weight loss obtained from TGA. Samples were tested as produced.

Polymer	M_w (g/mol)	M_n (g/mol)	PDI	DSC T_g^a (°C)	Rheology T_g^b (°C)	BDS T_g^c (°C)	TGA T (2% weight loss) (°C)	Density (g/cm ³)
BPADA-D	29k	18k	1.6	24	36	20	360	1.05
ODPA-D	32k	16k	2.0	13	25	11	380	1.05
6FDA-D	41k	20k	2.0	25	40	21	330	1.12
BPDA-D	37k	20k	1.9	22	33 ⁱ , 46 ⁱⁱ	18	350	1.05

^a T_g was calculated from the 2nd heating curve, 10°C/min.

^b T_g was taken as the maximum of the peak in the $\tan\delta$ curve from the temperature sweeps, performed in cooling ramp, 1°C/min.

^c T_g is obtained from the broadband dielectric spectroscopy (BDS) measurements, by extrapolating the VFT fit to the temperature at which τ_{\max} is equal to 100 s (see Figure S-4.5, SI).

^{i,ii} Polymer BPDA-D exhibits two T_g peaks [T_g (I) and T_g (II)] in rheological temperature sweep plots, which is shown and discussed later in the chapter.

As can be seen from the TGA curves (Figure S-4.2, SI), all polymers show a high thermal stability independent of the dianhydride architecture with values for the onset degradation temperature (2% weight loss) at 330-380°C (Table 4.I) similar to those of traditional commercial polyimides such as LaRC-IA. All samples showed only a small weight loss up to 0.6% until 200°C suggesting that almost no solvent (toluene or DMAc) was entrapped during the imidization and that the monomers were fully reacted. The resulting polymers were fully soluble in common organic solvents, such as toluene, THF and chloroform, which facilitates their processing (for example, in coatings, adhesives and thin films applications), as opposed to commercial polyimides.¹⁹ The GPC results are presented in Table 4.I. The small differences in the molecular weights might be due to various reasons, such as impurities or side-reactions but also differences in the electron affinities of the aromatic dianhydrides. As the susceptibility of the nucleophilic attack increases with the electrophilicity of the dianhydride group, the reactivity of the dianhydride monomer is related to its electron affinity: higher values indicate higher reactivity of the dianhydride. According to literature,^{18,26} the electron affinities of the dianhydrides used in this work increase in the order: BPADA-D < ODPA-D < BPDA-D < 6FDA-D.

The flexibility of the dianhydride moieties is reflected in the value of the T_g , where three polymers (BPADA-D, 6FDA-D and BPDA-D) exhibit a similar T_g , ranging from 22-25°C and ODPDA-D showing a lower value of 13°C. The T_g values of these PIs are incomparable to those of fully aromatic commercial PIs ($200 < T_g < 400^\circ\text{C}$),²⁷ which naturally excludes the possibility for their use in high-temperature applications. However, their T_g -s are higher than the ones of other reported polymers that contain fatty acid dimer as the building block that remained below room temperature. The ionic supramolecular networks prepared from fatty acid dimer by Aboudzadeh et al exhibit their T_g -s in the range $(-29) < T_g < 10^\circ\text{C}$.¹⁰ The fatty acid dimer based polyamides from Hablot et al showed $(-17) < T_g < (-5)^\circ\text{C}$,¹² while the values in the range $(-10) < T_g < (-0.9)^\circ\text{C}$ were obtained in the fatty acid dimer based polyamides synthesized by van Velthoven et al.¹³

The ODPDA and BPADA dianhydrides have a very flexible oxygen linker between the two phthalic anhydride parts of the molecule (Scheme 4.1). Comprising two oxygen linkers, BPADA may appear the most flexible out of the four dianhydrides used here, yet it does not exhibit the lowest T_g . This is likely to be caused by the increase in aromatic content compared to ODPDA-D, where the extra flexibility of the ether linkage is counterbalanced by the increased number of aromatic rings. Despite the structural differences, BPDA-D and 6FDA-D display a similar T_g . The expected increase in backbone flexibility of the 6FDA-D polymer may be compensated by the extra bulkiness of the CF_3 groups. A similar effect of dianhydride structure on the T_g of non-branched fully²⁰ and partially aromatic²⁸ polyimides was reported in literature, with exception of BPADA. A detailed DSC analysis (Figure S-4.3, SI) shows the absence of melting or crystallization peaks thereby reflecting the amorphous nature of all the polyimides in their state just after synthesis.

Rheological temperature sweeps were performed at a very slow cooling rate ($1^\circ\text{C}/\text{min}$) and the results are shown in Figure 4.2. Figure 4.2a shows the values of the storage modulus (G') and loss modulus (G'') while damping factors ($\tan\delta$) versus temperature at 1 Hz for all the samples studied are shown in Figure 4.2b.

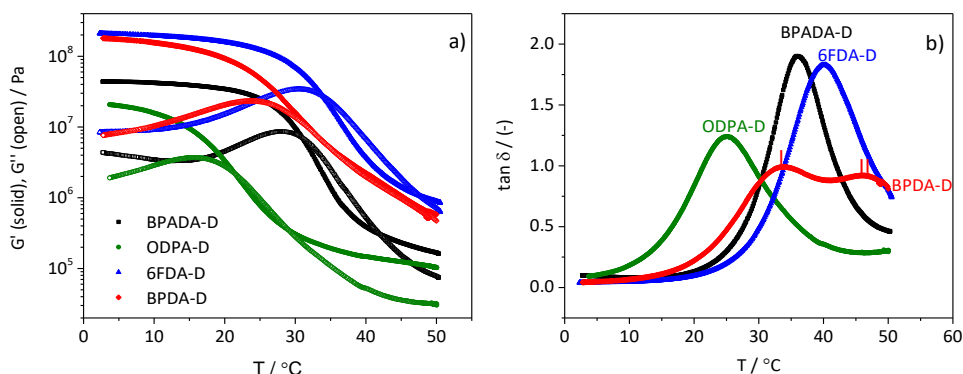


Figure 4.2. a) Storage (G') and loss (G'') moduli and b) $\tan \delta$ curves from the rheological temperature sweeps experiments, showing distinct T_g -relaxations of the four PIs.

The differences between the T_g values determined from the maximum of the $\tan \delta$ peak ($25^\circ\text{C} < T_g < 40^\circ\text{C}$) arise from the effect of different aromatic dianhydride structures on the glass transition processes. The width of the curves indicate the breadth of the temperature range over which the glass transition occurs but also the polymer structural heterogeneity.²⁹ The values of $\tan \delta$ of these polymers (especially BPADA-D and 6FDA-D with values close to 2) are remarkably high over a broad range of near-room temperatures, which makes them great candidates in applications where high damping properties are required at ambient conditions (noise or vibration insulating materials, shock absorbers and sealants). In general, damping materials with $\tan \delta > 0.5$ are considered for outdoor or machinery applications.³⁰ (As seen in Figure 4.2b, BPADA-D and 6FDA-D are displaying the narrowest $\tan \delta$ peaks. A somewhat broader curve was obtained with ODPA-D and the broadest with BPDA-D. Moreover, BPDA-D system exhibits stepwise glass transition (shown in Figure 4.2b as (I) and (II)), as opposed to the other three (BPADA-D, ODPA-D and 6FDA-D), which show single T_g .

Similar observations could be made from the broadband dielectric spectroscopy (BDS) data. The spectra corresponding to all four polymers over a wide range of frequencies at different temperatures are shown in Figure S-4.4, SI. T_g was calculated from the temperature dependence of the segmental relaxation times (τ_{max}).

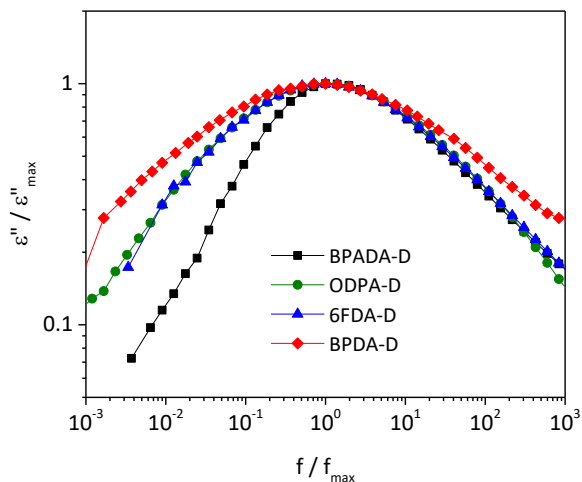


Figure 4.3. Normalized dielectric loss $\log(\epsilon'')$ vs. normalized frequency $\log(f)$ of PI samples with different dianhydrides at $T=50^\circ\text{C}$.

When this dependence follows a Vogel-Fulcher-Tammann (VFT) behaviour, T_g is obtained by extrapolating the VFT fit to the temperature at which τ_{\max} is equal to 100 s (See SI).³¹ The T_g -s calculated following this approach (Table 4.I) are similar to the values obtained by DSC and follow the same trend of increase among the four polymers investigated (ODPA-D < BPDA-D < BPADA-D < 6FDA-D), as seen by DSC and rheology. The temperature dependence of the relaxation times in the whole region of the segmental relaxation further supports the fact that the ODPA-D polymer has the least restricted dynamics (see SI).

In addition to a third estimate of T_g , BDS gave some further insights on the structure and polymer architecture of the studied PIs. By plotting the normalized dielectric loss vs normalized frequency, a clearer view on how the shape (symmetry, broadness) of the relaxation spectra varies is obtained. Figure 4.3 shows the normalized plots at a selected temperature ($T=50^\circ\text{C}$) at which the dielectric relaxation is clearly observable as a well-resolved peak in the frequency window for all polymers. Depending on the nature of the dianhydride incorporated into the polymer, clear differences in the shape of the spectra can be noticed. Schönhal's and Schlosser³² phenomenological model proposes that the shape of the normalized

dielectric loss peak is related to the behaviour of the polymer at low and high frequencies, controlled by inter- and intra-molecular interactions, respectively. The application of such a model to the studied polyimides suggests that the differences on the low frequency side may be related to the changes in the dynamics of the main chain segments due to the contribution/restriction imposed by the different dianhydrides, while the variations on the high frequency side can be attributed to the influence of the dangling side chains.

In order to quantify these differences, the dielectric strength ($\Delta\epsilon$) and the shape parameters b and c derived from the Havriliak-Negami (HN) fitting function (see SI) were calculated and shown in Figure 4.4. The b and c parameters characterize the symmetric and asymmetric broadening of the relaxation time distribution, respectively. The term $b*c$ is also shown in the same Figure. In a $\log(\epsilon'')$ vs $\log(f)$ plot, just as in Figure 4.3, the shape parameters b and $b*c$ correspond to the low- and high-frequency slopes of the relaxation function respectively, with regards to the position of the maximal loss.³³

A detailed analysis of the plots in Figure 4.4 gives better insight into the effect of different dianhydrides on the resulting polymer architectures. An increase in dielectric strength ($\Delta\epsilon$) can be understood in terms of an increasing number of mobile dipoles (increasing fraction of polar molecules) involved in the relaxation, indirectly reflecting stronger molecular interactions. We can therefore infer that the BPADA-D system has higher dipole interactions than the rest of the PI systems with other dianhydrides.

Recently, a research on the relaxation behaviour of thermo-reversible elastomer networks based on 2-ureido-4-pyrimidinone (UPy) dimers has been published by Luo et al.³⁴ In their work they report on the appearance of a new relaxation, seen as a shoulder close to the segmental relaxation, ascribed to the dissociation dynamics of dimer complexes within the network. They conclude that this new relaxation is related to the local UPy dimers dynamics resulting from the dissociation and reformation of the complexes. They also report an increase of $\Delta\epsilon$ due to the increased number of dissociated UPy units. In our work, there is no evidence of a new relaxation probably because they take place within the

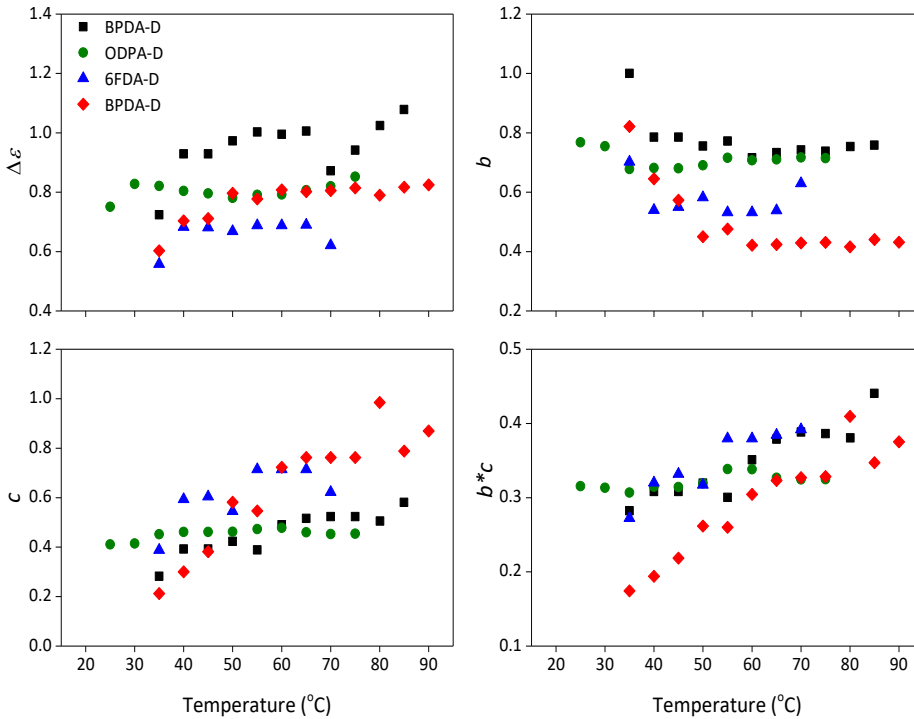


Figure 4.4. Dielectric parameters derived from the HN fitting function in the temperature range of the segmental relaxation.

temperature range within the glass transition, therefore any weaker relaxation is hidden by the strong segmental relaxation. Secondly, the fact that the b parameter is higher for the BPADA-D system reflects a narrower and more symmetrical loss peak. In terms of the polymer architecture, this would suggest a more homogeneous structure formed by polymer chains with similar large-scale motions. On the contrary, the lowest b value for the BPDA-D system suggests chain segments with different dynamics and thus a higher degree of structural heterogeneity, implying regions of distinct mobility. This hypothesis is confirmed by the presence of a stepwise glass transition, as reported by rheological measurements (Figure 4.2b). Moreover, the lowest $b*c$ parameter for BPDA-D is further confirming heterogeneous dynamics of this sample with a more visible temperature dependence. As temperature increases, the $b*c$ parameter tends to

increase, presuming the distinct heterogeneous mobility regions become more homogeneous, especially above 50°C. As will be discussed later, the increase on $b \cdot c$ values above 50°C could be related to local ordering present in the BPDA-D sample appearing at around 50°C.

Aromatic polyimides are well known for forming Charge Transfer Complexes (CTCs), which are widely claimed to be the reason behind their great mechanical and thermal properties, as well as their characteristic colors,¹⁸ due to their absorption characteristics tailings in the visible region caused by the intra and/or intermolecular charge transfer (CT) interactions of the PI backbones. Moreover, CTCs have a major effect on the chain packing.^{27, 35} In order to investigate the origin of the different coloration, the polymer optical properties were tested by fluorescence spectroscopy as typically used in polyimide research to identify the formation of CTCs.^{18, 35-39} The CTCs existence has been previously confirmed for not only fully aromatic PIs, but also in the semi-aromatic ones.⁴⁰ Our results showed that CTCs in the branched polyimides are identified by a long-wavelength absorption at $\lambda > 330$ nm, similar to those reported in literature.³⁷⁻³⁸ As can be seen in Figure 4.5, the four polyimides developed in this work are fluorescent in the CTC-region ($400 \text{ nm} < \lambda_{\text{em}} < 450 \text{ nm}$).

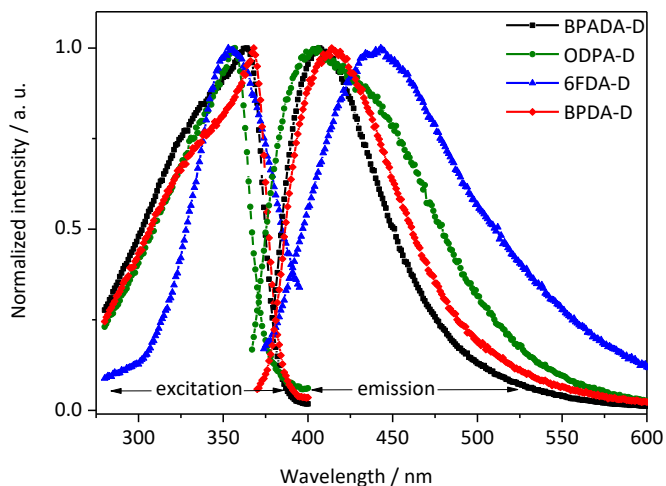


Figure 4.5. Optical properties of the four PIs: fluorescence excitation (left) and emission (right) spectra, normalized by maximum. $\lambda_{\text{exc}}=360$ nm.

4.3.2. Effect of the low temperature annealing on local ordering

Another important factor affecting the physical properties of polyimides is the aggregation state of polymer chains, i.e. macromolecular packing. Many have shown that imidization temperature affects the aggregation state of PIs,³⁸ but the post-imidization thermal treatment (i.e. annealing) does as well.⁴¹ In order to further explore the origin of physical constraints on the properties of the given set of DD1 based PIs, they were subjected to low temperature annealing, $T_{\text{ann}}=T(\tan\delta_{\text{MAX}})=T_g$ (see Table 4.II), for 1, 5 and 11 days. Their thermal, optical and mechanical properties were then evaluated as function of the annealing time. The DSC scans of all four polymers show no change in their T_g values.

However, as opposed to the other three polymers, a change in opacity with time was noticed for BPDA-D, turning from translucent to fully turbid after 5 and 11 days at T_{ann} . DSC scans of turbid BPDA-D show an appearance of a melting peak at 68°C (yet no change in the T_g value). The melt enthalpy increases from 5 J/g (for 5 days annealed) to 11 J/g (for 11 days annealed) with no change in T_m (Figure 4.6). As seen by polarized microscopy (Figure S-4.7, SI), the birefringence increases with annealing time as well.

These observations can be explained by the rigidity and planarity of the BPDA monomer which result in the chain regularity and hence efficient chain packing, allowing the BPDA-D polymer to crystallize.²⁸ At this stage it is not possible to unambiguously state which segments of the molecule crystallize. Nevertheless, the increase of order in chain packing with annealing time in BPDA-D polymer was confirmed by small angle X-ray scattering measurements, SAXS (Figure S-4.8, SI) by appearance of two additional peaks at annealing times 5 and 11 days, with respect to 1 day.

Table 4.II. The annealing temperatures taken as maxima of the $\tan\delta$ peak (T_g) of the rheological temperature sweep curves (Figure 4.2b).

Polymer	$T_{\text{ann}}=T(\tan\delta_{\text{MAX}})=T_g$ (°C)
BPADA-D	36
ODPA-D	25
6FDA-D	40
BPDA-D	33

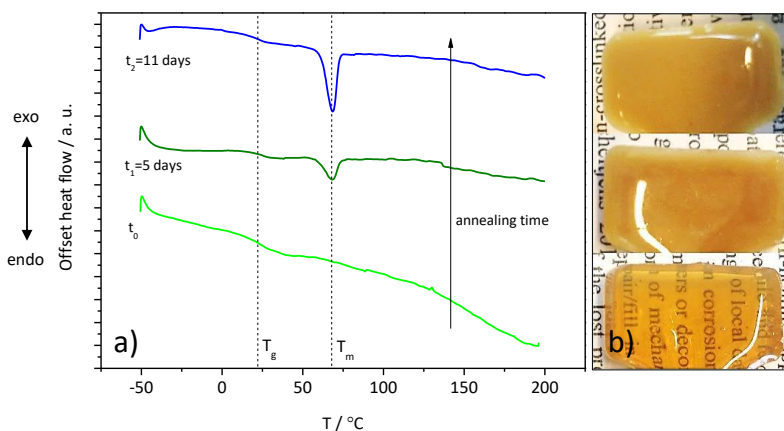


Figure 4.6. a) DSC traces from the second heating curve with T_g and T_m indicated by the dashed lines and b) corresponding images showing increase in opacity of BPDA-D polymer with annealing time. $T_{ann} = T(\tan \delta_{MAX}) = T_g$.

The peak ratio is $q_1 : q_2 : q_3 = 1 : 2 : 3$, which was previously reported to be related to the nano-phase separation in lamellar morphology.⁴² Taking in account that T_m is rather low (68°C) and considering reported similar range of T_m values for other partially aromatic polymers with alkyl side branches in literature,⁴³⁻⁴⁴ we suggest that crystals might be formed within the nanodomains of the alkyl side branches. As Beiner and Huth suggested, this may be a result of a confinement of the alkyl side chains by less-mobile main chains.⁴⁵ However, further research is necessary to confirm this hypothesis.

On contrary, the polymers with the other three dianhydrides remain fully amorphous with the annealing time. Even though rigid, the bulky hexafluoroisopropylidene spacer of 6FDA dianhydride causes distortions of backbone symmetry which prevents the parallel alignment of the chains. On the other hand, the ether linkages of BPADA and ODPDA are not bulky but offer high rotational freedom and flexibility which reduces the rigidity of the backbone, introduces kinks which hinder the co-planarity and thus prevent any efficient chain packing.^{22, 27-28}

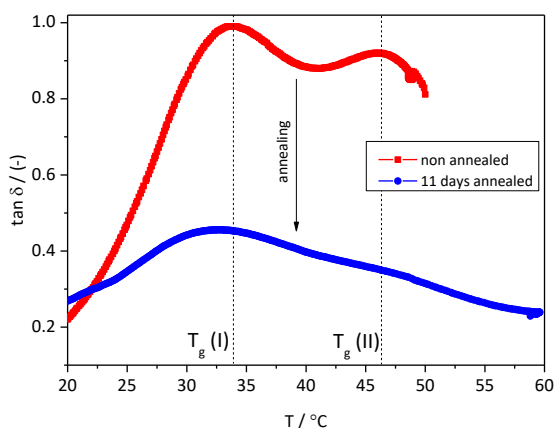


Figure 4.7. Rheological T -sweep curves. Effect of annealing on the glass transition relaxation behaviour of the BPDA-D polymer. Red curve represents the non-annealed polymer and the blue curve shows the polymer annealed for 11 days at $T_{\text{ann}} = T(\tan\delta_{\text{MAX}}) = T_g$.

For example, Arnold et al prepared nine polyimides using six different dianhydrides, including ODPA, 6FDA and BPDA among others. Only two polymers with different diamines were able to crystallize during drawing or/and annealing and both of them comprised BPDA as the dianhydride.⁴⁶

While the rheological temperature sweeps of the polymers BPADA-D, ODPA-D and 6FDA-D do not show any change with the annealing time, the BPDA-D polymer undergoes significant change in the glass transition region, as can be seen in Figure 4.7. After 11 days of annealing, the $\tan\delta$ decreases over the whole range of temperatures tested. Furthermore, the curve broadens, and the two peaks are less pronounced, which is expected, as the content of the amorphous phase decreases with the increase in the crystalline fraction. This multiple- T_g relaxation behaviour is characteristic for multiphase structures and incompatible blends. However, the behaviour noticed in BPDA-D polymer is peculiar because of the (consistently) reverse magnitudes of the two peaks ($T_g(\text{I})$, at the lower temperature and $T_g(\text{II})$, at the higher temperature). This can be expressed in terms of activation energies as well. Activation energies, E_a , are calculated from the Arrhenius plots (Figure S-4.6, SI), as described in the Supporting Information.

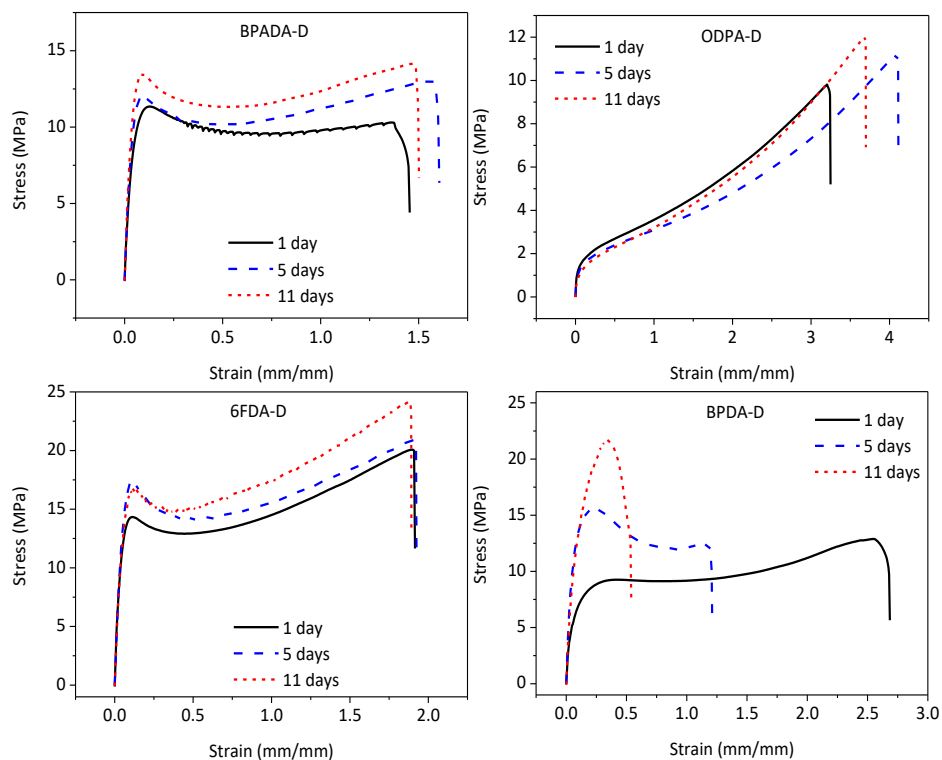


Figure 4.8. Effect of annealing time on the stress-strain behaviour of the four PIs. $T_{\text{ann}} = T(\tan\delta_{\text{MAX}}) = T_g$.

The peak at the lower temperature, $T_g(\text{I})$, exhibits higher E_a than the one at higher temperature, $T_g(\text{II})$ (see Table S-4.1, SI). Such an observation can be explained by assuming a less mobile phase present at the crystal-amorphous phase interface.⁴⁷

Thus, based on the literature and the DSC evidences that the BPDA-D polymer is the only semi-crystalline (Figure 4.6) polymer out of the four here investigated, we could explain the multiple $\tan\delta$ peaks as follows: the relaxation occurring at about 33°C is presumed to be the relaxation of the major part of the amorphous phase, a T_g per se. The relaxation occurring at a higher temperature of 46°C can be attributed to the restricted amorphous phase located in the interfacial region.

The effect of the aromatic dianhydride architecture on the mechanical properties was also evaluated. Figure 4.8 shows representative stress-strain curves of the four

PIs obtained at ambient temperature ($T_{\text{test}}=23\pm 2^{\circ}\text{C}$). The mechanical performance changes significantly with varying the dianhydride architecture. ODPA-D polymer shows elastomeric behaviour, which is as expected because its T_g is below T_{test} , as opposed to the other three polymers that are in their glassy state ($T_g > T_{\text{test}}$).

The stress at break values (σ_b) increase in the order: ODPA-D < BPADA-D < BPDA-D < 6FDA-D and the strain at break (ϵ_b) values in following: BPADA-D < 6FDA-D < BPDA-D < ODPA-D. The 6FDA-D system shows the highest toughness and strain hardening while BPADA-D exhibits strain softening, having yield stress higher than its stress at break value. Young's moduli are in a broad range, from 90 MPa (ODPA-D) to 430 MPa (6FDA-D), comparable to the fatty acid dimer based polyamides of Hablot et al.¹² When compared to commercial fully aromatic PIs, these materials are roughly one order of magnitude lower in strength.⁴⁸

The effect of annealing on the tensile properties is also shown in Figure 4.8. The three amorphous polymers (BPADA-D, ODPA-D and 6FDA-D) show minor improvement of the mechanical properties with annealing time, while the effect on the semi-crystalline BPDA-D is more evident. The stress at break value increases from 11 MPa to 20 MPa, and the strain at break value decreases from 260% to 35%, despite the non-relevant variation in T_g . The repeated fluorescence spectra after annealing the samples did not show any shifts in fluorescence peaks wavelengths.

4.4. Conclusions

A series of partially bio-based semi-aromatic polyimides varying in their aromatic dianhydride structure was synthesized in stoichiometric ratio with the fatty dimer diamine and their thermal, mechanical and optical properties were investigated. The polymers obtained were fully organo-soluble thermoplastic branched polyimides with glass transition temperatures close to room temperature. Their solubility, amorphous thermoplasticity and high thermal stability makes them easily processable and recyclable without deterioration of mechanical properties. The results have shown that the dianhydrides comprising a flexible ether spacer (BPADA and ODPA), as well as the one with rigid and bulky hexafluoroisopropylidene spacer (6FDA) were fully amorphous. However, the dianhydride with no spacer (BPDA) is providing a semi-crystalline structure with the annealing time, which leads to a constrained segmental relaxation. Despite their partially aliphatic and densely branched architectures, these polyimides are able to form the intermolecular charge transfer complexes, whose extent is dependent on the dianhydride electronic properties and evident from their fluorescence spectra and normalized dielectric loss. The increase in crystallinity with annealing time was shown to have a great effect on the tensile properties of the BPDA-D polymer despite no significant T_g variation was measured. The values of $\tan\delta$ of these polymers (especially BPADA-D and 6FDA-D with values close to 2) are remarkably high over a broad range of near-room temperatures, which makes them great candidates in applications where high damping properties are required at ambient conditions (noise or vibration insulating materials, shock absorbers and sealants).

References

1. Williams, C. K.; Hillmyer, M. A., Polymers from Renewable Resources: A Perspective for a Special Issue of Polymer Reviews. *Polymer Reviews* **2008**, *48* (1), 1-10.
2. Bozell, J. J., Feedstocks for the Future – Biorefinery Production of Chemicals from Renewable Carbon. *CLEAN – Soil, Air, Water* **2008**, *36* (8), 641-647.
3. Adekunle, K. F., A Review of Vegetable Oil-Based Polymers: Synthesis and Applications. *Open Journal of Polymer Chemistry* **2015**, *5* (3), 34-40.
4. Jain, J. P.; Sokolsky, M.; Kumar, N.; Domb, A. J., Fatty Acid Based Biodegradable Polymer. *Polymer Reviews* **2008**, *48* (1), 156-191.
5. Miao, S.; Wang, P.; Su, Z.; Zhang, S., Vegetable-Oil-Based Polymers as Future Polymeric Biomaterials. *Acta Biomaterialia* **2014**, *10* (4), 1692-1704.
6. Xia, Y.; Larock, R. C., Vegetable Oil-Based Polymeric Materials: Synthesis, Properties and Applications. *Green Chemistry* **2010**, *12* (11), 1893-1909.
7. Meier, M. A.; Metzger, J. O.; Schubert, U. S., Plant oil renewable resources as green alternatives in polymer science. *Chemical Society reviews* **2007**, *36* (11), 1788-1802.
8. Maisonneuve, L.; Lebarbe, T.; Grau, E.; Cramail, H., Structure-Properties Relationship of Fatty Acid-Based Thermoplastics as Synthetic Polymer Mimics. *Polymer Chemistry* **2013**, *4* (22), 5472-5517.
9. Cordier, P.; Tournilhac, F.; Soulie-Ziakovic, C.; Leibler, L., Self-Healing and Thermoreversible Rubber from Supramolecular Assembly. *Nature* **2008**, *451* (7181), 977-980.
10. Aboudzadeh, A.; Fernandez, M.; Muñoz, M. E.; Santamaría, A.; Mecerreyes, D., Ionic Supramolecular Networks Fully Based on Chemicals Coming from Renewable Sources. *Macromolecular Rapid Communications* **2014**, *35* (4), 460-465.
11. Lutz, A.; van den Berg, O.; Van Damme, J.; Verheyen, K.; Bauters, E.; De Graeve, I.; Du Prez, F. E.; Teryn, H., A Shape-Recovery Polymer Coating for the Corrosion Protection of Metallic Surfaces. *ACS Applied Materials & Interfaces* **2015**, *7* (1), 175-183.
12. Hablot, E.; Donnio, B.; Bouquey, M.; Avérous, L., Dimer Acid-Based Thermoplastic Bio-Polyamides: Reaction Kinetics, Properties and Structure. *Polymer* **2010**, *51* (25), 5895-5902.
13. van Velthoven, J. L. J.; Gootjes, L.; Noordover, B. A. J.; Meuldijk, J., Bio-Based, Amorphous Polyamides with Tunable Thermal Properties. *European Polymer Journal* **2015**, *66*, 57-66.

14. Boumbimba, R. M.; Wang, K.; Hablot, E.; Bahlouli, N.; Ahzi, S.; Avérous, L., Renewable Biocomposites Based on Cellulose Fibers and Dimer Fatty Acid Polyamide: Experiments and Modeling of the Stress–Strain Behaviour. *Polymer Engineering & Science* **2017**, *57* (1), 95-104.
15. Reulier, M.; Boumbimba, R. M.; Walsh Korb, Z.; Vaudemont, R.; Avérous, L., Thermomechanical and Cyclic Behaviour of Biocomposites Based on Renewable Thermoplastics from Dimer Fatty Acids. *Journal of Applied Polymer Science* **2017**, *134* (12), 44610.
16. Susa, A.; Bose, R. K.; Grande, A. M.; van der Zwaag, S.; Garcia, S. J., Effect of the Dianhydride/Branching Diamine Ratio on the Architecture and Room Temperature Healing Behaviour of Polyetherimides. *ACS Applied Materials & Interfaces* **2016**, *8* (49), 34068-34079.
17. van der Kooij, H. M.; Susa, A.; García, S. J.; van der Zwaag, S.; Sprakel, J., Imaging the Molecular Motions of Autonomous Repair in a Self-Healing Polymer. *Advanced Materials* **2017**, *29* (26), 1701017.
18. Ando, S.; Matsuura, T.; Sasaki, S., Coloration of Aromatic Polyimides and Electronic Properties of Their Source Materials. *Polymer Journal* **1997**, *29* (1), 69-76.
19. Ayala, D.; Lozano, A. E.; De Abajo, J.; De La Campa, J. G., Synthesis and Characterization of Novel Polyimides with Bulky Pendant Groups. *Journal of Polymer Science Part A Polymer Chemistry* **1999**, *37*, 805-814.
20. Hegde, M.; Shahid, S.; Norder, B.; Dingemans, T. J.; Nijmeijer, K., Gas Transport in Metal Organic Framework–Polyetherimide Mixed Matrix Membranes: The Role of the Polyetherimide Backbone Structure. *Polymer* **2015**, *81*, 87-98.
21. Ogieglo, W.; Madzarevic, Z. P.; Raaijmakers, M. J. T.; Dingemans, T. J.; Benes, N. E., High-Pressure Sorption of Carbon Dioxide and Methane in All-Aromatic Poly(etherimide)-Based Membranes. *Journal of Polymer Science Part B: Polymer Physics* **2016**, *54* (10), 986-993.
22. Ragosta, G.; Abbate, M.; Musto, P.; Scarinzi, G., Effect of the Chemical Structure of Aromatic Polyimides on Their Thermal Aging, Relaxation Behaviour and Mechanical Properties. *Journal of Materials Science* **2012**, *47* (6), 2637-2647.
23. Li, F.; Ge, J. J.; Honigfort, P. S.; Fang, S.; Chen, J.-C.; Harris, F. W.; Cheng, S. Z. D., Dianhydride Architectural Effects on the Relaxation Behaviours and Thermal and Optical Properties of Organo-Soluble Aromatic Polyimide Films. *Polymer* **1999**, *40* (18), 4987-5002.
24. McCreight, K. W.; Ge, J. J.; Guo, M.; Mann, I.; Li, F.; Shen, Z.; Jin, X.; Harris, F. W.; Cheng, S. Z. D., Phase Structures and Transition Behaviours in Polymers Containing Rigid Rodlike Backbones with Flexible Side Chains. V.

Methylene Side-Chain Effects on Structure and Molecular Motion in a Series of Polyimides. *Journal of Polymer Science Part B: Polymer Physics* **1999**, 37 (14), 1633-1646.

25. Wood-Adams, P.; Costeux, S., Thermorheological Behaviour of Polyethylene: Effects of Microstructure and Long Chain Branching. *Macromolecules* **2001**, 34 (18), 6281-6290.

26. Ghosh, A.; Mistri, E. A.; Banerjee, S., Fluorinated Polyimides: Synthesis, Properties, and Applications. In *Handbook of Specialty Fluorinated Polymers*, Banerjee, S., Ed. William Andrew Publishing: Amsterdam, 2015; pp 97-185.

27. Acar, H. Y.; Ostrowski, C.; Mathias, L. J., Investigation of Structure-Property Relationships in Aromatic Polyimides and Polyamides. In *Polyimides and Other High Temperature Polymers: Synthesis, Characterization and Applications*, Mittal, K. L., Ed. VSP: Zeist, 2001; Vol. 1, pp 3-18.

28. Wakita, J.; Sekino, H.; Sakai, K.; Urano, Y.; Ando, S., Molecular Design, Synthesis, and Properties of Highly Fluorescent Polyimides. *The Journal of Physical Chemistry B* **2009**, 113 (46), 15212-15224.

29. Szczepanski, C. R.; Pfeifer, C. S.; Stansbury, J. W., A New Approach to Network Heterogeneity: Polymerization Induced Phase Separation in Photo-Initiated, Free-Radical Methacrylic Systems. *Polymer* **2012**, 53 (21), 4694-4701.

30. Wu, C.-f.; Akiyama, S., Enhancement of Damping Performance of Polymers by Functional Small Molecules. *Chinese Journal of Polymer Science* **2002**, 20 (2), 119-127.

31. Angell, C. A., Relaxation in Liquids, Polymers and Plastic Crystals — Strong/Fragile Patterns and Problems. *Journal of Non-Crystalline Solids* **1991**, 131, 13-31.

32. Schönhals, A.; Schlosser, E., Dielectric Relaxation in Polymeric Solids Part 1. A New Model for the Interpretation of the Shape of the Dielectric Relaxation Function. *Colloid & Polymer Science* **1989**, 267 (2), 125-132.

33. Schönhals, A., Molecular Dynamics in Polymer Model Systems. In *Broadband Dielectric Spectroscopy*, Kremer, F.; Schönhals, A., Eds. Springer-Verlag: Berlin, 2003; pp 248-251.

34. Luo, M.-C.; Zhang, X.-K.; Zeng, J.; Gao, X.-X.; Huang, G.-S., Enhanced Relaxation Behaviour below Glass Transition Temperature in Diene Elastomer with Heterogeneous Physical Network. *Polymer* **2016**, 91, 81-88.

35. Hasegawa, M.; Horie, K., Photophysics, Photochemistry, and Optical Properties of Polyimides. *Progress in Polymer Science* **2001**, 26 (2), 259-335.

36. Tang, H.; Feng, H.; Luo, H.; Dong, L.; Feng, Z., The Aggregation State of Polyimide. *European Polymer Journal* **1997**, 33 (4), 519-523.

37. Wachsman, E. D.; Frank, C. W., Effect of Cure History on the Morphology of Polyimide: Fluorescence Spectroscopy as a Method for Determining the Degree of Cure. *Polymer* **1988**, *29* (7), 1191-1197.
38. Hasegawa, M.; Kochi, M.; Mita, I.; Yokota, R., Molecular Aggregation and Fluorescence Spectra of Aromatic Polyimides. *European Polymer Journal* **1989**, *25* (4), 349-354.
39. Hasegawa, M.; Mita, I.; Kochi, M.; Yokota, R., Charge-Transfer Emission Spectra of Aromatic Polyimides. *Journal of polymer science. Part C, Polymer letters* **1989**, *27* (8), 263-269.
40. García, M. G.; Marchese, J.; Ochoa, N. A., Aliphatic–Aromatic Polyimide Blends for H₂ Separation. *International Journal of Hydrogen Energy* **2010**, *35* (17), 8983-8992.
41. Luo, L.; Yao, J.; Wang, X.; Li, K.; Huang, J.; Li, B.; Wang, H.; feng, Y.; Liu, X., The Evolution of Macromolecular Packing and Sudden Crystallization in Rigid-Rod Polyimide via Effect of Multiple H-Bonding on Charge Transfer (CT) Interactions. *Polymer* **2014**, *55* (16), 4258-4269.
42. Yokoyama, H., Small Angle X-ray Scattering Studies of Nanocellular and Nanoporous Structures. *Polymer Journal* **2013**, *45* (1), 3-9.
43. Prosa, T. J.; Winokur, M. J.; McCullough, R. D., Evidence of a Novel Side Chain Structure in Regioregular Poly(3-alkylthiophenes). *Macromolecules* **1996**, *29* (10), 3654-3656.
44. Pankaj, S.; Beiner, M., Confined Dynamics and Crystallization in Self-Assembled Alkyl Nanodomains. *The Journal of Physical Chemistry B* **2010**, *114* (47), 15459-15465.
45. Beiner, M.; Huth, H., Nanophase Separation and Hindered Glass Transition in Side-Chain Polymers. *Nature Materials* **2003**, *2* (9), 595-599.
46. Arnold, F. E.; Bruno, K. R.; Shen, D.; Eashoo, M.; Lee, C. J.; Harris, F. W.; Cheng, S. Z. D., The Origin of β Relaxations in Segmented Rigid-Rod Polyimide and Copolyimide Films. *Polymer Engineering & Science* **1993**, *33* (21), 1373-1380.
47. Dechter, J. J.; Axelson, D. E.; Dekmejian, A.; Glotin, M.; Mandelkern, L., An Analysis of the β Transition of Linear and Branched Polyethylenes by Carbon-13 NMR. *Journal of Polymer Science: Polymer Physics Edition* **1982**, *20* (4), 641-650.
48. Yu, X.; Liang, W.; Cao, J.; Wu, D., Mixed Rigid and Flexible Component Design for High-Performance Polyimide Films. *Polymers* **2017**, *9* (9), 451.

SUPPORTING INFORMATION***Yield***

Percent yield of the polymer was calculated according to equation:

$$\text{Percent yield (\%)} = 100 \left(\frac{\text{Actual mass of the product}}{\text{Predicted mass of the product}} \right)$$

where predicted mass of the product was calculated according to the stoichiometric balance, assuming that 1 mol of a dianhydride (DAh) and 1 mol of DD1 give 1 mol of PI and 2 mol of water (4.25 wt% of water):

$$\text{Predicted mass of the product/g} = m(\text{DAh}) + m(\text{DD1}) - m(\text{H}_2\text{O})$$

¹H NMR spectra

Solution state ¹H NMR spectra were collected using the Agilent-400 MR DD2 at 25°C at 400 MHz. The solutions of polymers were prepared in CDCl₃. Spectra were referenced to the solvent residual peak for TMS. Spectra were not normalized.

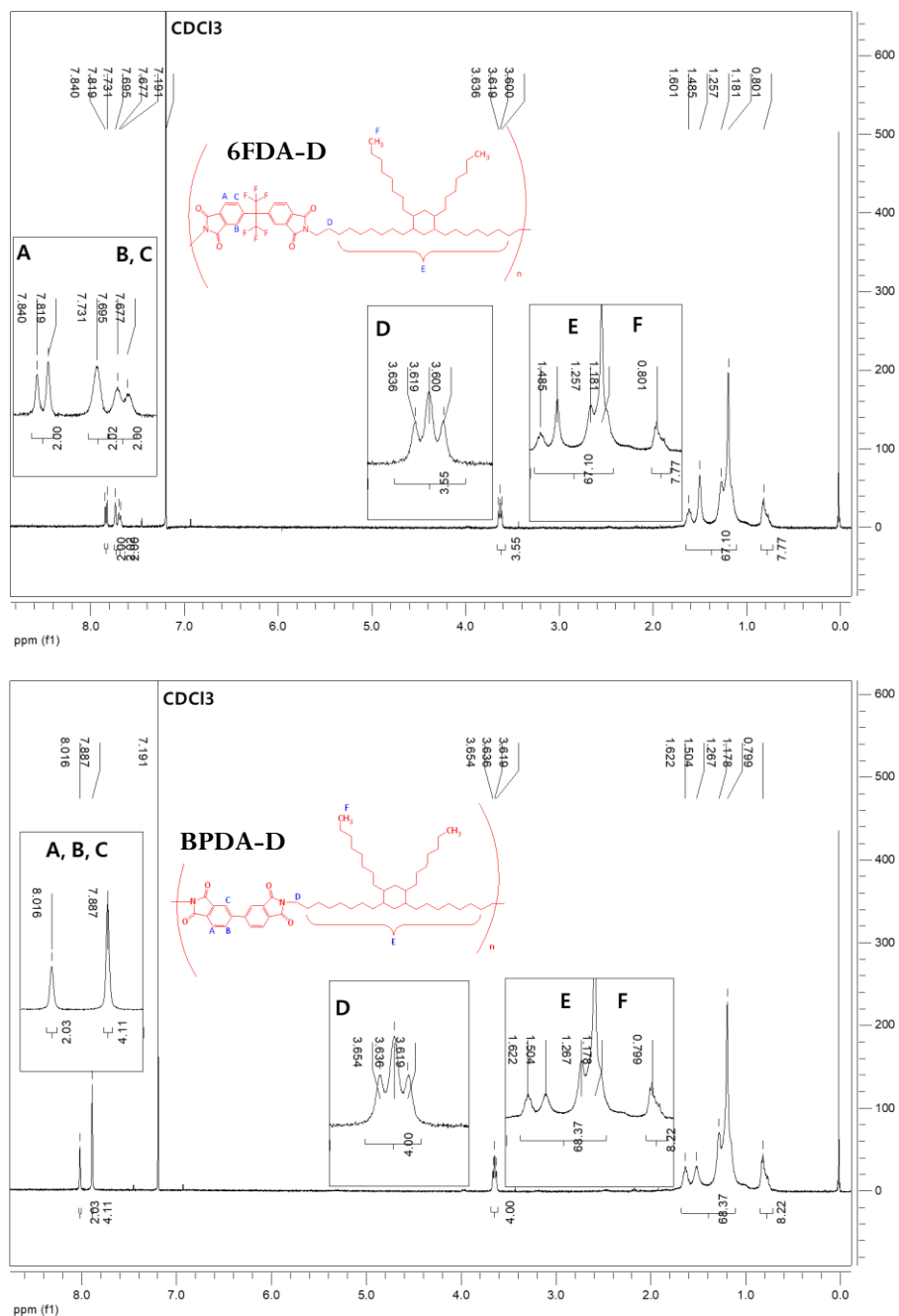


Figure S-4.1. ^1H NMR spectra of the four polymers in CDCl_3 and their assignment to the molecular structure.

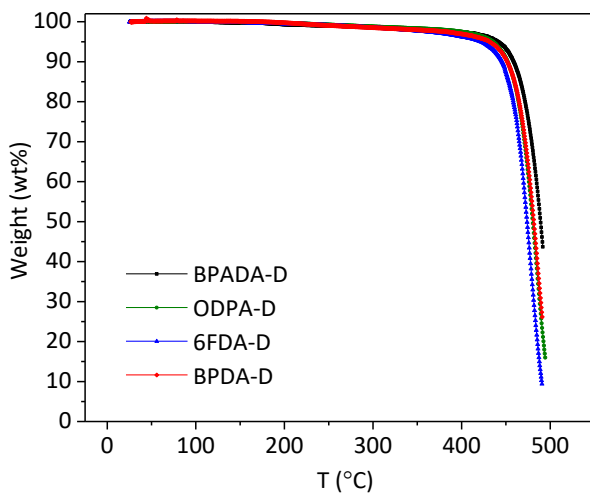


Figure S-4.2. TGA curves showing weight loss (wt%) with temperature of the four PIs in the as synthesized state.

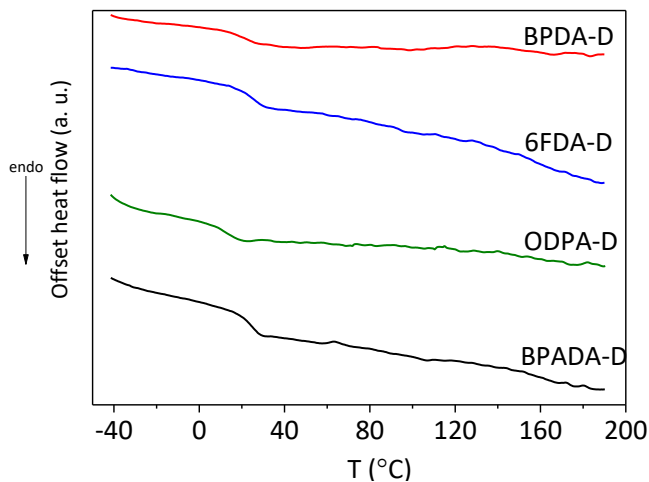


Figure S-4.3. DSC traces of the second heating curves, showing glass transitions of the four PIs in the as synthesized state.

Broadband dielectric spectroscopy (BDS) analysis

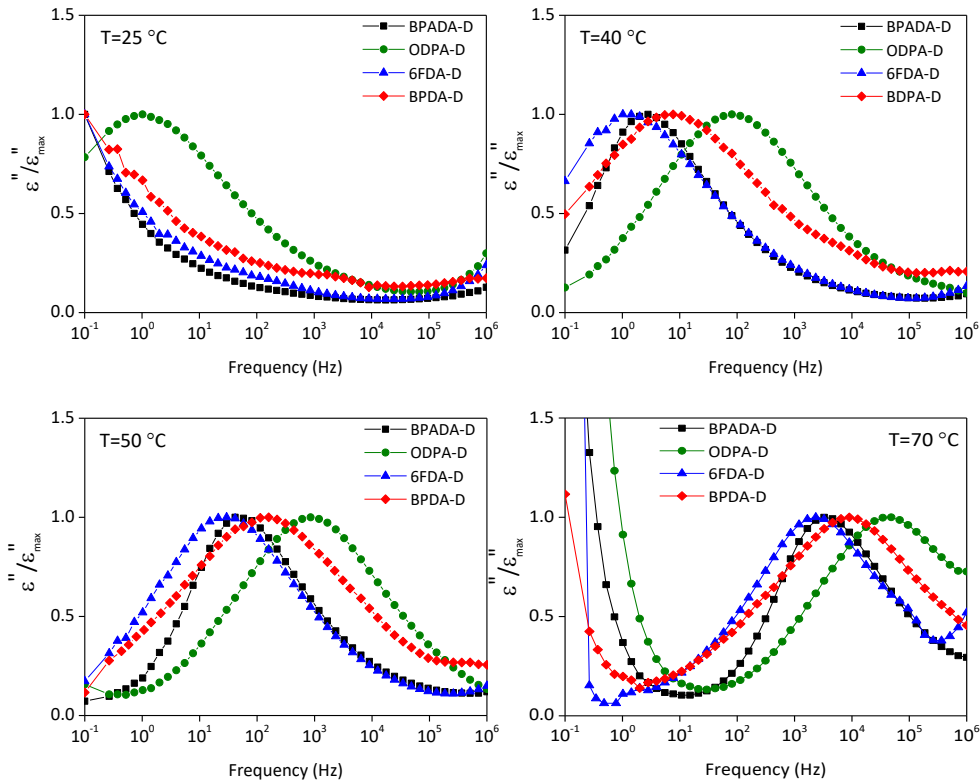


Figure S-4.4. Normalized dielectric loss (ϵ'') of PI samples with different dianhydrides at selected temperatures (25, 40, 50 and 70 °C).

The dielectric relaxation processes were analysed quantitatively by fitting the frequency spectra to the Havriliak-Negami (HN) function^{1,2} given by:

$$\epsilon^*(\omega) = \epsilon_{\infty} + \frac{\Delta\epsilon}{[1+(i\omega\tau_{\text{HN}})^b]^c} \quad (\text{S-4.1})$$

The difference in dielectric constant measured at low and high frequencies is the dielectric strength ($\Delta\epsilon$) of the relaxation and it is related to the area under the absorption curve given by ($\Delta\epsilon = \epsilon_s - \epsilon_{\infty}$), where ϵ_{∞} and ϵ_s are the unrelaxed and relaxed values of the dielectric constant respectively. τ_{HN} is the HN relaxation time,

representing the most probable relaxation time of the relaxation time distribution function,³ and b and c are shape parameters ($0 < b, c \leq 1$) which describe the symmetric and the asymmetric broadening of the equivalent relaxation time distribution function, respectively. Parameters b and c can be associated to the structure and polymer architecture heterogeneity with respect to the bulk polymer. The HN relaxation time τ_{HN} is related to the frequency of maximum loss, $f_{\text{max}}=1/(2\pi\tau_{\text{max}})$, by the following equation:⁴

$$\tau_{\text{max}} = \frac{1}{2\pi f_{\text{max}}} = \tau_{\text{HN}} \left(\sin \frac{b\pi}{2+2c} \right)^{-1/b} \left(\sin \frac{bc\pi}{2+2c} \right)^{1/b} \quad (\text{S-4.2})$$

Both characteristic relaxation times coincide when the relaxation spectrum is symmetric, i.e. $c=1$.

The temperature dependence of the segmental relaxation times (τ_{max}) was also studied. This dependency is well stated by the Vogel-Fulcher-Tammann (VFT) equation:⁵⁻⁸

$$\tau_{\text{max}} = \tau_0 \exp \left(\frac{B}{T-T_0} \right) \quad (\text{S-4.3})$$

where τ_0 and B are temperature-independent parameters, and T_0 is the so-called ideal glass transition or Vogel temperature which is found to be 30-70 K below T_g .⁹ To reduce the effect of misleading parameters on data fitting to the VFT equation over a limited frequency range, a value of $\tau_0 \approx 10^{-14}$ s was assumed, according to the values empirically found for many polymer systems lying between 10^{-14} and 10^{-12} . The dependence of τ_{max} with temperature is depicted in Figure S-4.4. This temperature dependency shows a clear curvature typical for cooperative motions.

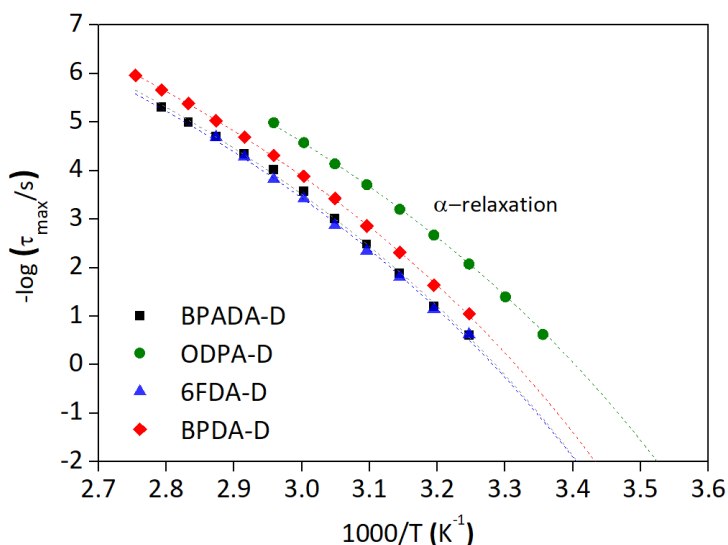


Figure S-4.5. Temperature dependence of the average relaxation time for the segmental mode of PIs. Dotted lines correspond to the VFT fit.

¹ Kremer, F.; Schönhal, A., *Broadband Dielectric Spectroscopy*. Springer: New York, **2003**; p 721.

² Havriliak, S.; Negami, S., A complex plane representation of dielectric and mechanical relaxation processes in some polymers. *Polymer* **1967**, *8* (4), 161-210.

³ Böttcher, C. J. F.; Bordewijk, P., *Theory of Electric Polarization*. Elsevier: **1978**; Vol. II.

⁴ Richert, R.; Angell, C. A., Dynamics of glass-forming liquids. V. On the link between molecular dynamics and configurational entropy. *J Chem Phys* **1998**, *108* (21), 9016-9026.

⁵ Fulcher, G. S., Analysis of recent measurements of the viscosity of glasses. *J Am Ceram Soc* **1925**, *8* (6), 339-355.

⁶ Vogel, H., The temperature dependence law of the viscosity of fluids. *Physikalische Zeitschrift* **1921**, *22*, 645-646.

⁷ Tammann, G.; Hesse, W., The dependency of viscosity on temperature in hypothermic liquids. *Zeitschrift Fur Anorganische Und Allgemeine Chemie* **1926**, *156* (4).

⁸ Bohmer, R.; Ngai, K. L.; Angell, C. A.; Plazek, D. J., Nonexponential relaxations in strong and fragile glass formers. *J Chem Phys* **1993**, *99* (5), 4201-4209.

⁹ Fischer, E. W., Light-scattering and dielectric studies on glass-forming liquids. *Physica A* **1993**, *201* (1-3), 183-206.

¹⁰ Wood-Adams, P.; Costeux, S., Thermorheological Behaviour of Polyethylene: Effects of Microstructure and Long Chain Branching. *Macromolecules* **2001**, *34* (18), 6281-6290.

Activation energies for the glass transition relaxations

From the shift factors obtained from the TTS mastercurves, the Arrhenius plots ($\ln a_T$ vs $1000/T$) were constructed and the activation energies were calculated from the slopes of the linear fit according to the Arrhenius equation:¹⁰

$$a_T = \exp \left[\frac{E_a}{R} \left(\frac{1}{T} - \frac{1}{T_{ref}} \right) \right] \quad (\text{S-4.4})$$

Where a_T is the shift factor, E_a is the activation energy, R is the gas constant and T_{ref} is the reference temperature at which the mastercurve is constructed.

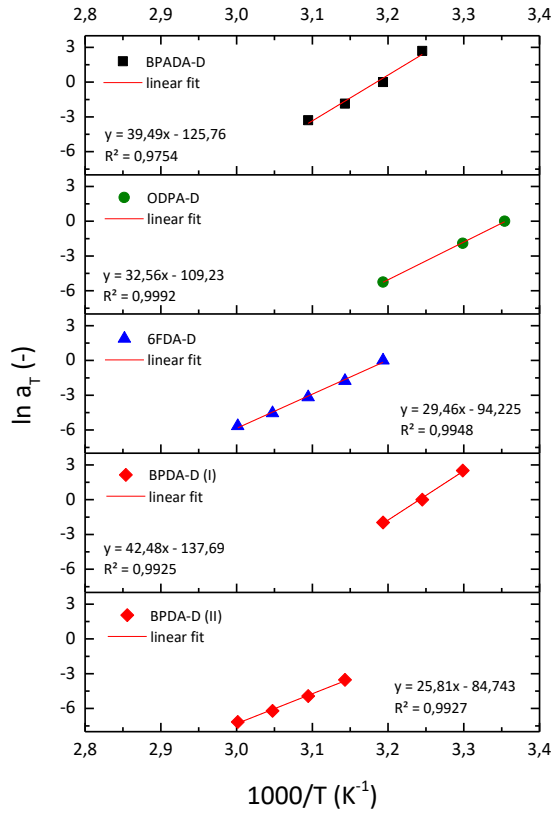


Figure S-4.6. Arrhenius plots of the time-temperature superposition shift factors a_T for the glass transition relaxations of the four PIs. Note that BPDA-D shows two T_g relaxations (I and II) while the other three polymers show only one. $T_{ref} = T(\tan\delta_{MAX}) = T_g$.

Table S-4.I. Activation energies for the glass transition relaxations.

Polymer	Relaxation process	E_a / kJmol^{-1}
BPADA-D		328
ODPA-D	T_g	271
6FDA-D		245
BPDA-D	T_g (I)	353
	T_g (II)	215

Birefringence with the annealing time

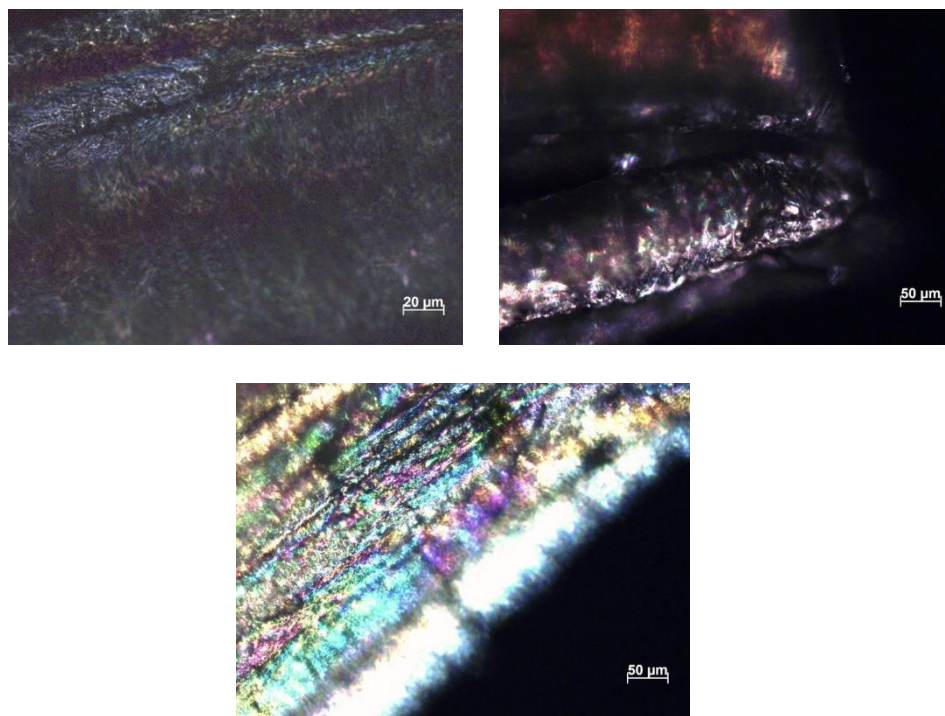


Figure S-4.7. Polarized microscopy images of the BPDA-D polymer showing the increase in birefringence with annealing time for a) non-annealed, b) 5 days annealed and c) 11 days annealed samples.

SAXS measurements

The SAXS diffractograms were collected using Anton Paar SAXSess, with a copper tube operated at 40 mA, 40 kV, using a multilayer mirror for focusing and monochromatisation of the emitted X-ray beam. The detector is a Dectris Mythen photon counting strip detector. The samples have been measured for 20 minutes each, with the sample mounted on a holder in vacuum. The data was corrected for dark-current, transmission and a background (empty holder subtracted). The data was subsequently de-smearred using a procedure available in the SAXSQuant software. The data was then regrouped or re-binned to reduce the number of datapoints and noise, taking care to propagate the uncertainties. The separation distances, d , are calculated according to $d=2\pi/q$.¹¹

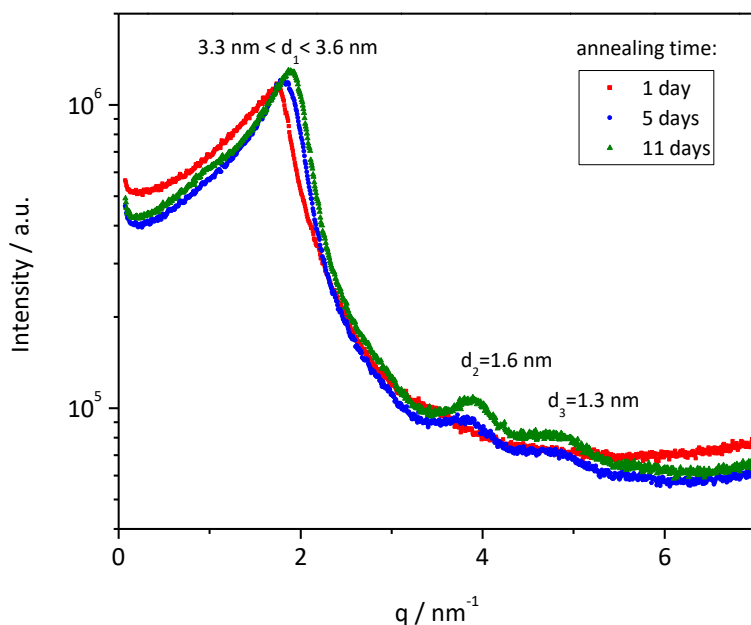


Figure S-4.8. SAXS diffractograms of BPDA-D polymer that was annealed at $T_{\text{ann}}=T(\tan \delta_{\text{MAX}})=T_g$ for different times: 1 day (■), 5 days (●) and 11 days (▲). The annealed samples show two additional peaks that indicate nanophase separation. The calculated separation distances, d , are assigned to each peak.

¹¹ Beiner, M.; Huth, H., Nanophase separation and hindered glass transition in side-chain polymers. *Nat Mater* **2003**, 2 (9), 595-599.

5

Identifying the role of primary and secondary interactions on the mechanical and healing properties

Good judgment comes from experience, and a lot of that comes from bad judgment.

Will Rogers

This chapter has been published as:

A. Susa, A. Mordvinkin, K. Saalwächter, S. van der Zwaag, S. J. García,
Macromolecules 2018, 51 (21), 8333–8345

Abstract

In this chapter we present a systematic study on the role of the aromatic dianhydride structure on the self-healing behaviour of fatty dimer diamine-based polyimides. By means of solid-state NMR and rheology, we studied the molecular and microscale dynamics of four polyimides comprising the same aliphatic branched diamine yet with variable dianhydride rigidities and correlated these to their macroscopic healing kinetics measured by tensile testing.

Following the two-step kinetics of the healing process, we were able to differentiate and quantify the extent of mechanical strength recovery in each of the healing stages, separately.

Moreover, the detailed rheology and solid-state NMR allowed us shedding light on the role of the aromatic interactions and branches on the mechanical properties and mechanical integrity during macroscopic healing. The study reveals the relevance and interplay of primary and secondary interactions in the development of non-crosslinked strong and healing polymers able to maintain mechanical integrity during healing.

5.1. Introduction

In intrinsic healing polymers the dynamic processes at the molecular length scale control the modes of healing of their microscopic damages or macroscopic mechanical properties.¹⁻³ Even though many different healing chemistries have been reported (different types of reversible covalent and non-covalent bonds, such as Diels-Alder, disulphide linkages, hydrogen bonds and ionic interactions),⁴ every form of intrinsic healing involves the various steps as defined in the physical model proposed by Wool and O'Connor:⁵⁻⁶ (i) surface rearrangement and approach; (ii) wetting; (iii) chain inter-diffusion; and (iv) randomization or/and chemical interactions. A preliminary step, that of 'bond breaking', should be added to the steps defined in the Wool-O'Connor model, as this is a necessary step in crosslinked healing polymers and high molecular weight non-cross-linked polymers. Hence the competition between diffusion and bond breakage and closure governs the overall healing kinetics and extent of final healing which can be reached. Furthermore, a smart design of the polymer architecture can be used to obtain a better balance between healing and mechanical properties such as using hard segments to enhance the mechanical performance and soft segments to incorporate self-healing functionality by allowing temporary local mobility.⁷⁻⁹ However, so far the effect of polymer architecture on the healing processes has not been studied sufficiently.¹⁰

To study and more importantly to quantify the healing kinetics and stages and the underlying mechanisms a combination of rheology^{2, 11-15} and macroscale techniques such as tensile, fracture or scratch testing is necessary.^{8, 15} For example, in a recent work of Bose et al, the authors show that viscoelastic contributions of the hard and soft blocks as well as the reversible interactions are both important in the self-healing phenomena after combining a rheological behaviour with macroscopic scratch healing.⁸

In our previous work, we patented¹⁶ and reported^{7, 17} a new family of aromatic-aliphatic polyetherimides comprising long alkyl branches capable to self-heal cuts at standard room temperatures (20-30°C). Dedicated rheological studies together with the kinetics of the mechanical properties' restoration showed that the healing mechanism is fully physical in nature and hence dependent on the peculiar relaxation behaviour of the polymers in a stepwise healing process. Nevertheless,

the individual roles of the aromatic hard block and the branched soft block on healing and mechanical integrity were unresolved.

In this work we present a systematic study on the role of the aromatic dianhydride structure on the healing behaviour of fatty dimer diamine-based polyimides. For this, we studied, by means of solid-state NMR and rheology, the molecular and microscale dynamics of four polyimides comprising the same aliphatic branched diamine yet with variable dianhydride rigidities,¹⁸ and correlated these to their macroscopic healing kinetics (tensile mechanical testing). The detailed rheology and solid-state NMR allowed us shedding light on the role of the aromatic interactions and branches on the mechanical properties and mechanical integrity during macroscopic healing. This strategy allowed us identifying the specific contribution of each block and physical interaction (aromatic or branch/friction) on the different healing stages showed by this class of tough healing polymers, namely initial tack followed by sticky Rouse diffusion while maintaining mechanical integrity and leading to very high healing degrees. We argue that by carefully choosing the architecture of the hard segment, one can tune each of the relaxation processes involved in a stepwise low-temperature physical healing of intrinsic healing polymers. This work shows how a smart selection of primary and secondary interactions embedded in polymer chains can lead to strong unentangled polymers with healing potential at mild temperatures.

5.2. Experimental

5.2.1. Materials

Four aromatic dianhydrides were used as hard aromatic block (Scheme 5.1): 4,4'-(4,4'-isopropylidenediphenoxy) bis-(phthalic anhydride) (BPADA) (97%, Sigma Aldrich), 4,4'-oxydiphthalic anhydride (ODPA) (98%, TCI Europe N.V.), 4,4'-(Hexafluoroisopropylidene) diphthalic anhydride (6FDA) (98%, TCI Europe N.V.), 3,3',4,4'-biphenyltetracarboxylic dianhydride (BPDA) (98%, TCI Europe N.V.). Besides for providing good mechanical and thermal properties due to their aromaticity, these particular dianhydrides were chosen for the differences in their linkers (connecting the two phthalic units) which enable a systematic variation in rigidity and planarity, resulting in the structure-related properties we wanted to investigate. The soft block was in all cases a fatty dimer diamine derived from vegetable oil (Priamine 1075™, here named DD1) (Croda Nederland B.V.) with structure as shown in Scheme 5.1. The amounts of each monomer were added at the theoretical stoichiometric ratio, calculated according to the molecular weights of the monomers ($MW_{\text{BPADA}}=520.49$ g/mol, $MW_{\text{ODPA}}=310.20$ g/mol, $MW_{\text{6FDA}}=444.24$ g/mol, $MW_{\text{BPDA}}=294.22$ g/mol and $MW_{\text{DD1}}=536.80$ g/mol) and assuming all chemicals are 100% difunctional. The synthesis was conducted in *N,N*-dimethylacetamide (DMAc, 99.5% extra dry, Acros Organics) polar aprotic solvent with total solids (monomers) content of 20 wt.%. Using a two-step polymerization process, four polymers were obtained: BPADA-D, ODPA-D, 6FDA-D and BPDA-D. The full synthesis description and thermo-mechanical and spectroscopic characterization of the four polymers can be found in *Chapter 4* and our published articles.^{7, 18}

5.2.2. Characterization methods

5.2.2.1. Tensile properties and interfacial healing evaluation

Tensile mechanical tests were performed using dog-bone specimens according to the ASTM D1708 standard (thicknesses, $t=2\pm 0.5$ mm) at 80 mm/min crosshead speed. To determine the healing behaviour, pristine samples were cut with a sharp razor blade at a temperature similar to the healing temperature ($T_{\text{cut}} \approx T_{\text{SH}}$). In order to avoid misleading temperature effects when comparing the kinetics of healing for polymers with a different T_g , the healing temperature (T_{SH}) for each polymer was determined from the temperature-sweep rheology and set to the temperature at the maximum of $\tan\delta$ (see details in the Figure S-5.1, Supporting Information). This effect was determined in our previous study.⁷ After cutting, the two broken pieces were carefully repositioned in a negative dog-bone shape PTFE mould and allowed to heal at their individual T_{SH} for 1, 5 and 11 days with no external pressure applied. The relative humidity was fixed to 15% to exclude the potential effect of moisture on the healing results.¹⁹ Three samples of each polymer composition were tested in the pristine state and three more samples in the healed state for reproducibility. To study the effect of the healing temperature and time on the undamaged polymer properties and discard major contributions of ageing phenomena on healing, the pristine samples were subjected to the same abovementioned thermal treatment as the healed ones in an annealing step ($T_{\text{ann}}=T_{\text{SH}}$). The healing efficiency was calculated based on the following equation:

$$\text{Healing efficiency (\%)} = \frac{p^{\text{healed}}}{p^{\text{pristine}}} \times 100 \quad (5.1.)$$

where p^{healed} and p^{pristine} are the properties of interest (Young's modulus, stress at yield, stress at break and strain at break) for healed and pristine samples, respectively.

5.2.2.2. Rheological measurements

The linear viscoelastic properties of the polyimides (PIs) were investigated by a Haake Mars III rheometer using the parallel plate geometry with a plate diameter of 8 mm. Preliminary strain amplitude sweeps at 1 Hz were performed at the highest and the lowest tested temperatures and ranged from 0.001% to 10% strain to evaluate the scope of the linear viscoelastic region for the different polymers. Based on these results, a shear strain of 0.5% for all four polymers was used to ensure the tests were performed in the linear viscoelastic region. Temperature sweep experiments were performed at 1 Hz in a cooling ramp from 50 to 5°C. The temperature sweep curves were used to determine the healing temperature as the temperature of the $\tan\delta_{\text{MAX}}$: $T_{\text{SH}}=T(\tan\delta_{\text{MAX}}$ in the dissipative regime) (see Table S-5.I and Figure S-5.1, Supporting Information). Frequency sweep experiments from 10 to 0.1 Hz were performed at temperatures between 110 and 10°C, in steps of 5°C. The rheological mastercurves were constructed from the obtained data applying the time-temperature superposition principle (TTS) at the reference temperatures corresponding to the healing temperature ($T_{\text{ref}} \approx T_{\text{SH}}$) using the dedicated Rheowin software. Tests were repeated twice and showed satisfactory reproducibility, meaning that the observed differences between polymer grades can be attributed to the polymer architecture effect, rather than inter-sample variations.

5.2.2.3. Solid state nuclear magnetic resonance

The ^1H solid-state NMR experiments were performed on a Bruker Avance III spectrometer with the double-resonance 4 mm MAS probe at a ^1H Larmor frequency of 400 MHz. The samples in the form of 3 mm diameter discs were packed between Kel-F inserts, which were subsequently put inside of 4 mm o.d. ZrO_2 MAS-rotors closed with Vespel caps. To enable the acquisition of high-resolution spectra, the samples in the rotors were spun at 10 kHz at the experimental temperature of $T_g+120^\circ\text{C}$. The experimental temperature was regulated by means of heated pressurized air using a BVT3000 temperature control unit, with an accuracy of around 1K. The ^1H spectra were acquired with recycle delays set to $5T_1$ and 90° pulses set to duration of 3.12 μs . A rotor-synchronized

Hahn echo pulse sequence was used to measure T_2 relaxation times free from contributions of magnetic-field inhomogeneities, thus providing information on molecular mobility.²⁰

5.3. Results and discussion

5.3.1. Tensile experiments

5.3.1.1. Tensile behaviour of as-produced and annealed undamaged polymers

Representative stress-strain curves of the as-produced and annealed undamaged polymers (i.e. pristine) obtained at 80 mm/min crosshead speed are shown in Figure 5.1a. The effect of the dianhydride structure and time at the annealing temperature T_{ann} on the general mechanical performance of pristine samples is shown on the left (Figure 5.1a) while the healed curves at comparable temperatures are shown on the right side (Figure 5.1b) and the reported differences will be discussed in 5.3.1.2. It should be noted that the samples were annealed at temperatures (T_{ann}) near their T_g since $T_{\text{ann}} = T_{\text{SH}} = T_{\text{tan } \delta_{\text{MAX}}}$ which was approximately 15°C above the calorimetric T_g (Table 5.I).

Table 5.I. Effect of the dianhydride type on M_w , M_n and PDI as calculated from the major peak obtained in GPC. T_g obtained from DSC, rheology and BDS and temperatures for 2% weight loss obtained from TGA.

Polymer	M_w (g/mol)	M_n (g/mol)	PDI	DSC T_g^a (°C)	Rheology T_g^b (°C)	BDS T_g^c (°C)	TGA T (2% weight loss) (°C)	Density (g/cm ³)
BPADA-D	29k	18k	1.6	24	36	20	360	1.05
ODPA-D	32k	16k	2.0	13	25	11	380	1.05
6FDA-D	41k	20k	2.0	25	40	21	330	1.12
BPDA-D	37k	20k	1.9	22	33 ^I , 46 ^{II}	18	350	1.05

^a T_g was calculated from the 2nd heating curve, 10°C/min.

^b T_g was taken as the maximum of the peak in the $\tan\delta$ curve from the rheological temperature sweeps, performed in cooling ramp, 1°C/min (Figure S-5.1b). These temperatures were used as annealing and healing temperatures (in case of BPDA-D, the temperature of the first peak was used).

^c T_g is obtained from the broadband dielectric spectroscopy (BDS) measurements, by extrapolating the VFT fit to the temperature at which τ_{max} is equal to 100 s (see Susa et al¹⁸).

^{I, II} Polymer BPDA-D exhibits two T_g peaks [T_g (I) and T_g (II)] in rheological temperature sweep plots, which is shown and discussed elsewhere.¹⁸

The pristine ODPA-D, BPADA-D and 6FDA-D polymers show a slight improvement of the mechanical properties with annealing after 1 day at T_{ann} (Figure 5.1a). BPDA-D on the other hand shows a significant effect of the annealing time on the mechanical behaviour due to an annealing-induced crystallization process as reported and discussed in our previous paper.¹⁸ The effect of dianhydride structure and annealing time at T_{ann} on the Young modulus (E), yield stress (σ_Y), stress at break (σ_b) and strain at break (ϵ_b) of the pristine materials is shown in Figure S-5.2, SI.

5.3.1.2. Effect of the dianhydride architecture on the macroscopic self-healing efficiency

As compared to the pristine ones (Figure 5.1a), the healed stress-strain curves show a global reduction in mechanical properties after damage-heal event (Figure 5.1b) except for ODPA-D at long healing times as previously reported.⁷ To gain more insight on the healing degree, Figure 5.2 shows the absolute values of the four relevant mechanical parameters (E , σ_Y , σ_b and ϵ_b) as function of the healing time. As expected, ODPA-D shows an almost complete restoration of all the individual mechanical parameters while BPDA-D shows almost no recovery of any of the tensile reference parameters at the studied T_{SH} , healing time and test conditions used ($T_{\text{test}}=23\pm 2^\circ\text{C}$, 80 mm/min). BPADA-D and 6FDA-D show an intermediate behaviour with good recovery of E and σ_Y and residual recovery of ϵ_b and σ_b . However, these strong differences in behaviour might be caused by the fact that ODPA-D is the only one with T_g close to the T_{test} and is therefore showing a higher interfacial deformation and stress at break than the other polymers at this testing conditions. In order to demonstrate the effect of the testing temperature on measured healing values with respect to the material T_g extra tests were performed at $T_{\text{test}}\approx T_g\approx T_{\text{SH}}$ and are shown in Figure S-5.3, SI. These tests confirm the almost complete absence of healing for the BPDA-D sample besides initial self-adhesion and the more elastomeric-like behaviour of samples BPADA-D and 6FDA-D leading to higher levels of measured healing degrees in terms of stress-strain at break.

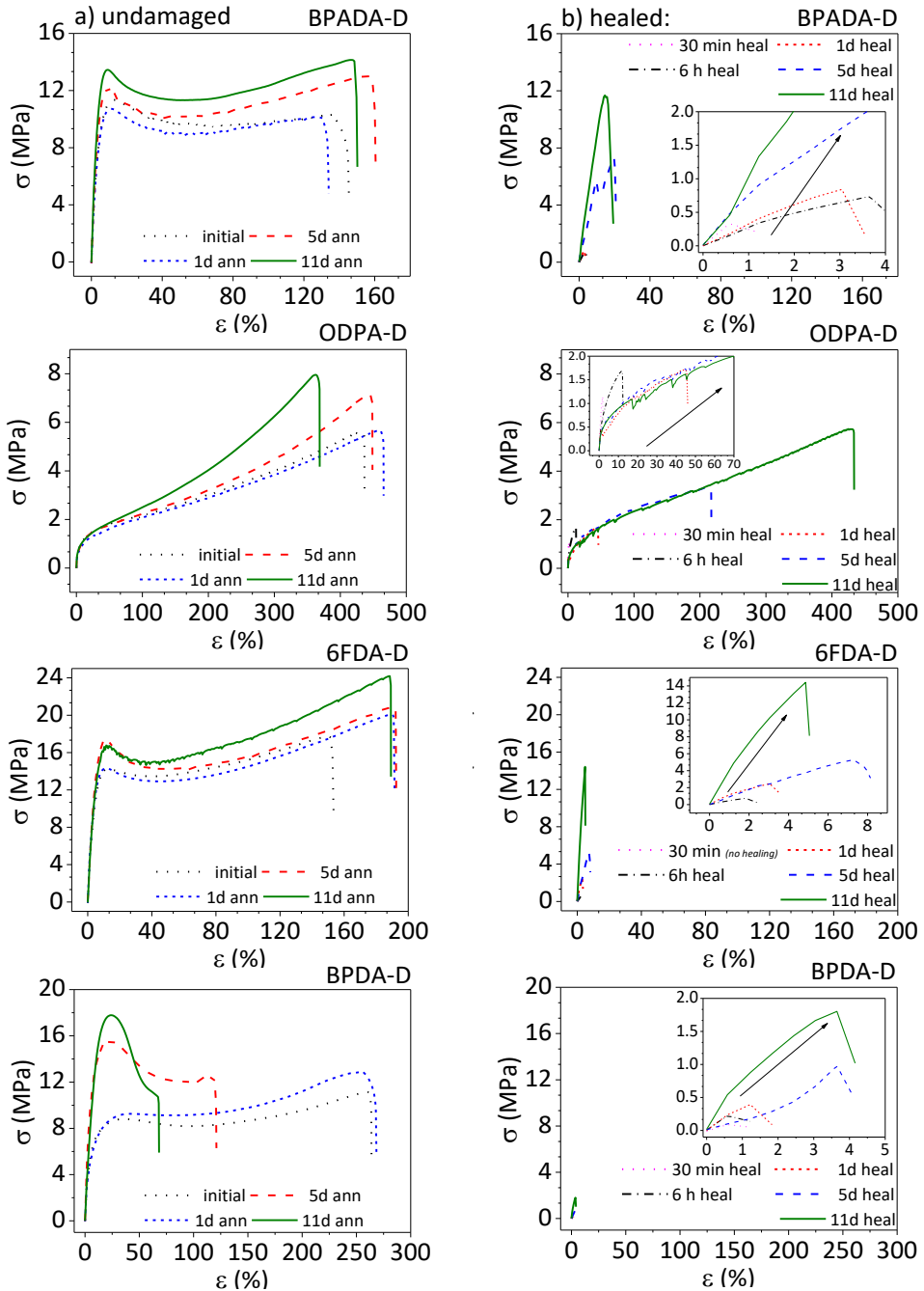


Figure 5.1. Representative stress-strain curves at 80 mm/min strain rate showing the effect of the dianhydride structure and annealing time at $T_{\text{ann}}=T_{\text{SH}}$ on the general mechanical performance of undamaged samples (a-left), and the effect of healing time at $T_{\text{ann}}=T_{\text{SH}}$ of healed samples (b-right). $T_{\text{test}}=23\pm 2^\circ\text{C}$.

In addition to the similarities and differences in ultimate healing levels achieved, Figure 5.2 also points at differences in the kinetics of the healing process amongst samples and mechanical characteristic parameter evaluated.

In general, the stress parameters σ_b and σ_Y reach values closer to the pristine ones earlier than E and ϵ_b . 6FDA-D and ODPA-D are capable of fully restoring the E modulus after 11 days of healing while the other two polymers are not. Interestingly, 6FDA-D and BPADA-D have the highest E and σ_Y and still show high levels of recovery of these two parameters even when their T_g -s are 10°C and 15°C above the testing temperature.

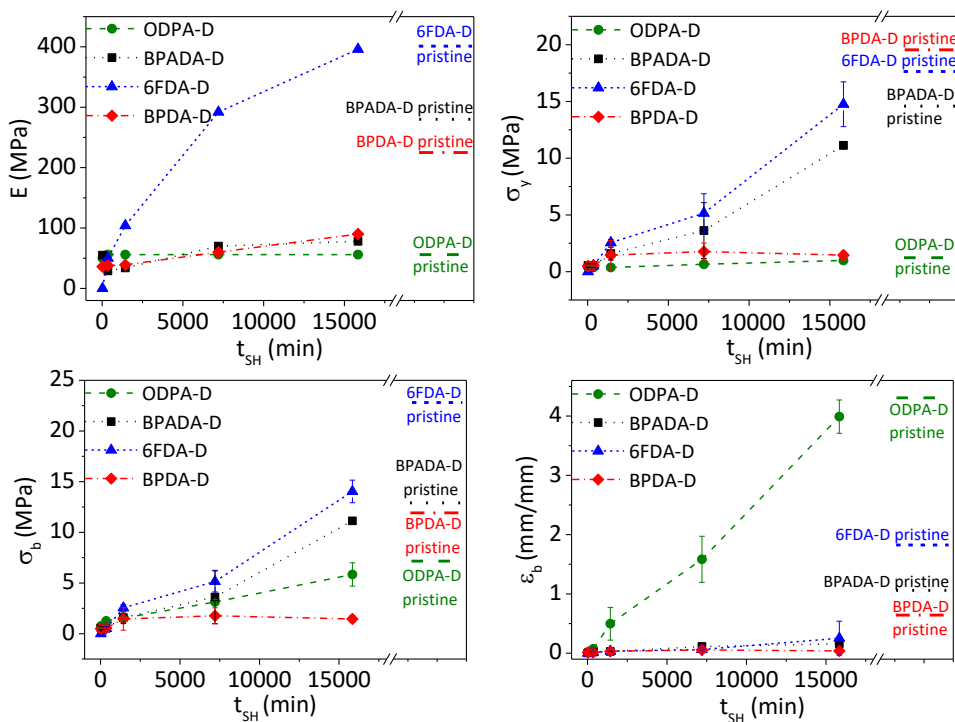


Figure 5.2. Effect of the dianhydride structure on the evolution of Young modulus (E), stress at yield (σ_Y), stress at break (σ_b) and strain at break (ϵ_b) with healing time (t_{SH}) at the individual T_{SH} . The values of the annealed undamaged samples are shown as dotted horizontal lines at the right part of each plot. It can be seen how the undamaged level of each mechanical parameter is reached at different healing times depending on the parameter and the polymer. $T_{test}=23\pm 2^\circ\text{C}$. Error bars are based on three repetitions.

In order to compare the healing rates more in detail, the calculated healing efficiencies as defined by Eq. 1 for each of the conventional mechanical parameters are plotted as a function of the healing time (Figure 5.3). This figure clearly shows that the recovery of each of the mechanical parameters follows different healing kinetics and that for a given property the kinetics depend on the polymer composition. ODPA-D shows a faster healing kinetic process in all cases leading to the highest healing efficiency in all four parameters of interest. On the other hand, BPDA-D only shows self-adhesion (tack) within 1 day with no further changes in time thereby pinpointing at short range chain interdiffusion in the studied time frame. It is evident that healing does not proceed at the same rate throughout the whole healing process.

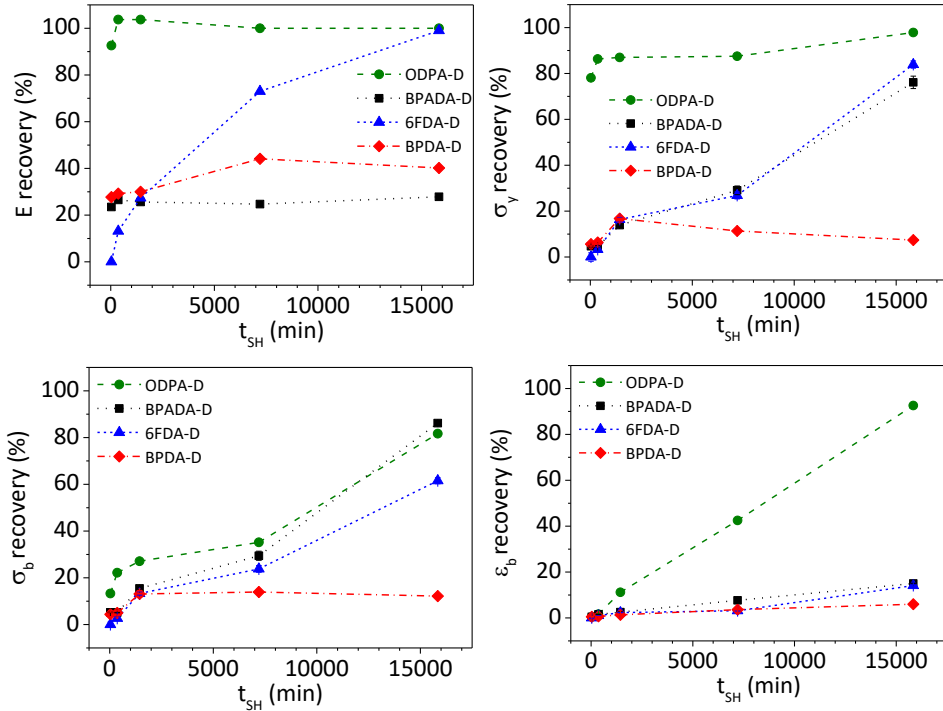


Figure 5.3. Effect of the healing time (t_{SH}) at the $T_{SH}=T_{tan\delta_{MAX}}$ on the recovery of the individual mechanical parameters: Young modulus (E), stress at yield (σ_y), stress at break (σ_b) and strain at break (ϵ_b) for different dianhydride types. $T_{test}=23\pm 2^\circ\text{C}$. Both pristine and healed samples were subjected to the same thermal treatment at T_{SH} for given t_{SH} .

Generally, the healing process progresses very rapidly during the first day (up to 5th day in some cases), especially for the case of E , σ_b and σ_Y , and then progresses more slowly. The polymers follow the same trend as that for the recovery of σ_b , ϵ_b and σ_Y parameters (i.e. ODPD-D>BPADA-D>6FDA-D>>BPDA-D). The recovery of the E appears as an outlier in this trend and may be explained by the fact that this parameter is extracted from the initial rise of the stress-strain curve (rather than being an ultimate property) measurable already at early healing stages, governed by very fast adhesion/tack phenomena.

5.3.2. Rheological experiments

To gain a better understanding of the effect of the dianhydride architecture on healing, the dynamics of the PIs were evaluated by frequency sweep experiments in parallel-plate geometry. The time-temperature superposition (TTS) approach was employed to show the polymer dynamics over a wide frequency domain ($10^{-7}<f<10^5$) at a fixed temperature ($T_{ref}=T_{tan\delta_{MAX}}=T_{SH}$) obtained from the temperature sweep curves (Figure S-5.1, SI). The resulting mastercurves of the elastic modulus (G'), viscous modulus (G'') and loss tangent ($\tan\delta$) horizontally shifted to the reference temperature $T_{ref}\approx T_{SH}$ are shown in Figure 5.4 while the extracted relevant parameters according to previous work⁷ are listed in Table 5.II. Defined by the multiple cross-over points between G' and G'' , there are four regions of polymer dynamics, as shown in Figure 5.4a and reported in Table 5.II: (i) $f>f_g$, glassy regime ($G'>G''$), (ii) $f_d<f<f_g$, dissipative regime ($G''>G'$), (iii) $f_s<f<f_d$, apparent elastic plateau ($G'>G''$), (iv) $f<f_s$, viscous flow ($G''>G'$).⁷

All four polymers exhibit terminal flow, as defined by the f_s intersection point at very low frequencies ($<10^{-4}$ Hz), indicating that there are no permanent crosslinks present. The G' and G'' slope values in the terminal relaxation region zone ($f<f_s$) are somewhat lower than those for the true terminal relaxation behaviour slopes of 2 and 1, respectively.²² This is indicative of an increasing dynamic inhomogeneity, as smaller slopes typically arise from a superposition of terminal modes. Such a behaviour was previously assigned to the presence of branches⁷ although in this work the role of the dianhydride becomes clearer showing that, the more rigid the dianhydride linker is, the more constrained dynamics are found

(G' slope decreases). Moreover, the terminal relaxation timescales (τ_s , Table 5.II) of the four PIs with different dianhydrides calculated from the f_s intersections, increase according to the dianhydride rigidity¹⁸ in the order BPADA-D < ODPA-D < 6FDA-D < BPDA-D.

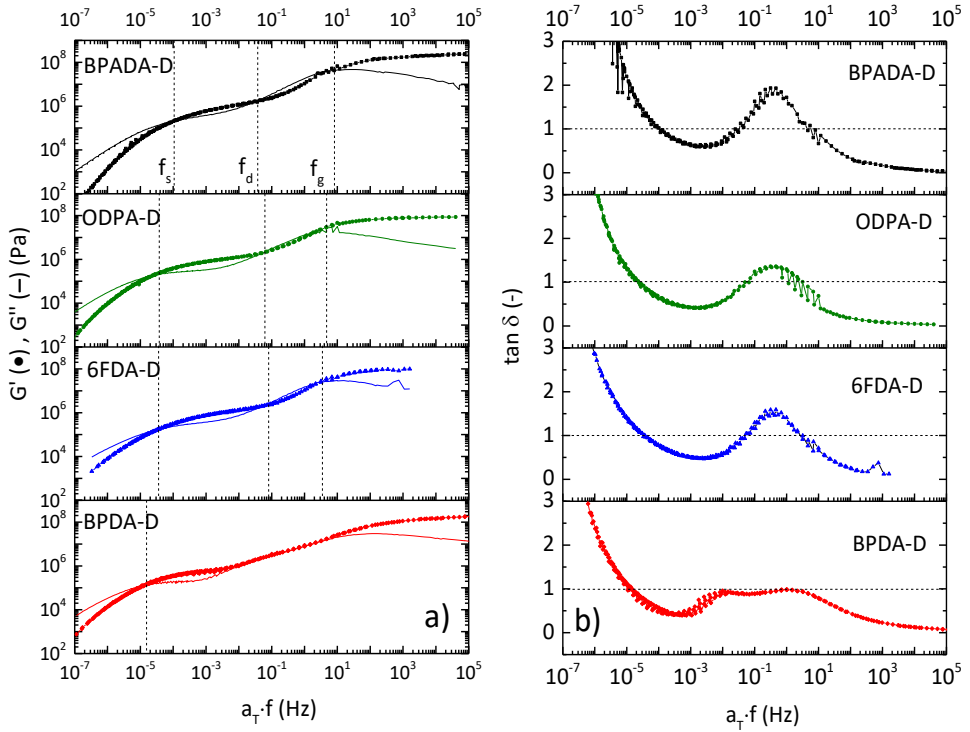


Figure 5.4. TTS mastercurves at $T_{ref} \approx T_{SH}$. a) Storage modulus (G' , symbols), loss modulus (G'' , line) and b) loss tangent ($\tan\delta$) as a function of shifted frequency ($a_T f$) for four PIs with different dianhydrides. Dashed lines are guidance for the eye to distinguish the regions of viscous ($G'' > G'$) and elastic ($G' > G''$) dominance.

Table 5.II. Characteristic rheological parameters extracted from the TTS mastercurves at $T_{\text{ref}} \approx T_{\text{SH}} = T_{\text{tan}\delta \text{ MAX}}$.

Polymer	f_s Hz	f_d Hz	f_g Hz	τ_s s	τ_d s	τ_g s	$\tan\delta$ MAX	G' slope at $f \lesssim f_s$	G'' slope at $f \lesssim f_s$	G_N^* Pa	$M_{e,\text{app}}^{**}$ g/mol	M_x^{***} g/mol
BPADA-D	1.0 $\cdot 10^{-4}$	0.03	5.4	1.0 $\cdot 10^4$	30	0.2	1.9	1.78	0.99	8.37 $\cdot 10^5$	3280	1057
ODPA-D	2.9 $\cdot 10^{-5}$	0.06	3.3	3.4 $\cdot 10^4$	17	0.3	1.4	1.57	0.91	9.34 $\cdot 10^5$	2890	847
6FDA-D	2.5 $\cdot 10^{-5}$	0.05	3.1	4.0 $\cdot 10^4$	20	0.3	1.6	1.44	0.87	8.87 $\cdot 10^5$	3290	981
BPDA-D	1.3 $\cdot 10^{-5}$	/	/	7.7 $\cdot 10^4$	/	/	0.9	1.27	0.81	5.7 $\cdot 10^5$	4680	831

* G_N calculated from the Van Gorp-Palmen plot, $\delta(|G|*)$,⁷ (Figure S-5.4, SI)

** $M_{e,\text{app}}$ (apparent) were calculated according to $M_e = \rho RT / G_N$ (Doi and Edwards) equation, using experimentally determined densities.¹⁸ In this case M_e values must be considered as pseudo- M_e values governed by 'transient interactions', not as molecular weight between entanglements.⁷

*** M_x =average molecular weight between the two neighbouring temporal junctions,²¹ in this case the DD1 side-chains.

The plateau moduli (G_N) for these polyimides are in the range between 0.6 and 1 MPa (Table 5.II, Figure S-5.4). The molecular weights between apparent entanglements calculated from the relation of rubber elasticity, $G_N = \rho RT / M_e$, are in the range of $2000 < M_{e,\text{app}} < 5000$ g/mol (Table 5.II). Considering that the molecular weights of these polymers (Table 5.I) are in the range $8 \cdot M_{e,\text{app}} < M_w < 12 \cdot M_{e,\text{app}}$, it can be stated that these are weakly entangled polymers according to the categorization for linear polymers. This behaviour is in line with the sticky Rouse²³⁻²⁷ and sticky reptation²⁸⁻³¹ models for unentangled and entangled chains, respectively, with sticker groups being more closely spaced than the entanglements. It is also compatible with a more recent model from Mateyisi et al³² which suggests that the transition from an enhanced first plateau modulus (related to stickers plus entanglements) to entanglement-dominated behaviour occurs at a modified Rouse time, where the stickers have an additive contribution to the effective friction. Owing to the weak entanglement level, our samples do not exhibit a second lower plateau but a direct transition to terminal dynamics at the lowest frequencies. The fact that the obtained $M_{e,\text{app}}$ values are higher than the average molecular weight M_x of the repeat unit containing one sticker group each (i.e. one aromatic dianhydride + one branched dimer diamine) may indicate that the thermodynamically incompatible components do not fully segregate, effectively leading to free stickers.³³⁻³⁴ In our previous work⁷ the plateau and sticky

Rouse like behaviour were related to the presence of branches in weakly entangled polymers. In order to explore the role of the aromatic interactions in this behaviour, a non-aromatic BPDA-D analogue was synthesized. The dianhydride molecular structure of the BPDA-like monomer (DCDA), synthesis of polymer DCDA-D and its properties are presented in the Supporting Information (Scheme S-5.1, Table S-5.I, Figure S-5.5). The TTS curves of DCDA-D show the absence of a clear elastic pseudo-plateau. Moreover, the terminal relaxation frequency is well separated from the Rouse/glassy upturn and is three orders of magnitude higher than the aromatic one while the terminal flow slopes are very similar (Table S-5.II). Furthermore, the TTS shift factors (a_T) are shifted to lower temperatures in the absence of the aromatics (Figure S-5.5b). The presence of a shift factor deviation at lower temperatures yet with reduced slope in the case of the non-aromatic sample suggests the major contribution of aromatic interactions as well as the presence of secondary physical associative effects. Similar observations were noticed by other authors studying associative polymers.³⁵⁻³⁶ Recently Zhang et al suggested to separately calculate the activation energies for each temperature dependence by using a ratio of two sets of shift factors (of both Rouse-type motion and sticker dissociation) rather than a single set of shift factor (of either Rouse-type motion and sticker dissociation).³⁶ However, well-known simple ionomeric model systems were used for that study. In contrast, the SH PIs studied here are relatively newly developed and have an altered complexity with respect to the model systems since they seem to exhibit two types of stickers (alkyl branches + aromatic interactions) with (yet) unknown association constants. A more detailed study on the distinction of each sticker contribution and their relaxation timescales is a topic of a follow-up research.

Finally, the Van Gorp-Palmen plot shows that the non-aromatic DCDA-D lacks the two maxima related to the observed crystallinity¹⁸ while the G_N values are of the same order of magnitude as the aromatic samples. This leads to comparable $M_{c,app}$ and therefore similar weakly entangled networks. All these results point at the elastic plateau appearance being highly governed by aromatic interactions and the terminal flow sticky Rouse behaviour being affected by secondary sticky physical interactions most likely due to the branches in the absence of clear H-bonding. This mechanistic picture will be refined later after addressing the microscopic information from the solid-state NMR experiments.

The dissipative regions of the mastercurves are defined by the intersection between the frequencies f_d and f_g , where $G'' > G'$ and the polymer goes through the glass transition. These relaxations are attributed to a combination of segmental relaxation and the local plasticizing effect of the dangling side chains, according to our previous findings.⁷ Three out of four polymers (BPADA-D, ODPA-D and 6FDA-D) display the $G' = G''$ ($\tan\delta = 1$) crossovers in the dissipative region, while BPDA-D does not. The dissipative relaxation processes can be better observed from the $\tan\delta$ curve (Figure 5.4b), where the shape, width and peak values can be discussed. The $\tan\delta$ curve of BPDA-D reveals two peaks, while the other three show only one peak.

The origin of this phenomenon lies in the nanophase separation and semi-crystallinity caused by a planar architecture of BPDA dianhydride, as we found via SAXS and DSC measurements in our previous study.¹⁸ BPADA-D has the widest dissipative region ($f_g - f_d$, Table 5.II), followed by 6FDA-D and ODPA-D. When these cross-over frequencies are converted to timescales τ_g and τ_d , as given in Table 5.II, an insight into the kinetics of these motions can be obtained. It is then noticed that the dissipative dynamics of BPADA-D are the fastest (the lowest τ_g) and last over the longest time (the largest $\tau_g - \tau_d$). The intensity of the maximum $\tan\delta$ peak reflects the extent of mobility of the polymer chain segments at the T_{ref} . Higher values of $\tan\delta$ peak indicate higher energy losses and a more viscous behaviour, whereas lower $\tan\delta$ values indicate less viscous and more elastic behaviour.³⁷ As compared to the other three polymers, BPDA-D has much lower $\tan\delta$ peak value which is below the value of 1 (0.9), indicating restricted segmental mobility and predominantly elastic behaviour. Similarly, in Figure S-5.5 it can be observed that the slope of the dissipative region in the BPDA-D (aromatic) and DCDA-D (non-aromatic) are roughly the same. Hence, the effect of the dianhydride architecture on the dissipative dynamics seems to be less pronounced than for the pseudo-plateau behaviour as discussed above. This correlates well with the finding that dissipative dynamics are partially related to the dangling side chains,⁷ whose motions are independent of the backbone rigidity at the $T \approx T_g$. Nevertheless, the high planarity of the BPDA aromatic dianhydride causes the whole chains to undergo higher structural ordering leading to crystallization and healing inhibition, thereby explaining why the dissipative region of BPDA-D is highly restricted, i.e.

no viscous dominance ($G'' > G'$) in the dissipative regime, as we elaborated in our previous work.¹⁸

5.3.3. Molecular dynamics by Solid State NMR

In order to better unravel the effect of dianhydride architecture on equilibrium molecular dynamics, the contributions of different molecular moieties to the PI dynamics were assessed by deconvolution of high resolution ^1H solid-state nuclear magnetic resonance (^1H SS NMR) spectra. Figure 5.5 shows ^1H SS NMR one-pulse spectra with a resolution sufficient to distinguish the following molecular moieties: aromatic protons of the different dianhydrides (6.5-8 ppm), aliphatic protons of the backbone and long side-chains (branches, 0-2.5 ppm), and methylene protons close to the imide group (3-3.5 ppm). The latter signal is spectrally well separated and only weakly affected by the chemical environment, such that it could be used to probe the local dynamics next to the aromatic dianhydrides through its well-defined and strong ^1H - ^1H dipolar coupling. Comparably, high spectral resolution was always attainable at experimental temperature $T_{\text{exp}} = T_{\text{tan}\delta\text{MAX}} + 120^\circ\text{C}$. Thereby, the high experimental temperature allowed investigations of long-range dynamic processes. The ^1H SS NMR experiments were thus performed under isofrictional conditions to reach comparable segmental mobility and study exclusively the effect of the dianhydride's nature on structural effects (e.g. supramolecular packing) that change the chains dynamics beyond simple T_g changes. Isofrictional conditions mean that molecules have the same effective friction coefficient, i.e. the local chain dynamics is on the same timescale. Such conditions can be realized by measurements at a temperature located at a fixed interval above the glass transition temperature of a sample.³¹ As opposed to the other three PIs, the larger chemical shift and the width of the BPDA-D aromatic peak indicates deshielding and immobilization³⁸ in agreement with the rheology results. Moreover, it directly confirms that the origin of the constrained dynamics lies in the aromatics, i.e. dianhydride segments of the polymer chains.

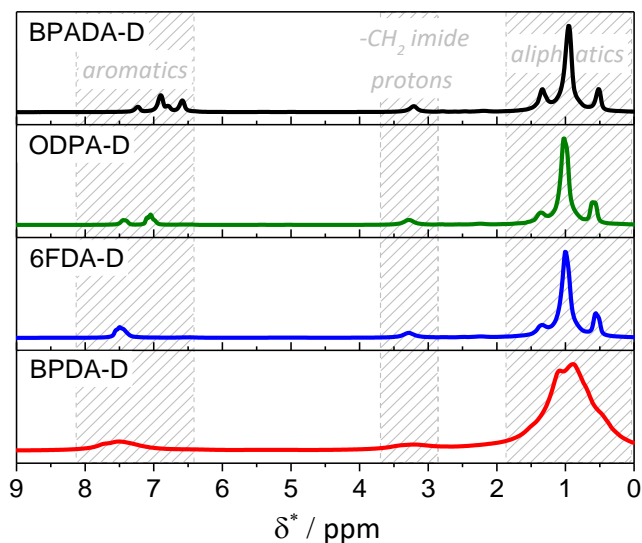


Figure 5.5. SS NMR One-pulse spectra, Magic Angle Spinning (MAS) at 10 kHz, $T_{\text{exp}} = T_{\text{tan}\delta_{\text{MAX}}} + 120^\circ\text{C}$.

As was mentioned in the experimental section, the molecular dynamics were studied by means of a rotor-synchronized Hahn-echo pulse sequence.²⁰ The Hahn echo curves belonging to the aforementioned molecular moieties (aromatic, CH_2 -imide, and aliphatic (CH_x)) of the four PIs can be seen in Figure 5.6. The experimental points were obtained as integrals of the corresponding signals normalized by the signal after a single 90° pulse. The aromatic and CH_2 -imide signals could be roughly separated from the overlapping wing of the large-amplitude aliphatic signals by treating the latter as a baseline contribution in a suitably narrow spectral range and subtracting it. The observed signal decays in the Hahn echo curves (intensity decay with time in Figure 5.6) are driven predominantly by the magnetic dipole-dipole couplings (DDCs) established through the interactions of the magnetic fields generated by the ^1H dipoles. The signal dependency on the molecular section orientation (DDC) enables the study of the molecular dynamics of the individual aromatic, aliphatic backbone and branches linked to local mobility and interactions.³⁹ The DDCs modulate the Larmor frequency, which causes additional signal dephasing and are distance- and orientation-dependent. Overall, it can be stated that a fast isotropic motion causes

complete averaging of the DDCs on the timescale of the experiment and thus slower signal decays (i.e. displacement of the curves towards longer times, t). In contrast to that, a slow or constrained motion lead to the DDCs averaging only to a certain level, leading to what is called residual DDCs (RDDCs). In agreement with this, larger RDDCs make the signal decay faster (displacement to shorter times).

For more dedicated analysis of the molecular dynamics the intensity signal decays related to DDC can be fit by the empirical Kohlrausch-Williams-Watts (KWW) function:

$$I(t) = e^{-\left(\frac{t}{T_2}\right)^\beta} \quad (5.2.)$$

where t is the length of the Hahn echo pulse sequence (echo time), T_2 is the spin-spin relaxation time characterizing the decays and serving as a dynamic parameter;⁴⁰ the exponent β can vary from below 1 up to 2. The β values equal to 1 and 2 can be underpinned by the Anderson/Weiss approximation⁴¹ applied to the Gaussian distributed interaction frequencies, justified by the presence of multiple spin couplings, driving a free induction decay in the case of the motional-averaging and (quasi-)static limits, respectively. The Anderson/Weiss approximation connects the observed T_2 and values β to the segmental autocorrelation function of motion ($C(t)$), which defines the probability to find a segment in the same orientation after the time t .⁴² In the case $C(t)$ is flat, in the rigid limit or in the plateau area defined by the residual motional anisotropy with a time-stable (R)DDCs, the signal decay becomes Gaussian with $\beta=2$. On the other hand, if $C(t)$ is steep, in the case of fast motions, the NMR signal decays monoexponentially. Intermediate cases are also feasible: $\beta < 1$ arises when the motional heterogeneity with the distribution of T_2 values is present, whereas $1 < \beta < 2$ corresponds to the case of $C(t)$ featuring a well-defined motional anisotropy with RDDCs which slightly decays as a result of intermediate motions (dangling chains and loops or local reptation) and/or motional heterogeneity.⁴³ The characteristic parameters from the KWW fitting (T_2 and β) are included in Figure 5.6. Since it was expected that the backbone and branches undergo a nanophase separation rendering their dynamic decoupling and, hence, are characterized by distinct T_2 parameters,⁴⁴ it was decided to use a sum of two KWW

functions to fit the intensity decays of the aliphatic component, weighed by the known fractions of the protons in the branches and backbone (A and $1-A$, respectively). As a consequence, the signal fitting for the aliphatic component shows two T_2 (T_{21} and T_{22}) and two β (β_1 and β_2) where the longer T_{21} and β_1 are assigned to the branch component (Figure 5.7). For all the studied molecular moieties, except for the branches, β was below 1 indicating a motional heterogeneity. In the case of the aliphatic backbone, this heterogeneity can be explained by the dynamic gradient along the chain,⁴⁵ with the dynamics being slowest close to the dianhydride and accelerating away from it, while in the case of the aromatic signal this heterogeneity is attributed to the dynamic equilibrium of open and closed states and the distribution of the bond lifetimes of the closed moieties.³⁴ The branches were found to exhibit $\beta_1 > 1$, which points at a dominance of quasi-static RDDCs arising from a well-defined motional anisotropy. Note that the fits with use of the sum of two monoexponential decay functions were also tested to check whether the overparametrization could have an effect on the obtained results, but the trends observed in the T_2 values stayed unchanged.

Figure 5.7 summarizes all T_2 results reflecting differences in the molecular dynamics of the different molecular moieties within the four PIs. In analogy to previous work,⁴³ the T_2 reflects molecular mobility in the fast motional regime because DDCs become increasingly averaged out with dynamic acceleration brought about by temperature elevation. Since the DDCs are distance-dependent, namely inversely proportional to the cube of the internuclear distance, the intramolecular DDCs govern the transverse relaxation, and the DDCs between the aliphatic and other CH_2 protons are larger than between aromatic protons. Hence, a T_2 of aliphatic moieties is a priori expected to be lower than an aromatic T_2 . To perform an important check whether dianhydrides interact with each other, T_2 values of the CH_2 -imide signals, closest to the aromatic dianhydrides, were analysed along with T_2 values of the rest of the aliphatic backbone signals.

As can be seen, the T_2 values, and hence mobilities, of the CH_2 -imide signals are lower than the corresponding T_2 values of the rest of the aliphatic backbone signals, meaning that dianhydrides indeed interact and serve as dynamic cross-links.

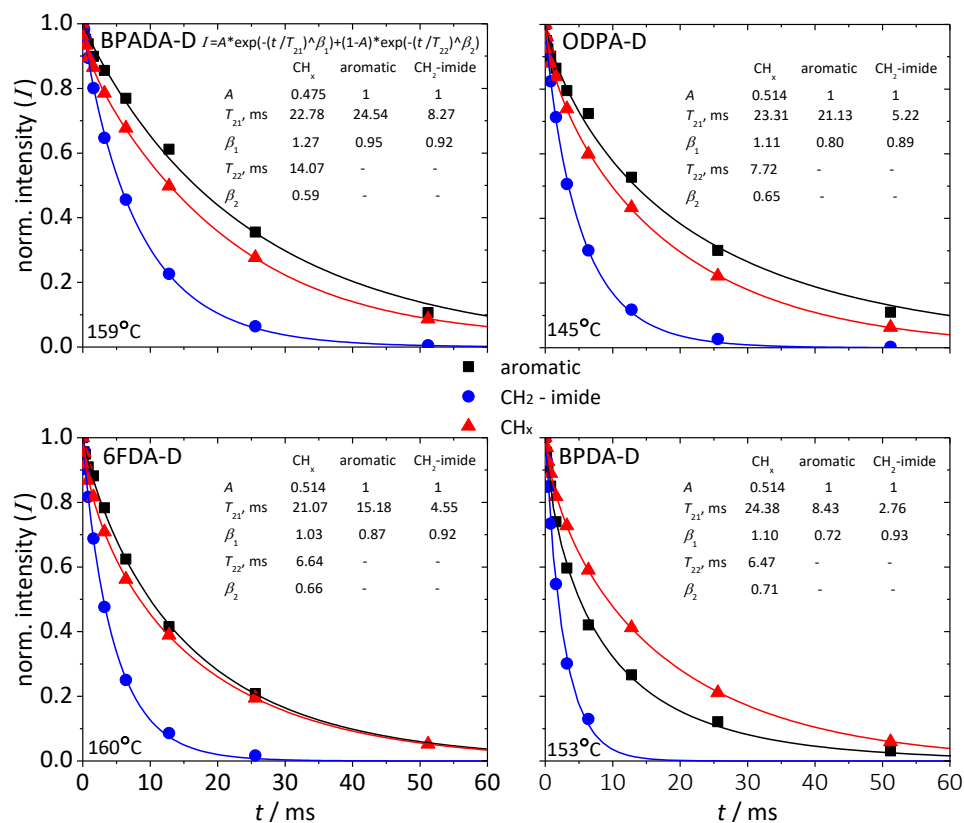


Figure 5.6. Results of the rotor-synchronized Hahn echo experiments for the four PIs. The corresponding experimental temperatures ($T_{\text{exp}} = T_{\text{tan}\delta_{\text{MAX}}} + 120^\circ\text{C}$) are specified. The solid lines represent the KWW fits (Eq. 5.2).

As can be seen in Figure 5.7, the T_2 values for the branches show no significant differences amongst the four polymers (within experimental error). The T_2 values for the aliphatic part of the backbone (CH_x) are the highest in case of BPADA-D polymer, while the other three polymers exhibit small decrease in the order: ODPA-D > 6FDA-D > BPDA-D. The same trend is reflected in the T_2 values of both the aromatic moieties and CH₂-imide protons (BPADA-D > ODPA-D > 6FDA-D > BPDA-D), however with more significant differences in the absolute values. From these results it becomes clear that the ¹H SS NMR study allowed revealing that the dynamics of both aromatic and aliphatic parts of the backbone are

completely defined by the motional freedom set by the hard block in question. As expected from the polymer architectures (Scheme 5.2) and the terminal relaxation timescales, τ_s , obtained from rheological experiments (Table 5.II), the backbone chain modes (given constant–isofrictional–segmental dynamics) accelerate in the order: BPDA-D < 6FDA-D < ODPA-D < BPADA-D. This trend follows the trend of dianhydride linker flexibility increase which correlates to their rotational energies' differences (Figures S-5.6 to S-5.9).

The fact that aromatic and aliphatic parts of the backbone have the same dynamic trends indirectly indicates that the aromatic dianhydride structure plays an important role in hindering polymer chains dynamics at temperatures significantly above the T_g ($T_{\text{exp}} = T_{\text{tan}\delta\text{MAX}} + 120^\circ\text{C}$), where polymers are in the terminal flow regime. The trend of the increased dynamics follows the trend of the terminal flow increase in the cross-over frequency f_s (decrease of the τ_s) from the results obtained by rheology, indicating that the slow dynamics (low frequencies/high temperatures) are a consequence of dianhydride architecture.

Conversely, the side-chains are much more mobile, and the dynamics are independent of the dianhydride architecture in this regime, as evidenced from the T_2 values for the branches being significantly larger than for the main-chain alkyl groups and the same regardless of the dianhydride used. This confirms the above rheological observations and suggests that the significantly rigid dianhydride regions (hard blocks) are the primary “stickers” that hinder the main-chain motion and impart elastic behaviour (pseudo plateau in rheology).

Based upon rheological and NMR insights, we propose a molecular model of the different polymers responsible for the observed differences in the mechanical and healing behaviour as shown in Scheme 5.2, where the side-chains are depicted in red, aliphatic backbone in green, dianhydride sections as black boxes, and the backbone rotation freedom set by the dianhydride linker in question is shown with (crossed) yellow arrows. The ether (-O-) linker in ODPA provides the highest rotational freedom, which is increasingly restricted on moving from ODPA to BPDA.

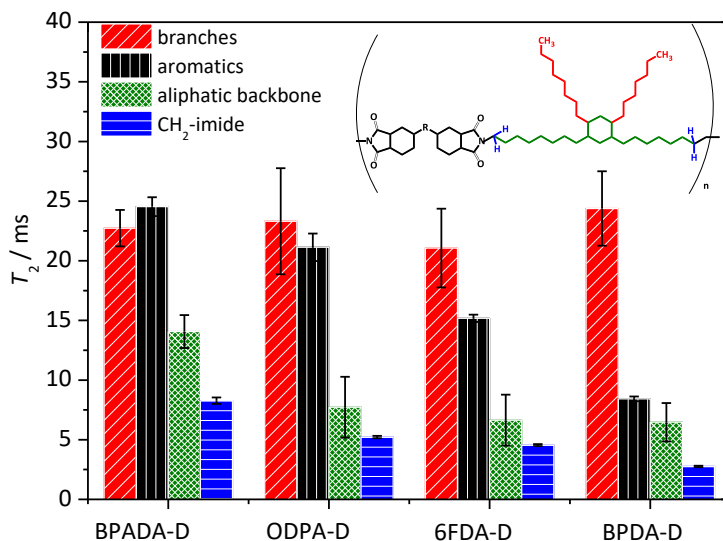
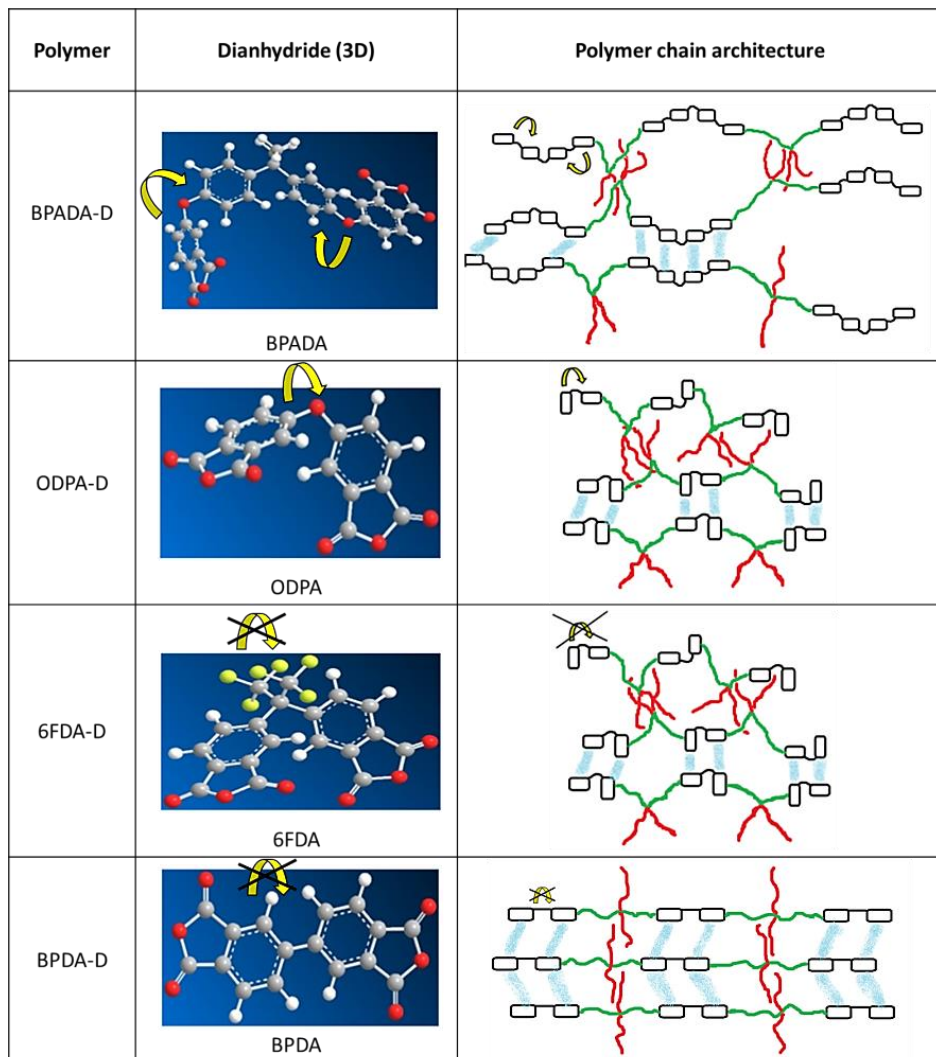


Figure 5.7. Extracted T_2 relaxation times of the studied PIs measured at $T_{\text{exp}} = T_{\text{tan}\delta_{\text{MAX}}} + 120^\circ\text{C}$. The absolute T_2 values cannot be compared between different species.

Even though simulations (Supporting Information, Figures S-5.6 to S-5.9) showed that 6FDA and BPDA have similarly high rotational energy (depicted by the crossed yellow arrows), they are significantly different in terms of planarity which explains the different aromatic chain restrictions. As opposed to the planar ground state of BPDA, bulky $-\text{CF}_3$ groups in 6FDA molecule lead to non-coplanarity, which increases the disorder and hinders ordered packing. BPDA, in turn, is fully planar and enables crystallization upon thermal annealing.¹⁸



Scheme 5.2. Idealized polymer architecture and secondary interactions of the studied polyimides as function of the aromatic hard block and based on the rheological and NMR analysis. The side-chains are depicted in red, aliphatic backbone parts in green and dianhydride moieties as black boxes. The (crossed) yellow arrows indicate the backbone motion freedom set by the dianhydride linker in question and the aromatic interactions are depicted in blue.

5.4. Correlation between macroscale healing and polymer dynamics

In order to unveil the effect of the dianhydride architecture on the macroscopic healing potential of branched PIs, it is necessary to correlate the macroscopic healing, as quantified by the parameters obtained from the tensile tests, to the polymer dynamics on microscopic scale (rheology) and molecular scale (SS NMR). From Figure 5.3, it appears that the healing process in the four polymers takes place in two differentiated steps at two different rates: (i) R_1 =fast recovery up to day 1 and (ii) R_2 =slower recovery from day 1 to day 11. Figure 5.8 shows the healing rates calculated from the slopes of σ_b recovery (healing efficiency, %, Eq. 1.) in time (healing time t_{SH} , min) from Figure 5.3. The cross-over frequencies for each polymer deduced from the rheological TTS mastercurves at $T_{SH}=T_{ref}=T(\tan\delta_{MAX})$ for two different dynamics are plotted in the same Figure: (i) f_g representing the onset of the fast motions related to the side-chains and (ii) f_s representing the start of the terminal flow (slow dynamics) governed by the aromatic interactions.

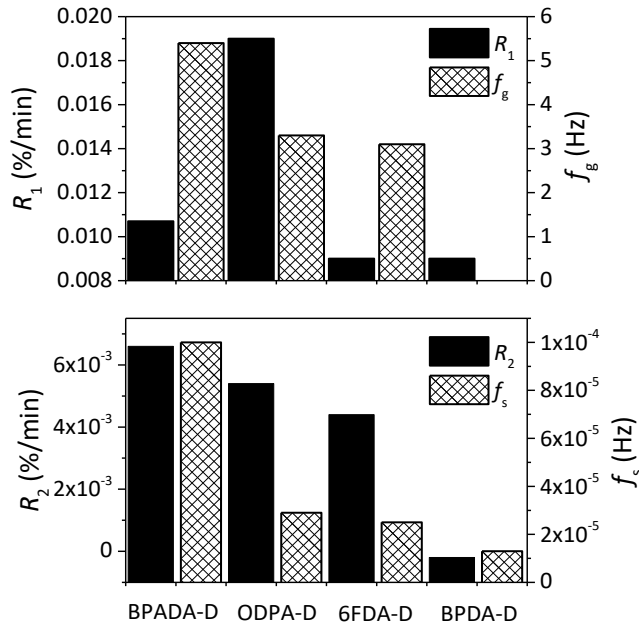


Figure 5.8. Comparison of the healing rates R_1 and R_2 for the stress at break recovery (up, full columns) and cross-over frequencies f_g and f_s (bottom, striped columns) for all four polymers. $T_{SH}=T_{ref}=T_{\tan\delta_{MAX}}=T_g$. $T_{\text{tensile test}}=23\pm 2^\circ\text{C}$.

In agreement with our previous findings,⁷ where the initial recovery of the mechanical (tensile) properties is attributed to the very fast interfacial interactions provided by the branches, it can be stated that f_g is related to R_1 . Similarly, the f_s cross-over frequency indicates the beginning of the second healing stage related to slow interdiffusion across the interface with slower kinetics governed by the aromatic hard block interactions and is therefore more likely to be related to the macroscopic healing kinetics R_2 and the high-temperature SS NMR results. From Figure 5.8 it can be seen how three parameters f_g , R_2 , and f_s clearly decrease with the following order BPADA-D > ODPA-D > 6FDA-D > BPDA-D. The R_1 parameter follows roughly the same trend although BPADA seems to be an outlier in this case possibly due to a very fast interfacial healing phenomenon not captured during the mechanical testing, this coinciding with the rest of the tests and overall hypothesis. According to obtained SS NMR parameters T_{21} and β_1 (Figure 5.6), the macroscopic dynamics related to the branches should show a weak dependency of the dianhydride aromatic linker rigidity (Figure 5.7 and 5.8). This is indeed observed in Figure 5.8, where the values of the macroscopic dynamic parameters R_1 and f_g do not follow the trend of increasing dianhydride rigidity. It seems nevertheless, that these parameters do depend on the architecture of the anhydride moieties, as seen by the very low level of healing of the BPDA-D polymer due to the planarity-induced crystallization observed.¹⁸ On the other hand, the T_2 (Figure 5.7), R_2 and f_s (Figure 5.8) values reflect the second healing stage dominated by interdiffusion, and are directly dependent on the dianhydride rigidity and less obviously on the dianhydride linker planarity, with BPADA-D showing the fastest healing due to its higher chain and linker flexibility.

5. Conclusions

This study sheds light on the importance of molecular architecture in obtaining tuneable stepwise healing dynamics in intrinsic self-healing polymers containing aliphatic branches, hence being advantageous for the future design of self-healing polymers with high mechanical properties and low healing temperatures, of other classes. To the best of our knowledge, the combination of low temperature healing and relatively high values of the mechanical properties obtained for the best performing polyimides reported here is unique. The (room temperature) Young modulus values of the polyimides reported here are in the range from 50 to 400 MPa. These values are up to three orders of magnitude higher than the ones reported for other room temperature healing polymers,⁴⁶ such as the ones based on H-bonds ($E \approx 0.25$ MPa),⁴⁷ those based on the combination of H-bonds and aromatic disulfides ($E \approx 0.10$ MPa)⁴⁸ or the H-bonds multiphase brush polymers from Chen et al ($10 < E < 40$ MPa).⁴⁹ Intrinsic self-healing polymers with higher modulus are made, but those need temperatures well above room temperature to heal. The difficulty to compare the healing performance of polymers objectively and quantitatively stems from the multidimensional nature of the issue and the absence of universal testing protocols.⁵⁰

The results and schemes indicate that aromatic interactions limit the mobility of the aliphatic backbone of the soft segment and not that of the branches, thereby being responsible for the limited entanglement and the elastic behaviour (pseudo-plateau) beyond the dissipative regime governed by the branches and segmental relaxation. The disturbance of these aromatic interactions at longer times and higher temperatures allows for sticky Rouse chain displacement in the terminal flow where secondary stickers (branches) play a governing role more or less independently of the aromatic dianhydride type. The results thus indicate that aromatics increase mechanical properties but should have low planarity to avoid undesired crystallization (BPDA case). Lower rigidity levels of the aromatic hard block allow for higher healing kinetics and higher healing degrees at the healing temperatures near T_g . Aliphatic branches in the soft block facilitate the healing by a plasticizing effect. It can therefore be stated that a combination of non-planar and flexible aromatic segments with high aliphatic branch density seems a good avenue to develop strong low-temperature healing polymers with good healing of

macroscopic damages. Lastly, we reported the effect of the tensile testing temperature on the apparent self-healing efficiency, identifying the glass transition temperature as the relevant factor enabling mobility and healing. The Young's modulus was considered as the least testing-dependent parameter to evaluate healing behaviour. When comparing healing polymers all mechanical tests should be performed at comparable (relative) temperature above the polymer T_g .

Following the two-step kinetics (R_1 and R_2) of the healing process, we were able to differentiate and quantify the extent of mechanical strength recovery in each of the healing stages. As the initial recovery of the mechanical (tensile) properties is given by very fast interfacial interactions provided by the branches, we argued that the crossover frequency in the dissipative regime is related to the first stage healing kinetics, R_1 , obtained from the self-healing efficiency in terms of stress at break recovery over healing time. Similarly, the cross-over frequency in the terminal flow region indicates the beginning of the second healing stage related to slow interdiffusion across the interface with slower kinetics and therefore is likely to be related to the macroscopic healing kinetics R_2 . Furthermore, we have correlated the macro- and microscale kinetic parameters (R_2 and f_s) to the molecular kinetic parameter T_2 (spin-spin relaxation time) obtained from the high-temperature solid-state NMR results. The results showed that the healing rate R_2 decrease with the increase of the hard-block rigidity and aromatic interactions, and the resulting inhibition of the backbone dynamics. Moreover, if the hard block is both rigid and planar (BPDA), the healing is hampered significantly due to crystallization which disables both the local mobility crucial for the first healing step, the self-adhesion, as well as the late-stage interdiffusion.

References

1. Chen, S.; Mahmood, N.; Beiner, M.; Binder, W. H., Self-Healing Materials from V- and H-Shaped Supramolecular Architectures. *Angewandte Chemie International Edition* **2015**, *54* (35), 10188-10192.
2. Bose, R. K.; Hohlbein, N.; Garcia, S. J.; Schmidt, A. M.; van der Zwaag, S., Connecting Supramolecular Bond Lifetime and Network Mobility for Scratch Healing in Poly(butyl acrylate) Ionomers Containing Sodium, Zinc and Cobalt. *Physical chemistry chemical physics: PCCP* **2015**, *17* (3), 1697-704.

3. Hernández, M.; Grande, A. M.; van der Zwaag, S.; García, S. J., Monitoring Network and Interfacial Healing Processes by Broadband Dielectric Spectroscopy: A Case Study on Natural Rubber. *ACS Applied Materials & Interfaces* **2016**, *8* (16), 10647-10656.
4. Döhler, D.; Michael, P.; Binder, W. H., Principles of Self-Healing Polymers. In *Self-Healing Polymers: From Principles to Applications*, Binder, W. H., Ed. Wiley-VCH: Weinheim, 2013; pp 7-60.
5. Wool, R. P.; O'Connor, K. M., A Theory Crack Healing in Polymers. *Journal of Applied Physics* **1981**, *52* (10), 5953-5963.
6. Kim, Y. H.; Wool, R. P., A Theory of Healing at a Polymer-Polymer Interface. *Macromolecules* **1983**, *16* (7), 1115-1120.
7. Susa, A.; Bose, R. K.; Grande, A. M.; van der Zwaag, S.; Garcia, S. J., Effect of the Dianhydride/Branching Diamine Ratio on the Architecture and Room Temperature Healing Behaviour of Polyetherimides. *ACS Applied Materials & Interfaces* **2016**, *8* (49), 34068–34079.
8. Bose, R. K.; Enke, M.; Grande, A. M.; Zechel, S.; Schacher, F. H.; Hager, M. D.; Garcia, S. J.; Schubert, U. S.; van der Zwaag, S., Contributions of Hard and Soft Blocks in the Self-healing of Metal-Ligand-Containing Block Copolymers. *European Polymer Journal* **2017**, *93*, 417-427.
9. An, S. Y.; Noh, S. M.; Oh, J. K., Multiblock Copolymer-Based Dual Dynamic Disulfide and Supramolecular Crosslinked Self-Healing Networks. *Macromolecular Rapid Communications* **2017**, *38* (8).
10. Garcia, S. J., Effect of Polymer Architecture on the Intrinsic Self-healing Character of Polymers. *European Polymer Journal* **2014**, *53* (0), 118-125.
11. Bose, R. K.; Hohlbein, N.; Garcia, S. J.; Schmidt, A. M.; van Der Zwaag, S., Relationship Between the Network Dynamics, Supramolecular Relaxation Time and Healing Kinetics of Cobalt Poly(butyl acrylate) Ionomers. *Polymer (United Kingdom)* **2015**, *69*, 228-232.
12. Liu, F.; Li, F.; Deng, G.; Chen, Y.; Zhang, B.; Zhang, J.; Liu, C.-Y., Rheological Images of Dynamic Covalent Polymer Networks and Mechanisms behind Mechanical and Self-Healing Properties. *Macromolecules* **2012**, *45* (3), 1636-1645.
13. Enke, M.; Bose, R. K.; Bode, S.; Vitz, J.; Schacher, F. H.; Garcia, S. J.; van Der Zwaag, S.; Hager, M. D.; Schubert, U. S., A Metal Salt Dependent Self-healing Response in Supramolecular Block Copolymers. *Macromolecules* **2016**, *49* (22), 8418-8429.
14. Yan, T.; Schröter, K.; Herbst, F.; Binder, W. H.; Thurn-Albrecht, T., Unveiling the Molecular Mechanism of Self-healing in a Telechelic, Supramolecular Polymer Network. *Scientific Reports* **2016**, *6*, 32356.

15. Grande, A. M.; Bijleveld, J. C.; Garcia, S. J.; van Der Zwaag, S., A Combined Fracture Mechanical – Rheological Study to Separate the Contributions of Hydrogen Bonds and Disulphide Linkages to the Healing of Poly(urea-urethane) Networks. *Polymer (United Kingdom)* **2016**, *96*, 26-34.
16. Smits, A. L. M.; van Triet, R. B.; Dingemans, T. J.; Garcia-Espallargas, S. J. Polyimide composition. 2014.
17. van der Kooij, H. M.; Susa, A.; García, S. J.; van der Zwaag, S.; Sprakel, J., Imaging the Molecular Motions of Autonomous Repair in a Self-Healing Polymer. *Advanced Materials* **2017**, 1701017-n/a.
18. Susa, A.; Bijleveld, J.; Hernandez Santana, M.; Garcia, S. J., Understanding the Effect of the Dianhydride Structure on the Properties of Semi-aromatic Polyimides Containing a Biobased Fatty Diamine. *ACS Sustainable Chemistry and Engineering* **2018**, *6* (1), 668–678.
19. Wittmer, A.; Brinkmann, A.; Stenzel, V.; Hartwig, A.; Koschek, K., Moisture-mediated intrinsic self-healing of modified polyurethane urea polymers. *Journal of Polymer Science Part A: Polymer Chemistry* **2018**, *56* (5), 537-548.
20. Hahn, E. L., Spin Echoes. *Physical Review* **1950**, *80* (4), 580-594.
21. Tanaka, F.; Edwards, S. F., Viscoelastic Properties of Physically Crosslinked Networks. 1. Transient Network Theory. *Macromolecules* **1992**, *25* (5), 1516-1523.
22. Knoben, W.; Besseling, N. A. M.; Bouteiller, L.; Cohen Stuart, M. A., Dynamics of Reversible Supramolecular Polymers: Independent Determination of the Dependence of Linear Viscoelasticity on Concentration and Chain Length by Using Chain Stoppers. *Physical Chemistry Chemical Physics* **2005**, *7* (11), 2390-2398.
23. Baxandall, L. G., Dynamics of reversibly crosslinked chains. *Macromolecules* **1989**, *22* (4), 1982-1988.
24. Rubinstein, M.; Semenov, A. N., Thermoreversible Gelation in Solutions of Associating Polymers. 2. Linear Dynamics. *Macromolecules* **1998**, *31* (4), 1386-1397.
25. Chen, Q.; Liang, S.; Shiau, H.-s.; Colby, R. H., Linear Viscoelastic and Dielectric Properties of Phosphonium Siloxane Ionomers. *ACS Macro Letters* **2013**, *2* (11), 970-974.
26. Tang, S.; Wang, M.; Olsen, B. D., Anomalous Self-Diffusion and Sticky Rouse Dynamics in Associative Protein Hydrogels. *Journal of the American Chemical Society* **2015**, *137* (11), 3946-3957.
27. Golkaram, M.; Fodor, C.; van Ruymbeke, E.; Loos, K., Linear Viscoelasticity of Weakly Hydrogen-Bonded Polymers near and below the Sol–Gel Transition. *Macromolecules* **2018**, *51* (13), 4910-4916.
28. Leibler, L.; Rubinstein, M.; Colby, R. H., Dynamics of reversible networks. *Macromolecules* **1991**, *24* (16), 4701-4707.

29. Rubinstein, M.; Semenov, A. N., Dynamics of Entangled Solutions of Associating Polymers. *Macromolecules* **2001**, *34* (4), 1058-1068.
30. Chen, Q.; Zhang, Z.; Colby, R. H., Viscoelasticity of entangled random polystyrene ionomers. *Journal of Rheology* **2016**, *60* (6), 1031-1040.
31. Gold, B. J.; Hövelmann, C. H.; Lühmann, N.; Székely, N. K.; Pyckhout-Hintzen, W.; Wischniewski, A.; Richter, D., Importance of Compact Random Walks for the Rheology of Transient Networks. *ACS Macro Letters* **2017**, *6* (2), 73-77.
32. Mateyisi, M. J.; Sommer, J.-U.; Müller-Nedebock, K. K.; Heinrich, G., Influence of weak reversible cross-linkers on entangled polymer melt dynamics. *The Journal of Chemical Physics* **2018**, *148* (24), 244901.
33. Yan, T.; Schröter, K.; Herbst, F.; Binder, W. H.; Thurn-Albrecht, T., Nanostructure and Rheology of Hydrogen-Bonding Telechelic Polymers in the Melt: From Micellar Liquids and Solids to Supramolecular Gels. *Macromolecules* **2014**, *47* (6), 2122-2130.
34. Chen, S.; Yan, T.; Fischer, M.; Mordvinkin, A.; Saalwächter, K.; Thurn-Albrecht, T.; Binder, W. H., Opposing Phase-Segregation and Hydrogen-Bonding Forces in Supramolecular Polymers. *Angewandte Chemie International Edition* **2017**, *56* (42), 13016-13020.
35. Chen, Q.; Tudryn, G. J.; Colby, R. H., Ionomer dynamics and the sticky Rouse model. *Journal of Rheology* **2013**, *57* (5), 1441-1462.
36. Zhang, Z.; Huang, C.; Weiss, R. A.; Chen, Q., Association energy in strongly associative polymers. *Journal of Rheology* **2017**, *61* (6), 1199-1207.
37. Hill, D. J. T.; Perera, M. C. S.; Pomery, P. J.; Toh, H. K., Dynamic Mechanical Properties of Networks Prepared from Siloxane Modified Divinyl Benzene Pre-polymers. *Polymer* **2000**, *41* (26), 9131-9137.
38. Brown, S. P.; Schnell, I.; Brand, J. D.; Mullen, K.; Spiess, H. W., The Competing Effects of π - π Packing and Hydrogen Bonding in a Hexabenzocoronene Carboxylic Acid Derivative: A ^1H Solid-state MAS NMR Investigation. *Physical Chemistry Chemical Physics* **2000**, *2* (8), 1735-1745.
39. Levitt, M. H., *Spin Dynamics: Basics of Nuclear Magnetic Resonance*. 2 ed.; John Wiley and Sons: Chichester, England, 2008; p 740.
40. McCreight, K. W.; Ge, J. J.; Guo, M.; Mann, I.; Li, F.; Shen, Z.; Jin, X.; Harris, F. W.; Cheng, S. Z. D., Phase Structures and Transition Behaviours in Polymers Containing Rigid Rodlike Backbones with Flexible Side Chains. V. Methylene Side-chain Effects on Structure and Molecular Motion in a Series of Polyimides. *Journal of Polymer Science Part B: Polymer Physics* **1999**, *37* (14), 1633-1646.
41. Kimmich, R., *NMR: Tomography, Diffusometry, Relaxometry*. Springer: Berlin, 1997.

42. Vaca Chávez, F.; Saalwächter, K., Time-Domain NMR Observation of Entangled Polymer Dynamics: Universal Behaviour of Flexible Homopolymers and Applicability of the Tube Model. *Macromolecules* **2011**, *44* (6), 1549-1559.
43. Schäler, K.; Roos, M.; Micke, P.; Golitsyn, Y.; Seidlitz, A.; Thurn-Albrecht, T.; Schneider, H.; Hempel, G.; Saalwächter, K., Basic Principles of Static Proton Low-Resolution Spin Diffusion NMR in Nanophase-Separated Materials with Mobility Contrast. *Solid State Nuclear Magnetic Resonance* **2015**, *72*, 50-63.
44. Beiner, M., Relaxation in Poly(alkyl methacrylate)s: Crossover Region and Nanophase Separation. *Macromolecular Rapid Communications* **2001**, *22* (12), 869-895.
45. Ferreira, T. M.; Coreta-Gomes, F.; Ollila, O. H. S.; Moreno, M. J.; Vaz, W. L. C.; Topgaard, D., Cholesterol and POPC segmental order parameters in lipid membranes: solid state 1H – 13C NMR and MD simulation studies. *Physical Chemistry Chemical Physics* **2013**, *15* (6), 1976-1989.
46. Kim, C.; Yoshie, N., Polymers healed autonomously and with the assistance of ubiquitous stimuli: how can we combine mechanical strength and a healing ability in polymers? *Polymer Journal* **2018**, *50* (10), 919-929.
47. Cordier, P.; Tournilhac, F.; Soulie-Ziakovic, C.; Leibler, L., Self-healing and thermoreversible rubber from supramolecular assembly. *Nature* **2008**, *451* (7181), 977-980.
48. Rekondo, A.; Martin, R.; Ruiz de Luzuriaga, A.; Cabañero, G.; Grande, H. J.; Odriozola, I., Catalyst-free room-temperature self-healing elastomers based on aromatic disulfide metathesis. *Materials Horizons* **2014**, *1* (2), 237-240.
49. Chen, Y.; Kushner, A. M.; Williams, G. A.; Guan, Z., Multiphase design of autonomic self-healing thermoplastic elastomers. *Nature Chemistry* **2012**, *4*, 467.
50. Bode, S.; Enke, M.; Hernandez, M.; Bose, R. K.; Grande, A. M.; van der Zwaag, S.; Schubert, U. S.; Garcia, S. J.; Hager, M. D., Characterization of Self-Healing Polymers: From Macroscopic Healing Tests to the Molecular Mechanism. In *Self-healing Materials*, Hager, M. D.; van der Zwaag, S.; Schubert, U. S., Eds. Springer International Publishing: Cham, 2016; pp 113-142.

SUPPORTING INFORMATION***Rheology – temperature sweeps***

The rheological temperature sweeps were performed in the cooling ramp, at 1°C/min cooling rate and the results are shown in Figure S-5.1 and were already discussed in our previous chapters. The temperature range selected (0-50°C) is showing the transition from the glassy to the dissipative regime of the polymer relaxation (T_g), which plays an important role in the self-healing (SH) mechanism of these polymers, as previously reported. The maximum of the $\tan\delta$ peak is taken to be the optimal healing temperature (T_{SH}), since it represents the maximum viscous dominance ($G'' > G'$), i.e. maximum mobility for healing, and it is responsible for the first healing step. Figure S-5.1a shows the storage modulus (G') and loss modulus (G'') curves while damping factors ($\tan\delta$) versus temperature at 1 Hz for all the samples studied are shown in Figure S-5.1b. The $T(\tan\delta_{MAX}) = T_g = T_{SH}$ values are given in Table S-5.I.

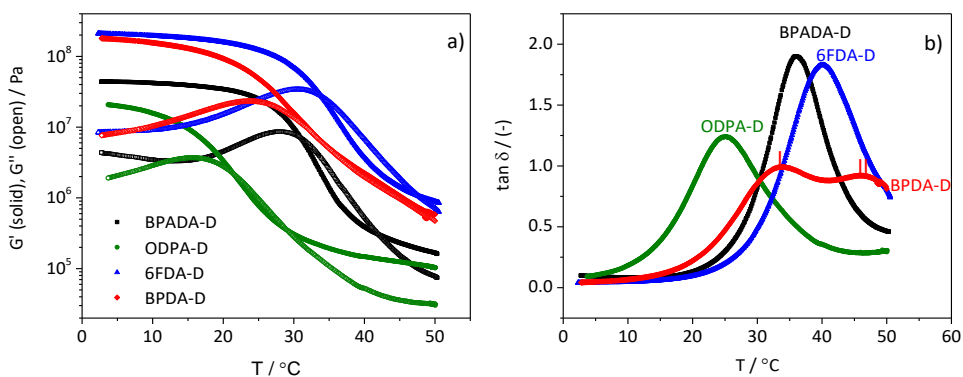


Figure S-5.1. a) Storage (G') and loss (G'') moduli and b) $\tan\delta$ curves from the rheological temperature sweeps experiments, showing distinct T_g -relaxations of the four PIs.

Tensile test

Tensile parameters – undamaged samples (pristine)

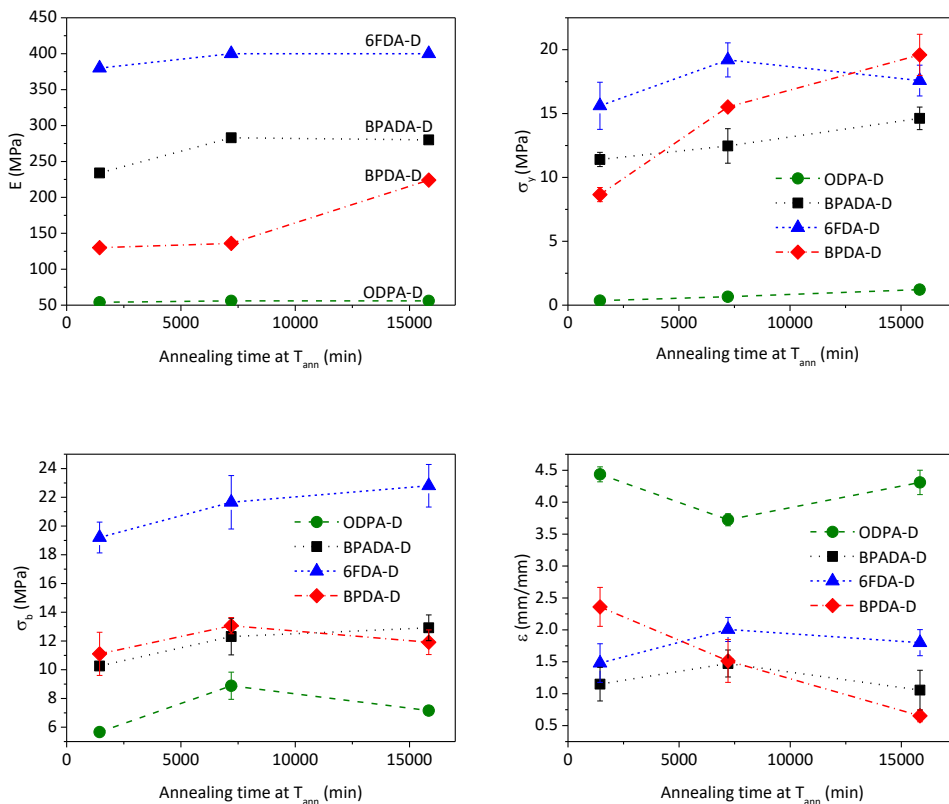


Figure S-5.2. The effect of dianhydride structure and annealing time at $T_{ann}=T_{SH}$ on the Young modulus (E), stress at yield (σ_y), stress at break (σ_b) and strain at break (ϵ_b) of the pristine materials.

Effect of testing temperature on the mechanical and healing properties

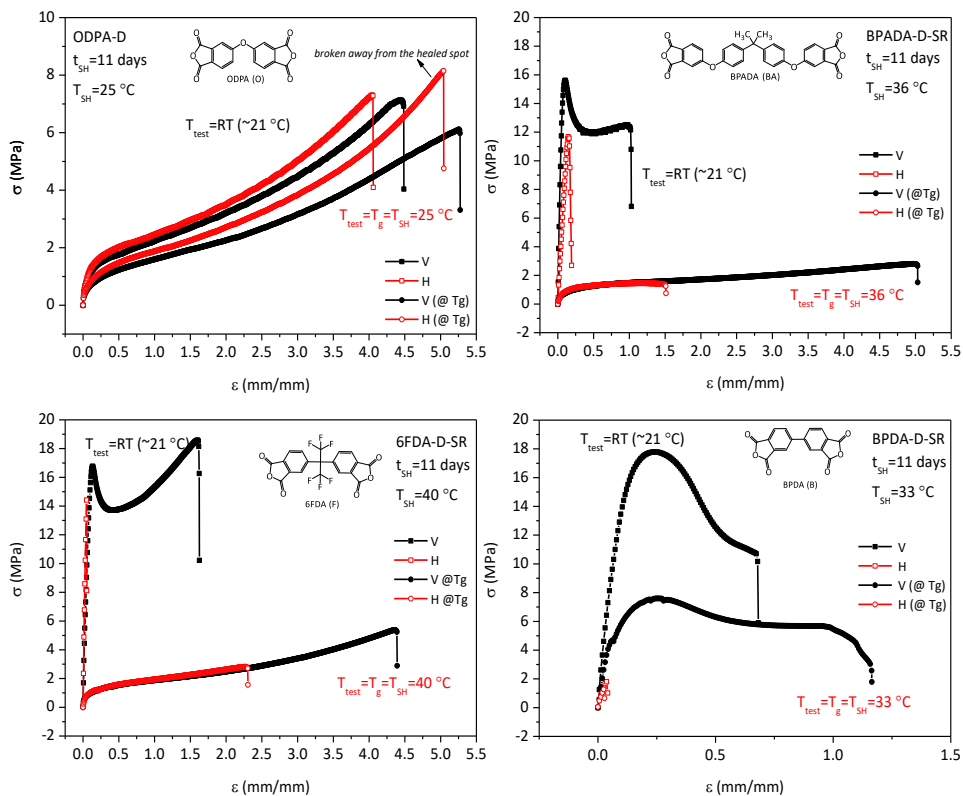


Figure S-5.3. Stress-strain curves at 80 mm/min strain rate showing the effect of the testing temperature on the general mechanical performance of pristine (V) and samples healed at their $T_{\text{SH}} = T_{\text{g}}$ for 11 days (H).

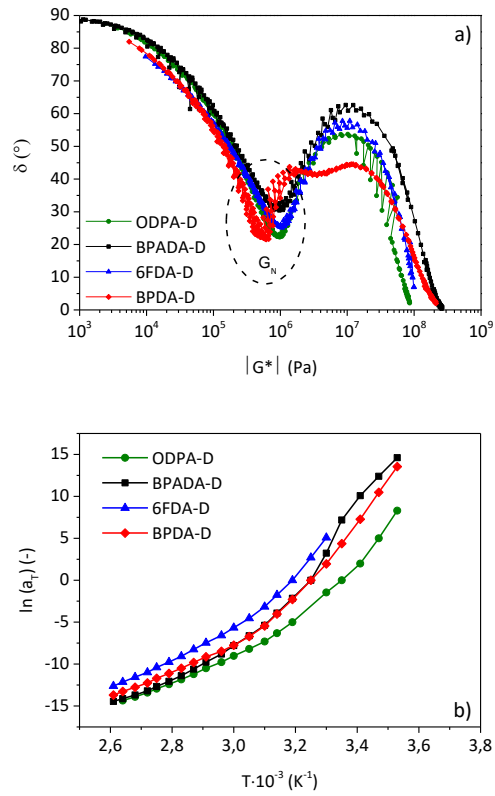
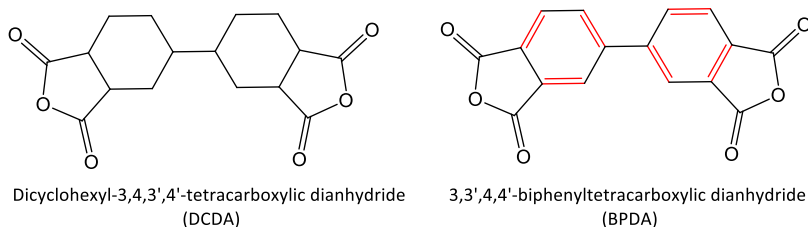
Rheological parameters

Figure S-5.4. a) Van Gorp-Palmen plot used for M_e calculations in Table 5.II; b) horizontal shift factors (a_T) from the TTS mastercurves.

Synthesis of the Non-Aromatic PI (reference)

In order to evaluate the effect of the aromatic interactions on the rheological behaviour of the PIs in this work, a non-aromatic PI (named DCDA-D) was prepared as a reference. Since DCDA dianhydride does not contain any linker between the cyclohexyl units, it can be considered a non-aromatic analogue of the BPDA dianhydride (See Scheme S-5.1). An alicyclic dianhydride dicyclohexyl-3,4,3',4'-tetracarboxylic dianhydride (DCDA) (99%, Advanced Organic Synthesis LLC) was reacted with the previously used fatty dimer diamine (Priamine™ 1075, here named DD1) (Croda Nederland B.V.). The amounts of each monomer were added at the theoretical stoichiometric ratio, calculated according to the molecular weights of the monomers ($MW_{DCDA}=306.31$ g/mol and $MW_{DD1}=536.80$ g/mol) and assuming both chemicals are 100% difunctional. The synthesis was conducted following the same procedure as for the other (aromatic) PIs in this work. The only difference was that the DCDA-based polymer remained soluble in the polymerization solvent (DMAc) even upon cooling down to room temperature, as opposed to the aromatic PIs. For this reason, the DCDA-D polymer did not precipitate from the solution. Vacuum distillation was performed at 70°C and 10 mbar for one hour and after that the usual drying and annealing protocol was continued (as for the aromatic PIs) to yield the specimens. The polymer obtained appeared softer, tackier and much less coloured (light yellow) than the aromatic ones (dark yellow to brown). The general properties are shown in Table S-5.I.



Scheme S-5.1. The molecular structures of the non-aromatic (DCDA) and aromatic (BPDA) dianhydrides.

Table S-5.I. The M_w , M_n and PDI as calculated from the major peak obtained in GPC. T_g obtained from DSC and rheology.

Polymer	M_w (g/mol)	M_n (g/mol)	PDI	DSC- T_g^a ($^{\circ}\text{C}$)	Rheology- T_g^b ($^{\circ}\text{C}$)
DCDA-D	21k	12k	1.8	10	22
BPDA-D	37k	20k	1.9	22	33 ⁱ , 46 ⁱⁱ

^a T_g was calculated from the 2nd heating curve, 10 $^{\circ}\text{C}/\text{min}$. ^b T_g was taken as the maximum of the peak in the $\tan\delta$ curve from the rheological temperature sweeps, performed in cooling ramp, 1 $^{\circ}\text{C}/\text{min}$ (Figure S-5.1b). These temperatures were used as annealing and healing temperatures (in case of BPDA-D, the temperature of the first peak was used).

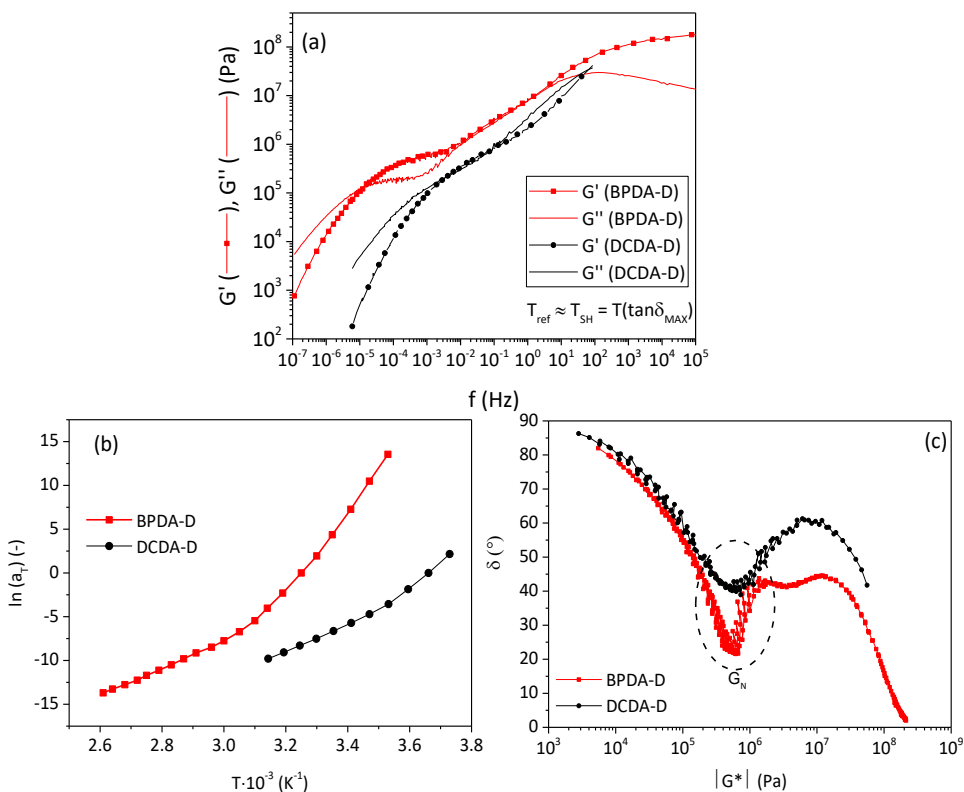


Figure S-5.5. a) TTS curves of the aromatic BPDA-D and non-aromatic DCDA-D branched polymers; b) shift factors as function of temperature and aromatics; and c) Van Gurp-Palmen plot used for G_N and M_c calculations.

Table S-5.II. Characteristic rheological parameters extracted from the TTS mastercurves at $T_{\text{ref}} \approx T_{\text{SH}} = T_{\text{tan}\delta \text{ MAX}}$

Polymer	f_s Hz	f_d Hz	f_g Hz	τ_s s	τ_d s	τ_g s	$\tan\delta_{\text{MAX}}$ -	G' slope at $f < f_s$	G'' slope at $f < f_s$	G' slope elastic plateau	G_N^* Pa	$M_{e,\text{app}}^{***}$ g/mol	M_x^{***} g/mol
DCDA-D	$3.5 \cdot 10^2$	0.09	70.0	28.6	11.2	0.01	1.7	1.37	0.83	0.34	$4.8 \cdot 10^5$	5420	843
BPDA-D	$1.3 \cdot 10^5$	/	/	$7.7 \cdot 10^4$	/	/	0.9	1.27	0.81	0.72	$5.7 \cdot 10^5$	4680	831

* G_N calculated from the Van Gorp-Palmen plot, $\delta(|G|)$, (Figure S-5.5, SI)

** $M_{e,\text{app}}$ (apparent) were calculated according to $M_e = \rho RT / G_N$ (Doi and Edwards) equation, using experimentally determined densities. In this case M_e values must be considered as pseudo- M_e values governed by 'transient interactions', not as molecular weight between entanglements.

*** M_x = average molecular weight between the two neighbouring temporal junctions, in this case the DD1 side-chains.

Calculation of rotation energies

To gain further insight on the flexibility of the different dianhydrides as function of their structural differences, a prediction was made using calculated rotation energy profiles of the dianhydrides around the different linkers. The energy of rotation is defined as the maximum energy difference between the different conformers of the dianhydride molecules. All energies and structural optimizations of the isolated molecules in the gas phase were calculated using density functional theory using a RB3LYP 6-31G* basis set. For BPDA, the energy of rotation was simply calculated while gradually changing the dihedral angle between the two phthalic anhydride rings (C1, C2, C3, C4). Because ODPA and 6FDA have two bonds that can be freely rotated, the dihedral angles C1-O2-C3-C4 and C1-C2-C3-C4 were fixed after which structure was optimized in energy. The resulting energy of the molecule was recorded and plotted versus the dihedral angle (Figures S-5.6 to S-5.9).

According to the results obtained, ODPA showed the lowest energy barrier for rotation, 3.5 kJ/mol, which is caused by the flexible ether (-O-) linker. BPDA and 6FDA showed similar barriers for rotation, 14 kJ/mol and 15 kJ/mol, respectively, although the energy profiles for rotation are different (discussed in the manuscript). In the case of 6FDA, the bulky fluor-containing -CF₃ groups hinder the rotation only close to the highest energy conformer, whereas in BPDA

the steric hindrance of the hydrogen atoms on the phthalic anhydride ring causes the maxima in energy to be broader.

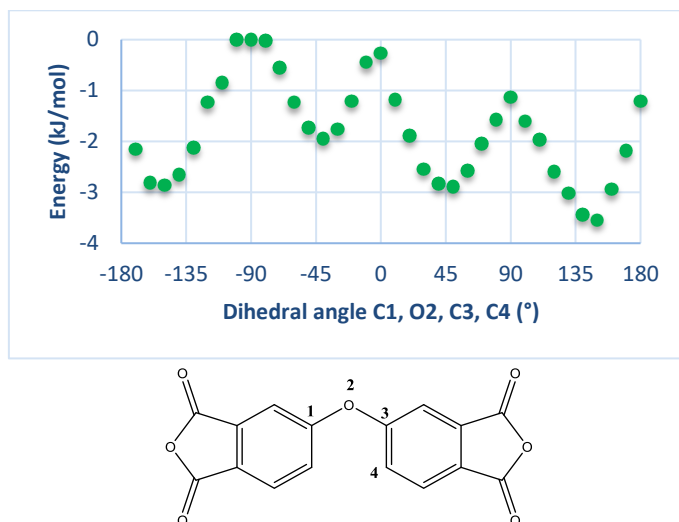


Figure S-5.6. Rotation energy profiles of ODPA

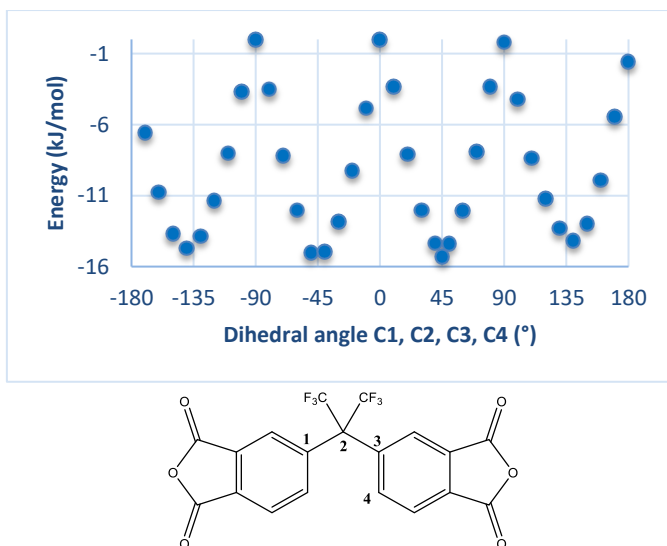


Figure S-5.7. Rotation energy profiles of 6FDA

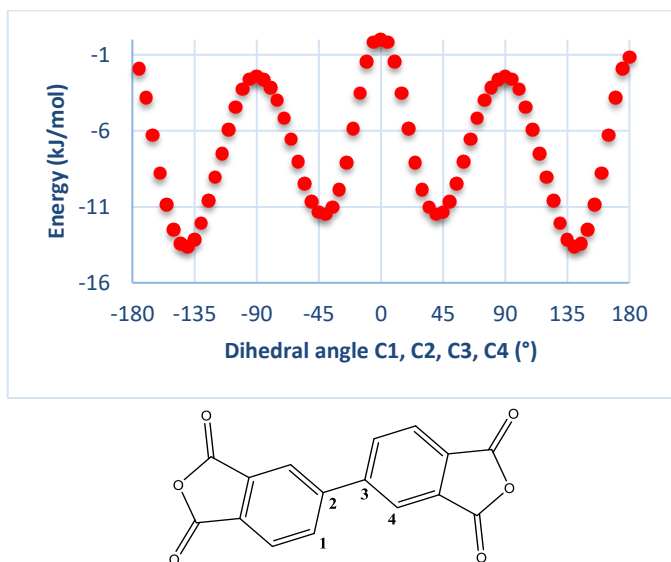


Figure S-5.8. Rotation energy profiles of BPDA

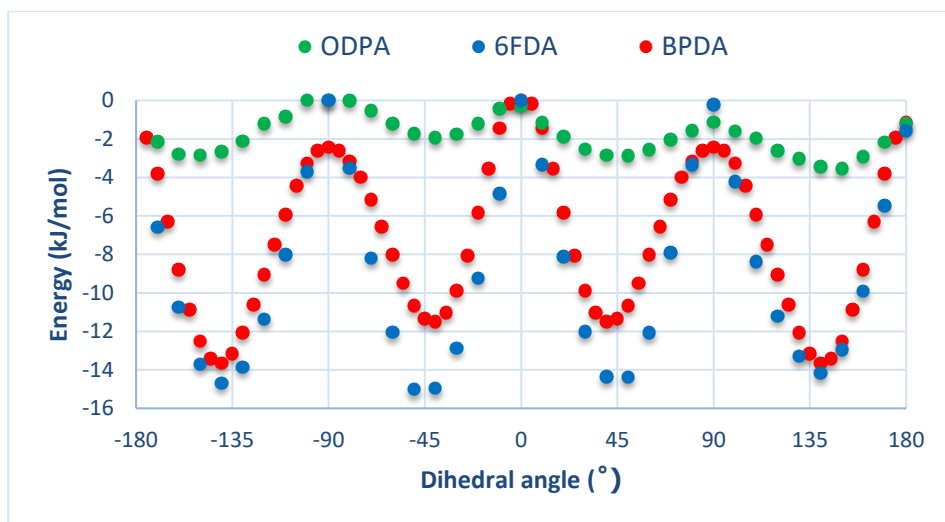


Figure S-5.9. Rotation energy profiles of the three dianhydrides combined in one plot for comparison.

6

Demonstrating autonomous healing of fatigue induced cracks in composites bonded with a self-healing polyimide interlayer

“What day is it?” asked Pooh.

“It’s today,” squeaked Piglet.

“My favourite day,” said Pooh.

Alan A. Milne

Co-contributors:

Fabício Nascimento Ribeiro, Santiago García, Sybrand van der Zwaag

Abstract

This chapter explores the feasibility of using the intrinsic room temperature healing polyimide developed in Chapter 2 as a thin film thermoplastic adhesive in an adhesively bonded joint in a commercial glass-fibre reinforced epoxy thermoset composite. A dedicated central cut plies (CCP) specimen geometry is used to induce mode II fatigue cracks in the adhesive layers by applying uniaxial tensile loading. Two methods are employed to evaluate the stiffness and crack evolution and to quantify the crack healing: the conventional clip-gauge method and a novel fibre-optics method.

The clip-gauge method allows us to calculate the average crack growth rate of the four cracks to be formed in the CCP sample from the reduction in sample stiffness, while the fibre-optics aims to provide an insight into the growth and closure of the individual cracks located directly below the appropriate part of the surface-mounted optical fibre. As shown by the fibre-optics results, the four cracks are not propagating equally nor symmetrically over the whole specimen.

Both methods demonstrate significant recovery of the crack and restoration of the local adhesive strength in the rebounded region upon healing the sample for 12 hours at 25°C. By comparing the two methods, a good yet only qualitative agreement for the crack lengths prior and after healing is obtained. However, the number of fatigue cycles required to reduce stiffness to the pre-healing values differs significantly.

6.1. Introduction

Adhesive bonding is a material joining process in which an adhesive is placed between the adherent surfaces. Adhesively bonded joints provide many advantages over conventional mechanical fasteners such as rivets and bolts. Some of these advantages include a lower structural weight due to the absence of fasteners, lower manufacturing costs and an improved damage tolerance. Furthermore, when using the traditional fasteners in fibre reinforced composites structures, the required drilling of holes results in broken fibres, therefore introducing additional stress concentrations, both of which impair the integrity of the structure. Adhesive bonding has found applications in various areas ranging from high technology industries, such as aeronautics, aerospace, automotive, maritime and electronics to more traditional industries such as construction, sports, and packaging.¹⁻³ Irrespective of the application, the integrity of the adhesive is really important as this determines the integrity of the entire structure.

A crucial issue in the development of reliable adhesives for bonding in composite structures is a non-destructive detection of small-scale local damage such as cracks formed under fatigue loading. Self-healing of adhesive bonds has been identified as an important field right from the start of the development of self-healing materials⁴ and a promising route to extend the service lifetime of bonded joints in composite structures.⁵ Self-healing methods for composites via encapsulated liquid healing agents⁶⁻¹¹ and hollow fibres¹²⁻¹³ have been extensively explored and reported since 2001. The common shortcoming of both methods is that they can only heal once. A big step further was taken by the development of microvascular systems¹⁴⁻¹⁷ and compartmented fibres^{4,18-20} which are capable of healing more than once. However, these methods are both complex and costly and the microcapsules or fibres might interfere with the adhesion between the substrate and the adhesive.

To circumvent these issues, using adhesives having an intrinsic self-healing ability should be considered. To date only a limited number of studies have been conducted based on the intrinsic healing approach using thermoplastic particles,²¹ thermally reversible covalent bonds²² or ionomers.^{4, 23} These approaches have yielded modest success and required external stimuli in the form of heat and pressure to heal effectively. The need for local pressure during healing is not related to the healing process as such but stems from the need for reasonably

intimate contact across the two faces of the crack formed for healing to be successful as the natural crack filling ability of intrinsic self-healing polymer by default is minimal. This minimal crack filling ability puts rather stringent requirements on the type of test to be used to demonstrate self-healing of cracks in adhesively bonded joints in composite structures. Out of various specimen geometries available, the Central Cut Plies (CCP) specimen is an interesting candidate to test self-healing adhesive implementation due to several reasons. Firstly, it is known for producing a stable crack growth under fatigue loading and for the ease of measuring average crack growth rate using conventional clip-gauges.²⁴⁻²⁶ Secondly, by applying uniaxial tensile loading to the specimen along its length direction, a transverse crack arises from the adhesive-rich section between the cut plies and rapidly grows within the adhesive layer following the contour of the central cut plies, thereby forming four cracks.² In general, the damage takes place cohesively within the adhesive which is crucial for the self-healing to take place and for monitoring the damage/healing events. The bonding interface in a bonded joint is expected to be loaded mainly in shear (mode II). The crack opening or peel mode (mode I) is a detrimental secondary loading mode as it enlarges the separation distance between the crack faces and that should be minimized during the structural design process.^{2, 27} For the CCP test there is only a small tendency for the crack faces to increase their separation distance as the cracks continue to grow.

This study aims to explore the feasibility of using the intrinsic self-healing polyimide developed in Chapter 2 which heals at room temperature, as the thermoplastic adhesive thin film in an adhesively bonded joint made of commercial glass-fibre reinforced epoxy thermoset. A dedicated CCP specimen geometry is used to induce mode II fatigue cracks in the adhesive layers by applying external uniaxial tensile loading. In addition to the standard clip-gauge device a novel fibre optics local surface strain monitoring system is used to get more detailed insight into the localized ply-dependence of damage and healing events at the interface directly below the optical fibre. The work as presented in this chapter is to be regarded as a model study as the intrinsic mechanical properties of the polyimide polymer are too low to lead to the excellent fatigue properties as obtained when using aerospace-grade, epoxy-based adhesive joints for the same composite configuration.

6.2. Experimental

6.2.1. Materials

Commercial unidirectional glass fibre reinforced polymer (GFE) prepregs comprised of S2 glass fibres and epoxy resin and supplied by Cyttec were used in the construction of the composite samples. Our experimental self-healing polyetherimide (SH PEI) was used as the thin film adhesive. It was synthesized using fatty dimer diamine (Priamine™ 1075, Croda BV) and an aromatic dianhydride 4,4'-oxydiphthalic anhydride (ODPA) in stoichiometric ratio, named ODPA-D. The optimal healing temperature of this polymer has been found to be $T_{SH}=25^{\circ}\text{C}$ for through-cut razor blade induced damages and the time to reach apparent 100% strength recovery in tensile test was around 11 days. The results of the extensive characterization (properties, healing mechanism and behaviour) of the polymer have been reported in Chapter 2 and published articles.²⁸⁻³⁰

6.2.2. Specimen manufacturing

CCP specimens (see Figure 6.1.) were manufactured in a dust-free clean room with controlled temperature, $T=23^{\circ}\text{C}$. First the sets of 12 (cut) and 6 (continuous) plies of GFE prepregs were prepared separately by manual ply-by-ply layering. For the adhesive, a 25 wt.% SH PEI polymer-toluene solution was prepared and cast on top of the continuous plies with help of a roll bar. The surfaces were left to dry at room temperature for 2 hours, until tack-free. The cut GFE plies were laid on top of the dried SH PEI layer and finished with the other set of continuous GFE plies on top. During manufacturing the fibre direction was carefully aligned with the specimen's length. The central cut plies were placed in contact with each other, later forming a minor adhesive gap pocket. The layered composite was placed on a steel substrate together with a peel ply, release film, breather cloth and the vacuum bag. The edges were sealed with a bag sealant tape and the air was evacuated via a vacuum port. The assembled composite was then cured in the autoclave for 1 hour at 120°C and 5 bars. The cured plates were C-scanned to inspect the specimens' interior to confirm the absence of inhomogeneities and defects. After cutting the plate and polishing the edges, the obtained external sample dimensions were 305

mm length, 30 mm width and 3.60 ± 0.02 mm thickness. The adhesive layer thickness of 0.15 ± 0.01 mm was determined by electronic microscopy. Finally, paper tabs were glued to the specimen edges to provide a better specimen grip during the fatigue tests. Each side of the specimen was painted with a thin white brittle coating for easier visual inspection of the length of each delaminated zone.

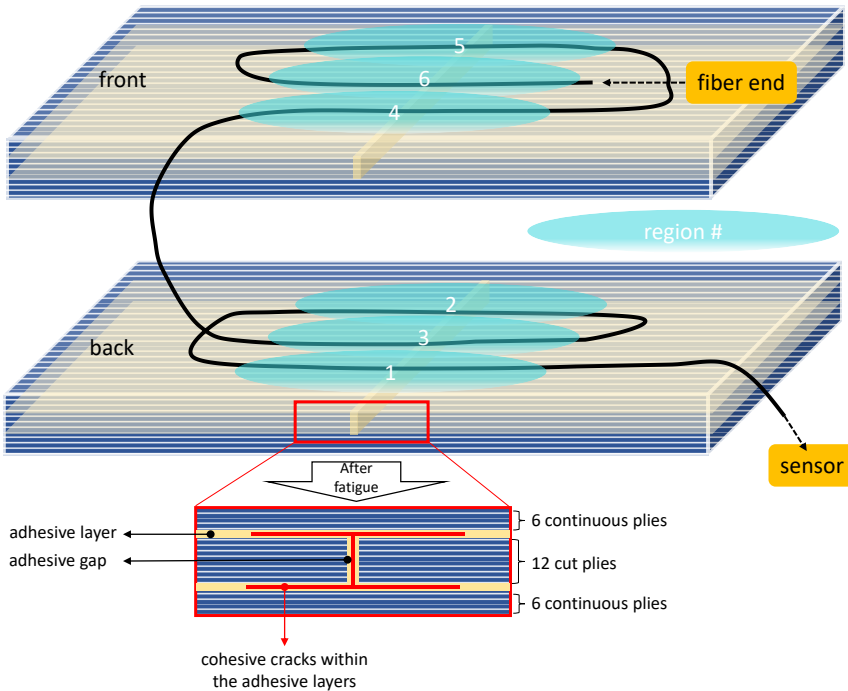


Figure 6.1. Positioning of the optical fibres along the front and back side of the specimen and the six marked regions of interest for the measurements. The bottom insert schematically indicates the cracks positions during the fatigue test.

6.2.3. Testing and monitoring the damage

The specimen was subjected to a multi-step fatigue test. Cyclic loading was applied with the MTS servo-hydraulic test frame of 100 kN capacity under load control. Based on preliminary experiments to determine the settings to yield a life time of over 200.000 cycles, the fatigue loading consisted of constant amplitude cycles with a maximum load of 3 kN, a load ratio (R-value) of 0.1 and 5 Hz test frequency. The transverse pre-crack (the crack positioned in the adhesive gap, see Figure 6.1.)

was formed under the same conditions, requiring around 24.800 cycles. After observing the transverse crack visually, the test was initiated to follow crack growth only. All reported numbers of cycles refer to the number of cycles in addition to the cycles used to create the starting condition. The strain data during the subsequent fatigue test was measured with an MTS 634.11 clip-gauge. Surface strain measurements were performed using a novel surface strain measurement technique: a surface mounted fibre optics distributed sensing system (Luna ODiSI-B) based on the Rayleigh Backscattering.³¹ The data were analysed following the procedure established by Ribeiro at al.² The optical fibre (with its six strain measuring regions) was placed on both the front and the back surfaces of the specimen using the path as shown in Figure 6.1. The regions where the optical fibre was glued to the specimen were the regions of interest to capture surface strain measurements, as shown in Figure 6.2. Every 3.000 cycles the test was paused at the maximum load for a couple of seconds to take the fibre optics measurements. After 72.000 and after 144.00 cycles the specimen was taken out of the test frame, laterally compressed with two paper clips ($F_{\text{compressive}}=115 \text{ N}$) and allowed to heal for 12h at $T_{\text{SH}}=25\pm 1^{\circ}\text{C}$. Preliminary experiments to conduct healing in-situ and under constant (maximum) load (in order to in-situ monitor crack closure during healing) showed too much creep straining and continued crack propagation and hence this condition was deemed unsuitable to achieve favourable for crack healing.

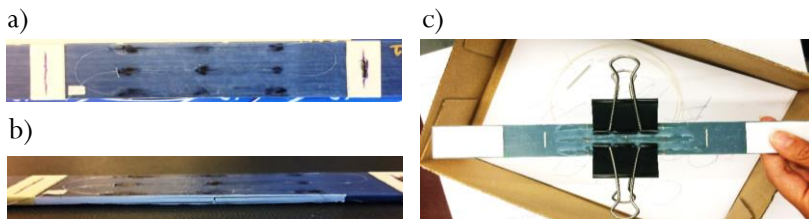


Figure 6.2. Specimen with the mounted optical fibre. a) top view, b) side view of the damaged specimen and c) top view of the specimen compressed with the paper clips during the healing stage. The points marked in black are the glued regions of interest for the measurements.

It is important to emphasize that the maximum load of 3 kN was chosen after several trials with identical other specimens aimed to establish the maximum load to get a decent fatigue life. Previous fatigue studies³² at Faculty of Aerospace Engineering with the same specimen geometry and ply components and using a

typical aerospace epoxy adhesive film (FM-94) required loads up to 30 kN. However, the self-healing polymer SH PEI used in this work is not as strong as FM-94, causing the need for a significant load reduction for its fatigue tests. 30 kN load, as used in epoxy bonded samples, would result in immediate and complete static failure within the SH PEI adhesive and no fatigue growth would be observed.

After dismantling the fatigued sample at the end of the 3rd block of fatigue loading, the damaged CCP specimen was split apart longitudinally to observe the fracture surfaces. Final sample splitting was done at room temperature. The (gold-sputtered) fracture surfaces were studied using Scanning Electron Microscopy (SEM).

6.3. Results and discussion

6.3.1. Clip-gauge measurements

The data collected from the clip-gauge during the fatigue test were used to calculate the transient stiffness values according to equation:

$$k = \frac{dP}{d\varepsilon^*} \quad (6.1.)$$

where k is stiffness, P is the applied tensile load and ε is the strain, and are plotted as function of the fatigue cycles in Figure 6.3a. For the purpose of a simplified analysis and a clearer visual representation, we made a corresponding scheme (Figure 6.3b) which emphasizes the points of interest marked by identifiers labelled A1-B3.

As can be seen from Figure 6.3, stiffness decays rapidly during the first 10.000 cycles and then it slows down, evidenced by the change in slope of the stiffness versus number of cycles curve. The rapid initial decay is attributed to the full development of the four cracks (see Figure 6.1) generated during the initial cycles for transverse crack formation. The steady state decay is attributed to the regular growth of the cracks. After the first fatigue block of un-interrupted loading cycles (the first 72.000 cycles), a total stiffness decrease ($y_{A0}-y_{A1}$) of ~ 3 kN/mm was obtained and the specimen was removed from the tensile tester and allowed to heal for 12h at 25°C. After the healing period and remounting the sample was subjected

to the second fatigue block. The first data point (A2) from the fatigue set 2 shows a higher stiffness value as compared to the last one from the fatigue set 1 (A1), before the healing took place. The increase translates into a 25% recovery of the sample stiffness, as calculated by equation 6.1. The healed specimen required around 7.000 fatigue cycles before reaching the stiffness value at the end of fatigue block 1, as evident from $\Delta x_A = x_{A2} - x_{A3}$ (see point A3). From then on, the stiffness continued to decrease more slowly until the end of the second block of fatigue cycles (data point B1). The rate of stiffness decrease in this part of the fatigue test was equal to the rate of stiffness decrease at the end of block 1. In order to demonstrate that healing for this intrinsic self-healing polymer is not restricted to a single healing event, after 144.000 cycles the dismantled specimen was healed for another 12h before being subjected to fatigue set 3. The initial stiffness recovery ($\approx 26\%$) after the second healing treatment (see point B2) was comparable to that after the first healing treatment ($\approx 25\%$). However, the number of cycles to reach the pre-healed value was reduced by half and the same stiffness value as at the end of fatigue block 2 (see point B3) was obtained after only 3.360 new cycles in block 3. During fatigue block 3, the sample stiffness continued to decrease but at a lower rate than in the first two loading blocks. The test was stopped after 216.000 cycles when the sample stiffness has dropped to 30 kN/mm (y_{c1}). After termination of the test the sample was removed from the tensile tester for final crack damage inspection. The average crack length can be calculated from the stiffness measurements (assuming all cracks to grow equally, and crack fronts to be perpendicular to the loading direction):^{2, 26}

$$da = \frac{1-\chi}{\chi} \left(\frac{EBtL_{gauge}}{2P} \right) d\varepsilon \quad (6.2.)$$

where a is the crack length (measured from the central crack initiating plane, see Figure 6.1), χ is the cut-ply ratio (number of cut plies over the total number of plies in the composite), B is the specimen width, t is the total thickness of the specimen and L_{gauge} is the gauge length. The calculated crack lengths during the entire fatigue test are shown in Figure 6.4a, while the Figure 6.4b shows the analysis scheme, analogous to the one in Figure 6.3b.

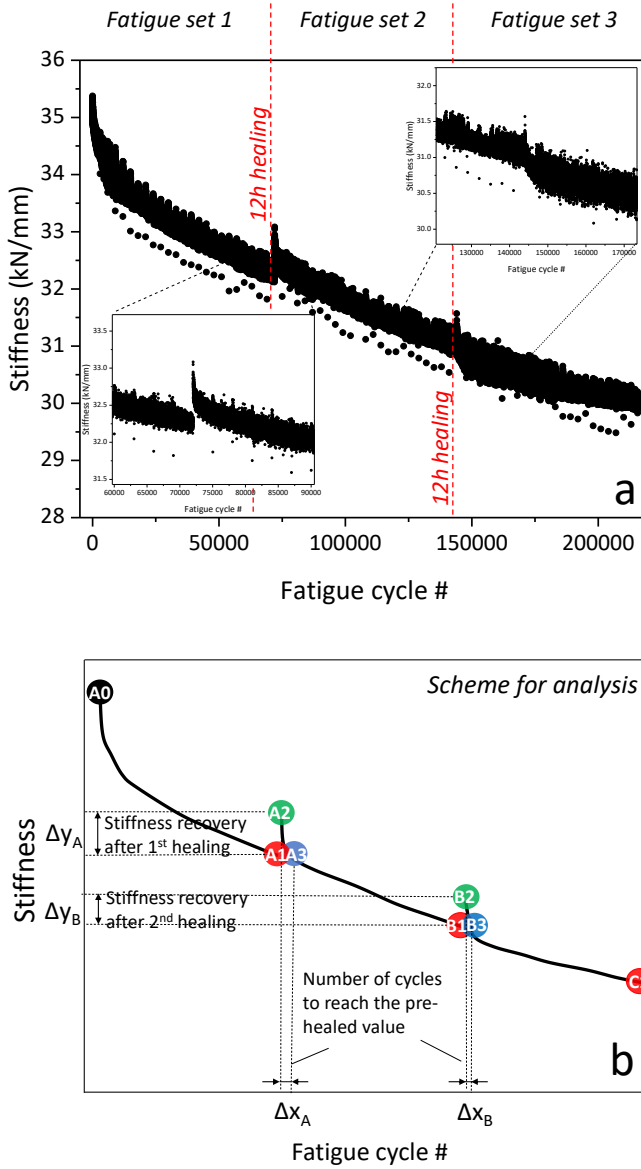


Figure 6.3. Stiffness as function of the fatigue cycles, calculated from the clip-gauge data (a) and corresponding scheme used for assigning the data points of interest for healing analysis (b). Inserts are showing the magnified regions of interest in-between the end of one fatigue set and the beginning of the next one after a healing period which is marked by red dashed line.

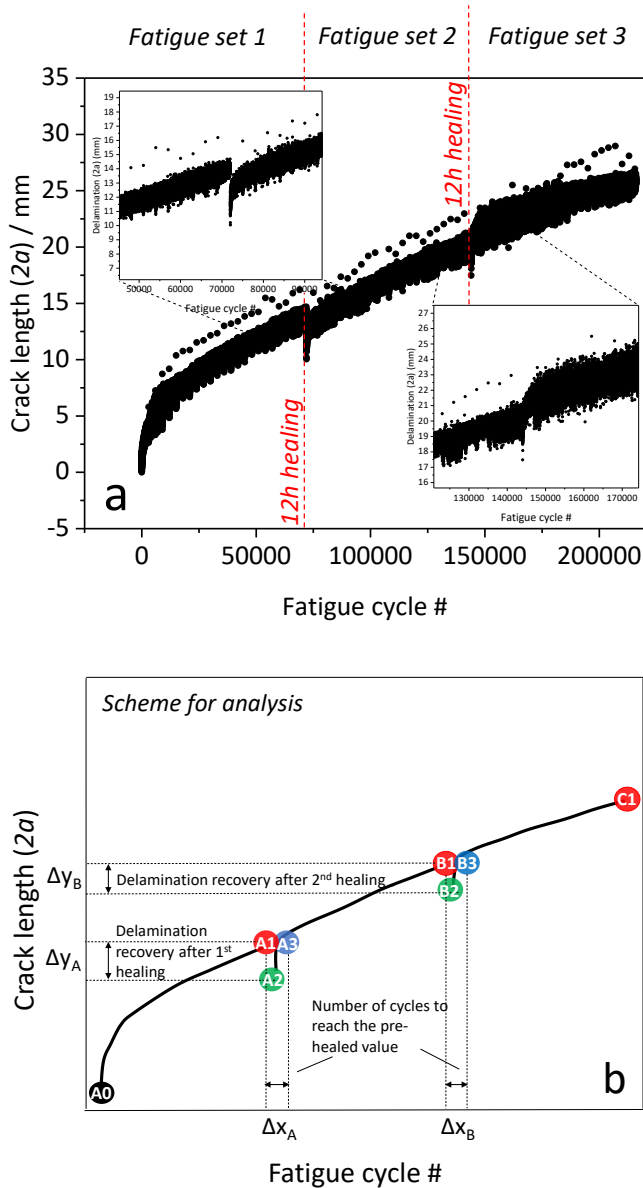


Figure 6.4. Crack length as a function of the number of fatigue cycles, calculated from the clip-gauge data (a) and corresponding scheme used for assigning the data points of interest for healing analysis (b). Insets are showing the magnified regions of interest in-between the end of one fatigue set and the beginning of the next one after a healing period which is marked by red dashed line.

The average crack length $2a$ after the fatigue set 1 was ~ 14 mm long (y_{A1}), point A1. The effective average crack length reduction (point A2) as a result of the first healing treatment was calculated to be 4 mm. In this calculation it was implicitly assumed that the crack resistance of the healed crack is equal to the crack resistance of the virgin material at that position. In case of partial recovery of the crack resistance in the healed material, the geometrical recovery of the crack length would be higher, i.e. the crack length would be reduced more than 4 mm (but the shear strength of the healed region would be lower than that of the material in the original state). As a result of the second healing treatment, the effective crack length reduced by 3 mm (point B2-point B1). At the end of the total fatigue test the effective crack length ($2a$) was calculated to be about 26 mm (y_{C1}).

6.3.2. Fibre-optics measurements

As stated in section 6.3.1, the conversion of the stiffness change in the average crack dimension is based on some important simplifications such as all four crack fronts growing equally and perpendicularly to the load direction, as illustrated in Figure 6.5a. However, such a situation is rather idealized, and the situation as shown in Figure 6.5b may be more realistic.



Figure 6.5. Schematic representation of the CCP specimen after fatigue-induced damages. a) Idealized, symmetric and straight crack evolution and b) realistic, unequal and non-straight cracks.

The strain profiles obtained from the optical fibre glued on both surfaces of the specimen (Figure 6.2.) were used to investigate individual crack growth at three

lateral positions on each side (front or back) of the sample. The method as developed by Ribeiro et al² was used to extract the point of crack (in the subsurface) from the local strain measurement. In the protocol used we could determine the total crack length ($2a$) (at a particular lateral position on the sample), but the signals did not always allow the determination of the local crack front with respect to the central vertical plane (in Figure 6.1) at which the cracks were initiated.

The cracks at the six positions over the CCP specimen, as calculated from the fibre-optics strain measurements, are plotted in Figure 6.6a. For each dataset a continuous growth of the apparent crack length (underneath that sensor segment) is observed. The local crack lengths vary as much as 10 mm, with region 4 generally showing the lowest value and region 6 the highest, indicative of skewed crack fronts. Although the optical test is supposed to measure only the effect of the crack just below it, we observe that cracks 1-5, 3-6 and 2-4 (see Figure 6.1) grow comparably to each other, probably because they are measuring regions on top of each other (see Figure 6.1), i.e. there is cross-talk in the signal or each crack influences the crack on the other crack plane, directly above or below it.

The occurrence of a drop in the crack length after each healing period as recorded in the clip-gauge data is evident from the fibre-optics data as well, thereby confirming that healing took place indeed. All datasets showed a significant reduction in the crack length upon healing, but the reduction in dataset 5 was significantly smaller, potentially indicative of some straightening of the crack fronts. The relative crack growth rate after the first healing treatment did not differ from that before the healing treatment (region 6 being the fastest and region 1 being amongst the slowest), with the exception of dataset 5, which showed a marked increase in local crack propagation rate all through the 2nd loading block. While the compliance-derived crack length data suggested a period of more rapid crack growth (the first 7.000 cycles after healing) after the first healing no such transition between a fast crack propagation through the healed material and a slower propagation when the crack propagated through pristine material is observed in any of the optical strain signals plotted in Figure 6.6a.

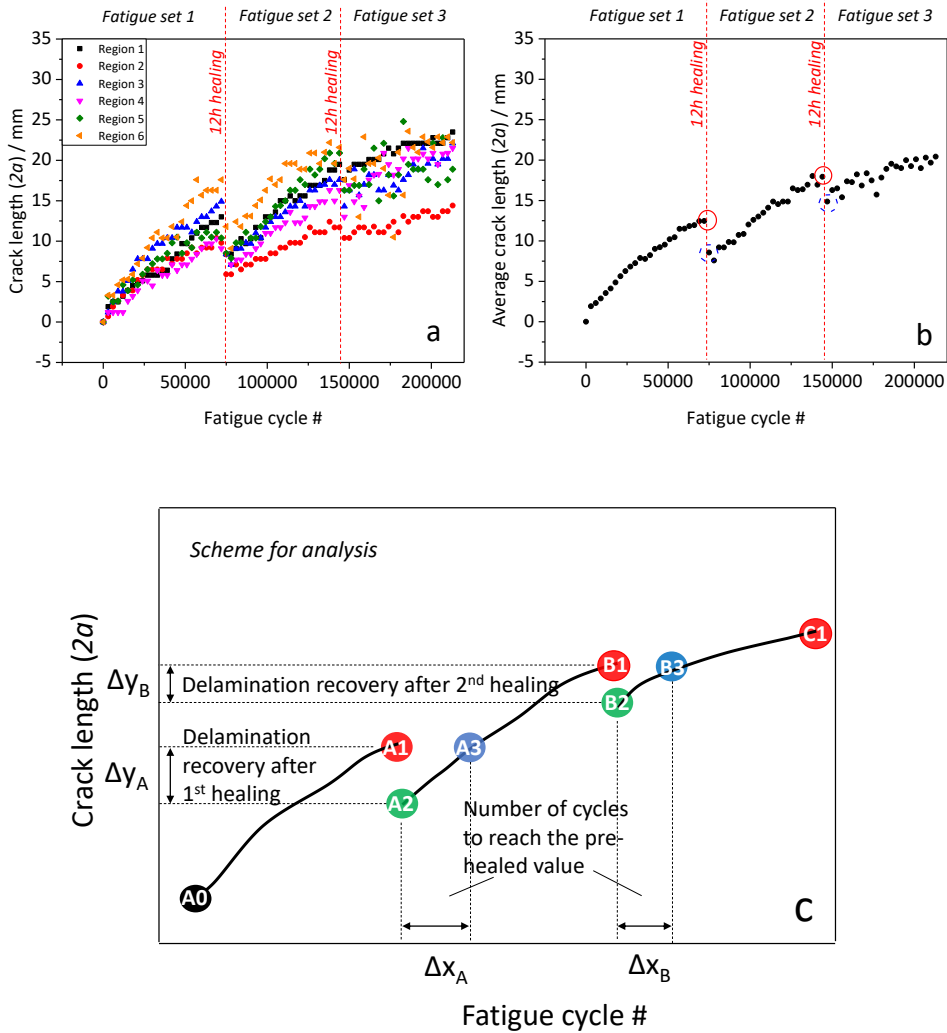


Figure 6.6. Crack length as function of the fatigue cycles, calculated from the fibre-optics data. a) Crack evolution per region individually; b) all six regions averaged and c) corresponding scheme used for assigning the data points of interest for healing analysis.

Comparison of the crack growth before and after the 2nd healing treatment showed that the healing treatment resulted once again in a (smaller) reduction in the apparent crack length and a further slowing down of the crack propagation rate, in accordance with the conclusions based on the clip-gauge measurements. The reduction of the apparent crack length is comparable for all datasets with the

exception of dataset 5. It is also observed that the strain measurements in block 3 for regions 4, 5 and 6 showed significantly more noise, but this occurrence of sudden noise could not be linked to a fracture mechanical origin and is therefore blamed on detector related damage during specimen handling in the second healing treatment.

6.3.3. Comparison of the two test methods

To compare the results obtained by two different methods, we calculated the averages of crack length curves obtained via fibre-optics (Figure 6.6b) and derived the corresponding scheme (Figure 6.6c).

Both the clip-gauge and the local optical strain methods demonstrate a comparable crack behaviour during the test which consisted of 3 periods of continuous fatigue loading and 2 periods of (ex-situ) healing. In all datasets there is a continuous growth of the (effective) cracks right from the onset of the fatigue loading (after the period of crack initiation (not reported here)). In the clip-gauge measurements after healing there is an initial period of faster crack growth followed by a period of a slower, constant crack growth rate. Taking the crack fronts to be equal and parallel, this behaviour would suggest the (shear) strength of healed material to be less than that of the original material. In the optical strain measurements, the crack growth rate seems to be rather constant, i.e. did not show this difference in growth rate when the crack tip was in the healed region or in the pristine region. However, in this test the local crack growth rates differed by a factor 2, which suggests a significant skewness of the crack fronts. The data of both tests suggest that the shear strength of the healed material is comparable if not equal to that of the undamaged material. Irrespective of the datasets and their interpretation, both datasets show that 1st healing treatment gives a significant reduction in the effective crack length (2a). The clip-gauge length measurements suggest that the (average) crack length reduction is of the order of 3.7 mm, while in the optical strain measurement yield an average crack length reduction of 4.8 mm, with crack length reductions for the individual datasets ranging from 3.9 to 5.5 mm. The clip-gauge data suggests that it takes about 8.000 cycles before the sample stiffness has returned to the value just before the healing treatment. However, according to the optical method about

30.000 cycles are required to bring the average crack length down to the pre-healed value. This value seems to apply to each of the 6 individual datasets which suggest that the healing was comparable for each of the 6 regions probed.

Both test methods suggest that the amount of healing in the second healing treatment is less than the first healing treatment, as the recovery of stiffness or the reduction in crack length is less than in the first healing treatment. Furthermore, for both test methods the number of new loading cycles required to restore the pre-healing damage state (3.000 and 15.000 for clip gauge and optical measurements, respectively) is less than for the first healing treatment. While both data analysis methods ultimately rely on the load transfer under shear, the results would be similarly affected by restoration of both the shear stiffness in the healed regions and the shear strength. Hence, there is no obvious explanation for the difference in number of cycles required to return to the damage state before healing. Detailed FEM calculations with (assumed) local values for shear strength and shear stiffness after healing might resolve the quantitative discrepancy between both testing methods but, given the complex viscoelastic and healing behaviour of the SH PEI adhesive used, a large modelling effort would be required which was outside the scope of this thesis.

6.3.4. Fracture surfaces

To study the damage evolution in the delaminated and healed zones, at the end of the test the damaged specimen was prized open longitudinally at room temperature, with the final crack propagation in the same direction to the crack propagation direction under fatigue loading. The SEM images of both the zone prized open in mode I (the final tear-down) and the zone fractured in shear mode II (the actual fatigue test) can be found in Figure 6.7, showing the typical features of the fracture mode I (left) and II (right).³²⁻³³ The mode II shows peculiar structures, commonly called hackles or cusps which are formed upon reverse repeated shear. The SEM images make it clear that the fracture took place within the SH PEI bond layer and that the fracture was cohesive. The observations of the surface profile in the fatigue loaded part of the sample showed a relatively smooth fracture surface with a fine profile which suggests that the two fracture surfaces

stayed in relatively close contact and that there must have been many local points of contact from which the crack closing process could have started.

Regrettably, in none of the fracture surfaces studied the crack front at the end of the fatigue testing could be detected with any spatial precision. Furthermore, also the two regions which must have undergone a damage, healing and re-damage process could not be distinguished. While the absence of a clear crack front at the end of the test was very disappointing (and could be blamed on the final tear-down being done at room temperature, rather than at liquid nitrogen temperature), the fact that the damaged/healed/re-damaged regions in the fatigued region could not be detected either could be regarded as an encouraging sign of the healing process being quite capable of restoring the material to its original state.

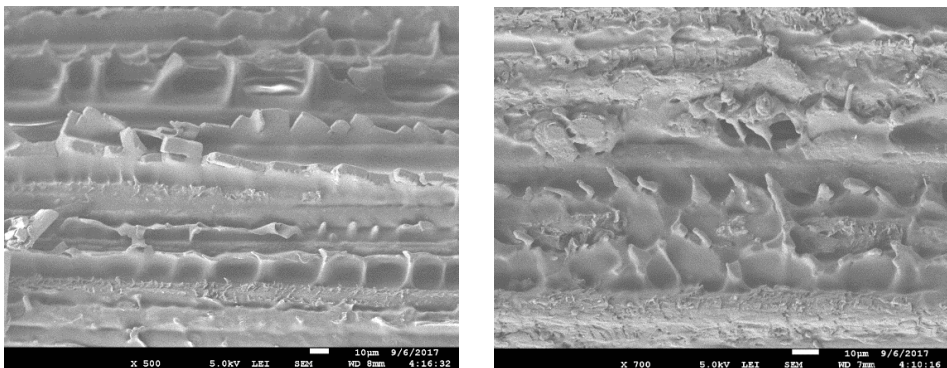


Figure 6.7. SEM fractography of the damaged interfaces after the test. The image on the left side was taken further away from the fatigue-induced crack. The image on the right side was taken at the fatigue-induced damage plane. Scale bar is 10 μm .

6.4. Conclusions

This work presents a first attempt to use an autonomous intrinsic healing PEI polymer to replace a thermoset adhesive layer in an adhesively bonded composite fabricated from commercial prepregs. A Central Cut Ply geometry was utilized to induce fatigue mode II cracks cohesively in the adhesive layer in order to maximize the impact of any healing if it was to take place. Two methods were employed to evaluate the stiffness and crack evolution and healing quantification; the common clip-gauge method and the novel fibre-optics method. The clip-gauge method allowed calculation of the average crack behaviour over the whole specimen, while fibre-optics were expected to provide an insight into the individual regional crack evolution. Both methods clearly showed that substantial healing took place during a (load-free) 12-hour healing treatment at room temperature. As shown by the fibre-optics results, the cracks were not propagating equally nor symmetrically over the whole specimen. By comparing the two methods, a good yet only qualitative agreement is obtained as for the reduction in absolute crack lengths. However, the number of fatigue cycles to reach the pre-healed values differed significantly in a manner which could not be explained without further research.

References

1. Banea, M.; da Silva, L., Adhesively Bonded Joints in Composite Materials: An Overview. *Proceedings of the Institution of Mechanical Engineers, Part L: Journal of Materials: Design and Applications* **2009**, *223* (1), 1-18.
2. Ribeiro, F.; Martinez, M.; Rans, C., Evaluation of Mode II Fatigue Disbonding Using Central Cut Plies Specimen and Distributed Strain Sensing Technology. *The Journal of Adhesion* **2018**, 1-27.
3. Li, G.; Ji, G.; Zhenyu, O., Adhesively Bonded Healable Composite Joint. *International Journal of Adhesion and Adhesives* **2012**, *35*, 59-67.
4. Post, W. Self-healing Polymer Composites. PhD Thesis, Delft University of Technology, Netherlands, 2017.
5. Banea, M.; da Silva, L.; Campilho, R.; Sato, C., Smart Adhesive Joints: An Overview of Recent Developments. *The Journal of Adhesion* **2014**, *90* (1), 16-40.
6. White, S. R.; Sottos, N. R.; Geubelle, P. H.; Moore, J. S.; Kessler, M. R.; Sriram, S. R.; Brown, E. N.; Viswanathan, S., Autonomic Healing of Polymer Composites. *Nature* **2001**, *409*, 794.
7. Mcllroy, D. A.; Blaiszik, B. J.; Caruso, M. M.; White, S. R.; Moore, J. S.; Sottos, N. R., Microencapsulation of a Reactive Liquid-Phase Amine for Self-Healing Epoxy Composites. *Macromolecules* **2010**, *43* (4), 1855-1859.
8. Hillewaere, X.; Du Prez, F., Fifteen Chemistries for Autonomous External Self-Healing Polymers and Composites. *Progress in Polymer Science* **2015**, *49-50*, 121-153.
9. Hillewaere, X.; Teixeira, R.; Nguyen, L.-T.; Ramos, J. A.; Rahier, H.; Du Prez, F., Autonomous Self-Healing of Epoxy Thermosets with Thiol-Isocyanate Chemistry. *Advanced Functional Materials* **2014**, *24* (35), 5575-5583.
10. Neuser, S.; Chen, P. W.; Studart, A. R.; Michaud, V., Fracture Toughness Healing in Epoxy Containing Both Epoxy and Amine Loaded Capsules. *Advanced Engineering Materials* **2014**, *16* (5), 581-587.
11. Mookhoek, S. D.; Blaiszik, B. J.; Fischer, H. R.; Sottos, N. R.; White, S. R.; van der Zwaag, S., Peripherally Decorated Binary Microcapsules Containing Two Liquids. *Journal of Materials Chemistry* **2008**, *18* (44), 5390-5394.
12. Bley, S. M.; Loader, C. B.; Hawyes, V. J.; Humberstone, L.; Curtis, P. T., A Smart Repair System for Polymer Matrix Composites. *Composites Part A: Applied Science and Manufacturing* **2001**, *32* (12), 1767-1776.
13. Pang, J.; Bond, I. P., A Hollow Fibre Reinforced Polymer Composite Encompassing Self-Healing and Enhanced Damage Visibility. *Composites Science and Technology* **2005**, *65* (11), 1791-1799.

14. Toohey, K. S.; Sottos, N. R.; Lewis, J. A.; Moore, J. S.; White, S. R., Self-Healing Materials with Microvascular Networks. *Nature Materials* **2007**, *6*, 581.
15. Toohey, K. S.; Hansen, C. J.; Lewis, J. A.; White, S. R.; Sottos, N. R., Delivery of Two-Part Self-Healing Chemistry via Microvascular Networks. *Advanced Functional Materials* **2009**, *19* (9), 1399-1405.
16. Trask, R. S.; Bond, I. P., Bioinspired Engineering Study of Plantae Vasculues for Self-Healing Composite Structures. *Journal of The Royal Society Interface* **2010**, *7* (47), 921-931.
17. Luterbacher, R.; Trask, R. S.; Bond, I. P., Static and Fatigue Tensile Properties of Cross-Ply Laminates Containing Vasculues for Self-Healing Applications. *Smart Materials and Structures* **2016**, *25* (1), 015003.
18. Mookhoek, S. D.; Fischer, H. R.; van der Zwaag, S., Alginate Fibres Containing Discrete Liquid Filled Vacuoles for Controlled Delivery of Healing Agents in Fibre Reinforced Composites. *Composites Part A: Applied Science and Manufacturing* **2012**, *43* (12), 2176-2182.
19. Prajer, M.; Wu, X.; Garcia, S. J.; van der Zwaag, S., Direct and Indirect Observation of Multiple Local Healing Events in Successively Loaded Fibre Reinforced Polymer Model Composites Using Healing Agent-Filled Compartmented Fibres. *Composites Science and Technology* **2015**, *106*, 127-133.
20. Post, W.; Jeoffroy, E.; Garcia, S. J.; van der Zwaag, S., Self-Healing Glass Fiber Reinforced Polymer Composites Based on Montmorillonite Reinforced Compartmented Alginate Fibers. *Polymer Composites*.
21. Zako, M.; Takano, N., Intelligent Material Systems Using Epoxy Particles to Repair Microcracks and Delamination Damage in GFRP. *Journal of Intelligent Material Systems and Structures* **1999**, *10* (10), 836-841.
22. Liu, Y.-L.; Chen, Y.-W., Thermally Reversible Cross-Linked Polyamides with High Toughness and Self-Repairing Ability from Maleimide- and Furan-Functionalized Aromatic Polyamides. *Macromolecular Chemistry and Physics* **2007**, *208* (2), 224-232.
23. Varley, R. J.; van der Zwaag, S., Towards an Understanding of Thermally Activated Self-Healing of an Ionomer System during Ballistic Penetration. *Acta Materialia* **2008**, *56* (19), 5737-5750.
24. Wisnom, M.; Jones, M.; Cui, W., Delamination in Composites with Terminating Internal Plies Under Tension Fatigue Loading. In *Composite Materials: Fatigue and Fracture*, Martin, R., Ed. ASTM International: West Conshohocken, PA, 1995; Vol. 5, pp 486-508.
25. Allegri, G., A New Semi-Empirical Model for Stress Ratio Effect on Mode II Fatigue Delamination Growth. *Composites Part A: Applied Science and Manufacturing* **2011**, *42* (7), 733.

26. Rans, C.; Atkinson, J.; Li, C., On the Onset of the Asymptotic Stable Fracture Region in the Mode II Fatigue Delamination Growth Behaviour of Composites. *Journal of Composite Materials* **2015**, *49* (6), 685-697.
27. Hart-Smith, L. J. *Adhesive-Bonded Double-Lap Joints*; Contract Rep CR-2218; NASA Hampton, Virginia, 1974.
28. Susa, A.; Bose, R. K.; Grande, A. M.; van Der Zwaag, S.; Garcia, S. J., Effect of the Dianhydride/Branched Diamine Ratio on the Architecture and Room Temperature Healing Behavior of Polyetherimides. *ACS Applied Materials and Interfaces* **2016**, *8* (49), 34068-34079.
29. van der Kooij, H. M.; Susa, A.; García, S. J.; van der Zwaag, S.; Sprakel, J., Imaging the Molecular Motions of Autonomous Repair in a Self-Healing Polymer. *Advanced Materials* **2017**, *29* (26).
30. Susa, A.; Bijleveld, J.; Hernandez Santana, M.; Garcia, S. J., Understanding the Effect of the Dianhydride Structure on the Properties of Semiaromatic Polyimides Containing a Biobased Fatty Diamine. *ACS Sustainable Chemistry and Engineering* **2018**, *6* (1), 668-678.
31. Inc, L. I. <http://lunainc.com/product/sensing-solutions/odisi/> (accessed 24 January 2018).
32. Bürger, D.; Rans, C. D.; Benedictus, R., Influence of Fabric Carrier on the Fatigue Disbond Behavior of Metal-to-Metal Bonded Interfaces. *The Journal of Adhesion* **2014**, *90* (5-6), 482-495.
33. Tay, T. E., Characterization and Analysis of Delamination Fracture in Composites: An Overview of Developments from 1990 to 2001. *Applied Mechanics Reviews* **2003**, *56* (1), 1-32.

Summary

Covalent reversible chemistries give rise to polymers with reasonable mechanical properties yet require external stimuli to heal. Oppositely, supramolecular systems can heal autonomously, but their properties are still far away from most of those set by application requirements. Both downsides need to be addressed before intrinsic healing polymers can emerge out of academic literature and be found in daily life products.

The aims of the research described in this thesis are: i) to develop intrinsic self-healing polymers with mechanical properties that significantly exceed those currently reported in the academic literature but can nevertheless repair cracks at room temperature; ii) to contribute to a better understanding of the importance of the polymer chain architecture on the physical processes during the repair of mechanical damage.

Chapter 2 describes the synthesis and exhaustive characterization of the room temperature healing thermoplastic elastomer polyetherimides based on alternating hard and soft constitutive blocks. The soft block, an aliphatic bio-based dimer diamine, bears dangling side chains and the hard block is a commercial aromatic dianhydride. This chapter reports the changes in molecular architecture and healing characteristics as a consequence of changes in the soft-hard block ratio. Two of the polymers synthesized show remarkable healing at room temperature combined with mechanical properties close to a level relevant to applications. However, a high excess of the soft block fraction resulted in a disappearance of the macroscopic healing due to covalent cross-linking reactions. On the other hand, a hard segments predominance led to a decrease of the room temperature healing kinetics due to restricted molecular mobility.

A dedicated macroscopic healing kinetics study combined with rheology for both branched polymers and a linear reference material provided insight into the actual healing mechanism and kinetics. The proposed healing mechanism for this type of polymer is a two-step process with a fast first step in which Van der Waals interactions between dangling aliphatic chains form a 2D interface, followed by a slower second step in which chain inter-diffusion develops a 3D interphase zone.

Given a sufficient equilibration time, the interphase disappears, resulting in the full restoration of polymer properties manifested by specimens breaking upon repeated testing at other locations than the healed spot. Although branched dimer building blocks have been used before in self-healing polymers, this is the first time, to the best of our knowledge, that the healing was obtained without covalent or supramolecular interactions (hydrogen, ionic, etc.) other than the weak omnipresent Van der Waals intermolecular forces.

Chapter 3 reveals the molecular repair in a self-healing polymer visualized by the Laser Speckle Interferometry technique recently developed at Wageningen University. It demonstrates quantitative imaging of molecular-scale dynamics with a high spatiotemporal resolution. It is observed that the process of damage results in breaking of cohesive interactions and viscoelastic deformations. The damage heals autonomously via: (i) fast elastic recovery of the material which brings the damaged surfaces into contact, allowing (ii) Van der Waals interactions to restore cohesion across the crack, which involves (iii) a zipper-like motion around the retracting crack tip and finally (not observable in these Laser Speckle Interferometry measurements) culminating in (iv) polymer chain interdiffusion across the interface and restoration of the material integrity. Strikingly, the local deformations involved in the crack closing process occur at a same frequency found in the linear rheological experiments in *Chapter 1*.

Due to the simplicity and non-invasive nature of the method, Laser Speckle Interferometry shows high extended potential to study self-healing in other materials or polymers with different non-linear deformation and recovery mechanics. Finally, illuminating and disentangling the convolution of diverse dynamics inherent to highly localized mechanics may significantly contribute to valuable input for tailoring the design of high-performing self-healing polymers and other materials in general.

In *Chapter 2* we investigated the role of the soft block on the healing and properties of these polyimides, yet we have not studied the role of the hard block. Hence, *Chapter 4* reports a series of polyimides systematically varying in their aromatic dianhydride structure. The results show that the dianhydrides comprising a flexible ether spacer, as well as the one with a rigid and bulky hexafluoroisopropylidene spacer, yielded fully amorphous polymers showing good healing.

On the other hand, a more planar dianhydride with no spacer yielded a semi-crystalline polymer, which has a constrained segmental relaxation. Their fluorescence spectra and normalized dielectric loss show that these polyimides can form intermolecular charge transfer complexes, whose extent depends on the dianhydride electronic properties. It is further noticed that rheological data show that these polymers have a high $\tan\delta$ values over a broad range of near-room temperatures, which marks their potential in applications where high damping properties at low frequencies at ambient temperatures are required (noise or vibration insulating materials, shock absorbers and sealants).

Chapter 5 further explores the dynamics of the polymers developed in *Chapter 4* on several scales: macro-, micro- and molecular scale, in relation to their healing kinetics. The results shed light on the importance of the molecular architecture in obtaining tuneable stepwise healing dynamics. Following the two-step kinetics of the healing process ($R1$ and $R2$), we disentangle and quantify the extent of mechanical strength recovery in each of the healing stages.

The relaxation frequency of the branches in the dissipative regime is correlated to the mechanical kinetic parameter $R1$, representing the initial recovery of the mechanical properties given by fast Van der Waals interactions. Analogously, the terminal flow region indicates the beginning of the second healing stage related to slow interdiffusion across the interface with slower kinetics and therefore is related to the macroscopic healing kinetics $R2$. Subsequently, we correlate the macro- and microscale kinetic parameters to their molecular origin via the experimentally determined kinetic parameter $T2$ (spin-spin relaxation time) obtained by solid-state nuclear magnetic resonance experiments.

It is found that the second healing step slows down as the rigidity of the hard block increases. Moreover, if the hard block is both rigid and planar, healing is prohibited due to crystallization which disables both the local mobility crucial for the first healing step and the later inter-diffusion step. It is found that a combination of nonplanar and flexible aromatic segments with a high aliphatic branching density make for a successful recipe to develop strong low-temperature healing polyimides.

Chapter 6 presents a first attempt to use the autonomous intrinsic healing polyimide to replace a thermoset adhesive layer in an adhesively bonded composite based on commercial glass fibre prepregs. Fatigue mode II damages are developed cohesively in the adhesive layer, by using a dedicated Central Cut Ply specimen geometry. The crack propagation and the crack length reduction upon healing are evaluated by two different techniques: the conventional clip-gauge method to determine average crack length values over the whole specimen and a novel fibre-optics for localized monitoring of the crack growth and its healing. The fibre-optics results indicate that the four cracks in the adhesive layer are not propagating equally nor symmetrically over the whole specimen. Both methods show good qualitative agreement for the absolute crack lengths. However, the number of fatigue cycles to reach the pre-healed values differs significantly in a manner which could not be explained without further research. Nevertheless, both methods confirm that substantial and repetitive healing took place during a load-free 12-hour resting period at room temperature.

Samenvatting

Covalente reversibele bindingen resulteren in polymeren met redelijke mechanische eigenschappen, maar deze polymeren hebben externe stimuli nodig om scheuren in het materiaal autonoom te kunnen herstellen. Supramoleculaire polymeersystemen daarentegen kunnen dergelijke schade zelfstandig en zonder externe interventie herstellen, maar hebben mechanische eigenschappen die ver onder de gangbare vereisten liggen. Beide tekortkomingen moeten opgelost worden voordat intrinsiek ‘zelfherstellende’ polymeren de stap maken van wetenschappelijk interessante systemen naar polymeren met een praktisch nut. Het doel van het onderzoek beschreven in dit proefschrift is tweevoudig. Enerzijds om bij te dragen aan de ontwikkeling van volledig intrinsiek zelfherstellende polymeren met mechanische eigenschappen die de nu gerapporteerde waarden ver overschrijden maar die desondanks bij kamertemperatuur scheuren kunnen herstellen. Anderzijds om bij te dragen aan het betere begrip van het belang van de ketenarchitectuur op de fysische processen tijdens het herstel van mechanische schade.

Hoofdstuk 2 beschrijft de synthese en de uitgebreide karakterisering van polyetherimide elastomeren die scheuren autonoom en bij kamertemperatuur kunnen herstellen. Deze imides bevatten opeenvolgende harde en zachte segmenten. Het zachte segment, een uit organische grondstoffen verkregen alifatisch diamine dimeer, bevat flexibele zijgroepen, terwijl het harde segment bestaat uit een commercieel verkrijgbaar aromatisch dianhydride. Dit hoofdstuk beschrijft de veranderingen in de moleculaire architectuur en het zelfherstellende gedrag als functie van de verhouding tussen de harde en zachte segmenten. Twee van de ontwikkelde polymeren vertonen een opmerkelijk goed zelfherstellend vermogen bij kamertemperatuur en dat in combinatie met eigenschappen die in de buurt komen van wat nodig is voor daadwerkelijke toepassingen. Een overmaat van zachte segmenten leidt tot netwerkvorming en een verlies aan zelfherstellend vermogen. Een overmaat aan harde segmenten leidt tot een afname in de snelheid van het herstel van eigenschappen als gevolg van een afname in moleculaire beweeglijkheid. De combinatie van herstelproeven en bijpassende reologische metingen aan deze polymeren en een lineair referentie polymeer heeft meer inzicht gegeven in het moleculaire mechanisme van het herstel en de kinetiek ervan. We

stellen vast dat het herstelproces voor dit type polymeer bestaat uit twee stappen: een snelle eerste stap waarin de Vanderwaalskrachten tussen de alifatische zijketens een 2D grensvlak opbouwen, gevolgd door een langzamere tweede stap waarin door moleculaire diffusie een 3D tussenlaag ontstaat. Bij een voldoende lange hersteltijd verdwijnt deze tussenlaag weer en keert het materiaal ook lokaal terug naar zijn oorspronkelijke toestand en set van eigenschappen. Dit laatste is te concluderen uit het feit dat de herstelde proefstukken op een andere plaats zijn gebroken dan op de plek van de oorspronkelijke scheur. Vertakte dimere bouwstenen zijn eerder gebruikt voor de synthese van zelfherstellend polymeren, maar dit is de eerste keer voor zover wij weten dat zelfherstel verkregen werd zonder covalente of supramoleculaire interacties anders dan de altijd aanwezige Vanderwaalsinteractiekrachten.

Hoofdstuk 3 laat de moleculaire verplaatsingen zien die plaatvinden rond een zich herstellende scheur in het stoichiometrische PEI van *Hoofdstuk 2*. Hiertoe werd een nieuwe, aan de Universiteit van Wageningen ontwikkelde, Laser Speckle Interferometrische (LSI) techniek met bijbehorend gegevensverwerkingsalgoritme gebruikt. De techniek laat moleculaire verplaatsingen zien met een hoge plaats- en tijdsresolutie. De waarnemingen laten zien dat scheurvorming gepaard gaat met het verbreken van lokale interacties en viscoelastische vervormingen. Het herstel van de schade geschiedt vervolgens via i) het langzaam vloeien van het materiaal waardoor de breukvlakken weer met elkaar in contact komen en waardoor ii) Vanderwaalskrachten de cohesie over het grensvlak herstellen, waardoor iii) er een terugtrekkende beweging van de scheurtip optreedt die te vergelijken is met het sluiten van een rits. De laatste stap van het herstelproces (die niet met de LSI techniek te volgen was) is iv) interdiffusie en herstel van de structuur. Het is opmerkelijk dat de tijdsconstante van de processen bij het sluiten van de scheur goed overeenkomen met de tijdsconstanten in de reologische proeven beschreven in *Hoofdstuk 1*. Vanwege zijn relatieve eenvoud en het niet-invasieve karakter biedt deze LSI methode ongekende mogelijkheden om de diverse gelijktijdig optredende processen te scheiden en verder in detail te onderzoeken en zo input te geven aan het ontwerpproces van nieuwe zelfherstellende polymeren en andere materialen.

In *Hoofdstuk 2* is de rol van het zachte segment in de PEI op de eigenschappen en het herstelgedrag onderzocht en werd het harde segment constant gehouden. Vandaar dat in *Hoofdstuk 4* een serie polyimides beschreven wordt die verschillen

in de structuur van het harde aromatische dianhydride segment. De resultaten laten zien dat de anhydriden met een flexibele ether brug of met een rigide en grote hexafluoroisopropylidene brug een aantrekkelijk zelfherstellend gedrag vertoonden. Daarentegen resulteerde een PEI met een vlakke dianhydride zonder brug in een semi-kristallijn polymeer met bijbehorende gereduceerde moleculaire beweeglijkheid. Dit polymeer had derhalve een beperkt zelfherstellend vermogen. Fluorescentie en di-elektrische metingen lieten zien dat in deze polyimides intermoleculaire ladingsoverdracht ('charge transfer') optreedt waarvan de sterkte afhankelijk is van de elektronische eigenschappen van het dianhydride. Tevens laten reologische metingen zien dat deze polymeren een hoge maximale verliesfactor $\tan\delta$ hebben wat aangeeft dat deze materialen in principe goede dempingseigenschappen bij kamertemperatuur hebben en toepassing kunnen vinden in applicaties zoals geluidsabsorptie, mechanische demping en elastische verbindingen.

In *Hoofdstuk 5* wordt het effect van de macro-, micro- en moleculaire dynamica op het herstelgedrag van de in *Hoofdstuk 4* gepresenteerde polymeren beschreven. De resultaten werpen nieuw licht op het belang van de architectuur van het molecuul in het verkrijgen van het gewenste tweetraps herstelproces. De relaxatiefrequenties van de zijketens in de zogenaamde dissipatie-fase bleken te correleren met de kinetiek van dat deel van het herstel dat toegeschreven is aan de Vanderwaalsinteracties. Soortgelijk bleek de eindstroming ('terminal flow') tijdsconstante goed te correleren met de langzame interdiffusie en het daaraan toegeschreven deel van het herstelproces. Beide tijdsconstants werden gecorreleerd aan de kinetische parameter T_2 (spin-spin interactie) uit vaste-stof NMR metingen. Gevonden werd dat de tweede stap in het herstelproces trager verloopt als de stijfheid van het harde segment toeneemt. Als het harde blok heel stijf en ook nog vlak is, wordt kristallisatie bevorderd waardoor zowel de eerste als de tweede herstelstap effectief geblokkeerd wordt. Er is gevonden dat de combinatie van flexibele en niet-vlakke aromatische segmenten en een passende fractie alifatisch vertakte segmenten de sleutel is tot de ontwikkeling van imides die bij kamertemperatuur zelfherstellend zijn en toch goede mechanische eigenschappen vertonen.

Hoofdstuk 6 beschrijft de eerste pogingen om een film van een bij kamertemperatuur zelfherstellend PEI te gebruiken als lijm tussen commerciële glas vezel-epoxy laminaten om zo een composiet te verkrijgen. Een speciale ‘Central Cut Ply’ preparaat configuratie was gebruikt om Mode II vermoeiingsscheuren te genereren. Twee verschillende meetmethoden voor het meten van de scheurgroei en het scheurherstel werden gebruikt: i) de gangbare methode gebaseerd op het gebruik van een extensometer waarbij een gemiddelde scheurlengte voor de vier gevormde scheuren berekend kan worden uit het verlies van preparaatstijfheid en ii) een nieuwe vezel-optische methode waarmee in beginsel de lokale positie van elk einde van elke scheur op een drietal plaatsen over de breedte van het preparaat bepaald kan worden. De vezel-optische methode liet zien dat de scheuren elk een eigen gedrag vertoonden en zeker niet loodrecht op de belastingrichting stonden. Beide methoden toonden een vergelijkbare reductie in de scheurlengte als gevolg van de twee tussentijds toegepaste herstelbehandelingen. Daarentegen gaven beide methoden een sterk verschillend aantal belastingscycli aan wat nodig was om de scheurlengte-na-herstel terug te brengen naar het niveau van voor de herstelbehandeling. Desalniettemin lieten beide methoden onomstotelijk zien dat er meermalen significant lokaal schadeherstel op kan treden dankzij een onbelaste herstelperiode van 12 uur bij kamertemperatuur.

Acknowledgements

This thesis is my child and I love it just the way it is (amazing), but it took a village to raise it and let it run freely into the curious hands of You who read it. That special village embodies people that all have their different ways of being there for you. Some push you to the critical limits, some motivate you gently, some comfort you, some admire you, some make you cry, and some make you laugh. Well now you know what it takes to write a book like this one and not go (completely) crazy.

At the beginning, I would like to thank my promotor Sybrand van der Zwaag for welcoming me into the world of science by giving me the opportunity to pursue my PhD at Novel Aerospace Materials (NovAM) group. Your condition of uncompromising excellence has brought my knowledge, experience and this thesis to the heights that make me truly proud and ready for the new title. I owe you tremendous gratitude for your incredible effort, drive and energy to get me to the finish line, especially during the final stages of thesis writing despite your all-over-the-globe lifestyle. Thank you also for creating the uniquely fun, social and family-like environment that NovAM is famous for.

Many thanks to Santiago García, my daily supervisor. Your optimism, energy and passion for innovation are contagious and uplifting, often crucial for moving forward after disappointments. Thank you for showing me that one can learn more from a failed experiment than from a successful one. Thank you for teaching me how to collaborate, present my work, overcome a fear of inadequacy and never give up. And finally, thank you for knowing how to relax with a lot of laugh and dance, making all our conference experiences unforgettable.

I am thankful to the IOP program Self-Healing Materials of the Dutch Ministry of Economic Affairs for funding this project, and also Annette Steggerda and Danielle van Loon for organizing all the famous IOP symposia and summer schools, and relaxing laughing sessions during our many dinners and trips. I was very lucky to have had two industrial partners in the project. I would like to express my gratitude to Angela Smits, Hans Ridderikhoff and Remco van Triet from Croda, for their continuous involvement in the project. Angela, thank you for all your scientific input and support during our progress meetings. I would also like to thank Ricardo and Berend from Tata Steel for their interest in exploring the application potential

of self-healing polyimides. Many thanks to José Flores, a former partner at Tata Steel, who later became my dear friend, for abundant optimism, encouragement, jokes and funny emails, as well as for showing continued interest in my work.

I had a privilege to collaborate with many incredible scientists from other universities. Joris and Hanne, infinite thanks for opening the world of magic by visualizing our self-healing molecules with your home-built LSI instrument. Apart from being a part of exciting, professional and inspiring science, it was a pure pleasure to communicate and spend time with kind and fun individuals you are. I would also like to thank Kay and Anton for their devoted contribution in discovering the smallest scale motions of self-healing, all their fast throughout responses and efforts leading to a proud publication in *Macromolecules*. I owe my immense gratitude to Ranjita, Antonio, Marianella, Johan and Maruti for sharing their expertise with me patiently and generously through the first years. Your contribution was certainly a foundation of this thesis.

Working in the aircraft hall wouldn't be the joyful experience it is without its people. Berthil, Gertjan, Johan, Misja, Victor, Johan, Marianne and Frans, big thanks for always being ready to help with a warm smile. Marianne, thanks for all our wonderful conversations and hugs. Gertjan, thanks for all your creative and immediate solutions, your energy and positivity always made my day brighter. Frans, I will never forget our endless SEM sessions where you used to make me laugh till my stomach hurts. Thank you also for saving me from bleeding out when I tested the self-healing kinetics of my own hand. Peter, Rob and Ed from the DEMO workshop thank you for readily materializing my every weird idea, and there were quite some. Special thanks to Fabrício from the FabAS team, for being crazy enough to jump along with me on a train called Last Chapter In A Field Outside Of My Expertise. We had the most incredible last PhD months of whole-day camping in the aircraft hall, broken bones, endless data analyses, relieving stress with fun and dance, desperation and (hysterical) laughter. Apart from being the most patient mentor of all times, thanks for being an amazing friend above all. Shanta, dear NovAM mama, thank you for so many things...for all the fun, conversations, sobering advices, solving problems, hugs, bringing me up on my feet too many times, for believing in me and helping me believe in myself too. Thank you for making sure that NovAM functions as a family above all.

Huge thanks to all the NovAM people, NovAM refugees, spouses and friends: Hari, Ugo, Mladen, Casper, Anna, Ann-Sophie, Jasper, Jelmer, Kevin, Željka, Slaviša, Zoran, Michiel, Jimmy, Hamideh, Taylor, Tomasso, Christian, Kimberly, Pui, Alex, Marlies, Hongli, Hussein, Paul, Giorgos, Vincenzo, Amael, Evelien, Silvia, Kleopatra, Amber, Big and Small Adri, Prem, Manas, Wandong, Nikos, Eirini, Ilias, Tian, Zahid, Niels, Pedro, Lucas, Chirag, Nicolas, Clemens, Calvin, Marcías, Michiel, Johan, Fardin, and others I might have forgotten, for all the fun we had together during lunches, coffee break, parties, RPK courses and every Atmosfeer Friday, which always turned lemons into beers. Wouter Post, Michael, Birdie, Nan, Martino and Daniella, you were the best fellows one can ask for. We were each other's brothers, sisters, tutors, psychologists and pain-killers on a daily basis, thanks so much for everything. I would also like to thank Sarav for all the good days filled with great jokes, amazing food and traveling, there were many. Miljen Martić, Filip Biljecki and Jure Zlopaša, thanks for all your help prior to my arrival to the Netherlands, as well as to Pavla for making my new life in Utrecht feeling more like home. Many thanks to all my colleagues at Wageningen Food and Biobased Research for their support during the thesis writing period.

I owe my laughing wrinkles and emotional health to my BBs Jelena and Gaytrie, Marija Mučibabić zvana Maki and Sapatao. Ladies, I am pretty sure I would not make it this far without you bringing me up on my feet so many times, also literally. You help me realize my own strength. Vi ste mi pokazale 'Gde Su Mi Krila'. I am so lucky that leaving Croatia behind never affected my life-long friendships with many many wonderful people. Hvala Lejla, Ana, Darija, Melita, Danči, Marina, Splećo, Škeki, Buraz Ante, Pavlin, Draks, Orač, Gogi, Jelena, Kiki, Darac and all the friends from Pivnica Gaj for believing in me, being proud of me and pretending to understand what I am talking about with eyes wide open in awe. Thanks for never let us feel like strangers, even if we were spending only a few weeks per year together. Hvala što postojite. Ljubav.

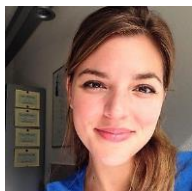
Another proof that time spent together doesn't reflect the quality of relationships are Tim and his family, Visjes and The FenOmmenals: Marijke, Fred, Sander, Funda, Felix, Rob, Arie and Truus. Even though I met you only one year ago, you have brought such ease and joy into my (thesis-writing-stage of) life. Dank jullie wel for including me so warmly into your lives, as well as for your encouragement and support about finishing the thesis.

Tim, thank you for introducing me back to certain long-neglected aspects of life: relaxation, culture, fun and ease of being myself. Thank you for your magical optimism, warmth, care, encouragement and patience during the thesis writing months, which made it so much more bearable. Thanks also for your professional touch in making this book a lot prettier than it would originally be.

In the end, it all comes back to the beginning: family, my pillars. Endless HVALA to Kukec, Uzelac and Suša families, adored late nona Aliče who was always my devoted cheerleader, especially my brother Armando and my mother Doris for their unconditional love and support. Mami, beskrajna hvala na svoj snazi, volji, ljubavi, savjetima i što si nas uzdigla iz pepela u nebeske visine. Ovaj doktorat je u tvoju čast, ništa drugo nego još jedan dokaz da smo nezaustavljivi!

Šta 'ne može' ?? Tko je rekao da ne može ??

Curriculum Vitae



Arijana Suša was born on January 20th, 1986 in Rijeka, Croatia where she obtained her Gymnasium degree at Prva Sušačka Hrvatska Gimnazija in 2004. She studied Sanitary Engineering at the Faculty of Medicine, University of Rijeka until 2006, when she moved to the University of Zagreb. She obtained her BSc degree in Chemical Engineering in 2010 from the Faculty of Chemical Engineering and Technology, having followed a Chemistry and Materials Engineering course. Her BSc thesis reported research conducted on predicting the lifespan of polymers upon cyclic loading. As a part of her BSc program, she did an internship at the quality control department of DIOKI-Organic Petrochemicals and Polymers Factory in Zagreb.

She continued with an MSc study in Chemical Engineering at the same Faculty. During that period, she conducted a student research project on novel copolymer synthesis, compounding and characterization, for insulating coatings applications. In 2012 she obtained her MSc degree in Chemical Engineering, with a thesis on isothermal crystallization behaviour of polylactic acid nanocomposites.

She started pursuing her PhD in July 2013 at Delft University of Technology, Faculty of Aerospace Engineering. There she joined the Novel Aerospace Materials group to study under the supervision of Professor Sybrand van der Zwaag and Associate Professor Santiago García.

She presented her PhD work at four national and two international conferences and published a book chapter and several peer-reviewed articles in high-impact journals. Having successfully completed four modules of National Dutch Graduate School of Polymer Science and Technology (PTN) courses, she obtained the title of Accredited Polymer Scientist (RPK) in 2016.

In October 2017 she started working as a research project leader at the Wageningen Food and Biobased Research institute, in the Sustainable Chemistry group of the Biobased Products unit.

List of publications

Journal publications

A. Susa, A. Mordvinkin, K. Saalwächter, S. van der Zwaag, S. J. García
Identifying the Role of Primary and Secondary Interactions on the Mechanical Properties and Healing of Densely Branched Polyimides
Macromolecules **2018**, 51 (21), 8333–8345

A. Susa, J. Bijleveld, M. Hernandez Santana, S. J. García
Understanding the Effect of the Dianhydride Structure on the Properties of Semiaromatic Polyimides Containing a Biobased Fatty Diamine
ACS Sustainable Chemistry and Engineering **2018**, 6 (1), 668-678

H. M. van der Kooij, **A. Susa**, S. J. García, S. van der Zwaag, J. Sprakel
Imaging the Molecular Motions of Autonomous Repair in a Self-Healing Polymer
Advanced Materials **2017**, 29 (26), 1701017

A. Susa, R. K. Bose, A. M. Grande, S. van der Zwaag, S. J. García
Effect of the Dianhydride/Branched Diamine Ratio on the Architecture and Room Temperature Healing Behavior of Polyetherimides
ACS Applied Materials and Interfaces **2016**, 8 (49), 34068-34079

Book chapter

A. Susa, S. van der Zwaag, S. J. García
Room Temperature Self-Healing Polyetherimides Based on a Long Chain Aliphatic Diamine
Self-Healing Materials: Pioneering research in the Netherlands, 2015, IOS Press,
pp. 19-26

Selected conference contributions

* presenting author

A. Susa*, S. van der Zwaag, S. J. García

Oral presentation: *The development of a self-healing polyetherimide and its underlying healing principle*

6th International Conference on Self-Healing Materials, Friedrichshafen, Germany, June 2017

A. Susa*, S. van der Zwaag, S. J. García

Oral (plenary) presentation: *The development of a self-healing polyetherimide and its underlying healing principle*

Dutch Polymer Days, Lunteren, The Netherlands, March 2017

A. Susa*, S. van der Zwaag, S. J. García

Poster presentation: *Robust Elastomeric Autonomous SH PEIs*

Dutch Polymer Days, Lunteren, The Netherlands, March 2016

A. Susa*, S. van der Zwaag, S. J. García

Oral presentation: *Effect of the stoichiometry on the healing of an aromatic-aliphatic PEI*

5th International Conference on Self-Healing Materials, Durham, USA, June 2015

A. Susa*, S. van der Zwaag, S. J. García

Oral presentation: *Self-Healing Polyimides from Renewable Resources*

IOP SHM symposium, Gouda, The Netherlands, October 2014

A. Susa, S. van der Zwaag, S. J. García*

Oral presentation: *The Role of Polymer Architecture in Tailoring SH PIs Properties*

Coatings Science International, Noordwijk, The Netherlands, June 2014

